

# Deep learning methods for the estimation of preload and physiological control of heart assist devices

**Author:**

Fetanat Fard Haghghi, Masoud

**Publication Date:**

2021

**DOI:**

<https://doi.org/10.26190/unswworks/24669>

**License:**

<https://creativecommons.org/licenses/by/4.0/>

Link to license to see what you are allowed to do with this resource.

Downloaded from <http://hdl.handle.net/1959.4/100962> in <https://unswworks.unsw.edu.au> on 2024-12-20

# **Deep learning methods for the estimation of preload and physiological control of heart assist devices**

Masoud Fetanat

A thesis in fulfilment of the requirements for the degree of  
**Doctor of Philosophy**



Graduate School of Biomedical Engineering  
Faculty of Engineering  
The University of New South Wales  
February 2021



# Thesis/Dissertation Sheet

Surname/Family Name	:	Fetanat
Given Name/s	:	Masoud
Abbreviation for degree as give in the University calendar	:	PhD
Faculty	:	Engineering
School	:	Graduate School of Biomedical Engineering
Thesis Title	:	Deep learning methods for the estimation of preload and physiological control of heart assist devices

## Abstract (350 words maximum)

Heart failure (HF) is one of the most prevalent life-threatening cardiovascular diseases, affecting more than 23 million worldwide. Although heart transplantation is the gold standard treatment for end-stage HF patients, the number of donor hearts is significantly less than the demand. Mechanical circulatory support for a patient with a failing left ventricle can be achieved by implanting a left ventricular assist device (LVAD) by pumping blood from the left ventricle to the aorta. Currently, clinicians set the LVAD speed at a fixed value, which can lead to different hazardous events. A physiological control system (PCS), which automatically adjusts pump speed can mitigate the hazardous events and improve a patient's mobility, lifespan and quality of life. However, there are two main reasons that the current PCSs are not used commercially. Firstly, previously developed PCSs have been evaluated in specific conditions for only single-patient scenarios. Secondly, previously developed PCSs require implanted pressure or flow sensors. Therefore, the aim of this thesis was to design novel methods for estimation of preload and sensorless PCS for LVADs than can accommodate interpatient and intrapatient variations (IAIV), by way of three objectives. The first objective was to design a PCS for an implantable heart pump that accommodates IAIV. A novel model free adaptive control (MFAC) system was developed that maintained the preload in the normal range of 3 to 15 mmHg for different patient conditions. The second objective was to design a sensorless PCS for LVADs across different patient conditions, by combining a preload estimator using a deep learning method and the MFAC. The third objective was to design an improved non-invasive preload estimator, based on deep learning methods using LVAD flow waveforms recorded clinically. The proposed preload estimator was extremely accurate with a correlation coefficient of 0.97 and root mean squared error of 0.84 mmHg. The proposed sensorless PSC works similarly to the preload-based PCS using measured preload to prevent suction and congestion. This study shows that the LVADs can respond appropriately to changing patient states and physiological demands without the need for additional implanted sensors.

## Declaration relating to disposition of project thesis/dissertation

I hereby grant to the University of New South Wales or its agents a non-exclusive licence to archive and to make available (including to members of the public) my thesis or dissertation in whole or in part in the University libraries in all forms of media, now or here after known. I acknowledge that I retain all intellectual property rights which subsist in my thesis or dissertation, such as copyright and patent rights, subject to applicable law. I also retain the right to use all or part of my thesis or dissertation in future works (such as articles or books).

Signature

Date

The University recognises that there may be exceptional circumstances requiring restrictions on copying or conditions on use. Requests for restriction for a period of up to 2 years can be made when submitting the final copies of your thesis to the UNSW Library. Requests for a longer period of restriction may be considered in exceptional circumstances and require the approval of the Dean of Graduate Research.

## ORIGINALITY STATEMENT

'I hereby declare that this submission is my own work and to the best of my knowledge it contains no materials previously published or written by another person, or substantial proportions of material which have been accepted for the award of any other degree or diploma at UNSW or any other educational institution, except where due acknowledgement is made in the thesis. Any contribution made to the research by others, with whom I have worked at UNSW or elsewhere, is explicitly acknowledged in the thesis. I also declare that the intellectual content of this thesis is the product of my own work, except to the extent that assistance from others in the project's design and conception or in style, presentation and linguistic expression is acknowledged.'

Signed

Date:

## COPYRIGHT STATEMENT

'I hereby grant the University of New South Wales or its agents a non-exclusive licence to archive and to make available (including to members of the public) my thesis or dissertation in whole or part in the University libraries in all forms of media, now or here after known. I acknowledge that I retain all intellectual property rights which subsist in my thesis or dissertation, such as copyright and patent rights, subject to applicable law. I also retain the right to use all or part of my thesis or dissertation in future works (such as articles or books).' 'For any substantial portions of copyright material used in this thesis, written permission for use has been obtained, or the copyright material is removed from the final public version of the thesis.'

Signed

Date:

## AUTHENTICITY STATEMENT

'I certify that the Library deposit digital copy is a direct equivalent of the final officially approved version of my thesis.'

Signed

Date:

## Inclusion of Publications Statement

UNSW is supportive of candidates publishing their research results during their candidature as detailed in the UNSW Thesis Examination Procedure.

**Publications can be used in their thesis in lieu of a Chapter if:**

- The candidate contributed greater than 50% of the content in the publication and is the “primary author”, ie. the candidate was responsible primarily for the planning, execution and preparation of the work for publication
- The candidate has approval to include the publication in their thesis in lieu of a Chapter from their supervisor and Postgraduate Coordinator.
- The publication is not subject to any obligations or contractual agreements with a third party that would constrain its inclusion in the thesis

Please indicate whether this thesis contains published material or not:

- This thesis contains no publications, either published or submitted for publication  
*(if this box is checked, you may delete all the material on page 2)*
- Some of the work described in this thesis has been published and it has been documented in the relevant Chapters with acknowledgement  
*(if this box is checked, you may delete all the material on page 2)*
- This thesis has publications (either published or submitted for publication) incorporated into it in lieu of a chapter and the details are presented below

**CANDIDATE'S DECLARATION**

I declare that:

- I have complied with the UNSW Thesis Examination Procedure
- where I have used a publication in lieu of a Chapter, the listed publication(s) below meet(s) the requirements to be included in the thesis.

<b>Candidate's Name</b>	<b>Signature</b>	<b>Date (dd/mm/yy)</b>
Masoud Fetanat		

**POSTGRADUATE COORDINATOR'S DECLARATION**

I declare that:

- the information below is accurate
- where listed publication(s) have been used in lieu of Chapter(s), their use complies with the UNSW Thesis Examination Procedure
- the minimum requirements for the format of the thesis have been met.

<b>PGC's Name</b>	<b>PGC's Signature</b>	<b>Date (dd/mm/yy)</b>

For each publication incorporated into the thesis in lieu of a Chapter, provide all of the requested details and signatures required.

<b>Details of publication #1:</b>						
<p><b>Full title:</b> Physiological Control System for an Implantable Heart Pump that Accommodates for Interpatient and Intrapatient Variations</p> <p><b>Authors:</b> Masoud Fetanat, Michael Stevens, Christopher Hayward, Nigel H. Lovell</p> <p><b>Journal or book name:</b> IEEE Transactions on Biomedical Engineering</p> <p><b>Volume/page numbers:</b> Volume 67, Issue 4, pages 1167-1175</p> <p><b>Date accepted/ published:</b> Published, April 2020</p>						
Status	Published	X	Accepted and in press		In progress (submitted)	
<b>The Candidate's Contribution to the Work</b>						
Masoud Fetanat designed the methods, performed the simulations and data analysis, wrote and edited the paper.						
<b>Location of the work in the thesis and/or how the work is incorporated in the thesis:</b>						
This article has been used as Chapter 3 in this thesis.						
<b>PRIMARY SUPERVISOR'S DECLARATION</b>						
I declare that:						
<ul style="list-style-type: none"> <li>• the information above is accurate</li> <li>• this has been discussed with the PGC and it is agreed that this publication can be included in this thesis in lieu of a Chapter</li> <li>• All of the co-authors of the publication have reviewed the above information and have agreed to its veracity by signing a 'Co-Author Authorisation' form.</li> </ul>						
<b>Primary Supervisor's name</b>	<b>Primary Supervisor's signature</b>			<b>Date (dd/mm/yy)</b>		

**Details of publication #2:**

**Full title:** A Sensorless Control System for an Implantable Heart Pump using a Real-time Deep Convolutional Neural Network

**Authors:** Masoud Fetanat, Michael Stevens, Christopher Hayward, Nigel H. Lovell

**Journal or book name:** IEEE Transactions on Biomedical Engineering

**Volume/page numbers:** Volume 68, Issue 10, pages 3029-3038

**Date accepted/ published:** Published, 2021

Status	Published	X	Accepted and in press		In progress (submitted)	
--------	-----------	---	-----------------------	--	-------------------------	--

**The Candidate's Contribution to the Work**

Masoud Fetanat designed the methods, performed the simulations and data analysis, wrote and edited the paper.

**Location of the work in the thesis and/or how the work is incorporated in the thesis:**

This article has been used as Chapter 4 in this thesis.

**PRIMARY SUPERVISOR'S DECLARATION**

I declare that:

- the information above is accurate
- this has been discussed with the PGC and it is agreed that this publication can be included in this thesis in lieu of a Chapter
- All of the co-authors of the publication have reviewed the above information and have agreed to its veracity by signing a 'Co-Author Authorisation' form.

Primary Supervisor's name	Primary Supervisor's signature	Date (dd/mm/yy)
---------------------------	--------------------------------	-----------------

**Details of publication #3:**

**Full title:** Fully Elman Neural Network: A Novel Deep Recurrent Neural Network Optimized by an Improved Harris Hawks Algorithm for Classification of Pulmonary Arterial Wedge Pressure.

**Authors:** Masoud Fetanat, Michael Stevens, Pankaj Jain, Christopher Hayward, Erik Meijering and Nigel H. Lovell

**Journal or book name:** IEEE Transactions on Biomedical Engineering

**Volume/page numbers:** Volume 69, Issue 5, pages 1733-1744

**Date accepted/published:** Published, 2022

Status	Published	X	Accepted and in press	In progress (submitted)	
--------	-----------	---	-----------------------	-------------------------	--

**The Candidate's Contribution to the Work**

Masoud Fetanat designed the methods, performed the simulations and data analysis, wrote and edited the paper.

**Location of the work in the thesis and/or how the work is incorporated in the thesis:**

This article has been used as Chapter 5 in this thesis.

**PRIMARY SUPERVISOR'S DECLARATION**

I declare that:

- the information above is accurate
- this has been discussed with the PGC and it is agreed that this publication can be included in this thesis in lieu of a Chapter
- All of the co-authors of the publication have reviewed the above information and have agreed to its veracity by signing a 'Co-Author Authorisation' form.

Primary Supervisor's name	Primary Supervisor's signature	Date (dd/mm/yy)
---------------------------	--------------------------------	-----------------

## Abstract

Heart failure (HF) is one of the most prevalent life-threatening cardiovascular diseases, affecting 6.5 million people in the USA and more than 23 million worldwide. Although heart transplantation is the gold standard treatment for end-stage HF patients, the number of donor hearts is significantly less than the demand for heart transplantation and therefore the mortality of people on the waitlist is high. Mechanical circulatory support for a patient with a failing left ventricle can be achieved by implanting a left ventricular assist device (LVAD) as a bridge to transplant, bridge to recovery or destination therapy by pumping blood from the left ventricle to the aorta. Currently, clinicians set the LVAD speed at a fixed value, which can lead to hazardous events such as insufficient cardiac perfusion, ventricular suction or pulmonary congestion. A physiological control system, which automatically adjusts pump speed according to hemodynamic variations or pump variables, can mitigate these hazardous events and improve a patient's mobility, lifespan and quality of life. Researchers have been developing physiological control systems for LVADs for the last 30 years, however there are none used commercially, for two reasons. Firstly, previously developed physiological control systems have been evaluated in specific conditions for single-patient scenarios, and so there is still no physiological control system which has been shown to reliably work across different patient conditions or for different patients. Secondly, previously developed physiological control systems require pressure or flow sensors implanted into the HF patient's body. However, there are several challenges

with using these sensors such as drift, additional power consumption, interference from radiation, thrombus formation and device failure. Therefore, the aim of this thesis was to design and develop novel methods for estimation of preload, and a sensorless physiological control system for a LVAD that can accommodate interpatient and intrapatient variations, by way of three objectives.

The first objective was to design a physiological control system for an implantable heart pump that accommodates interpatient and intrapatient variations. A novel adaptive physiological control system was developed that maintained the left-ventricular-end-diastolic-pressure (LVEDP) in the normal range of 3 to 15 mmHg to prevent ventricular suction and pulmonary congestion. Model-free adaptive control (MFAC) was employed to control the pump speed and provide consistent control performance regardless of the patient condition. It was evaluated via simulation of 100 different patient conditions in six different patient scenarios and compared to standard proportional-integral-derivative (PID) control. Controller performance was tracked using the sum of the absolute error (SAE) between the desired and measured LVEDP. In four out of six patient scenarios, MFAC tracking performance was better than the PID controller. The control performance can therefore be guaranteed across different patients and conditions when using MFAC over PID control. The limitation of this study is that the left ventricular pressure must be measured. However, currently, there is no long-term implantable sensor for LV pressure measurement.

The second objective was to design a sensorless physiological control system for LVADs across different patient conditions, by combining the MFAC system and the preload estimator using a deep learning method. First, a novel real-time deep convolutional neural network (CNN) for estimation of preload based on the LVAD flow was proposed. Second, a new sensorless adaptive physiological control system for an LVAD pump was developed using the full dynamic form of model free adaptive control (FFDL-MFAC) and the proposed preload estimator to maintain the patient conditions in safe physiological ranges. The CNN model for preload estimation was trained and evaluated through 10-fold cross validation on 100 different simulated patient conditions and the proposed sensorless control system was assessed on a new testing set of 30 different patient conditions across six different patient scenarios. The proposed preload estimator was extremely accurate with a correlation coefficient of 0.97, root mean squared error of 0.84 mmHg, reproducibility coefficient of 1.56 mmHg, coefficient of variation of 14.44 %, and bias of 0.29 mmHg for the testing dataset. The results also indicate that the proposed sensorless physiological controller works similarly to the preload-based physiological control system using measured preload to prevent ventricular suction and pulmonary congestion. This study shows that the LVADs can respond appropriately to changing patient states and physiological demands without the need for additional pressure or flow measurements.

The third objective was to design an improved non-invasive preload estimator using advanced machine and deep learning methods based on the pump variables derived from a clinical dataset. Although measuring preload for heart

HF patients is a difficult task, it can be indirectly measured by pulmonary arterial wedge pressure (PAWP). Therefore, a method of estimating PAWP was developed. First, an improved Harris Hawks optimizer algorithm called HHO+ is presented and tested on 24 unimodal and multimodal benchmark functions. Second, a novel fully Elman neural network (FENN) was proposed to improve the classification performance. Finally, four 18-layer deep learning methods comprising of a convolutional neural network (CNN) with multi-layer perceptron (CNN-MLP), a CNN with Elman neural networks (CNN-ENN), a CNN with fully Elman neural networks (CNN-FENN), and a CNN with fully Elman neural networks optimized by HHO+ algorithm (CNN-FENN-HHO+) were developed and evaluated for the classification of abnormal and normal PAWP. The proposed methods were evaluated on an imbalanced clinical dataset using 10-fold cross-validation. The proposed CNN-FENN-HHO+ method outperformed the CNN-MLP, CNN-ENN and CNN-FENN methods and improved the classification performance metrics with an average sensitivity of 89.82%, accuracy of 88.86% and specificity of 86.08 %. The proposed methods can reduce the likelihood of hazardous events like pulmonary congestion and ventricular suction for HF patients and notify identified abnormal cases to the hospital, clinician and cardiologist for emergency action, which can decrease the mortality rate of HF patients. Therefore, the CNN-FENN-HHO+ is the most suitable approach for developing an estimator for preload.

Future work will include validating the proposed preload estimator and the sensorless physiological controller in more detail with in-vitro, in-vivo and clinical experiments.

**Keywords:** Deep learning, physiological control systems, left ventricular assist devices, machine learning, convolutional neural networks, sensorless control, Elman neural network, model free adaptive control, recurrent neural networks, pulmonary arterial wedge pressure, heart assist devices and Harris Hawks optimizer.

## Acknowledgements

I would like to greatly appreciate my supervisors Dr. Michael Stevens and Prof. Nigel Lovell for their guidance and support throughout my PhD studies and this thesis. I have thoroughly learnt and enjoyed in the last few years and have gained so much from them personally and professionally. Thank you for all your time, supports and advice during my PhD studies.

I would also like to thank Prof. Christopher Hayward at the department of Cardiology, St Vincent's hospital for his guidance and clinical input into this thesis. His valuable insights regarding ventricular assist devices have improved this study. I would like to appreciate Prof. Erik Meijering for his guidance on the developed machine learning algorithms in this thesis.

I would like to thank all my friends and colleagues at UNSW, especially Dr. Parisa Moazzam, Dr. Arash Khatamianfar, Gabriel Matus Vazquez and Farzaneh Ziae. I have learnt many things from each of them.

I would like to really acknowledge my parents throughout my whole life.

I would like to thank Australia National Health and Medical Research Council Centers for Research Excellence and Graduate School of Biomedical Engineering at UNSW for their financial support throughout my candidature.

# Table of Contents

LIST OF PUBLICATIONS .....	XX
LIST OF FIGURES .....	XXIII
LIST OF TABLES .....	XXXIII
LIST OF ABBREVIATIONS AND SYMBOLS .....	XXXV
CHAPTER 1. INTRODUCTION .....	1
1.1 AIM AND OBJECTIVES .....	5
1.2 RESEARCH BACKGROUND .....	6
1.2.1 <i>Cardiac cycle</i> .....	6
1.2.2 <i>The heart</i> .....	9
1.2.3 <i>The Circulatory system</i> .....	11
1.2.4 <i>The Frank-Starling mechanism of the healthy heart</i> .....	14
1.2.5 <i>Heart failure</i> .....	16
1.2.6 <i>Treatment of heart failure</i> .....	16
1.3 THESIS OUTLINE .....	17
CHAPTER 2. LITERATURE REVIEW .....	20
2.1 GENERATIONS OF VENTRICULAR ASSIST DEVICES .....	21
2.2 EVALUATION PLATFORMS FOR PHYSIOLOGICAL CONTROL OF LVAD .....	25
2.2.1 <i>Numerical models (in silico study)</i> .....	25
2.2.2 <i>Mock circulation loops (in vitro study)</i> .....	27
2.2.3 <i>Animal tests (in vivo study)</i> .....	30
2.2.4 <i>Clinical trials</i> .....	31
2.3 PHYSIOLOGICAL CONTROL OF LVADS .....	32
2.3.1 <i>Differential pressure control (<math>\Delta P</math> control)</i> .....	33
2.3.2 <i>Aortic pressure control (Afterload control)</i> .....	35
2.3.3 <i>Left ventricular end diastolic pressure control (Preload control)</i> .....	37
2.3.4 <i>Left ventricular systolic pressure control (SP control)</i> .....	39
2.3.5 <i>Flow control</i> .....	40
2.3.6 <i>Frank-Starling control (FS control)</i> .....	41
2.3.7 <i>Left ventricular volume control (LVV control)</i> .....	44

2.3.8 Multi-objective control (MO control) .....	47
2.4 TYPES OF CONTROLLER IMPLEMENTATION .....	53
2.4.1 Proportional-Integral-Derivative controller (PID controller) .....	53
2.4.2 Model predictive controller (MPC) .....	54
2.4.3 Fuzzy logic controller (FL controller).....	55
2.4.4 Adaptive controller.....	57
2.5 NON-INVASIVE ESTIMATION, MONITORING AND CONTROL APPROACHES FOR LVAD .....	58
2.5.1 Pump flow estimation .....	59
2.5.2 Ventricular suction detection .....	62
2.5.3 Aortic valve (AoV) status detection .....	63
2.5.4 Pressure estimation.....	64
2.5.5 Estimation of patient activities .....	65
2.5.6 Sensorless physiological control systems .....	66
2.6 INTRODUCTION TO MACHINE AND DEEP LEARNING .....	67
2.6.1 Convolution operation layer.....	69
2.6.2 Pooling operation layer.....	70
2.6.3 Fully connected layer.....	71
2.6.4 ReLU Layer.....	72
2.7 CONCLUSION .....	72
<b>CHAPTER 3. A PHYSIOLOGICAL CONTROL SYSTEM FOR AN IMPLANTABLE HEART PUMP THAT ACCOMMODATES FOR INTERPATIENT AND INTRAPATIENT VARIATIONS.....</b>	<b>75</b>
3.1 ABSTRACT .....	76
3.2 INTRODUCTION.....	77
3.3 METHODOLOGY.....	80
3.3.1 Numerical model of cardiovascular system.....	80
3.3.2 Real-time LVEDP detection.....	82
3.3.3 Model free adaptive control (MFAC).....	86
3.3.4 Different patient condition and scenarios .....	89
3.3.5 MFAC evaluation .....	93
3.4 RESULTS.....	95
3.4.1 LVEDP detection .....	95
3.4.2 Sensitivity analysis.....	102
3.4.3 MFAC evaluation .....	103

3.5 DISCUSSION .....	107
3.6 CONCLUSION .....	113
3.7 ACKNOWLEDGMENT .....	113
<b>CHAPTER 4. A SENSORLESS CONTROL SYSTEM FOR AN IMPLANTABLE HEART PUMP USING A REAL-TIME DEEP CONVOLUTIONAL NEURAL NETWORK.....</b>	<b>114</b>
4.1 ABSTRACT .....	115
4.2 INTRODUCTION.....	116
4.3 METHODOLOGY.....	120
<i>4.3.1 Model of Cardiovascular System and LVAD .....</i>	<i>120</i>
<i>4.3.2 Deep Convolutional Neural Network for Preload Estimation .....</i>	<i>122</i>
<i>4.3.3 Full Dynamic Form of Model Free Adaptive Control (FFDL-MFAC).....</i>	<i>126</i>
<i>4.3.4 Different Patient Conditions and Scenarios.....</i>	<i>131</i>
<i>4.3.5 Evaluation of Sensorless Control .....</i>	<i>135</i>
4.4 RESULTS.....	137
<i>4.4.1 Preload Estimation Using Deep Convolutional Neural Network .....</i>	<i>137</i>
<i>4.4.2 Evaluation of Sensorless Control Using Deep Convolutional Neural Network and FFDL-MFAC ..</i>	<i>139</i>
4.5 DISCUSSION .....	142
4.6 CONCLUSION .....	149
4.7 ACKNOWLEDGMENT .....	149
<b>CHAPTER 5. FULLY ELMAN NEURAL NETWORK: A NOVEL DEEP RECURRENT NEURAL NETWORK OPTIMIZED BY AN IMPROVED HARRIS HAWKS ALGORITHM FOR CLASSIFICATION OF PULMONARY ARTERIAL WEDGE PRESSURE.....</b>	<b>150</b>
5.1 ABSTRACT .....	151
5.2 INTRODUCTION.....	152
5.3 METHODOLOGY.....	158
<i>5.3.1 Dataset .....</i>	<i>158</i>
<i>5.3.2 Data pre-processing .....</i>	<i>158</i>
<i>5.3.3 Background materials .....</i>	<i>159</i>
<i>5.3.3.1 The Harris Hawks optimizer (HHO).....</i>	<i>159</i>
<i>5.3.3.2 Exploration phase.....</i>	<i>160</i>
<i>5.3.3.3 Transition from exploration to exploitation .....</i>	<i>161</i>
<i>5.3.3.4 Exploitation phase.....</i>	<i>161</i>
<i>5.3.3.5 Convolutional neural network with multi-layer perceptron (CNN-MLP).....</i>	<i>167</i>

5.3.3.6 Elman neural network (ENN).....	170
5.3.4 <i>The improved Harris Hawks algorithm (HHO+)</i> .....	172
5.3.4.1 Improving exploration and exploitation algorithm (IEEA) .....	172
5.3.4.2 Quasi-oppositional based learning (QOBL).....	176
5.3.4.3 The proposed HHO+ .....	177
5.3.5 <i>The proposed fully Elman neural network (FENN)</i> .....	180
5.3.6 <i>The proposed combined CNN with fully Elman neural network (FENN) and improved Harris Hawks optimizer algorithm (CNN-FENN and CNN-FENN-HHO+)</i> .....	183
5.3.7 <i>Experimental setup, structure and parameters of HHO+, CNN-FENN and CNN-FENN-HHO+</i> .....	186
5.3.8 <i>Performance evaluation metrics</i> .....	197
5.3.9 <i>K-fold stratified cross validation</i> .....	197
5.3.10 <i>Loss function</i> .....	198
5.4 RESULTS.....	199
5.4.1 <i>Benchmark function validation</i> .....	199
5.4.2 <i>Application of the proposed FENN and HHO+ on the classification of pulmonary arterial wedge pressure</i> .....	210
5.5 DISCUSSION .....	210
5.6 CONCLUSION .....	213
5.7 ACKNOWLEDGEMENT .....	214
<b>CHAPTER 6. CONCLUSION, LIMITATIONS AND FUTURE WORK .....</b>	<b>215</b>
6.1 CONCLUSIONS .....	216
6.2 THESIS LIMITATIONS .....	218
6.3 FUTURE WORK .....	219
<b>REFERENCES.....</b>	<b>220</b>

# List of Publications

## Journal publications

- **M. Fetanat**, M. Stevens, P. Jain, C. Hayward, Erik Meijering, and N. H. Lovell, “Fully Elman Neural Network: A Novel Deep Recurrent Neural Network Optimized by an Improved Harris Hawks Algorithm for Classification of Pulmonary Arterial Wedge Pressure.”, accepted, *IEEE Transactions on Biomedical Engineering*, 2021.
- **M. Fetanat**, M. Stevens, C. Hayward, and N. H. Lovell, “A Sensorless Control System for an Implantable Heart Pump using a Real-time Deep Convolutional Neural Network.”, *IEEE Transactions on Biomedical Engineering*, vol. 68, no. 10, pp. 3029–3038, 2021, doi: [10.1109/TBME.2021.3061405](https://doi.org/10.1109/TBME.2021.3061405).
- **M. Fetanat**, M. Stevens, C. Hayward, and N. H. Lovell, “A Physiological Control System for an Implantable Heart Pump That Accommodates for Interpatient and Intrapatient Variations.” *IEEE Transactions on Biomedical Engineering*, vol. 67, no. 4, pp. 1167–1175, 2020, <https://doi.org/10.1109/tbme.2019.2932233>.

## Conference abstracts

- **M. Fetanat**, M. Stevens, C. Hayward, and N. Lovell, “Aortic valve status detection for heart failure patient with LVAD using deep neural networks,” *The Journal of Heart and Lung Transplantation*, vol. 40, no. 4, p. S178, 2021, doi: [10.1016/j.healun.2021.01.522](https://doi.org/10.1016/j.healun.2021.01.522).

- **M. Fetanat**, M. Stevens, C. Hayward, and N. Lovell, “Adaptive sensorless control of LVAD using deep convolutional neural network,” *The Journal of Heart and Lung Transplantation*, vol. 40, no. 4, p. S172, 2021, doi: 10.1016/j.healun.2021.01.507.
- **M. Fetanat**, M. Stevens, C. Hayward, P. Jain and N. H. Lovell, “Classification of Abnormal and Normal Pulmonary Arterial Wedge Pressure using a Deep Learning method.” *The International Journal of Artificial Organs*, vol. 42, no. 8, p. 401, 2020.
- S. Emmanuel, M. Stevens, GM Vazquez, **M. Fetanat**, A. Al. Abed, N. Lovell, C. Hayward, “A Novel Means of Mechanical Circulatory Support Speed Variation: Utilizing the Sino-Atrial Node.” *The Journal of Heart and Lung Transplantation*, vol. 39, no. 4, S412-S413, 2020, <https://doi.org/10.1016/j.healun.2020.01.176>
- **M. Fetanat**, M. Stevens, C. Hayward, and N. H. Lovell. “LAP Estimation Based on Heart Pump Characteristics Using Machine Learning Approach.” *The International Journal of Artificial Organs*, vol. 42, no. 8, p. 401, 2019.
- X. Yeong, N. Rainnie, D. Robson, S. Shehab, A. Doyle, **M. Fetanat**, K. Muthiah, et al. “Acoustic Characterisation of the HeartWare Left Ventricular Assist Device.” *The Journal of Heart and Lung Transplantation*, vol. 38, no. 4, p. S346, 2019, <https://doi.org/10.1016/j.healun.2019.01.877>.

- **M. Fetanat**, M. Stevens, C. Hayward, N. H. Lovell, “Heart Failure patients can live longer: sensorless Estimation of Left Atrial Pressure using Artificial Intelligence.”, *Postgraduate Symposium UNSW 2019*.
- **M. Fetanat**, M. Stevens, and N. H. Lovell, “Physiological Control System for an LVAD That Can Accommodate Interpatient and Intrapatient Variation.” *Artificial Organs*, vol. 43, no. 9, p. E198, 2019.

## List of Figures

Figure 1-1 Cardiac cycle for left heart side including changes in left atrial pressure (LAP), left ventricular pressure (LVP), aortic pressure (AoP), left ventricular volume (LVV), electrocardiogram (ECG), and phonocardiogram [25].....	8
Figure 1-2 The relationship between left ventricular volume and intraventricular pressure during four phases of the cardiac cycle [25]. .....	9
Figure 1-3 Anatomy of the human heart [25].....	10
Figure 1-4 Human Circulatory System [26]. .....	11
Figure 1-5 Distribution of blood (in percentage of total blood) in the different parts of the circulatory system [25].....	13
Figure 1-6 Normal blood pressures in the different sections of the circulatory system [25].....	13
Figure 1-7 Relationship between left and right ventricular flow and preload as a result of the Frank-Starling mechanism [25].....	14
Figure 1-8 Cardiac output curves for different degrees of maximum sympathetic, normal sympathetic, zero sympathetic and parasympathetic stimulation [25].....	15
Figure 2-1 First generation of ventricular assist devices. Left: Thoratec Implantable VAD (IVAD) (Abbott Laboratories, formerly Thoratec Corporation,	

Pleasanton, CA, USA), Right: Abiomed BVS 5000 (Abiomed Inc., Danvers, MA, USA) [10] .....	22
Figure 2-2 Second generation of ventricular assist devices. Left: HeartMate X (Abbott Laboratories, formerly Thoratec Corporation, Pleasanton, CA, USA), Right: HeartMate II (Abbott Laboratories, formerly Thoratec Corporation, Pleasanton, CA, USA) [10].....	22
Figure 2-3 Third generation of ventricular assist devices. Upper left: HeartWare HVAD (Medtronic Inc., FL, USA), Upper right: Abbott HeartMate 3 (Abbott Laboratories, formerly Thoratec Corporation, Pleasanton, CA, USA), Lower: Berlin Heart INCOR (Berlin Heart GmbH., Berlin, Germany) [10]. .....	23
Figure 2-4 The HeartMate II and its placement in the HF patient's body [10]. .....	24
Figure 2-5 Electrical equivalent circuit analogue of the cardiovascular system and an LVAD. P, pressures; R, resistances; E, elastances (=1/compliances); L, inertances; D, diodes. The model consists of two main components: (1) the cardiovascular model includes left heart, systemic circulation, right heart, pulmonary circulation (la, left atrium; lv, left ventricle, ao, aorta; sa, systemic peripheral vessels, including the arteries and capillaries; sv, systemic veins, including small and large veins; vc, vena cava; ra, right atrium; rv, right ventricle; pa, pulmonary peripheral vessels, including pulmonary arteries and capillaries; pu, pulmonary veins and (2) heart-pump model includes the LVAD and RVAD, (Rin and Rout , inlet and outlet cannulae resistances; Lin and Lout,	

inlet and outlet cannulae inertances; Rlsuc, left suction resistance, Rrsuc, right suction resistance, Rband, banding resistance) [44].....	27
Figure 2-6 (a) Mock circulation loop (MCL) and (b) schematic of MCL with an LVAD. Left atrium (LA), mitral valve (MV), left ventricle (LV), aortic valve (AoV), aortic compliance chamber (AoV), systemic flow meter (SQ), right atrium (RA), tricuspid valve (TV), right ventricle (RV), pulmonary valve (PV), systemic vascular resistance (SVR), systemic venous compliance chamber (SVC), pulmonary arterial compliance chamber (PAC), pulmonary flow meter (PQ), pulmonary vascular resistance valve (PVR), pulmonary venous compliance chamber (PVC), left ventricular assist device (LVAD), left ventricular assist device flow meter (LVADQ) [7], [57].....	29
Figure 2-7 <i>In vivo</i> trial on a pig with an HVAD pump on the evaluation of the physiological control system for LVAD (Taken by Masoud Fetanat). .....	31
Figure 2-8 Block diagram of conventional LVAD operation [10]. .....	32
Figure 2-9 Block diagram of a physiological control system for LVAD [10].....	33
Figure 2-10 Block diagram of the proposed $\Delta P$ control by Giridharan et al. [76]. .....	34
Figure 2-11 Block diagram of the proposed AoP and $\Delta P$ control by Wu et al [40]. Q: pump flow, W: pump speed, V: pump voltage, rm: reference aortic pressure, $PA$ : estimated aortic pressure and e: error between estimated and reference aortic pressure. .....	37

Figure 2-12 Block diagram of the sensorless physiological control of pump inlet pressure by Alomari et al. [86]. r: reference pump inlet pressure, $P$ : estimated mean pump power, $w$ : estimated mean pump speed, $Pin$ : estimated mean pump inlet pressure, $P$ : measured mean pump power, $w$ : measured mean pump speed, $f$ : mean steady-state pump flow and $PWM$ : mean pump pulse with modulation (control input signal).....	39
Figure 2-13 Block diagram of the SP control proposed by Petrou et al. [87]. SP: systolic pressure, $SP_{ref}$ : reference systolic pressure and $N_{ref}$ : reference speed. ....	40
Figure 2-14 Block diagram of the preload-based Starling-like control by Mansouri et al. [16]. CVS: cardiovascular system, <b>HCVS</b> : head pressure, $Q_p$ : pump flow, $QP$ : mean pump flow, $QP_{ref}$ : reference mean pump flow, $w$ : pump speed, $w$ : mean pump speed, $u$ : control input signal and PLVED: left ventricular end-diastolic pressure. ....	43
Figure 2-15 Deltastream DP2 (Medos Medizintechnik AG, Stolberg, Germany) pump-power lookup table [98]. $Rsa$ : systemic arterial resistance. ....	45
Figure 2-16 EDV-stroke work relationship [98]. <b>EDV0</b> : end-diastolic volume at zero pressure, PPLUT: pump-power lookup table and $kprsw$ : gain for adjusting preload recruitable stroke work.....	46
Figure 2-17 The structure of the LVV control proposed by Ochsner et al. [98]. HR: heart rate, EDV: end-diastolic volume, <b>EDV0</b> : end-diastolic volume at zero	

pressure, <b>kprsw</b> : gain for adjusting preload recruitable stroke work, PPLUT: pump-power lookup table and <b>PPdes</b> : desired hydraulic pump power.....	46
Figure 2-18 Schematic of multiobjective physiological control system with four different control objectives [62].....	48
Figure 2-19 Block diagram of the centralized multi-objective control of BiVADs proposed by Koh et al. [38]. FS: Frank-starling and CVS: cardiovascular system.	
.....	52
Figure 2-20 Block diagram of a Proportional-Integral-Derivative (PID) controller [101]. <b>K<sub>p</sub></b> : proportional gain, <b>T<sub>i</sub></b> : integral gain and <b>T<sub>d</sub></b> : derivative gain. ....	53
Figure 2-21 Block diagram of the model predictive controller (MPC) [107]... <td>55</td>	55
Figure 2-22 Structure of a fuzzy rule-based system [108].....	56
Figure 2-23 Block diagram of the fuzzy login controller for pump flow control proposed by Casas et al. [109].....	56
Figure 2-24 Block diagram of adaptive control systems [112]. u: control signal and y: system output.....	57
Figure 2-25 The convolution operator between a filter with the size of $5 \times 5 \times 3$ and an input layer with the size $32 \times 32 \times 3$ resulted in output layer with the size of $28 \times 28 \times 5$ [144].....	70

Figure 2-26  $3 \times 3$  max-pooling operation with the stride size of 1 and 2. The resulted output are layers with the size of  $5 \times 5$  and  $3 \times 3$ , respectively [144].

..... 71

Figure 3-1 Block diagram of developed methodology ..... 80

Figure 3-2 Electrical equivalent circuit analogue of cardiovascular with heart–pump interaction model. P, pressures; R, resistances; E, elastances (=1/compliances); L, inertances; D, diodes. The model consists of two main components: (1) the cardiovascular model includes left heart, systemic circulation, right heart, pulmonary circulation (la, left atrium; lv, left ventricle, ao, aorta; sa, systemic peripheral vessels, including the arteries and capillaries; sv, systemic veins, including small and large veins; vc, vena cava; ra, right atrium; rv, right ventricle; pa, pulmonary peripheral vessels, including pulmonary arteries and capillaries; pu, pulmonary veins and (2) heart-pump model includes the LVAD and RVAD, (Rin and Rout , inlet and outlet cannulae resistances; Lin and Lout, inlet and outlet cannulae inertances; Rlsuc, left suction resistance, Rrsuc, right suction resistance, Rband, banding resistance). The intrathoracic pressure, Pthor was assigned  $-4$  mmHg during closed-chest simulated conditions [44]. ..... 81

Figure 3-3 Real-time LVEDP detection, (a) left ventricle pressure (LVP) in transition from rest to exercise for patient 1 with white noise variance of 2 mmHg, (b) zoomed LVP. ..... 85

Figure 3-4 A sample simulation for comparison of MFAC and PID in transition from rest to exercise for patient 45.....	102
Figure 3-5 Comparison of SAE of MFAC and PID controller in different scenarios via box plot, the central mark (red line) shows the median, and the bottom and top edges (blue lines) of each box show the 25th and 75th percentiles. The whiskers extend to the most extreme data points not considered outliers, and the outliers are plotted individually using the '+' symbol. (a) rising $R_{sa}$ (1300 to 600 dyne.s.cm <sup>-5</sup> ) and falling $R_{sa}$ (1300 to 2600 dyne.s.cm <sup>-5</sup> ) (b) rising $R_{pa}$ (100 to 40 dyne.s.cm <sup>-5</sup> ) and falling $R_{pa}$ (100 to 500 dyne.s.cm <sup>-5</sup> ) (c) transition from rest to exercise and passive postural change. .....	106
Figure 4-1 Block diagram of the proposed sensorless physiological control system for LVAD. $u(k)$ is the control signal (pump speed), and $e(k)$ is the error between reference and estimated preload. $m$ , $d$ and $n$ are the number of delays from pump speed, pump flow and estimated preload, respectively. CNN: convolutional neural network, CVS: cardiovascular system and LVAD: left ventricular assist device. Medtronic Heartware HVAD Illustration, "Reproduced with permission of Medtronic".....	120
Figure 4-2 Electrical equivalent circuit analogue of cardiovascular system with LVAD interaction model. $P$ , pressures; $R$ , resistances; $E$ , elastances ( $=1/compliances$ ); $L$ , inertances; $D$ , diodes. The model consists of two main components: (1) the cardiovascular model includes left heart, systemic circulation, right heart, pulmonary circulation (la, left atrium; lv, left ventricle, ao, aorta; sa, systemic peripheral vessels, including the arteries and capillaries;	

sv, systemic veins, including small and large veins; vc, vena cava; ra, right atrium; rv, right ventricle; pa, pulmonary peripheral vessels, including pulmonary arteries and capillaries; pu, pulmonary veins and (2) LVAD model includes Rin and Rout, inlet and outlet cannulae resistances; Lin and Lout, inlet and outlet cannulae inertances; Rlsuc, left suction resistance, Rrsuc, right suction resistance, Rband, banding resistance. The intrathoracic pressure, Pthor was assigned -4 mmHg during closed-chest simulated conditions [29].

.....121

Figure 4-3 Architecture of the proposed deep CNN model for estimation of preload. 600 samples from the peak of the pump flow signal in each cardiac cycle are fed to the CNN as input. Afterwards, it is followed by four convolutional layers including batch normalization layers. Subsequently, two convolutional, max-pooling layers with stride 2 and batch normalization layers are placed. Then, it is followed by two convolutional layers including batch normalization layers. Finally, fully-connected layers with 100 and 20 neurons, activation function of LeakyReLU and a dropout layer with probability of 20% are then used to estimate preload. .....123

Figure 4-4 A sample simulation for comparison of FFDL-MFAC for measured and estimated preload in falling SVR (patient 23). .....140

Figure 5-1 Main phases of classical HHO [198]. .....159

Figure 5-2 A 2-D schematic of hard besiege with progressive rapid dives [198].  
.....165

Figure 5-3 Architecture of the ENN model. $u(t-1)$ , which is the vector of the input layer at the moment $t-1$ , is fed to the input layer, $xt$ and $ct$ represent the vector of hidden layer and context layer at the moment $t$ , and $yt$ is the vector of output layer at the time $t$ .....	171
Figure 5-4 2D trajectory of (a) Levy-flight distribution and (b) Gaussian distribution. Each color shows one step of the distribution.....	175
Figure 5-5 Architecture of the proposed FENN model. $u(t-1)$ is the vector of the input layer at the moment $t-1$ , $xt$ represents the vector of hidden layer, and $xct, yc1(t)$ and $yc2(t)$ represent context layer for hidden layer, output context layer 1 and output context layer 2 at the moment $t$ , and $yt$ is the vector of output layer at the time $t$ .....	182
Figure 5-6 Architecture of the proposed CNN-FENN model for classification of the abnormal and normal PAWP. 300 samples of pump flow signal are fed to the CNN-FENN as input. This is followed by three convolutional layers as well as batch normalization layers. Five convolutional, max-pooling layers with stride 2 and batch normalization layers are placed in the subsequent layers. The proposed FENN layer is located in the last layer of the CNN-FENN model to classify the abnormal and normal PAWP.....	185
Figure 5-7 Flowchart of the proposed CNN-FENN-HHO+ system.....	186
Figure 5-8 3D demonstration of benchmark functions F1 to F24.....	195
Figure 5-9 Convergence curves for F1 to F24.....	207

Figure 5-10 Scalability results of the proposed HHO+ with different dimensions.....	208
Figure 5-11 Scalability results of the proposed HHO+ with different dimensions for F16 and F19 (normal scale).....	209

## List of Tables

Table 3-1 Normal values and description of cardiovascular model parameters for interpatient and intrapatient simulations .....	91
Table 3-2 Six different patient scenarios and their simulations conditions....	93
Table 3-3 Evaluation of LVEDP detection (number of cardiac cycles in each simulation) .....	96
Table 3-4 Sensitivity analysis of $R_{pa}$ change based on PID controller (5 most effective parameters highlighted from dark to light green in each category)	97
Table 3-5 Sensitivity analysis of $R_{sa}$ change based on PID controller (5 most effective parameters highlighted from dark to light green in each category)	98
Table 3-6 Sensitivity analysis of transition from rest to exercise and passive postural changes based on PID controller (5 most effective parameters highlighted from dark to light green in each category).....	100
Table 3-7 Simulation of interpatient and intrapatient variations via changing the most effective parameters in each scenario.....	101
Table 3-8 Results of the Wilcoxon's test in comparison of MFAC and PID for different patient scenarios .....	107
Table 4-1 Normal values and descrption of cardiovascular model parameters for interpanient and intrapatient simulations .....	132
Table 4-2 Six different patient scenarios and their simulations conditions..	135

Table 4-3 Performance of the proposed deep CNN on the estimation preload for each validation fold through 10-fold cross-validation on 100 patients ..	138
Table 4-4 Performance of the proposed deep CNN combined with FFDL-MFAC on the estimation of preload for each scenario on new 30 patients.....	141
Table 4-5 Comparison of the proposed physiological control system using FFDL-MFAC for measured and estimated preload on new 30 patients in six different scenarios .....	142
Table 5-1 Detail of CNN-MLP structure.....	169
Table 5-2 Parameter settings for the optimization algorithms. All these parameters were taken from the original papers .....	189
Table 5-3 Detail of benchmark functions for dimension 1000 .....	190
Table 5-4 Detail of CNN-ENN and CNN-FENN structures .....	196
Table 5-5 The fitness value of each benchmark function for dimension 1000. Bold indicates the minimum value across all methods .....	200
Table 5-6 Statistical results of Wilcoxon rank sum test and Friedman's test for dimension 1000. NaN refers to not a number showing all the elements of two compared vectors using Wilcoxon rank sum test are equal to zero.....	203
Table 5-7 The comparison of performances of the proposed classification methods across 10-fold cross-validation .....	210

## **List of Abbreviations and Symbols**

ANN	: Artificial neural network
CO	: Cardiac output
CNN	: Convolutional neural network
CS	: Constant speed
CVS	: Cardiovascular system
DLT	: Dynamic linearization technique
Eao	: Aortic elastance
Eao	: Aortic elastance
ECG	: Electrocardiogram
Eesla	: Left atrial end systolic elastance
Eesla	: Left atrial end systolic elastance
Eeslvf	: Left ventricular end systolic elastance
Eeslvf	: Left ventricular end systolic elastance
Eesra	: Right atrial end systolic elastance
Eesra	: Right atrial end systolic elastance

Eesrvf	: Right ventricular end systolic elastance
Eesrfv	: Right ventricular end systolic elastance
ENN	: Elman neural network
Epa	: Pulmonary arterial elastance
Epu	: Pulmonary vein elastance
Esa	: Systemic arterial elastance
Esv	: Systemic vein elastance
Evc	: Vena cava elastance
FLC	: Fuzzy logic control
FS	: Frank-starling
FENN	: Fully Elman neural network
HHO	: Harris Hawks optimizer
HHO+	: Improved Harris Hawks optimizer
HF	: Heart failure
HR	: Heart rate
Lao	: Aortic inertance
Lpa	: Pulmonary arterial inertance

LVAD	: Left ventricular assist device
LVEDP	: Left ventricular end diastolic pressure
MCL	: Mock circulation loop
MFAC	: Model free adaptive control
MLP	: Multi-layer perceptron
P0la	: Left atrial end diastolic stiffness scaling term
P0lvf	: Left ventricular end diastolic stiffness scaling term
P0ra	: Right atrial end diastolic stiffness scaling term
P0rvf	: Right ventricular end diastolic stiffness scaling term
PAWP	: Pulmonary arterial wedge pressure
PCWP	: Pulmonary capillary wedge pressure
PID	: Proportional-integral-derivative
PLA	: Left atrial pressure
PLV	: Left ventricular pressure
PPD	: Pseudo-partial derivative
PRA	: Right atrial pressure
PRV	: Right ventricular pressure

PSO	: Particle swarm optimization
PVR	: Pulmonary vascular resistance
Q	: Flow rate
Qlvad	: LVAD flow rate
Rao	: Aortic resistance
Rav	: Aortic valve resistance
Rmt	: Mitral valve resistance
RNN	: Recurrent neural network
Rpv	: Pulmonary valve resistance
Rra	: Right atrium resistance
Rsv	: Systemic venous resistance
RVAD	: Right ventricular assist device
SAE	: Sum of absolute error
SISO	: Single-input single-output
SVR	: Systemic vascular resistance
Tc	: Heart rate coefficient
Tsys0	: Maximum systolic heart period

V0la	: Left atrial end diastolic volume at zero pressure
V0lvf	: Left ventricular end diastolic volume at zero pressure
V0ra	: Right atrial end diastolic volume at zero pressure
V0rvf	: Right ventricular end diastolic volume at zero pressure
VAD	: Ventricular assist device
Vdla	: Left atrial end systolic volume at zero pressure
Vdlvf	: Left ventricular end systolic volume at zero pressure
Vdra	: Right atrial end systolic volume at zero pressure
Vdrvf	: Right ventricular end systolic volume at zero pressure
Vtotal	: Total blood volume
Vuao	: Aortic unstressed volume
Vupa	: Pulmonary arterial unstressed volume
Vupu	: Pulmonary vein unstressed volume
Vusa	: Systemic arterial unstressed volume
Vusv	: Systemic vein unstressed volume
Vuvc	: Vena cava unstressed volume
$\lambda_{la}$	: Left atrial end diastolic stiffness coefficient

- $\lambda_{lvf}$  : Left ventricular end diastolic stiffness coefficient
- $\lambda_{ra}$  : Right atrial end diastolic stiffness coefficient
- $\lambda_{rvf}$  : Right ventricular end diastolic stiffness coefficient

# **Chapter 1. Introduction**

Cardiovascular disease (CVD) is a highly prevalent illness affecting 26.7 million people in the United States of America (11.5% of the population) [1]. 1.2 million (6% of the population) adult Australians had one of the symptoms of CVD including stroke in 2017 [2]. CVD caused 17.8 million deaths in 2017 globally which was a 21.1% increase from 2007 [3]. In 2015-2016, the cost of CVD in Australia was \$10.4 billion (8.9% of total disease expenditure), which was one of the most expensive disease groups in Australia [4].

Heart failure (HF) is one type of CVD and is defined by any condition leading to insufficient cardiac output. An estimate of 104,900 adults had HF in Australia, of which 66% were aged 65 years or more in 2017 [2]. 6.5 million people are suffering from HF in the USA and more than 23 million worldwide [1], [5]. The prevalence of HF will increase by 46% from 2012 to 2030, leading to more than 8 million adult with HF according to the American Heart Association [1].

Heart transplantation is the gold standard treatment for HF patients. However, transplantation relies on the donation of organs. In 2019, only 113 heart transplantations were performed in Australia while there were more than 100,000 HF patients [2], [6]. As the number of donor hearts is significantly less than the demand for heart transplantation, alternative treatments are employed. These treatments include surgical, medical or mechanical treatments [7]. Surgical and medical methods are associated with high risk of death [7], [8]. Furthermore, surgical treatments can only work on limited number of patients via bypassing the coronary arteries, heart valve replacement and pacemaker implantation [7], [9].

Mechanical circulatory support is one of the most suitable treatments for HF patients. This is achieved in one of two ways: by implanting one or two mechanical pumps, called ventricular assist devices (VADs), into the HF patient's body [1], [5], or completely replacing the two failed ventricles with a single device called a total artificial heart (TAH) [7]. VADs can be used to support the left side of the heart which is called left ventricular assist device (LVAD), the right side of the heart (called right ventricular assist device (RVAD)) or both sides (called a biventricular assist device (BiVAD)) [10]. VADs can be employed to assist HF patients during bridge to transplant, bridge to recovery or destination therapy [10]. The first generation of VADs, which delivered pulsatile flow, were large devices and associated with high risk of device failure. This was because these VADs had several mechanical components such as valves, bearings, and membranes that were subject to wear. However, VADs with continuous flow rotary pumps are smaller and more power efficient, resulting in longer support and patient outcome improvements [10], [11].

Clinically, LVADs are currently operated at a constant speed. LVAD speeds are only adjusted by clinicians in hospitals using echocardiography and invasive cardiovascular measurements. This means that LVADs are insensitive to changes in patient conditions during different levels of activities such as sleeping, standing, walking and exercising [10], [12]. Operating LVADs in constant speed mode can lead to hazardous events such as ventricular suction (ventricular collapse due to low pressure in the ventricle) or pulmonary congestion (a condition caused by excess fluid in the lungs due to high pressure in the ventricle) which may reduce the patient's exercise capacity [10], [12].

LVAD speed can be automatically adjusted by a physiological control system in response to changes in the circulatory system, which can improve the quality of life of HF patients by increasing cardiac output (CO) in response to demand and preventing adverse events such as ventricular suction and pulmonary congestion.

CO varies based on the patient's activity level and heart condition by the Frank-Starling (FS) mechanism. The FS mechanism automatically changes the blood flow based on the preload, which is defined by the left ventricular pressure at the end of diastole (LVEDP). Therefore, preload is a vital clinical variable. Physiological control systems that work based on the measuring and control of LVEDP can improve the quality of life of HF patients, increase their lifespan, reduce incidence of hazardous events and increase exercise capacity by providing higher pump flow as needed [12]–[14].

There are several shortcomings of the current physiological control schemes. The first is that the current physiological control systems have been evaluated (using numerical models, mock circulation loops or animal tests) in specific conditions for single-patient scenarios and so there is still no physiological control system which has shown to reliably work in different patient conditions or for different patients [12], [15]–[17]. Furthermore, the most current physiological control systems require pressure or flow sensors implanted into the HF patient's body [13]. As there are currently no commercial long-term implantable pressure or flow sensors, these measurements must be estimated

by pump variables or measured by manufacturing reliable implantable long-term pressure or flow sensors [13], [18].

The existing preload estimators and sensorless physiological control systems have limited robustness and accuracy [19]–[24]. Therefore, further development is needed to be undertaken on the algorithms for estimation of preload and sensorless physiological control systems for LVADs.

## 1.1 Aim and objectives

The thesis aims to design, develop and evaluate novel methods for estimation of preload and sensorless physiological control system for LVADs. In order to meet this aim, three main objectives were proposed as follows:

- Design a physiological control system for an implantable heart pump that accommodates for interpatient and intrapatient variations.
- Design a sensorless physiological control system for LVADs across different patient conditions.
- Design an improved non-invasive preload estimator using advanced machine and deep learning methods based on the pump variables and test on a clinical dataset.

As the majority of the VAD patients only need an LVAD [5], this research has only been focused on developing physiological control systems for LVADs. However, findings from this research could be extended to RVAD and BiVAD by additional validation and research.

The next section will describe necessary background knowledge for the reader to understand the research conducted in this thesis.

## **1.2 Research background**

Design and development of a physiological control system for an LVAD requires knowledge of the cardiac cycle, heart, circulatory system, HF condition, FS mechanism in healthy and heart pathological and treatments for HF. A brief description for understanding of these topics is provided in the following sections.

### **1.2.1 Cardiac cycle**

The cardiac cycle can be divided into two main phases of contraction and relaxation for each heartbeat. Contraction and relaxation correspond to systole, in which the ventricles pump blood, and diastole, in which the ventricles fill with blood, respectively. However, the cardiac cycle can be further divided into four separate phases [25].

Phase I corresponds to ventricular filling, in which blood flows from atria to ventricles through mitral and tricuspid valves. This flow continues until the ventricular pressure equals the atrial pressure. This phase can be divided into three stages: rapid flow, diastasis and atrial systole. The rapid flow stage consists of fast filling of ventricles with blood. During the diastasis stage, the ventricle fills with a small amount of blood from venous flow. In the atrial systole stage, contraction of the atria provides additional blood to flow into the ventricle [25].

Phase II corresponds to isovolumetric contraction. In this phase, ventricular contraction begins, which leads to a sharp increase in ventricular pressure while the ventricular volume remains constant. This is because all the heart valves (mitral, tricuspid, aortic and pulmonary) are closed preventing flow to the atria, aorta and pulmonary artery. The end of this phase occurs when the ventricular pressures reach the aortic or pulmonary arterial pressure. This results in opening of the aortic and pulmonary valves, which normally lasts about 50 ms [25].

Phase III corresponds to ejection in which the ventricles pump the blood to the aorta or pulmonary arteries. Ejection occurs once the ventricular pressure rises above a threshold for left and right heart sides, respectively. These high pressures push the aortic and pulmonary valves open. The ejection phase continues until the ventricular pressure falls below the arterial pressure [25].

Phase IV corresponds to isovolumetric relaxation in which ventricles relax leading to a rapid fall in the ventricular pressure while the volume of the ventricle remains constant. This is because all the heart valves are closed preventing flow to atria, aorta, and pulmonary artery. The relaxation phase ends once the ventricular pressure falls below the atrial pressure and the cardiac cycle repeats the four phases again which normally lasts about 50 ms [25].

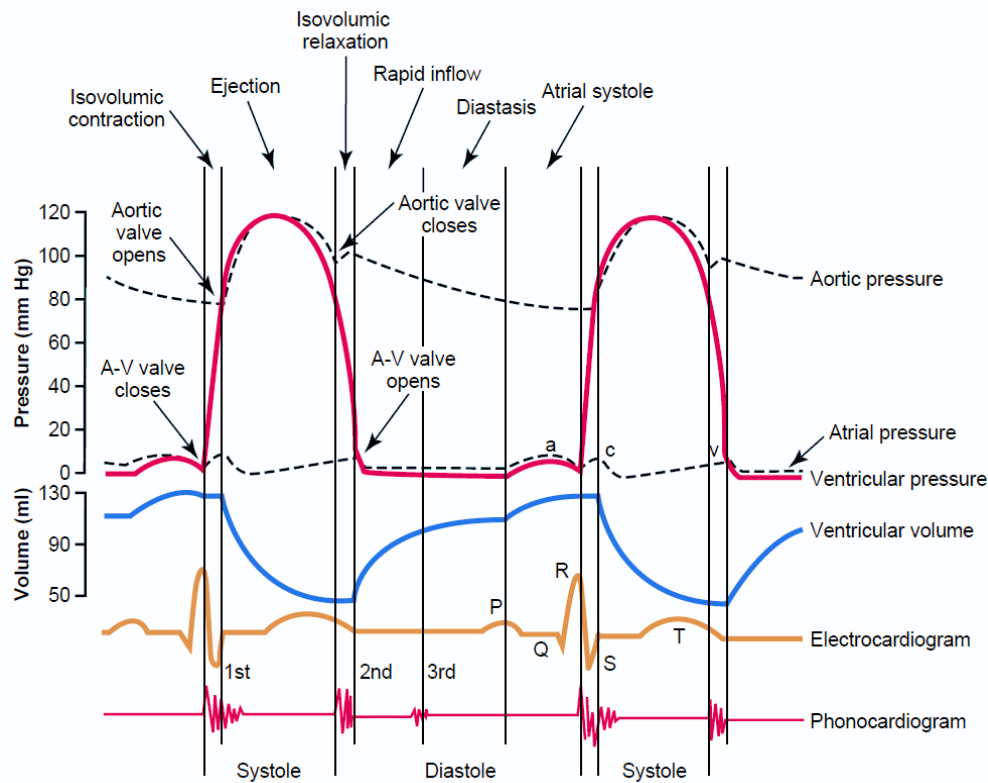


**Figure 1-1 Cardiac cycle for left heart side including changes in left atrial pressure (LAP), left ventricular pressure (LVP), aortic pressure (AoP), left ventricular volume (LVV), electrocardiogram (ECG), and phonocardiogram [25].**

Figure 1-1 shows cardiac cycles for the left heart side including atrial pressure (LAP), left ventricular pressure (LVP), aortic pressure (AoP), left ventricular volume (LVV), electrocardiogram (ECG), and phonocardiogram during the four phases of the cardiac cycle. The relationship between LVV and intraventricular pressure during four phases of the cardiac cycle is shown in Figure 1-2. The stroke volume (SV) is defined by the difference between end-diastolic volume (EDV) and end-systolic volume (ESV). Furthermore, stroke work (SW) can be determined by area within the pressure-volume loop as shown in Figure 1-2.

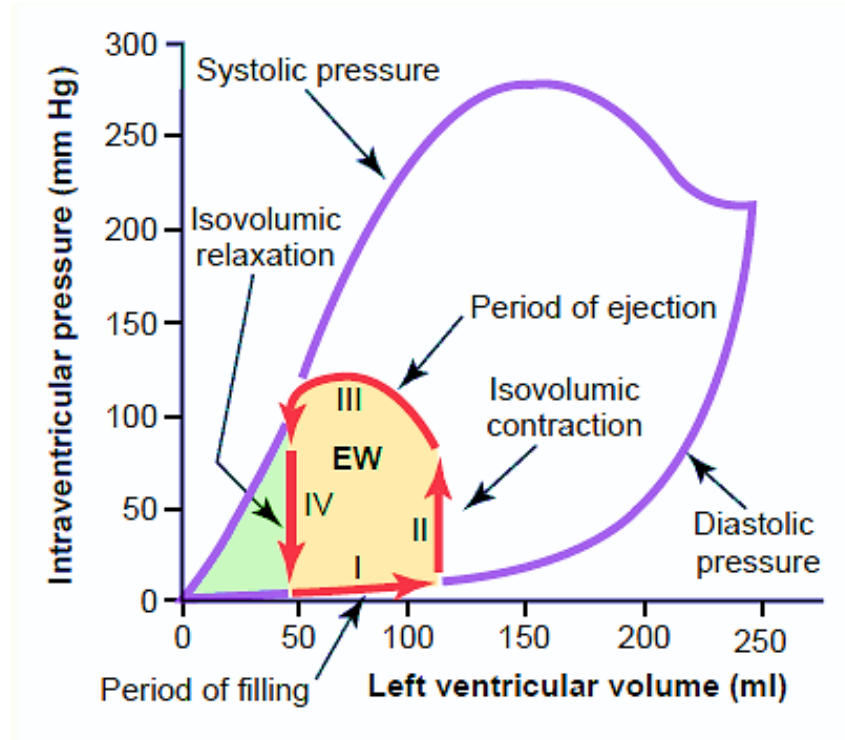


**Figure 1-2 The relationship between left ventricular volume and intraventricular pressure during four phases of the cardiac cycle [25].**

### 1.2.2 The heart

The anatomy of the human heart is depicted in Figure 1-3. The human heart consists of left and right sides which are separated by a flexible septum, and are shown in red and blue colors in Figure 1-3. Each side of heart consists of two chambers: a ventricle and an atrium. The atria act to help to fill ventricles during ventricular diastole, while the ventricles pump blood through the circulatory system. The left ventricle pumps the blood with higher force compared to the right ventricle. This is because the systemic circulation is larger than pulmonary circulation and therefore has higher resistance. The right side of the heart pumps deoxygenated blood to the lung through the

pulmonary circulation while the left side of the heart pumps the oxygenated blood to the tissues via the systemic circulation. Atrioventricular valves, including mitral and tricuspid valves for left and right sides of the heart respectively, prevent backflow from the ventricles to the atria. The aortic and pulmonary valves prevent regurgitation from the arteries into the ventricles on the left and right sides of the heart respectively [25].

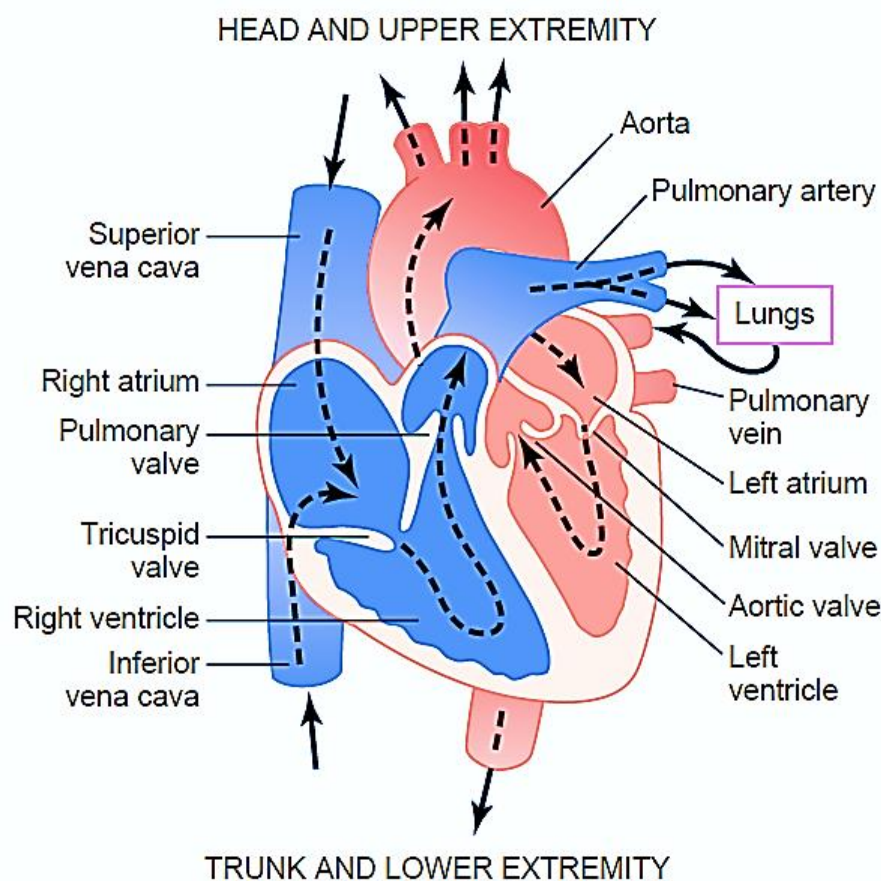


**Figure 1-3 Anatomy of the human heart [25].**

### 1.2.3 The Circulatory system

The circulatory system consists of two series parts: systemic and pulmonary circulation. The systemic side pumps oxygenated blood throughout the body while the pulmonary side delivers deoxygenated blood to the lungs as show in Figure 1-4. Oxygenated blood from the left atrium flows into the left ventricle via mitral flow.

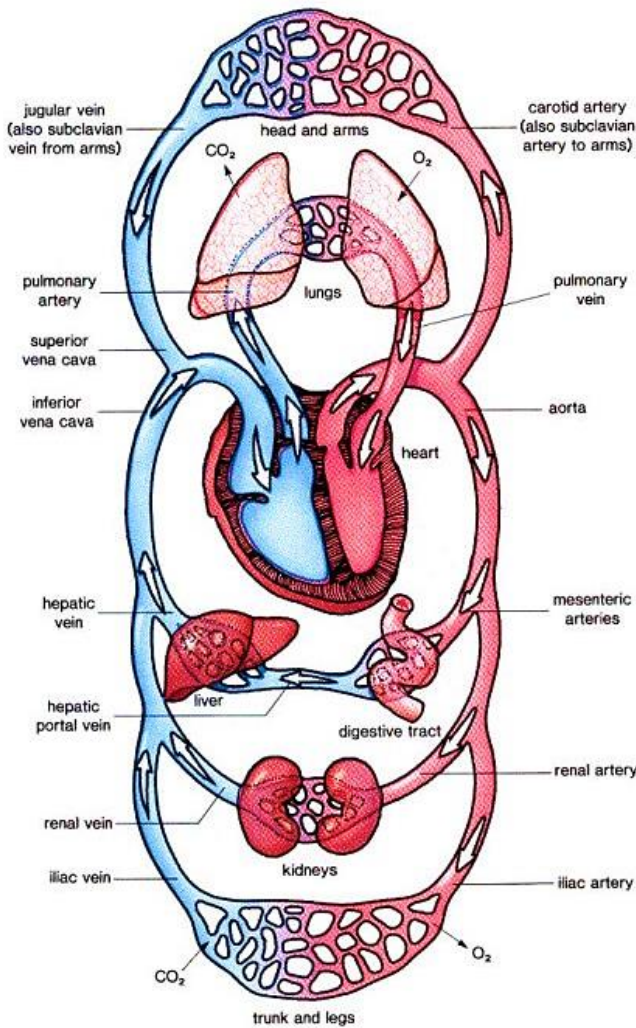
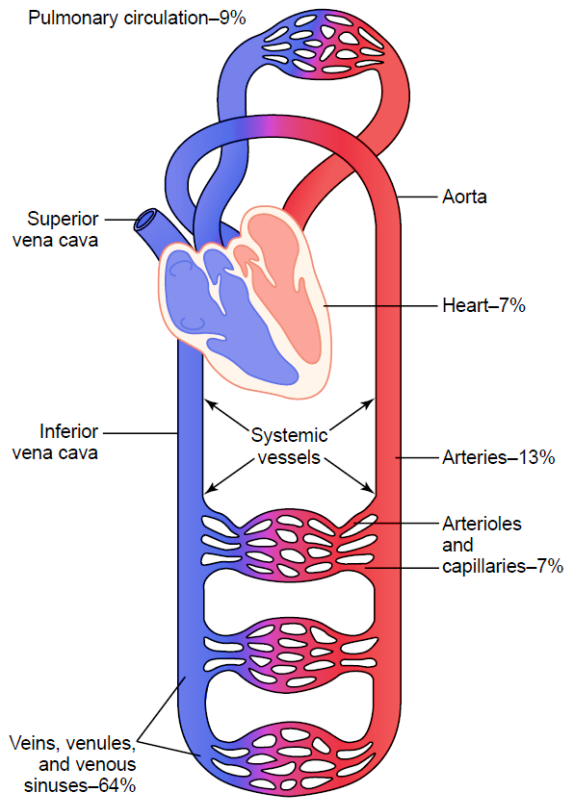


Figure 1-4 Human Circulatory System [26].

Blood is then pumped into the aorta via the aortic valve. Afterward, the blood provides oxygen and nutrients to the muscle and organs through the systemic circulation. The deoxygenated blood passes from the systemic venous circulation into the right atrium via the superior vena cava and inferior vena cava corresponding to the upper and lower body. The blood then flows into the right ventricle via the tricuspid valve. Once ventricular contraction occurs, the deoxygenated blood in the right ventricle is ejected to the lungs via the pulmonary valve and pulmonary artery. The blood is oxygenated in the lungs, moves into the left atrium and the cycle begins again [25].

The distribution of blood (in percentage of total blood) in the different parts of the circulatory system is depicted in Figure 1-5. This figure shows that the highest portion (about 64%) of the blood in the circulatory system is located in veins, venules, venous sinuses. The arteries, pulmonary circulation, arterioles and capillaries, and heart comprise of 13%, 9%, 7% and 7% of total blood of the circulatory system respectively [25].

Figure 1-6 shows the normal blood pressures in the different sections of the circulatory system. As can be seen from this figure, the pressure is only pulsatile from the aorta to arterioles and pulmonary arteries to capillaries in the systemic and pulmonary circulation respectively [25].



**Figure 1-5 Distribution of blood (in percentage of total blood) in the different parts of the circulatory system [25].**

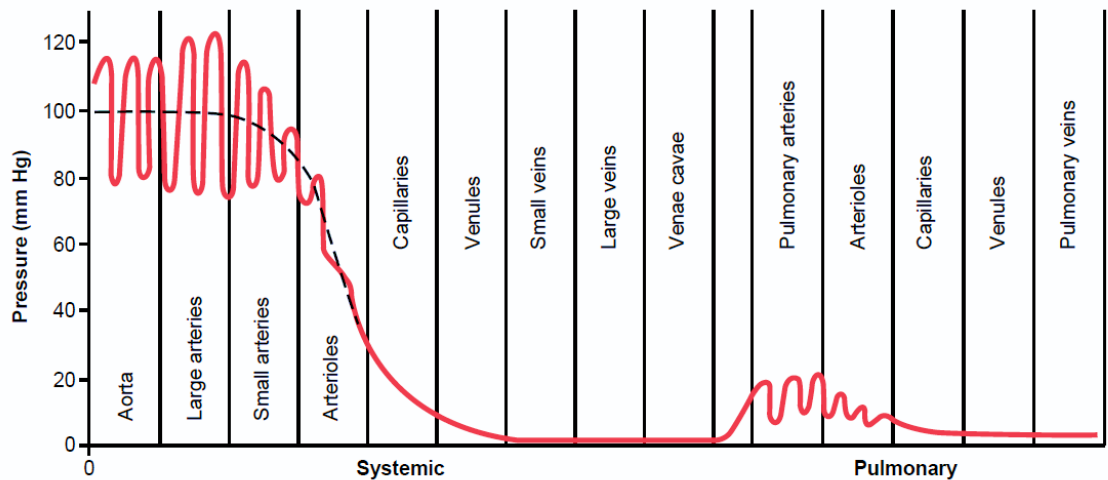


**Figure 1-6 Normal blood pressures in the different sections of the circulatory system [25].**

#### 1.2.4 The Frank-Starling mechanism of the healthy heart

The strength of ventricular contraction depends on the volume of venous return which is known as the FS mechanism. This is because when end-diastolic volume increases due to more venous return, heart muscle is further stretched than normal and therefore results in greater force of contraction. The FS mechanism is also referred to as preload sensitivity. The relationship between left and right ventricular flow and preload as a result of the FS mechanism is shown in Figure 1-7. This figure shows how CO is proportional to the end-diastolic pressure of ventricle (preload) or its equivalent (atrial pressure).

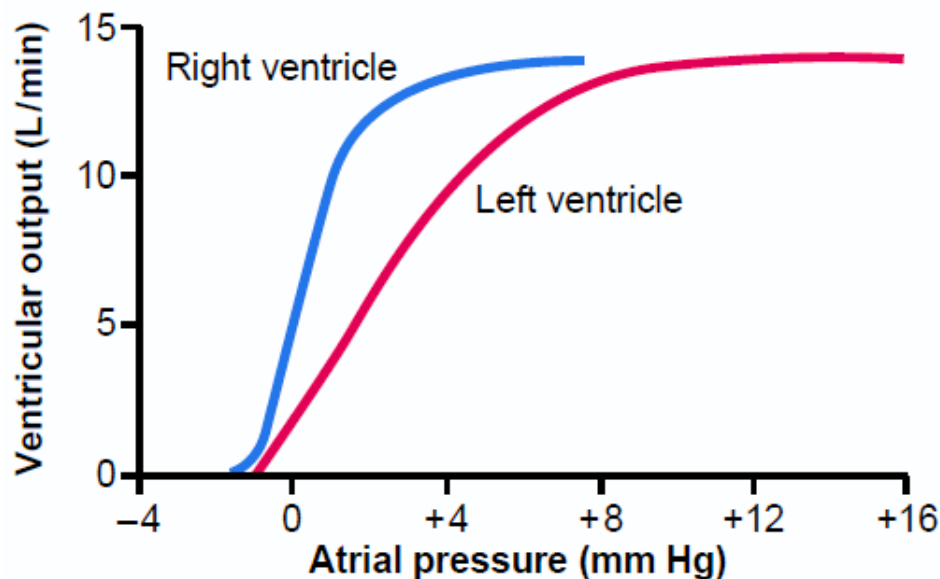


**Figure 1-7 Relationship between left and right ventricular flow and preload as a result of the Frank-Starling mechanism [25].**

There is no unique FS curve for describing the FS mechanism in a patient at any given time. Accordingly, a series of FS curves based on the degree of sympathetic and parasympathetic stimulation determines the slope and maximum value of the FS curves [25]. Figure 1-8 shows the CO curves for different degrees of maximum sympathetic, normal sympathetic, zero sympathetic and parasympathetic stimulation.

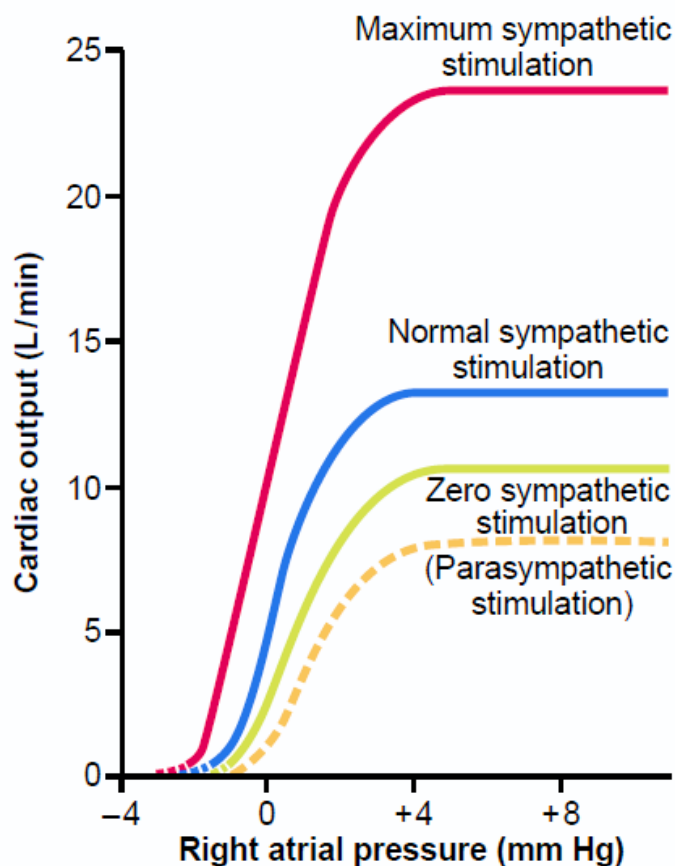


**Figure 1-8 Cardiac output curves for different degrees of maximum sympathetic, normal sympathetic, zero sympathetic and parasympathetic stimulation [25].**

### **1.2.5 Heart failure**

Heart failure can be defined as any condition that prevents the heart from supplying enough volume of blood to the tissues and organs in which exercise capacity, quality, and duration of lives of patients are reduced. The reduced CO results in insufficient oxygen and nutrients to the vital organs such as brain, kidney, and liver. Heart failure can affect the left side, right side or both sides of the circulation, during systole and/or diastole. It is caused by coronary artery disease, myocardial infarction, idiopathic cardiomyopathy, chronic hypertension and valve disease [7], [9], [25].

### **1.2.6 Treatment of heart failure**

Treatment of HF patients depends on the severity and type of HF. In some case of HF, patient conditions can be improved by changing their diet exercise and quitting smoking and drinking. The first formal treatment for HF includes a combination of medications. These medications lead to a lower heart workload which limit the mobility of the HF patients during exercise, and resulting in inferior quality of life [27]. However, this approach can only work on early stages of HF [9].

In more severe conditions, various surgical methods are considered as the second treatment for HF patients [9]. This method includes heart valve replacement, implantation of pacemakers and coronary artery bypass [9], [27]. When these treatments are not able to improve the patient's condition, HF is diagnosed as end-stage. Although the gold-standard method for end-stage HF

patients is the heart transplantation, there is a vast difference between the supply and demand of donor hearts. In 2019 while there were more than 100,000 HF patients in Australia, only 113 patients received heart transplantations [6].

The last treatment for HF discussed in this section, which is mechanical circulatory support, is achieved by implanting one or two VADs into the patient's body. This method can be considered for HF patients as bridge to transplant, bridge to recovery and destination therapy.

### **1.3 Thesis outline**

According to the aims and objectives in section 1.1 , the structure of this thesis is briefly described as follows:

**Chapter 2** presents the general literature review for this thesis. This chapter includes a description of VADs, various physiological control systems for LVADs, different types of controllers, the evaluation platforms and scenarios for physiological control systems, comparison of different control strategies for LVADs, as well as non-invasive estimation, monitoring and control approaches for LVAD, and a short introduction to machine and deep learning methods.

As the existing physiological control systems have been evaluated in specific conditions for single-patient scenarios, a novel adaptive physiological control system which can reliably work in different patient conditions has been designed and validated. **Chapter 3** describes the first objective of this thesis,

which is designing of a physiological control system that accommodate the interpatient and intrapatient variations. The chapter includes a description of a computational model of the cardiovascular system, real-time LVEDP detection, sensitivity analysis, model free adaptive controller and physiological control system evaluation. This chapter is based on the publication “A physiological control system for an implantable heart pump that accommodates for interpatient and intrapatient variations”, published in IEEE Transactions on Biomedical Engineering, vol. 67, no. 4, pp. 1167–1175, 2020.

The most current physiological control systems rely on measuring the pressure or flow sensors implanted into the HF patient’s body. Due to lack of reliable implantable pressure and flow sensors, these measurements must be estimated by pump variables. Physiological control systems acting based on the measuring of preload, which is a vital clinical variable, can improve the quality and duration of lives of HF patients and increase their exercise capacity [12]–[14]. A sensorless physiological control system can be proposed to automatically adjust the pump speed to restore preload to a safe level for different patient conditions using a robust preload estimator. **Chapter 4** describes the second objective of this thesis, which is developing of a sensorless physiological control system for LVADs across different patient conditions. The chapter includes a novel deep learning method for preload estimation, and a full form of model free adaptive control and physiological control system evaluation. This chapter is based on the publication “A sensorless control system for an implantable heart pump using a real-time

deep convolutional neural network”, submitted to IEEE Transactions on Biomedical Engineering.

However, pulmonary arterial wedge pressure (PAWP) can be measured more easily compared to preload by pulmonary artery catheterization [10], [23], [28], [29] to produce a dataset for estimation of PAWP as surrogate of preload.

**Chapter 5** describes the third objective of this thesis, which is designing an improved non-invasive preload estimator using advanced machine and deep learning methods based on the pump variables and test on a clinical dataset. The chapter includes a description of a new improved Harris Hawks optimizer algorithm (HHO+), a new fully Elman neural network (FENN) and four novel 18-layer deep learning methods of convolutional neural networks (CNNs) with multi-layer perceptron (CNN-MLP), CNN with Elman neural networks (CNN-ENN), CNN with fully Elman neural networks (CNN-FENN) and CNN with fully Elman neural networks optimized by HHO+ algorithm (CNN-FENN-HHO+) for classification of abnormal and normal PAWP using pump flow. This chapter is based on the publication “FENN: A novel deep recurrent neural network optimized by improved Harris hawk’s algorithm for classification of pulmonary arterial wedge pressure”, submitted to Future Generation Computing Systems.

**Chapter 6** summarizes the conclusions from all chapters, states the limitations of this research and recommends future work.

## **Chapter 2. Literature Review**

In this chapter, first a review of generations of VADs is presented. Afterwards, a review of different evaluation platforms for physiological control of LVADs is presented. Then, a comprehensive review of different physiological control strategies including types of controllers for LVADs is described. Subsequently, non-invasive estimation, monitoring and control approaches for LVADs are described. This chapter then comprises a brief introduction of machine and deep learning methods. Finally, a conclusion regarding the current limitations of physiological control systems is presented.

## **2.1 Generations of ventricular assist devices**

VADs are classified by their generation, or mode of operation, into three classes. The examples of first, second and third generations of VADs are shown in Figure 2-1, Figure 2-2 and Figure 2-3 respectively [10]. First generation VADs are pulsatile flow blood pumps, which operate like the native ventricle to deliver a flow pulse via volume displacement to the circulatory system, mimicking normal CO. These pumps were extremely large due to their many moving parts, large membranous sacs and reliance on compressed air or pusher plate technology, which limited patient mobility. Furthermore, these

pumps were associated with significant hemolysis, thrombus formation and severe postoperative bleeding [30].



**Figure 2-1 First generation of ventricular assist devices. Left: Thoratec Implantable VAD (IVAD) (Abbott Laboratories, formerly Thoratec Corporation, Pleasanton, CA, USA), Right: Abiomed BVS 5000 (Abiomed Inc., Danvers, MA, USA) [10].**

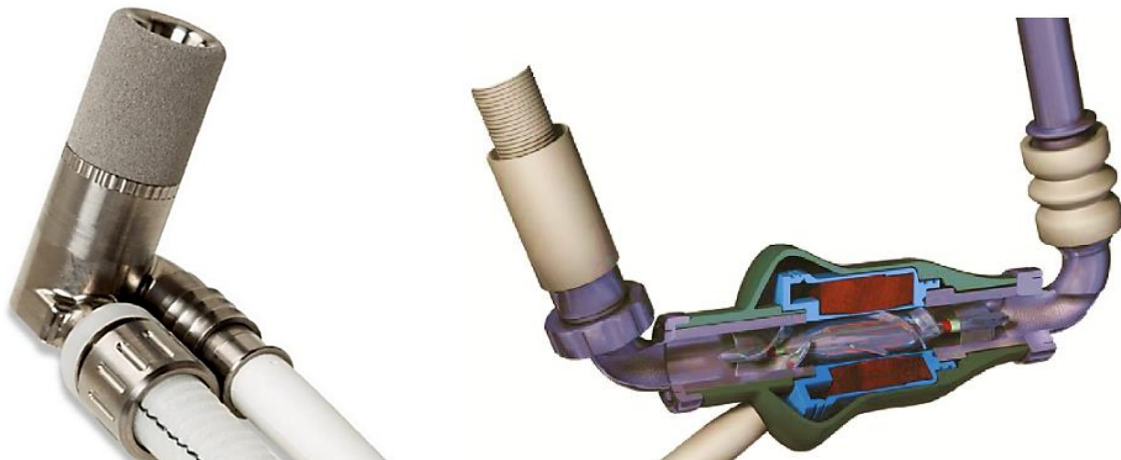


**Figure 2-2 Second generation of ventricular assist devices. Left: HeartMate X (Abbott Laboratories, formerly Thoratec Corporation, Pleasanton, CA, USA), Right: HeartMate II (Abbott Laboratories, formerly Thoratec Corporation, Pleasanton, CA, USA) [10].**



**Figure 2-3 Third generation of ventricular assist devices. Upper left: HeartWare HVAD (Medtronic Inc., FL, USA), Upper right: Abbott HeartMate 3 (Abbott Laboratories, formerly Thoratec Corporation, Pleasanton, CA, USA), Lower: Berlin Heart INCOR (Berlin Heart GmbH., Berlin, Germany) [10].**

Second generation VADs are either axial or centrifugal continuous flow blood pumps which usually operated with a few moving parts such as shaft driven or incorporating pivot bearing. Although these pumps improved the quality of lives of patients compared to the first generation of VADs, these were still associated with thrombosis and hemolysis since these pumps are much smaller and have smaller gaps between different parts of the pump [31], [32].

The HeartMate II and its placement (pump inlet is connected to the left ventricle and pump outlet is connected to the aorta) in the HF patient's body as well as the batteries and controller are shown in Figure 2-4.

Third generation VADs are continuous flow blood pumps with magnetic and/or hydrodynamic contactless bearings (fully levitated impeller/rotor with no mechanical contact between the rotating and stationary parts of the pump), leading to long-term wear-free operation, reduced blood-trauma adverse events, and improved hemocompatibility [10], [33].

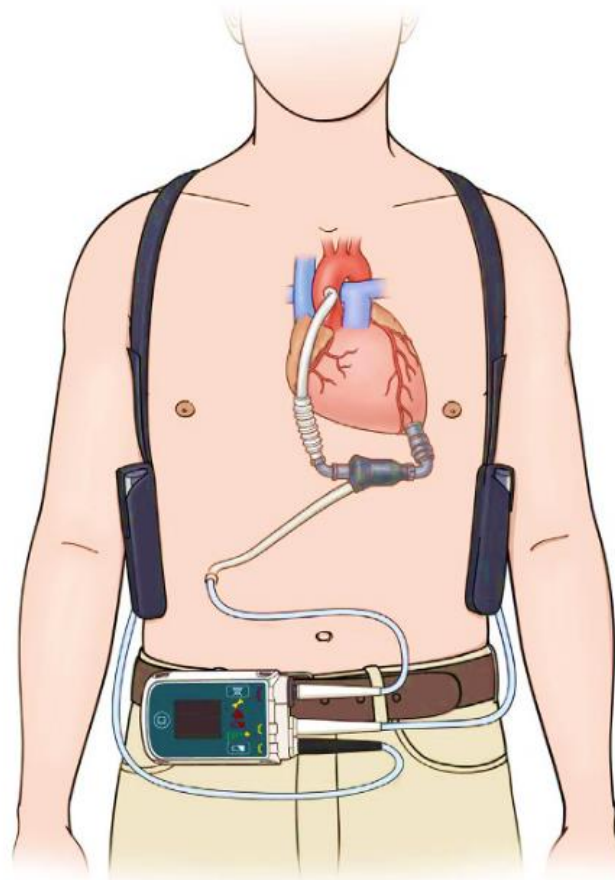


**Figure 2-4 The HeartMate II and its placement in the HF patient's body [10].**

## 2.2 Evaluation platforms for physiological control of LVAD

The performance of physiological control for LVADs should be evaluated thorough computational numerical models (*in silico* studies), mock circulation loops (*in vitro* studies) and animal tests (*in vivo* studies) respectively before clinical trials in order to validate and prove their efficacy. A brief description of each evaluation platform is described in this section.

### 2.2.1 Numerical models (*in silico* study)

A numerical model of the CVSs is widely used for preliminary physiological control system design and evaluation [24], [34]–[39], because circulatory parameters such as resistances and compliances can be varied easily and provide a safe environment for validation of many different patient conditions and scenarios before *in vitro*, *in vivo* and clinical evaluations [7]. In addition, it is an inexpensive approach compared with *in vitro* and *in vivo* approaches [10]. However, in all the studies performed for evaluation of physiological control systems on a numerical model, only a single patient condition was simulated [10], which makes it difficult to validate different physiological scenarios across a wide range of patient conditions. Furthermore, it is hard to evaluate the interaction between LVAD and body due to the absence of accurate physical model of the pump and its controller [10]. Several simplified models of the CVS were proposed by different research groups [34], [35], [40]–[43] to design a simple model-based controller (adaptive, robust, iterative and model predictive controllers) for adjusting the speed of LVAD and BiVADs. One of the

most comprehensive numerical model of CVS was proposed by Lim et al. [44], [45], which was derived using first principles and validated using in-vitro tests and in-vivo animal experiments. This numerical model of CVS consists of four main sections: 1. left heart including left atrium and ventricle, 2. right heart including right atrium and ventricle, 3. systemic circulation and 4. pulmonary circulation [44]. A numerical model of CVS, which is represented an electrical equivalent circuit analogue of the CVS and an LVAD, is shown by Figure 2-5. In the electric equivalent circuit, the pressure, flow rate, vascular compliance, vascular resistance, flow inertance and heart valves are represented as the electrical voltage, current, capacitance, resistance, inductance, and diode, respectively.

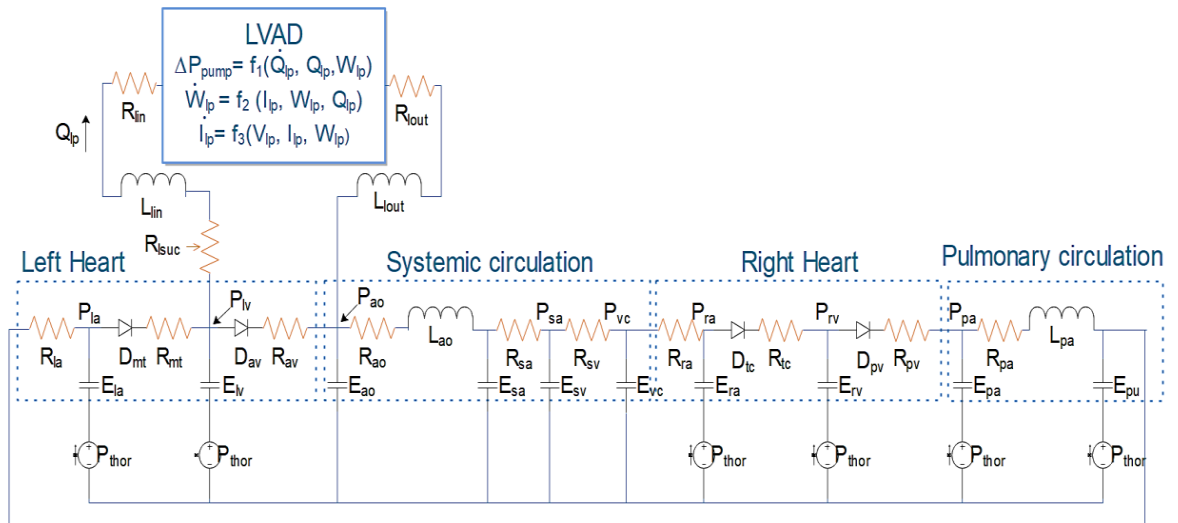


**Figure 2-5 Electrical equivalent circuit analogue of the cardiovascular system and an LVAD.** P, pressures; R, resistances; E, elastances (=1/compliances); L, inertances; D, diodes. The model consists of two main components: (1) the cardiovascular model includes left heart, systemic circulation, right heart, pulmonary circulation (la, left atrium; lv, left ventricle; ao, aorta; sa, systemic peripheral vessels, including the arteries and capillaries; sv, systemic veins, including small and large veins; vc, vena cava; ra, right atrium; rv, right ventricle; pa, pulmonary peripheral vessels, including pulmonary arteries and capillaries; pu, pulmonary veins and (2) heart-pump model includes the LVAD and RVAD, (Rin and Rout , inlet and outlet cannulae resistances; Lin and Lout, inlet and outlet cannulae inertances; Rlsuc, left suction resistance, Rrsuc, right suction resistance, Rband, banding resistance) [44].

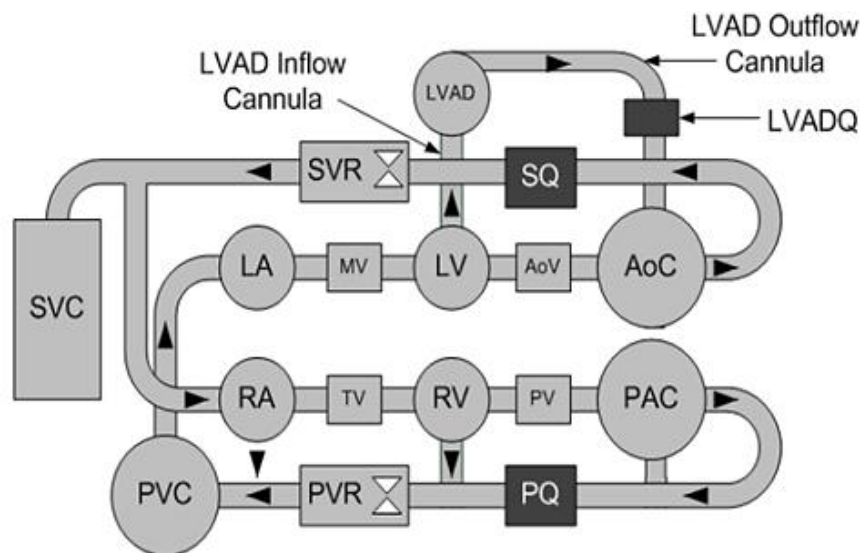
## 2.2.2 Mock circulation loops (*in vitro* study)

A mock circulation loop (MCL) is a benchtop artificial circulatory system which is typically used for evaluation of physiological control systems designed and validated by way of numerical model [46]. An example MCL and its schematic are shown in Figure 2-6. The fluid in the MCL is made from a water-glycerol solution (60 to 40% by mass), replicating the viscosity of blood. Like numerical models, some physiological parameters can be varied easily, and the patient scenarios are repeatable. As the MCL includes real clinical pumps and similar

fluid which replicates the blood viscosity, the effects of the fluid and pump dynamics and non-linearities, and pump limitations can be evaluated. Therefore, there are many physiological control systems which have been designed, evaluated and validated *in vitro* [47]–[56]. However, through MCL evaluation, it is hard to change the compliance, and it is difficult to model suction events, thrombosis and hemolysis. In addition, the difficulty with maintenance and the cost of the MCL are considerably more than the numerical models because of the mechanical nature of the MCL [7].



(a)



(b)

**Figure 2-6 (a) Mock circulation loop (MCL) and (b) schematic of MCL with an LVAD. Left atrium (LA), mitral valve (MV), left ventricle (LV), aortic valve (AoV), aortic compliance chamber (AoC), systemic flow meter (SQ), right atrium (RA), tricuspid valve (TV), right**

**ventricle (RV), pulmonary valve (PV), systemic vascular resistance (SVR), systemic venous compliance chamber (SVC), pulmonary arterial compliance chamber (PAC), pulmonary flow meter (PQ), pulmonary vascular resistance valve (PVR), pulmonary venous compliance chamber (PVC), left ventricular assist device (LVAD), left ventricular assist device flow meter (LVADQ) [7], [57].**

### **2.2.3 Animal tests (*in vivo* study)**

Animal tests are necessary evaluations before clinical trials can be performed. Pigs and sheep have been commonly used in the *in vivo* evaluations of physiological control systems for LVADs and BiVADs [58]–[60]. The advantage of an *in vivo* test is that it analyzes both physiological control system performance and biological implication including hemolysis and thrombosis. However, the animal tests are associated with higher cost compared to *in silico* and *in vitro* evaluations [61]. Furthermore, ethics approval for these tests is difficult and time-consuming. In addition, extreme conditions for evaluation of physiological control system in animal tests can only be tested with death of the animal. Therefore, animal trials should only be performed if physiological control system performance of established *in silico* and *in vitro* evaluations has shown robust results. An *in vivo* trial on a pig with an HVAD pump for the evaluation of a physiological control system for an LVAD is depicted in Figure 2-7.

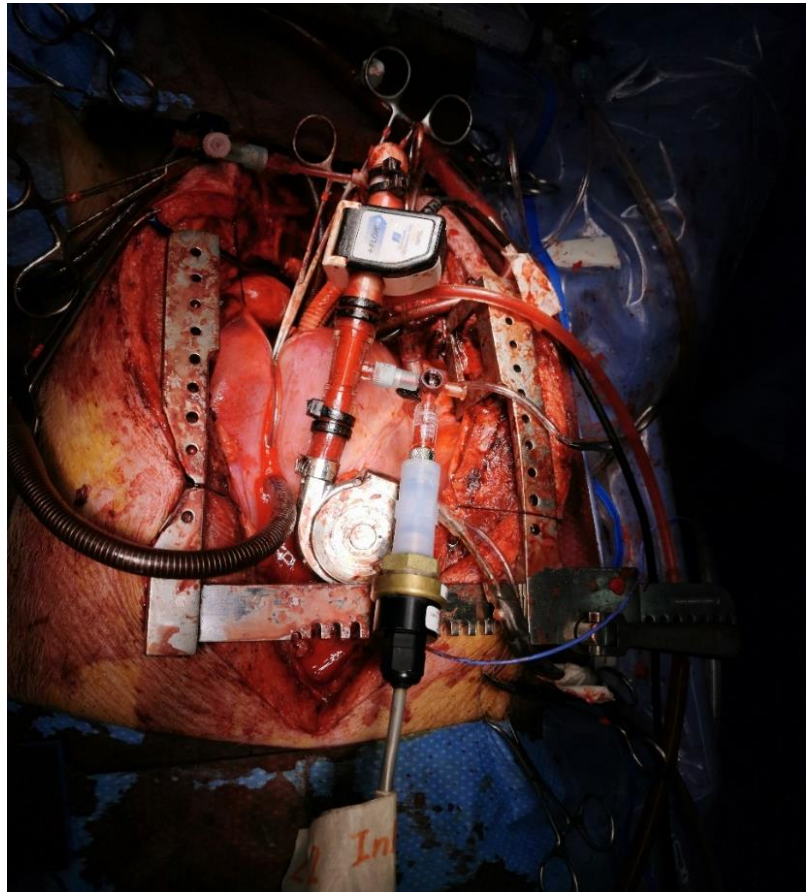


**Figure 2-7** *In vivo* trial on a pig with an HVAD pump on the evaluation of the physiological control system for LVAD (Taken by Masoud Fetanat).

#### 2.2.4 Clinical trials

The first clinical trial for physiological control systems was performed in 2005 by Vollkron et al. [62] and Schima et al. [63]. However, no other physiological control system has been evaluated in clinical trials. While clinical trials are mandatory for validation of physiological control systems to achieve regulatory approval for medical devices, these trials are associated with high cost and risk as human patients are involved in trials. Therefore, the

physiological control systems must be validated accurately through *in silico*, *in vitro* and *in vivo* evaluations before clinical trials.

## 2.3 Physiological control of LVADs

LVADs are currently operated at a constant speed, resulting in a preload sensitivity three times lower than that of the native ventricle [64], [65]. This can increase the risk of adverse events such as ventricular suction and pulmonary congestion [10], [64], [65]. The LVAD speed (speed set point) is adjusted by clinicians based on feedback from physiological variables of the patient as well as pump parameters, as shown in Figure 2-8. A low-level control system is employed to adjust the current or voltage of the pump to maintain the speed set point [9].

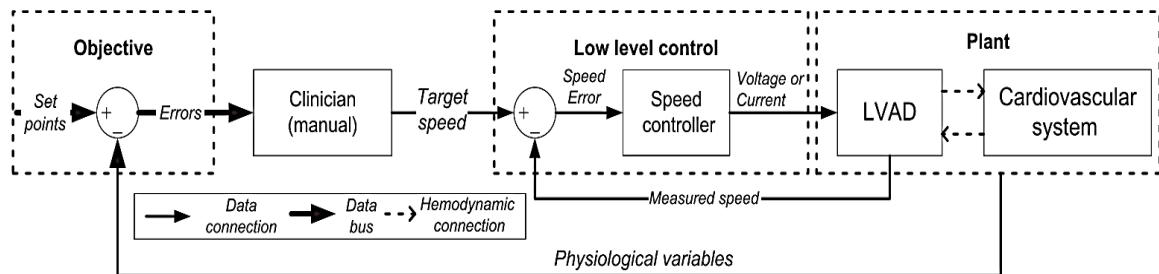


Figure 2-8 Block diagram of conventional LVAD operation [10].

Physiological control systems for LVADs are designed to automatically adjust the pump speed in order to meet the cardiac demand, which can improve the quality of lives of HF patients by balancing CO in response to the patient's activity, increase HF patient's lifespan and prevent hazardous events such as ventricular suction and pulmonary congestion [9].

A physiological controller is a high-level control system which can be used to replace the clinicians in the control loop as shown in Figure 2-9. This enables variation of the pump speed in a real-time mode based on the patient's conditions and therefore better meeting the patient's cardiac demand [9].

Design of a physiological control system for an LVAD includes a selection of suitable controlled variables (variables from the CVS or LVAD) and the desired set point, which can be constant or time-varying, corresponding to the controlled variables. A large variety of physiological control systems for LVADs have been proposed by researchers [19], [39], [73], [74], [42], [66]–[72]. In the following section, these physiological control systems are briefly described.

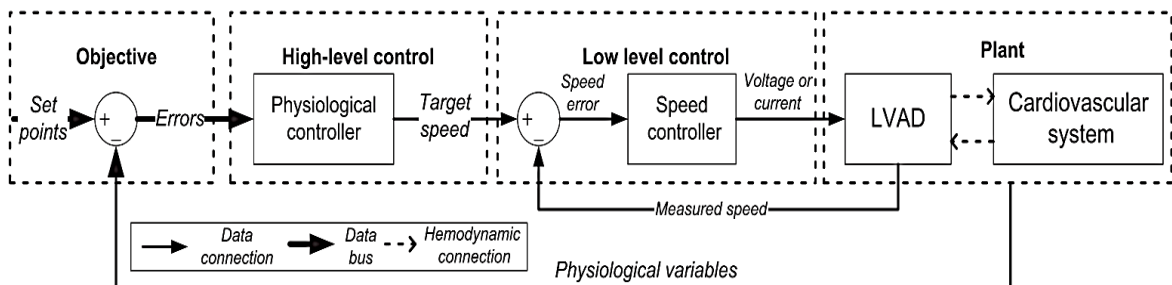


Figure 2-9 Block diagram of a physiological control system for LVAD [10].

### 2.3.1 Differential pressure control ( $\Delta P$ control)

The first pressure-based control systems were designed to maintain the average differential pressure ( $\Delta P$ ) between the outlet and the inlet of the pump (pressure of aorta and ventricle) to a specified reference of 75 mmHg [75], [76] and 110 mmHg [77]. This was based on the hypothesis that  $\Delta P$  is maintained constant by the native ventricle and therefore LVAD should do the

same. The block diagram of the proposed  $\Delta P$  control by Giridharan et al. is demonstrated in Figure 2-10 [76]. These strategies were evaluated on different physiological conditions using a numerical model of the CVS (*in silico*). This approach requires two implantable pressure sensors to measure aortic and ventricular pressures, even though there were no commercialized long-term implantable pressure sensors at that time. However, Giridharan [78] later proposed a novel method to estimate differential pressure using measurements of pump flow rate, current and speed which was evaluated *in silico*. The estimation algorithm was proposed based on the assumption that blood is a Newtonian fluid and the effects of inertia and viscosity of the blood ignored.

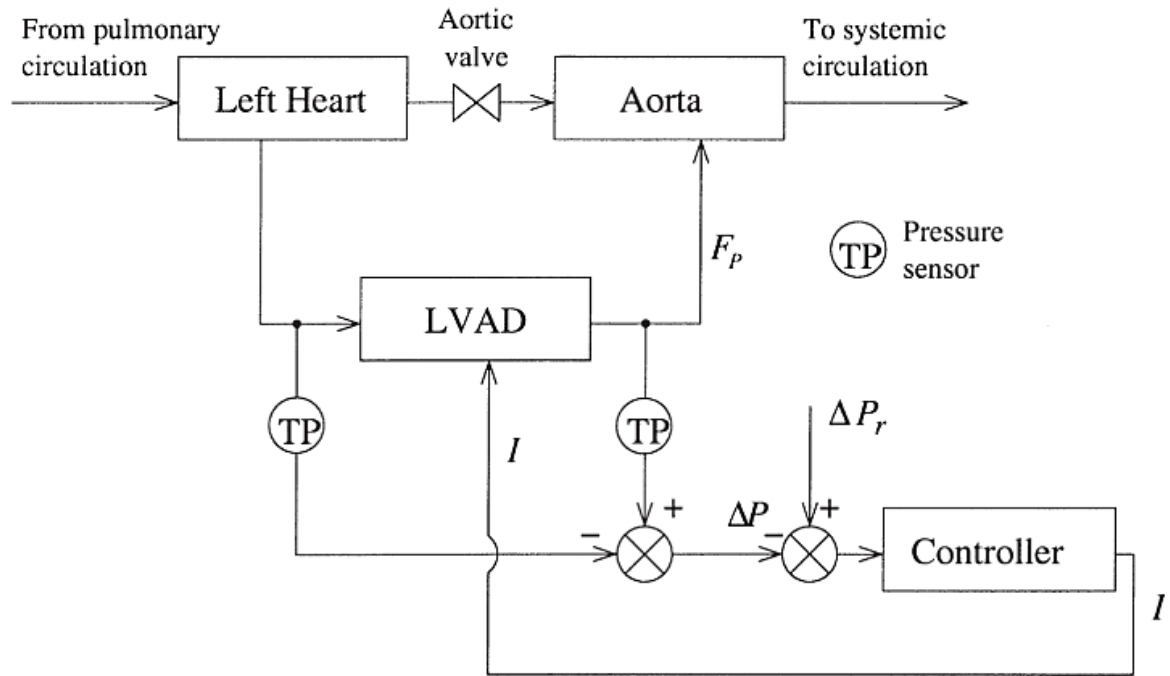


Figure 2-10 Block diagram of the proposed  $\Delta P$  control by Giridharan et al. [76].

Giridharan et al. [79] suggested a novel concept of maintaining differential pressure between the pulmonary vein and aorta ( $\Delta P_a$ ) constant in order to remove the influence of cannula resistance and systolic portion of left ventricular pressure. The results showed a better performance on adaption of pump flow in an exercise scenario compared to  $\Delta P$ , which was validated using a mock circulation loop (*in vitro*).

The first disadvantage of these differential pressure control systems is that this strategy makes the LVAD both preload and afterload sensitive. However, the native heart is preload sensitive and afterload insensitive. Secondly, this approach cannot prevent ventricular suction and backflow occurring [13].

Arndt et al. [73], [80] proposed a new control strategy based on the amplitude of differential pressure (difference between maximum and minimum) over a cardiac cycle, which is called differential pressure pulsatility  $\Delta P_{pulse}$ . Although these approaches led to robust results across different cardiovascular scenarios, these strategies were only assessed *in silico* and showed a very long settling time of about 500 seconds, which can lead to adverse events such as suction and congestion.

### **2.3.2 Aortic pressure control (Afterload control)**

Aortic pressure (AoP) control aimed to maintain AoP at a constant desired value. Wu et al. proposed a new approach on AoP control including two objectives [81]:

1. Maintaining AoP at a desired value of 145 mmHg to compensate for a patient's elevated total peripheral resistance.
2. Maintaining differential pressure at a value of 110 mmHg.

The justification for these objectives is that maintaining aortic and differential pressure at constant desired values makes the left ventricular pressure constant as well, which can help to prevent ventricular suction. The results showed no ventricular suction in rest to exercise and  $\pm 20\%$  total peripheral resistance variation scenarios *in silico* [81]. Wu et al. also proposed a new combined AoP and  $\Delta P$  control in which AoP reference was set by a nonlinear function of  $\Delta P$ , and AoP was estimated by an observer using pump speed and  $\Delta P$  as shown in Figure 2-11. The results showed that the average estimation error for AoP was maintained less than 2 mmHg and the controller could restore abnormal hemodynamic variables back to normal range *in silico* and *in vitro* [40].

This control strategy requires a robust estimation algorithm or pressure sensors to maintain AoP and prevent suction. Furthermore, this approach was only validated by systemic vascular resistance variations and transition from rest to exercise scenarios *in silico*, and changes in contractility *in vitro*, using a single simulated patient scenario. Moreover, maintaining AoP at the value of 145 mmHg is quite high since the mean arterial pressure for a healthy person is between 100 to 120 mmHg [81]. Therefore, further investigation is necessary for this approach.

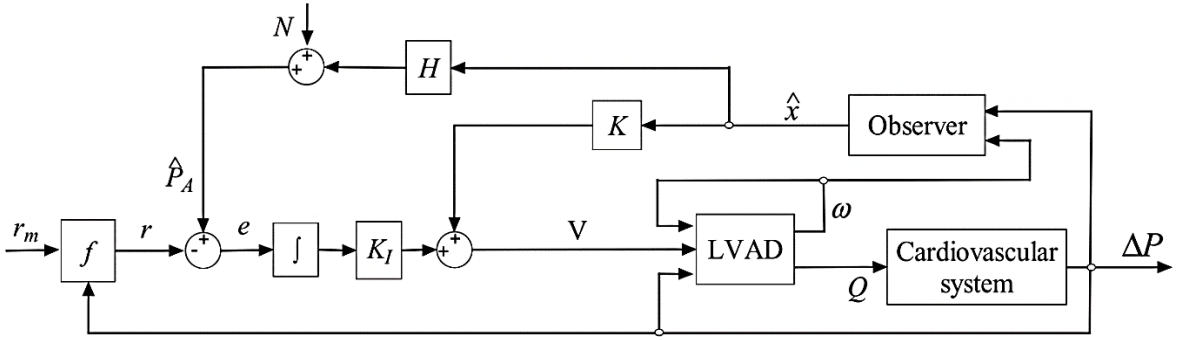


**Figure 2-11 Block diagram of the proposed AoP and  $\Delta P$  control by Wu et al [40].** Q: pump flow, W: pump speed, V: pump voltage, rm: reference aortic pressure,  $\hat{P}_A$ : estimated aortic pressure and e: error between estimated and reference aortic pressure.

### 2.3.3 Left ventricular end diastolic pressure control (Preload control)

Maintaining left ventricular end-diastolic pressure (LVEDP or preload) at a constant desired value using a custom-made pressure sensor was proposed by Bullister et al. [14], [82]. The desired value for preload was automatically adjusted to keep AoP at a suitable level and preload in a user-defined range. The results showed that this control approach maintained preload in the normal range while there was no evaluation on suction prevention. Pauls et al. performed more evaluation on this control strategy *in vitro* and found that this approach can lead to a lower number of ventricular suction and can increase the exercise capacity by increasing CO [13]. While this control strategy seems to work, the corresponding pressure sensor proposed by Bullister is not on the market yet. Furthermore, sensor implantation enhances the risk of thrombus formation [9]. Currently, there are two implantable pressure sensors CardioMEMS (FDA-approved) [83] for pulmonary artery pressure

measurement and HeartPOD [84] for left atrial pressure measurement. However, these pressure sensors have not been employed for physiological control of LVADs [10]. Furthermore, CardioMEMS and HeartPOD have resulted in errors of  $-0.8 \pm 1.3$  and  $0.8 \pm 4.0$  mmHg for mean pulmonary artery and left atrial pressures, respectively [84], [85], which make them difficult to use for physiological control of LVADs.

A sensorless physiological control of pump inlet pressure using a deadbeat control algorithm and an autoregressive exogenous model of the system was proposed by Alomari et al. in 2011 as shown in Figure 2-12 [86]. In this study, non-invasive measurements of motor power and rotational speed were employed to estimate pump inlet pressure [86]. The evaluation was performed on several scenarios such as healthy, reduced heart contractility and low afterload *in vivo*. Results showed that the pump inlet pressure control strategy can track the reference with minimum error [86]. However, this study has been performed on a VentrAssist<sup>TM</sup> pump which is no longer used clinically. Moreover, online measurement of hematocrit (HCT) is required in this approach. Furthermore, this study has only been evaluated on a single simulated patient.

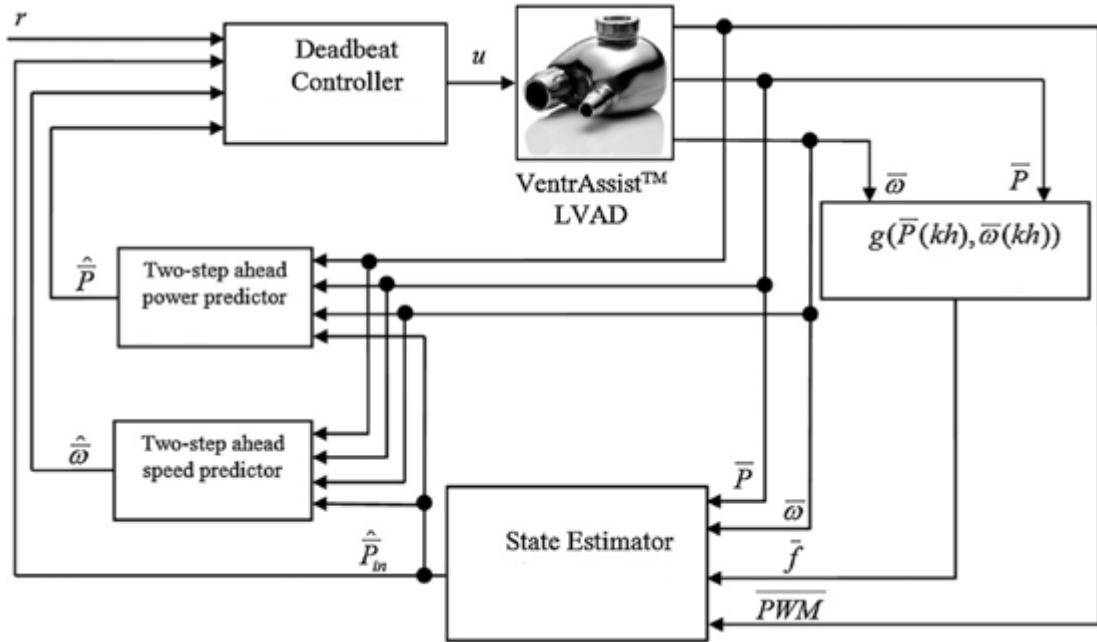


**Figure 2-12 Block diagram of the sensorless physiological control of pump inlet pressure by Alomari et al. [86].**  $r$ : reference pump inlet pressure,  $\hat{P}$ : estimated mean pump power,  $\hat{\omega}$ : estimated mean pump speed,  $\hat{P}_{in}$ : estimated mean pump inlet pressure,  $\bar{P}$ : measured mean pump power,  $\bar{\omega}$ : measured mean pump speed,  $\bar{f}$ : mean steady-state pump flow and  $PWM$ : mean pump pulse with modulation (control input signal).

### 2.3.4 Left ventricular systolic pressure control (SP control)

Adjusting the speed of the LVAD using left ventricular systolic pressure (SP) as the controlled variable was proposed by Petrou et al. in 2016 [87]. This approach requires measurement of the maximum value of pump inlet pressure over a cardiac cycle. The structure of the SP controller is shown in Figure 2-13. In this study, the difference between measured and target SP is multiplied by a proportional gain and then is added to the reference speed to make the final desired pump speed. The target SP and reference speed were obtained by a calibration process [87]. The results demonstrated that SP control is robust to sensor drift and noise, but it fails to avoid pulmonary

congestion at very low cardiac contractility. This is because a reduction in cardiac contractility leads to a decrease in SP level and therefore results in a drop in the pump speed which can cause an LVEDP of more than 20 mmHg. In addition, this approach requires a long-term implantable pressure sensor, and there is no investigation on SP control via the currently available pressure sensors such as CardioMEMS and HeartPOD. Furthermore, this approach has only been assessed on a single simulated patient.

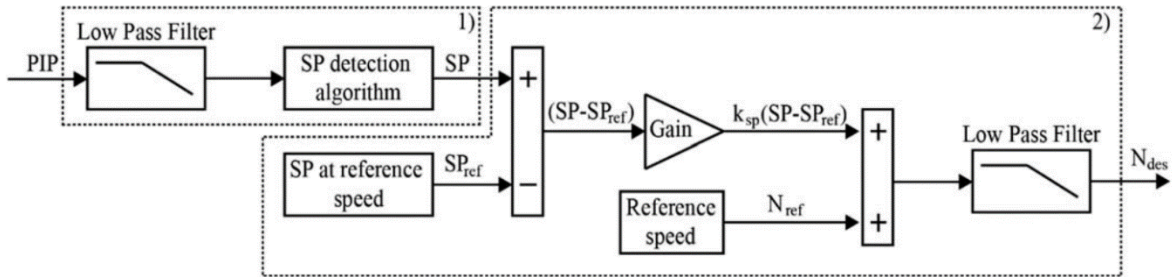


**Figure 2-13 Block diagram of the SP control proposed by Petrou et al. [87].** SP: systolic pressure, SP<sub>ref</sub>: reference systolic pressure and N<sub>ref</sub>: reference speed.

### 2.3.5 Flow control

Maintaining CO at a desired flow rate by adjusting pump speed regardless of preload and afterload ensures end organ perfusion. Nishida et al. and Casas et al. [88], [89] proposed constant flow control strategies for adjusting the LVAD speed used for cardiopulmonary bypass (CPB) and extracorporeal membranous oxygenation (ECMO). However, cardiac demand in the recovered LVAD patients can be varied during different activity levels and therefore a constant flow control strategy is not an appropriate strategy [10]. In addition, this approach requires implantable flow sensors. Currently only

one FDA approved LVAD with an implantable flow probe is the HeartAssist-5 (HA5). All other LVADs rely on estimated flow as a feedback variable [10].

Control of pulsatile pump flow for an LVAD using a deadbeat controller was proposed by Lim et al. [66]. In this study, noninvasive measurements of pump speed and current were used to estimate pulsatile pump flow. This approach was evaluated on constant and sinusoidal pulsatile pump flow references. The results demonstrated that the proposed controller tracks the references with minimal error. However, this strategy was only validated on transition from rest to exercise *in silico* and therefore further investigation is necessary. Furthermore, the target mean flow is not adapted with changes in different activity levels. Moreover, this study has only been evaluated on a single simulated patient.

A constant level of flow pulsatility, in which pulsatility was defined by the amplitude of the absolute value of flow when baseline drift was removed from flow, using a fuzzy controller was proposed by Choi et al. to avoid ventricular suction and deliver optimized pump flow [90]. While this study showed promising results *in silico*, *in vitro* and animal testing (*in vivo*), this approach is not able handle variable heart contractility between patients or over time.

### **2.3.6 Frank-Starling control (FS control)**

Maslen et al. [91] proposed the first physiological control system that imitates the FS mechanism of the native heart by changing the pump flow with preload. The reasoning behind this approach was that mimicking the FS mechanism can

restore preload sensitivity for HF patients. The first implementation and evaluation of FS control was performed by Salamonsen et al. in 2012 [92]. In this study, a target pump flow rate was set based on a linear function of measured pump flow pulsatilities (as a surrogate for preload). Four pulsatility measures including flow, speed, current and differential pressure from peak-to-trough amplitude of fluctuations over a cardiac cycle were used with a validated numerical model [92]. The results showed that FS control in which average pump flow changes with flow pulsatility is more similar with changes in LV stroke before opening of the aortic valve (AoV) [92]. *In vitro* evaluations of FS control showed that this strategy can prevent ventricular suction and pulmonary congestion, and increase preload sensitivity and pump flow rate during exercise [13], [15], [16], [93]. A model for pump flow estimation and a sliding mode controller were implemented on FS control by Bakouri et al. [94], [95]. In this approach, a linear relationship between estimated mean pump flow and pump flow pulsatility was derived to determine the desired pump flow. Then a sliding model controller was able to adjust the pump speed based on the desired pump flow. The results demonstrated that the proposed system could track the desired reference pump flow in different scenarios such as changes in contractility, SVR and circulatory volume. Employing left ventricular pressure instead of pump flow pulsatility for controlling LVAD speed resulted in a higher mean pump flow (increase of 54%) with minimum loading on the LV during exercise [96]. This is because pump flow pulsatility relies on ventricular contractility and therefore it is not an appropriate variable to be used as a surrogate of preload in the FS control for severe HF conditions.

Furthermore, FS control strategies require implantation of pressure and flow sensors into the patient's body which may lead to thrombus formation and device failure. In addition, this approach has only been evaluated on a single simulated patient. The structure of the preload-based Starling-like controller proposed by Mansouri et al. [16] is shown in Figure 2-14. In this approach, a new Starling-like controller was proposed to maintain mean pump flow with respect to mean LVEDP. *In vitro* and *in silico* results showed 37% increase of mean pump flow in exercise simulation compared to constant speed controller. Moreover, the proposed controller could maintain mean arterial pressure (MAP) and mean pump flow during severe reduction in the left ventricular contractility. However, this method requires implantation of pressure sensor and the evaluations have been performed on a single simulated patient.

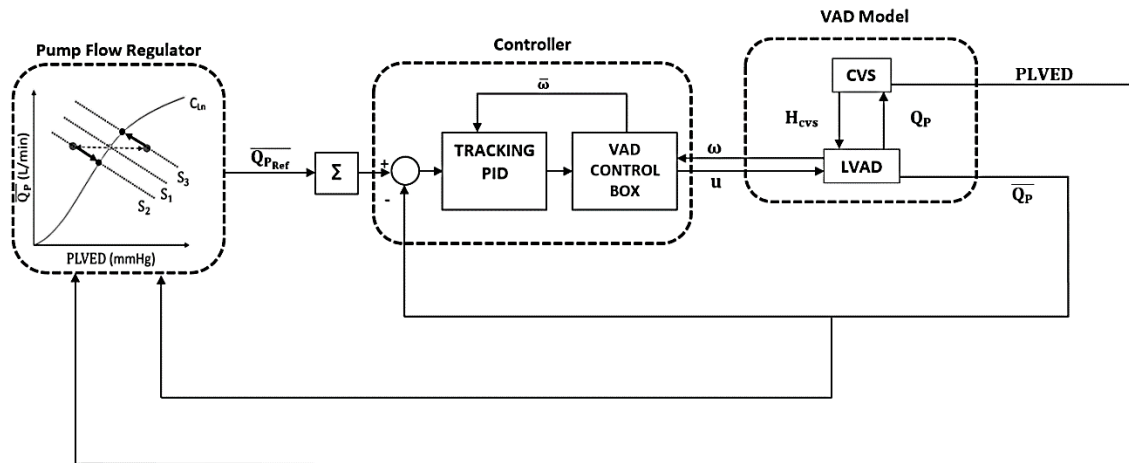


**Figure 2-14 Block diagram of the preload-based Starling-like control by Mansouri et al. [16]. CVS: cardiovascular system,  $H_{CVS}$ : head pressure,  $Q_p$ : pump flow,  $\bar{Q}_p$ : mean pump flow,  $Q_{p\text{ref}}$ : reference mean pump flow,  $w$ : pump speed,  $\bar{w}$ : mean pump speed,  $u$ : control input signal and PLVED: left ventricular end-diastolic pressure.**

Moscato et al. proposed a new Starling-like controller *in silico* in which the pump flow changes linearly with left ventricle pressure estimation to maintain a constant afterload impedance [97]. The proposed control system also mimics the FS mechanism. The results showed that this approach can adjust the pump speed automatically based on venous return and reduce the risk of ventricular suction. In this study, left ventricle pressure was estimated based on AoP measurement. This requires implanting a pressure sensor in the aorta which is currently unavailable. In addition, the relationship between AoP and ventricular pressure can change over time or from one patient to another. This relationship should be considered accurately since the proposed controller must work across different patient conditions regardless of the variations. Furthermore, it was assumed that LVAD works in the full support mode (LVAD is only responsible for supplying the CO), while more investigation should be performed as to what would happen when the AoV opens.

### **2.3.7 Left ventricular volume control (LVV control)**

In 2014, Ochsner et al. [98] proposed a new physiological control system, which works on the LVV as the controlled variable. This approach consists of three stages: 1. HR and end diastolic volume (EDV) calculation, 2. desired pump power calculation and 3. converting the desired pump power to desired pump speed using a pump power look-up table (relation between the hydraulic pump power and speed) as shown in Figure 2-15. In this approach, first HR and EDV were extracted from LVV. Afterward, preload recruitable stroke work (PRSW) was calculated based on the EDV-stroke work relationship shown in

Figure 2-16. Then, the desired hydraulic pump power was calculated based on HR and PRSW. Finally, the desired speed was determined by the pump power look-up table. The structure of the LVV control is shown in Figure 2-17. The results showed that LVV control leads to increased preload sensitivity and reduced afterload sensitivity, similar to the native heart in different circulatory variations such as changes in HR, systemic arterial resistance and unstressed volume of the systemic veins. However, there is currently no long-term implantable volume sensor, making implementation difficult. Moreover, this study has only been evaluated on a single patient scenario.

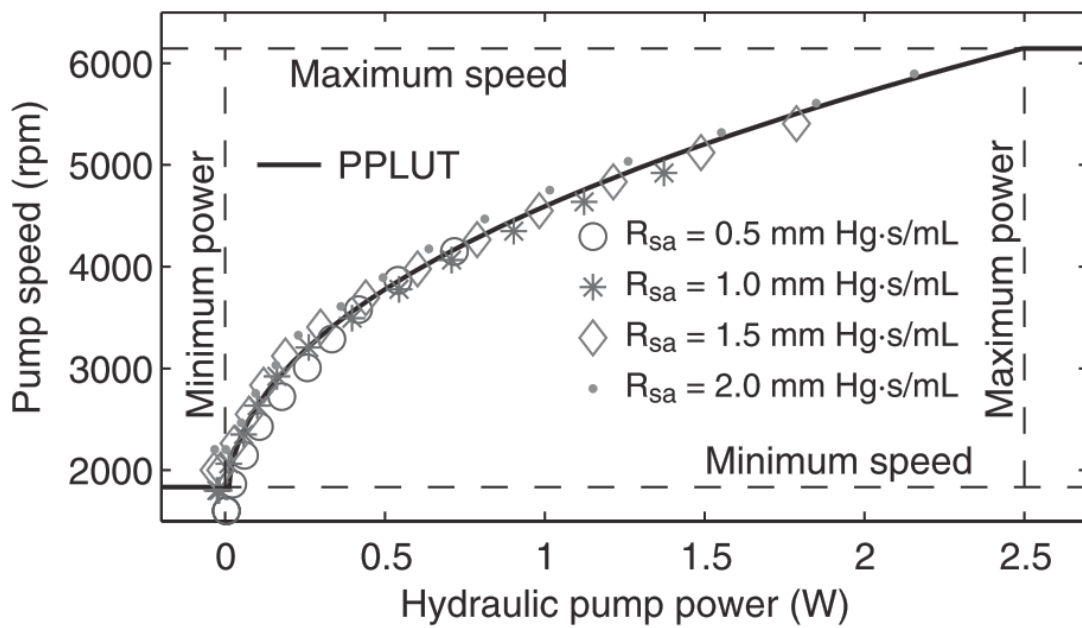


**Figure 2-15** Deltastream DP2 (Medos Medizintechnik AG, Stolberg, Germany) pump-power lookup table [98].  $R_{sa}$ : systemic arterial resistance.

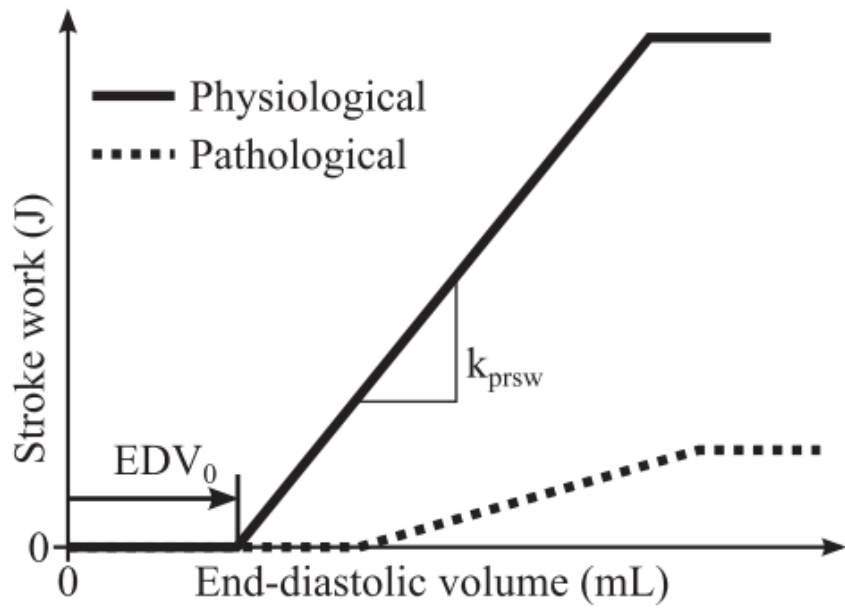


**Figure 2-16 EDV-stroke work relationship [98].** EDV<sub>0</sub>:end-diastolic volume at zero pressure, PPLUT: pump-power lookup table and k<sub>prsw</sub>: gain for adjusting preload recruitable stroke work.

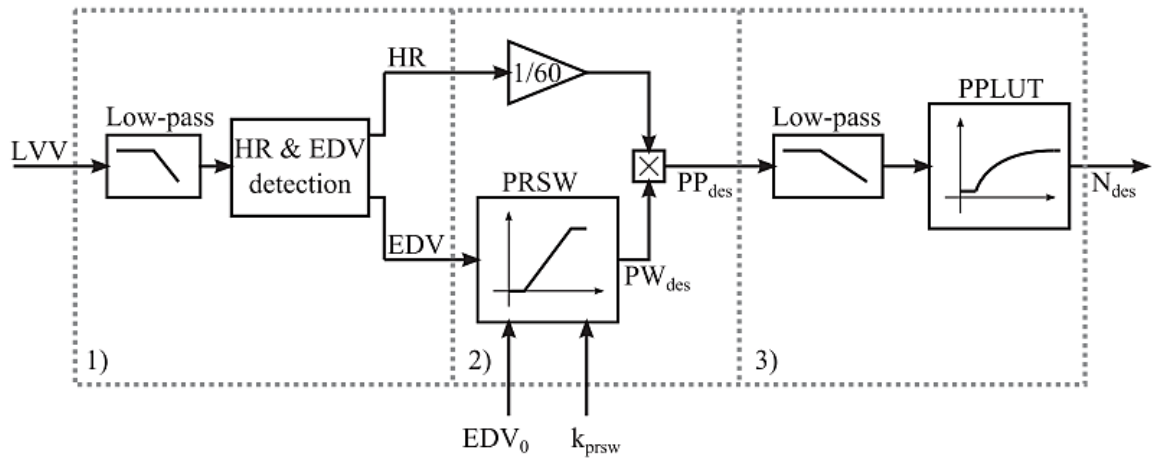


**Figure 2-17 The structure of the LVV control proposed by Ochsner et al. [98].** HR: heart rate, EDV: end-diastolic volume, EDV<sub>0</sub>: end-diastolic volume at zero pressure, k<sub>prsw</sub>: gain for adjusting preload recruitable stroke work, PPLUT: pump-power lookup table and PP<sub>des</sub>: desired hydraulic pump power.

### **2.3.8 Multi-objective control (MO control)**

Multi-objective control approaches involve combining two or more control objectives, using several feedback variables and targets to address the shortcomings of single control approaches.

The first multi-objective control was proposed by Vollkron et. al in 2005 [62]. In this work, the pump flow was adjusted based on the cardiac demand *in vitro* and from data in a clinical study (15 patients). The results demonstrated reduction on the number of ventricle suctions. This system involves four different control objectives:

1. Maintaining a desired flow rate based on heart rate.
2. Limiting maximum acceptable power.
3. Maintaining the desired flow pulsatility (was defined as the difference between maximum and minimum of the pump flow in one hear cardiac cycle) in the range of 1.5 to 2 liters/min to avoid suction.
4. Ensuring a minimal acceptable flow.

Each objective was then weighted and combined using gains and minimum and maximum operations as shown in Figure 2-18. The clinical results demonstrated a significant increase in pump flow during exercise occurred which improved the patients' movability. However, in this study, it was assumed that the heart has some contractility, and it is unclear whether this strategy will work in a patient with a weakened heart, therefore more

investigation should be considered in the case of severe HF with no ventricular contractility.

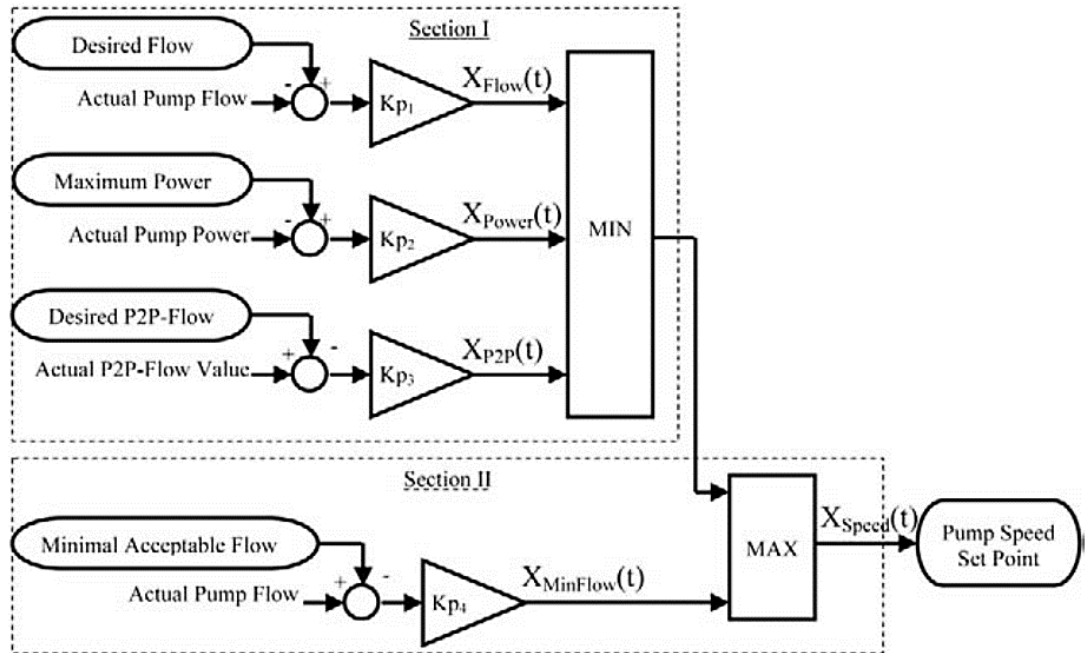


**Figure 2-18 Schematic of multiobjective physiological control system with four different control objectives [62].**

Boston et al. proposed a new multi-objective control system which is based on three different control objectives [99]:

1. CO should be higher than a minimum value.
2. Left atrial pressure should be higher than 0 mmHg and lower than 10-15 mmHg to prevent ventricular suction and pulmonary congestion.
3. Systemic arterial pressure should be maintained between 70-150 mmHg.

Different coefficients were assigned to each objective to create a cost function based on their relative importance. The default control was constant speed to provide minimum CO to the patients. However, if ventricular suction was detected, the pump speed was automatically changed to prevent suction. Several suction indicators such as pump flow pulsatility, rate of pump flow to pump speed, minimum pump flow, and pump current were used to detect the ventricular suction. The results showed that combining these objectives decreased the rate of suction events.

A novel multi-objective control approach was proposed by Gwak et al. [100] based on two different control objectives:

1. Venous return index (VRI), which is the pump flow rate to pump speed.
2. Harmonic suction index (HSI), which is defined as the ratio of the power of harmonics above the fundamental harmonic to the total power of the flow.

The first objective was used to optimize the pump flow rate and the second objective was employed to avoid ventricular suction. Each objective was implemented by a proportional-integral (PI) controller; however, both objectives were combined with equal weights of 0.5 to maintain perfusion flow and prevent suction equally. The result showed that the proposed multi-objective controller can prevent ventricular suction even with a sudden step decrease in preload. The evaluation of the proposed controller was performed on variation of preload and afterload *in vitro* which needs to be extended to

more challenging scenarios including HR and contractility variations *in vitro* and *in vivo* studies.

Petrou et al. [55] proposed a new multi-objective control based on the pump inlet pressure with six different objectives:

1. Pump flow adaptation according to physiological requirements of the patients.
2. Augmentation of aortic pulse pressure.
3. Opening of AoV for a certain period of time.
4. Monitoring of preload, afterload and heart rate.
5. Preventing ventricular suction.
6. Preventing pulmonary congestion.

In addition, several controllers such as pump flow adaptation, AoV opening, safety and speed amplitude were included in the proposed multi-objective control system. Since these controllers can contradict each other, a safety controller (LV suction, LV overload and backflow controllers) had the priority, followed by AoV opening and pump flow adaptation controllers. The performance of the proposed control system was evaluated *in vitro* via changes in preload, afterload and contractility, and the results showed a safe physiological controller in response to changes in perfusion requirements. In addition, the status of the AoV can be detected with overall accuracy of 86%. Furthermore, the risk of myocardial atrophy decreased. However, the MAP

estimator only worked when the AoV was detected as open. Further investigation is required on evaluation of the AoV opening method *in vivo* and clinical studies since this method has only been assessed on a single simulated patient.

Leao et al. [53] proposed a novel multi-objective control *in vitro* using a fuzzy logic controller, which consisted of three layers:

1. Pump speed control.
2. LVAD flow control.
3. Fuzzy control system with input variables of heart rate, average arterial pressure, minimum pump flow, level of physical activity (from patient) and clinical condition (from physician).

Furthermore, pump flow, heart rate and average arterial pressure are estimated from pump speed and power. The results showed that the proposed control system can maintain MAP and CO in the normal physiological range under different HF scenarios. However, inserting physical activity level manually to the fuzzy controller by the patient is not desirable since the patient can forget to change the level of physical activity. Moreover, the proposed method has only been evaluated on a single simulated patient.

Centralized multi-objective control of BiVADs *in silico* and *in vitro* were proposed by Koh et al. [38], [49] as shown in Figure 2-19. In these studies, model predictive control was employed to meet three objectives:

1. Providing pump flow rate based on the FS mechanism.
2. Prevent suction.
3. Prevent congestion.

Although the results showed that the proposed control prevent ventricular suction and congestion compared to the FS strategy with PI controller (FS-PI), this study has only been evaluated on a single simulated patient.

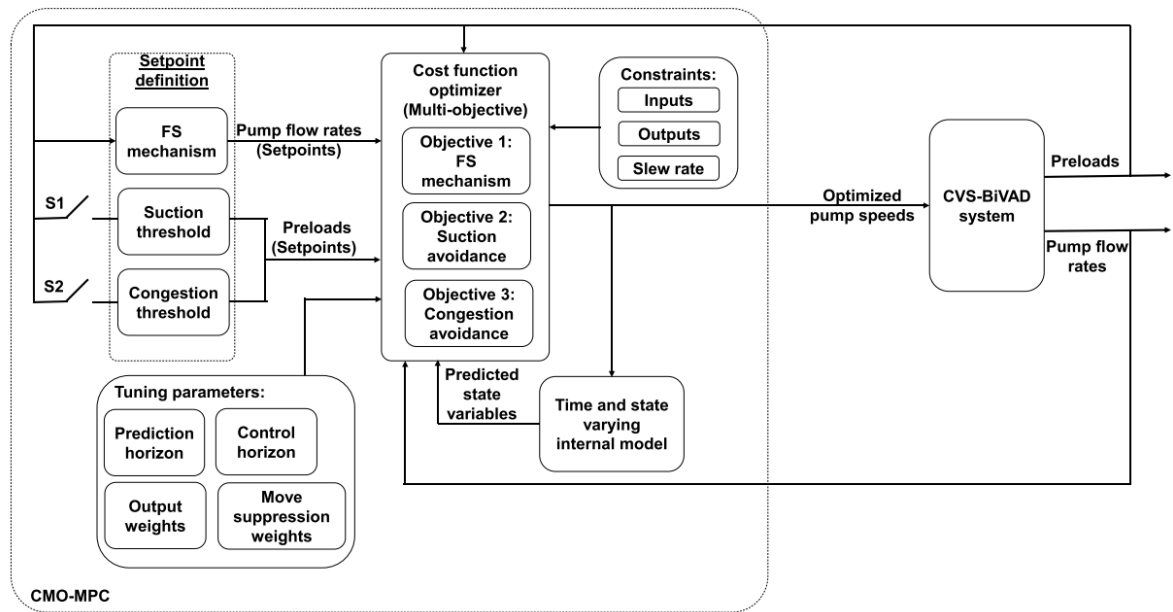


**Figure 2-19 Block diagram of the centralized multi-objective control of BiVADs proposed by Koh et al. [38]. FS: Frank-starling and CVS: cardiovascular system.**

In summary, more control objectives make the control strategy more complex and may need more sensor implementations. Therefore, suitable design and selection of each objective and their interactions to other objectives should be considered carefully.

## 2.4 Types of controller implementation

During the last 20 years, many types of controllers have been employed to implement physiological control of VADs from simple proportional-integral (PI) controllers to advanced controllers such as model predictive controllers to deal with uncertainties, nonlinearities of VADs and CVSs. In the following section a very brief description of the popular controllers used for physiological control of VADs is presented.

### 2.4.1 Proportional-Integral-Derivative controller (PID controller)

The proportional-Integral-Derivative (PID) controller is the most common controller used in the industry and for physiological control of VADs [19]. The design of a PID controller involves tuning of three parameters of proportional ( $K_p$ ), integral ( $T_i$ ), and derivative ( $T_d$ ) gains as shown in Figure 2-20 to meet the desired response or performance. A PI controller is a special case of a PID controller in which the coefficient of the derivative part ( $T_d$ ) is zero [101].

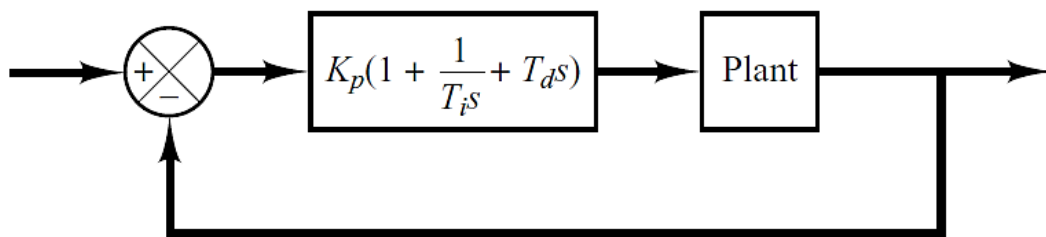


**Figure 2-20 Block diagram of a Proportional-Integral-Derivative (PID) controller [101].  $K_p$ : proportional gain,  $T_i$ : integral gain and  $T_d$ : derivative gain.**

PI or PID controllers have been widely used in many physiological control systems such as [12], [36], [37], [39], [50], [52], [102]–[104].

Although a PID controller can be tuned by Ziegler-Nichols (ZN) methods easily, it is not able to deal with highly nonlinear systems and therefore can result in poor performance [101]. Furthermore, the PID controllers used for physiological control systems were tuned to provide optimal performance only for special -single-patient conditions. Therefore, this control type cannot guarantee a robust response across different patients or conditions. Moreover, tuning the PID gains requires control engineering knowledge to make the adjustment to achieve the satisfactory performance, and therefore clinicians are unlikely to have the skillset.

#### **2.4.2 Model predictive controller (MPC)**

Model predictive control (MPC) is a kind of control in which the control signal is achieved by optimization of a cost function with constraints based on the prediction of the plant as shown in Figure 2-21. This cost function is usually made by the error (difference between predicted output and future reference) and slew rate (the rate of control signal change) to minimize the tracking error and limit the changes of control signal due to practical issues [19], [38].

MPCs have been used to control LVADs and BiVADs by several researchers [38], [49], [105], [106]. Koh et al. compared MPC with FS proportional integral (FS-PI) controller for adjusting the speed of BiVADs [38], [49]. The results demonstrated that an MPC was able to prevent ventricular suction and congestion while a FS-PI controller could not. While an MPC is a model-based controller and requires an accurate model of the CVSs, a simplified model of

the CVS has been used in these studies which can lead to inaccuracy of simulations.

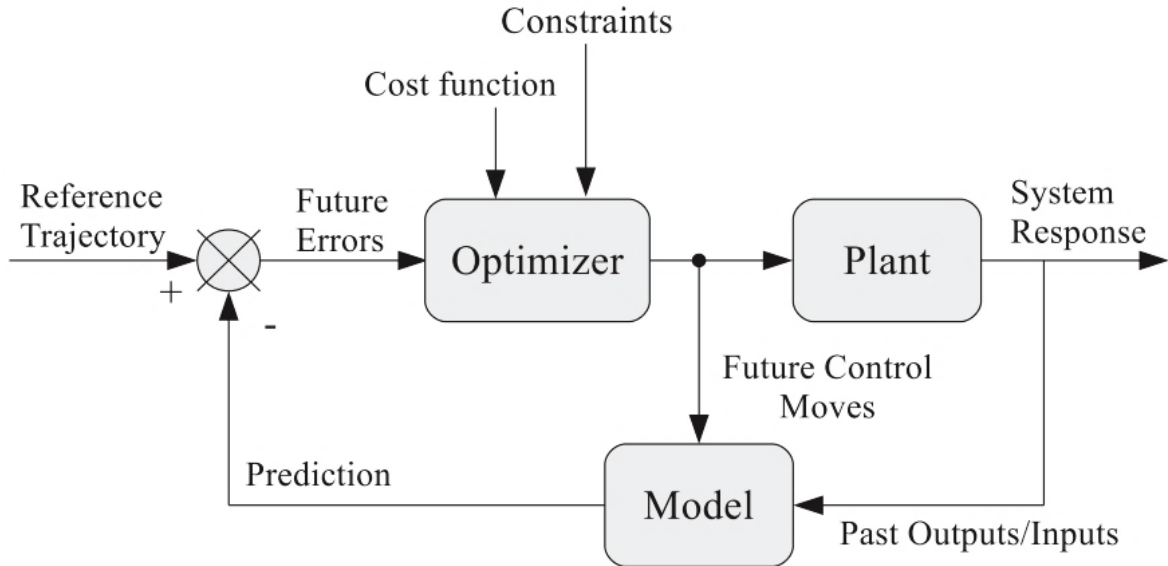


**Figure 2-21 Block diagram of the model predictive controller (MPC) [107].**

### 2.4.3 Fuzzy logic controller (FL controller)

Fuzzy logic (FL) controllers can provide a systematic approach to incorporate human experience into the controller design via different rules, fuzzification and defuzzification interfaces as shown in Figure 2-22 [19]. FL control is a model-free method in which the model of the system being controlled is not necessary to be known [108]. FL controllers have been employed for physiological control of VADs by several research groups [53], [90], [109], [110]. Figure 2-23 depicts the block diagram of the FL controller for pump flow control proposed by Casas et al. [109]. Choi et al. showed that a FL controller is more robust to parameter changes compared to a PI controller [90]. Animal

trial results also demonstrated that their proposed FL controller is able to provide sufficient CO and prevent ventricular suction [90]. However, designing a FL controller requires determination of different rules, which can be a time-consuming task and requires some intuitive understanding of the plant by the operators. In addition, due to the highly nonlinearity of the CVS, designing such rules to cover all the possible scenarios for different patients would be difficult.

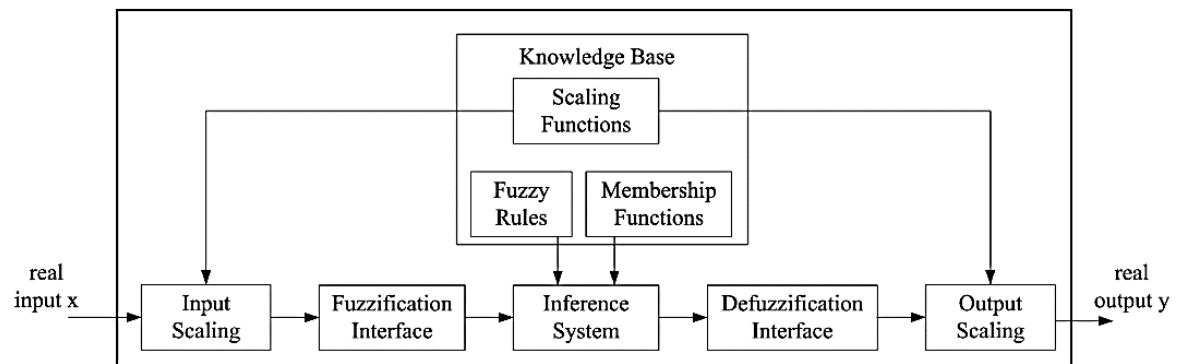


**Figure 2-22 Structure of a fuzzy rule-based system [108].**

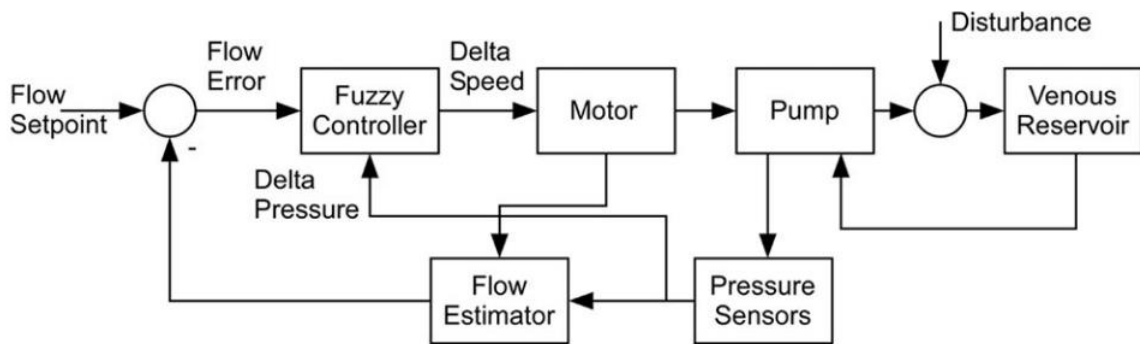


**Figure 2-23 Block diagram of the fuzzy login controller for pump flow control proposed by Casas et al. [109].**

#### 2.4.4 Adaptive controller

An adaptive control system can automatically adjust its parameters based on the error, output, control signal and the characteristics of the plant in response to the disturbances, uncertainties and unmodelled dynamics as shown in Figure 2-24 [111], [112].

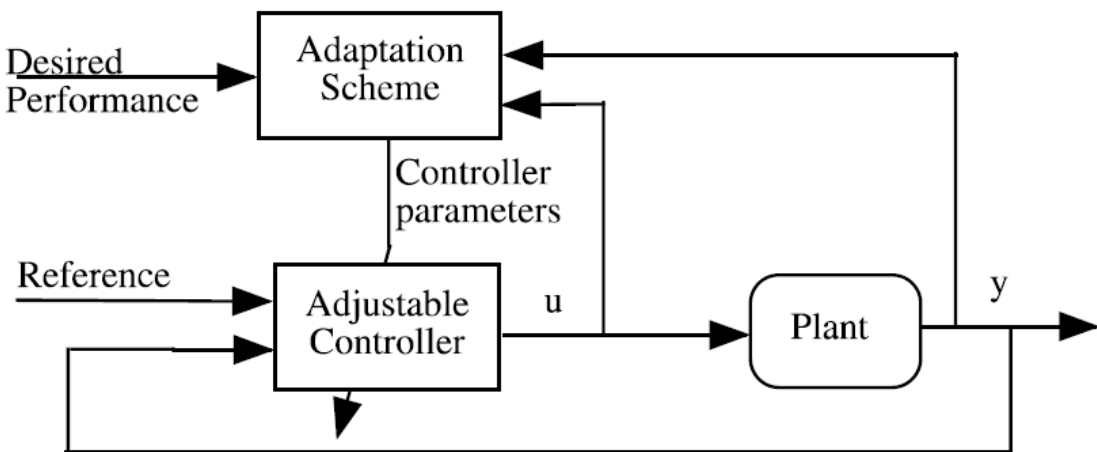


**Figure 2-24 Block diagram of adaptive control systems [112]. u: control signal and y: system output.**

Controlling VADs using adaptive controller and can robustly improve the performance of tracking of reference variables [40], [113]. In these works, Wu et al. proposed a linear state-space model which could estimate mean AoP based on the pump head pressure and speed. The estimated AoP is then adjusted by an adaptive controller to track the reference AoP [40], [113]. However, in these studies, a linear state-space model of CVS was used. Using a linear model instead of a nonlinear or numerical model of CVS can lead to inaccuracy of simulation and therefore unreliable control performance. This is

because a nonlinear or numerical model of CVS is linearized around an operating point which is only valid in a small region around the point, and it cannot be used to robustly simulate different patient conditions.

A neural network (NN) controller, which is one type of adaptive controller was employed to control dual rotary VADs [17]. Although the NN controller was able to improve the performance of the physiological control systems compared to a PID controller [17], these controllers requires training data, which is time-consuming to collect or produce.

## **2.5 Non-invasive estimation, monitoring and control approaches for LVAD**

Monitoring and different control strategies for LVAD patients require implantation of reliable transducers. These transducers for clinical implementation are faced with several challenges such as drift, interference from radiation and device failure, resulting in slow progress in developing implantable transducers [10].

CardioMEMS (St. Jude Medical, Minnesota, US) is the only FDA-approved pressure transducer (FDA P100045) clinically used for pulmonary artery pressure measurement, which is implanted into the distal pulmonary artery via right heart catheterization [83]. The result of evaluation of a CardioMEMS sensor on 17 HF patients has shown an average error of  $-4.4 \pm 0.3$ ,  $2.5 \pm 1.0$ , and  $-0.8 \pm 1.3$  mmHg for systolic, diastolic, and mean pulmonary artery pressures, respectively [85]. The HeartPOD (St. Jude Medical, Minnesota, US)

is an implantable left atrial pressure sensor, which has not been FDA approved yet [84]. Evaluation of HeartPOD accuracy on 84 HF patients has shown an error of  $0.8 \pm 4.0$  mmHg, which can result in 4.7 mmHg drift after three months [84]. Both CardioMEMS and HeartPOD have not been incorporated into LVAD physiological control systems [10]. The HeartAssist-5 (HA5) and aVAD (ReliantHeart Inc., Houston, Texas, USA) are the only axial flow LVADs with an integrated flow transducer. Both LVADs are approved for implantation in Europe [10]. However, the HA5 has only been FDA approved for a pediatric use in the USA [10], [114]. The implanted sensors uses an ultrasonic transit time method to measure the flow rate [10].

Although there has recently been some progress on implantable sensors, there is still a long way to use them for LVAD patients incorporated into physiological control systems in clinical practice. Therefore, non-invasive estimation algorithms for monitoring and control in the LVAD patient should be considered.

### **2.5.1 Pump flow estimation**

Reliable estimators for pump flow have been evaluated *in vitro* and *in vivo* by several researchers. The first pump flow estimator based on the pump intrinsic variables was proposed by Tsukiya et al. through a static model [115]. Kitamura et al. [116], Granegger et al. [117] and Moscato et al. [118] have extended the flow estimator using a dynamic model of pump intrinsic variables. Kitamura et al. [116] estimated the pump flow based on the pump speed, current and some viscosity-dependent parameters using a least square method, which resulted

in a correlation coefficient of 0.9941. Granegger et al. [117] used pump current, pump speed and fluid viscosity to estimate pump flow. The flow estimator outperformed the clinical estimator used in HVAD pump. The results showed the mean difference between the estimated and measured average flows of  $0.06 \pm 0.31$  L/min and  $-0.27 \pm 0.2$  L/min for nonpulsatile and pulsatile environments, respectively. Moscato et al. used pump head pressure and speed to estimate pump flow using *in vitro* experimental data [118]. The root mean square error between the predicted and measured flow was 7.4 ml/sec and absolute error never exceeded 24.9 ml/sec [118]. Autoregressive exogenous (ARX) models have been employed to estimate pump flow based on pump variables [119]–[122]. Tanaka et al. [119] used pump current, voltage and speed to estimate pump flow using an ARX model. The results showed estimation error of 0.27 L/min and correlation coefficient of 0.875. Yoshizawa et al. [120] employed pump power, pump speed and a bias for estimation of pump flow using an ARX model, which resulted in estimation error of 1.66 L/min and correlation coefficient of 0.850. Karantonis et al. [121] used pump speed, current and power for pulsatile flow estimation in a glycerol solution with viscosity between 2.05 to 3.56 mPas equivalent to 20-50% blood HCT using an ARX model. The resultant model yielded mean flow errors of 0.270 L/min. Alomari et al. [122] employed pump power, pump speed, bias and some parameters related to HCT to estimate pulsatile flow using an ARX model. The results showed a coefficient of determination of 0.982 and 0.849 and mean absolute error of 0.323 L/min and 0.584 L/min for *in vitro* and *ex vivo* experimental datasets, respectively. Adding blood viscosity or HCT of blood as

one of the inputs to model of pump flow estimator can improve the performance of the estimator [117], [122], [123]. Viscosity estimation on a MagLev pump using glycerol-sodium-water solution based on phase difference between the current in the magnetic bearing and the displacement of the impeller was proposed by Hijikata et al. [124]. The result of viscosity estimation showed a high coefficient of determination of 0.992. However, the proposed method was validated via a constant pump speed with a Newtonian liquid. Pump current is continuously changing due to variation of pump speed and therefore only using pump current does not suffice to estimate viscosity or even possible adverse events [125]. Petrou et al. proposed four different strategies for estimation of pump flow rate *in vitro* and *in vivo* [126]:

1. Model-based approach.
2. Optimal filtering approach using (EKF).
3. Pump inlet pressure-based approach
4. Hydraulic model approach.

These approaches were validated by variation of preload, afterload, viscosity, contractility and pump speed. The results demonstrated that use of a hydraulic model (using head pressure) led to the most reliable flow estimator. However, measuring VAD's head pressure require implementation of two sensors which is impossible with the current technology. The other approaches need a smaller number of sensors at the cost of a lower estimation accuracy than the hydraulic model approach.

Petrou et al. proposed a new method to estimate HCT based on the inlet pressure and the pump intrinsic variables using a mock circulation loop [127]. The best models were found using a Gaussian process, which were combined using stacked generalization method to create the final model. The final model was then assessed on an unseen dataset. The results showed a successful estimation of HCT with a mean absolute deviation of 1.81%. However, further investigation must be performed on the evaluation of the method with blood. Overall, there have been many flow estimators developed for a range of VADs, with most exhibiting high accuracy.

### **2.5.2 Ventricular suction detection**

Ventricular suction is a hazardous event for LVAD patients. However, accurate detection of suction requires long-term implantable ventricular pressures or volume sensors which are currently unavailable. This has led to development of algorithms that can detect suction non-invasively. Vollkron et al. proposed novel approaches to detect ventricular suction based on the pump flow rate using an adaptive threshold, which is dependent on heart rate [128], [129], however these methods were not able to detect all the suction events. From the final database consisting of 1196 samples, 5 false positive events (0.42%) and 18 false negative decisions (1.5%) were detected. Mason et al. [130] proposed seven suction indices created from pump speed to detect suction events. The best sensitivity (the ability of a test to correctly identify patients with a disease) of 95% and specificity (the ability of a test to correctly identify people without the disease) of 99% were derived from the method. Wang et

al. [131] employed a Lagrangian support vector machine (LSVM) to detect suction based on the six suction indices extracted from the pump flow waveform. The proposed method was assessed on *in vivo* experimental data. The results showed a sensitivity of  $98.67 \pm 0.84$  and specificity of  $99.59 \pm 0.29$  for suction detection. Voigt et al. [132] used a threshold from pump speed and current waveforms to detect suction events for both pulsatile and nonpulsatile conditions using *in vitro* and *in vivo* experimental datasets. The results showed a positive and false suction detection rate of 89% and 2.5% for *in vitro* and a positive and false suction detection rate of 79% and 6% *in vivo* datasets, respectively. Overall, suction detection algorithms have been heavily explored in the literature; however, in general they need to be further evaluated on clinical data.

### **2.5.3 Aortic valve (AoV) status detection**

The condition of the AoV for LVAD patients changes over time and can lead to adverse events such as commissural fusion, valve insufficiency and thrombus formation. To prevent these adverse events and adjust the pump speed, detection of AoV opening becomes important. In addition, maintaining an open AoV for a long period of time shows an improvement of cardiac function and can be a sign of myocardial recovery [133]. Several studies show that AoV opening status can be derived from pump variables such as speed, current and pump flow [133]–[136]. These studies were evaluated using different performance metrics such as sensitivity and specificity. Granegger et al. [133] extracted different features from pump speed changes such as skewness,

kurtosis, and crest factor to determine AoV opening. The results of their proposed method showed a sensitivity of 91.0% and specificity of 91.2%. Hayward et al. [134] used the area under the curve (AUC) of the power spectral density analysis of pump speed signal to determine the of AoV opening status. The sensitivity and specificity of the proposed method were 95% and 91%, respectively. Granegger et al. [135] also used skewness, kurtosis, and crest factor from the pump flow waveform to detect AoV opening. The results showed a specificity of 99.9% and 86.8%, and sensitivity of 99.5% and 96.5% for computer simulation and animal experiments, respectively. Bishop et al. [136] used the magnitude of the projection of the pump current waveform onto the eigenvectors to detect AoV opening. The results showed that the method could identify 4 out of 6 patients correctly when the AoV was closed, which was confirmed by echocardiography. However, more studies are needed to be performed to improve the sensitivity and specificity of AoV opening status in animal and clinical trials.

#### **2.5.4 Pressure estimation**

Although there are some studies on the estimation of pump pressure head based on the pump variables [120], [137], [138], there is no reliable estimator or long-term implantable pressure sensor for estimation or measuring preload. However, as pulmonary arterial wedge pressure (PAWP) can be more easily measured, non-invasive estimation of PAWP can therefore be used as a surrogate of preload. PAWP can be measured by right heart catheterization into the pulmonary artery of patients using a Swan-Ganz catheter. However,

measuring the PAWP by pulmonary artery catheterization can only work for a short period of time in hospital settings as most of these patients are discharged home and therefore don't have access to this technique [23]. Therefore, a non-invasive estimation of PAWP becomes more critical. Estimation and classification of PAWP based on the pump flow on clinical data has been conducted by several researchers [22], [23], [139]. Lai et al. [23] employed multiple linear regression to estimate high PAWP ( $\text{PAWP} \geq 20 \text{ mmHg}$ ) using the slope of the HVAD flow waveform at diastole for HF patients. The results showed a sensitivity of 77% and specificity of 86% for estimation of high PAWP. Grinstein et al. [139] used a multivariable regression to estimation high PAWP ( $\text{PAWP} \geq 18 \text{ mmHg}$ ) using the slope of the ventricular filling phase based on 15 HVAD patients. The results showed a sensitivity of 87% and specificity of 95% for only high PAWP. Imamura et al. employed the slope of the ventricular filling phase to estimate  $\text{PAWP} \geq 8 \text{ mmHg}$  using a linear regression. Sensitivity of 91.5% and specificity of 95.2% was derived in this study for estimation of high PAWP [22]. However, these studies were only able to estimate or classify high PAWP. None of these studies could provide an accurate estimation of the true value of PAWP, limiting their application in physiological control systems.

### **2.5.5 Estimation of patient activities**

The heart rate, patient's activity and cardiac properties can also be derived by pump variables [140]–[142]. This can also help to monitor patients and adjust the pump speed. Moscato et al. [140] used the pump flow waveform to

identify cardiac rhythms such as tachograms and arrhythmias. The results showed that tachycardia and atrial fibrillation were accurately detected from pump flow. Furthermore, there was small difference of  $0.3 \pm 1.0$  in the average heart-beat duration between pump flow waveform and a simultaneously recorded ECG signal. Moscato et al. [141] also employed the minimum rate ( $dQ/dt_{min}$ ) and the time constant of pump flow decrease to estimate minimum rate ( $dP/dt_{min}$ ) and the time constant of left ventricular pressure decrease to identify cardiac diastolic dysfunction. The results showed a correlation of coefficient (R) of greater than 0.97 between those variables. Naiyanetr et al. [142] proposed a new index ( $I_Q$ ), which was defined as the slope of a linear regression between the maximum derivative of the pump flow and its peak-to-peak value to determine the contractility of the heart. This index was then compared with maximal derivative of ventricular pressure ( $dP/dt_{max}$ ) versus end-diastolic volume (EDV). The results showed a coefficient of determination ( $R^2$ ) of 0.87 and 0.61 between  $I_Q$  and  $dP/dt_{max}$  vs EDV for computer simulation and animal studies, respectively. However, the experiments were performed on healthy animals instead of animals with HF or the method was evaluated only on numerical simulations. Therefore, these studies require more investigations.

## **2.5.6 Sensorless physiological control systems**

Several sensorless physiological control systems for VAD patients were proposed by different research groups [24], [37], [90]. Meki et al. [24] proposed a sensorless control for a continuous flow LVAD via setting

differential pump speed (difference between max and min of pump speed in each cardiac cycle) of 800 rpm, which could maintain physiological perfusion and avoid ventricular suction. However, there was not any information about how the proposed method can prevent pulmonary congestion. Wang et al. [37] proposed a sensorless physiological control system for BiVADs, which was able to prevent suction, restore physiologic perfusion and maintain left and right balance using intrinsic pump variables such as speed and power via maintaining differential pump speeds. However, these studies were only performed on numerical models of VAD and the circulatory systems on a single simulated patient. Choi et al. [90] proposed a fuzzy sensorless physiological control of a LVAD using a constant level of flow pulsatility (flow pulsatility was defined by the amplitude of the absolute value of flow when baseline drift was removed from flow) to avoid ventricular suction and deliver optimized pump flow. However, the proposed approach was not able handle variable heart contractility between patients or over time. Furthermore, all these studies were evaluated in single-patient condition, which can result in limited robustness and accuracy for evaluation of the methods with different patients. Therefore, further investigation should be done on different patients *in silico*, *in vitro* and *in vivo*.

## 2.6 Introduction to machine and deep learning

Machine and deep learning methods are parts of artificial intelligence (AI), which are able to learn a pattern from a training dataset automatically and then predict correct outputs on the new testing data. Machine and deep

learning methods are mainly used in a variety of classification and regression (or estimation) problems. The selection of an appropriate machine or deep learning approaches is crucial as it greatly affects the performance and generalizability of estimation or classification problem [143].

Shallow artificial neural networks (ANNs) are made by a set of weights, linear and nonlinear activation functions. They have been used for classification and estimation problems [143]. ANNs can learn patterns through a training process, which is optimization of the weights between the neurons to minimize a cost function defined as the error between actual output and target. A multilayer ANN with one hidden layer of neuron (a layer between input and output layer) can estimate any continuous nonlinear function, which is referred as a universal approximation theorem [143]. However, shallow ANN models require manually extracting relevant features from the data, which is a time-consuming and complicated process. Furthermore, the extracted features need to be ensured to be robust to signal variations [143]. Accordingly, researchers are currently applying deep learning neural network methods in different areas, which are able to automatically extract features from the raw signals [144].

Convolutional neural networks (CNNs) are one of the most powerful deep learning neural network methods, as was proposed by Fukushima in 1980 [145] and improved by Lecun in 1998 [146]. CNNs are basically simple artificial neural networks, in which a convolution operator instead of a matrix multiplication is employed in at least one of the layers [147]. CNNs can

automatically extract features from the raw data using different filters and convolutional functions and then feed these features to multilayer ANNs to classify them into different classes [144], [148]. Four types of layers that are commonly used in CNNs are convolution operation, pooling operation, fully connected and rectified linear unit (ReLU) [144] described as follows.

### **2.6.1 Convolution operation layer**

The convolution operation places a filter or kernel at each position of the image or signal to fully cover the whole image or signal and perform a dot product between the filter and input image or signal. The size of output layer (after performing convolutions) in the  $q+1^{\text{th}}$  layer is calculated as follows:

$$L_{q+1} = L_q - F_q + 1 \quad (1-2)$$

$$W_{q+1} = W_q - F_q + 1 \quad (2-2)$$

$$D_{q+1} = F_q \quad (3-2)$$

where  $L_q$ ,  $W_q$  and  $D_q$  are the length, width and depth at layer  $q^{\text{th}}$ , respectively, and  $F_q$  is the size of the filter [144].

Figure 2-25 shows the input layer, filter and the results output layer after convolution operation [144]. It shows that the convolution operator between a filter with a size of  $5 \times 5 \times 3$  and an input layer with a size  $32 \times 32 \times 3$  resulted

in an output layer with a size of  $28 \times 28 \times 5$ . The parameters of each filter for each layer is determined in the training phase of CNNs [144].

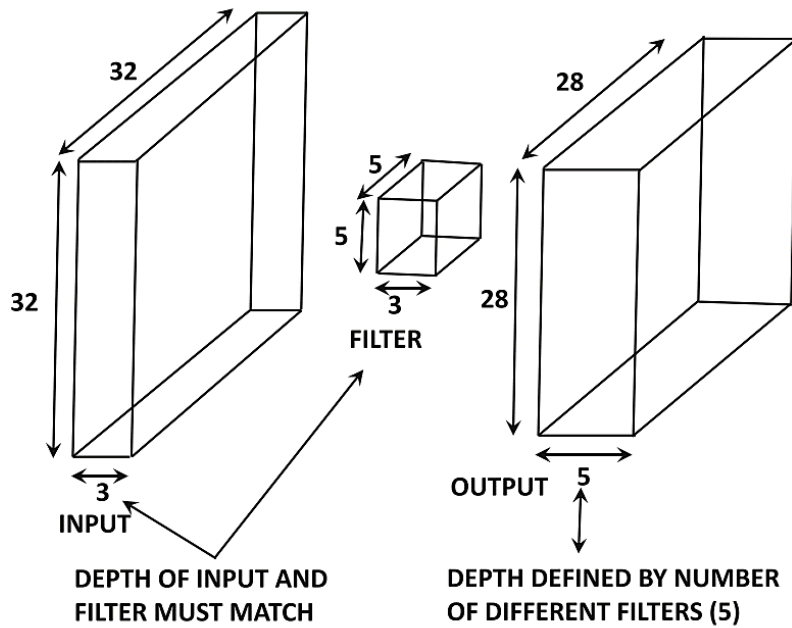


**Figure 2-25** The convolution operator between a filter with the size of  $5 \times 5 \times 3$  and an input layer with the size  $32 \times 32 \times 3$  resulted in output layer with the size of  $28 \times 28 \times 5$  [144].

## 2.6.2 Pooling operation layer

Pooling operation works in a small window with size of  $P_q \times P_q$  at each position of the image or signal, which creates a layer with the same depth but different size unlike the filters in convolution operations [144]. The pooling operation is used to reduce the number of features and only keep the essential ones to improve performance metrics [144]. Max-pooling is the most common pooling operation, which is derived by taking maximum values of a squared region of  $P_q \times P_q$  [144]. The final size of the layer (after performing max-pooling) with the stride (reducing factor) of  $S_q$  is calculated as follows:

$$L_{q+1} = \frac{(L_q - P_q)}{S_q} + 1 \quad (4-2)$$

Figure 2-26 depicts a  $3 \times 3$  max-pooling operation with stride size of 1 and 2. The resultant outputs are layers with sizes of  $5 \times 5$  and  $3 \times 3$ , respectively [144].

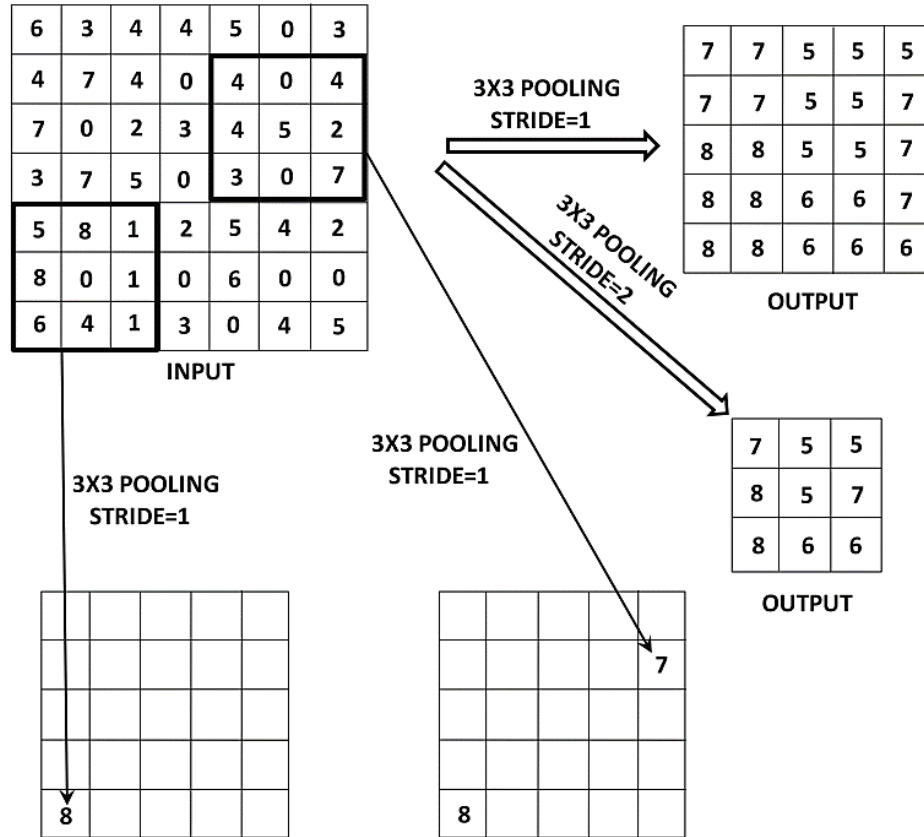


Figure 2-26  $3 \times 3$  max-pooling operation with the stride size of 1 and 2. The resulted output are layers with the size of  $5 \times 5$  and  $3 \times 3$ , respectively [144].

### 2.6.3 Fully connected layer

A fully connected layer works the same as a traditional feed-forward artificial neural network same as a multi-layer perceptrons (MLPs) which is made by weights, and linear and nonlinear activation functions. Each feature made

from the previous layers (convolution and pooling layers) is fed to the fully connected layer to create the final output of the CNN [144]. It is common that CNNs have more than one fully connected layer to increase the computational power and improve performance metrics [144]. The number of outputs in the fully connected layer is selected based on the specific application like the number of the classes in a classification problem or number of the regressors in a regression problem [144].

#### **2.6.4 ReLU Layer**

The ReLU is basically a nonlinear activation function which is applied in a traditional neural network [144]. The ReLU activation function is a recent evolution in the field of machine learning, which has been widely used instead of common activation functions such as sigmoid and tanh. It was shown that use of ReLU can improve performance metrics and speed of training over those activation functions [144].

### **2.7 Conclusion**

Several physiological control strategies have been highlighted in this chapter. It is concluded that constant inlet pressure control, constant afterload impedance control and FS control can prevent ventricular suction and pulmonary congestion and can increase CO and therefore improve the exercise capacity based on the evaluation of different scenarios [13], [103].

However, the first limitation of current physiological control systems is that these controllers have been evaluated in specific conditions for single-patient

scenarios. There is no guarantee of similar performance when these control systems are applied to different patients in different conditions. Therefore, further investigations are essential to design a robust physiological controller that can reliably work in different patient conditions and different patients. This shortcoming will be addressed in Chapter 3.

Another shortcoming of current physiological control systems is that these control systems mostly rely on pressure or flow measurements. As there is no reliable long-term implantable pressure or flow sensors for LVAD patients in clinical practice, LVADs are still driven at a constant speed resulting in no speed adaption in response to patient changes. One of the possible ways to overcome this limitation is to develop reliable pressure and flow estimators based on the strategy of a chosen physiological control system. Preload-based physiological control systems can prevent ventricular suction, pulmonary congestion and improve cardiac perfusion. Therefore, noninvasive estimation of preload can be used for controlling of LVAD speed. This will be addressed in Chapter 4.

The final limitation of current sensorless physiological control systems is that there are no reliable pressure or flow estimators and robust control systems which can work together to adjust LVAD speed noninvasively across different patient condition. Therefore, designing a robust sensorless physiological control system is necessary for LVAD patients. This shortcoming will be addressed in Chapter 5.

In the next chapter, we address the first objective of this study, which is design a physiological control system for an implantable heart pump that accommodates for interpatient and intrapatient variations.

## **Chapter 3. A Physiological Control System for an Implantable Heart Pump that Accommodates for Interpatient and Intrapatient Variations**

The study presented in Chapter 3 has been published in *IEEE Transactions on Biomedical Engineering*:

[29] **M. Fetanat**, M. Stevens, C. Hayward, and N. H. Lovell, “A physiological control system for an implantable heart pump that accommodates for interpatient and intrapatient variations.”, *IEEE Trans. Biomed. Eng.*, vol. 67, no. 4, pp. 1167–1175, 2020.

### **3.1 Abstract**

Left ventricular assist devices (LVADs) can provide mechanical support for a failing heart as bridge to transplant and destination therapy. Physiological control systems for LVADs should be designed to respond to changes in hemodynamic across a variety of clinical scenarios and patients by automatically adjusting the heart pump speed. In this study, a novel adaptive physiological control system for an implantable heart pump was developed to respond to interpatient and intrapatient variations to maintain the left-ventricle-end-diastolic-pressure (LVEDP) in the normal range of 3 to 15 mmHg to prevent ventricle suction and pulmonary congestion. A new algorithm was also developed to detect LVEDP from pressure sensor measurement in real-time mode. Model free adaptive control (MFAC) was employed to control the pump speed via simulation of 100 different patient conditions in each of six different patient scenarios and compared to standard PID control. Controller performance was tracked using the sum of the absolute error (SAE) between the desired and measured LVEDP. The lower SAE on control tracking performance means the measured LVEDP follows the desired LVEDP faster and with less amplitude oscillations preventing ventricle suction and pulmonary congestion (mean and standard deviation of SAE (mmHg) for all 600 simulations were  $18813 \pm 29345$  and  $24794 \pm 28380$  corresponding to MFAC and PID controller respectively). In four out of six patient scenarios, MFAC tracking performance was better than the PID controller. This study shows the control performance can be guaranteed across different patients and conditions when

using MFAC over PID control, which is a step towards clinical acceptance of these systems.

### 3.2 Introduction

Left ventricular assist devices (LVADs), which are mechanical pumps implanted in patients with heart failure, have been used as a mechanical circulatory support to assist a failing left ventricle during bridge to transplant, bridge to recovery and destination therapy [149]. Operating LVADs at constant speed may lead to ventricular suction (ventricular collapse due to low pressure in the ventricle) or pulmonary congestion (a condition caused by excess fluid in the lungs due to high pressure in the ventricle). Ventricular suction may lead to hemolysis, heart tissue damage near the pump inlet, right ventricular dysfunction or release of ventricular thrombus and subsequent stroke, while pulmonary congestion may lead to flooding of the lungs (pulmonary edema) and shortness of breath [10], [128], [150].

To prevent these hazardous events, physiological control systems for LVADs can be used to automatically adjust pump speed in response to changes in hemodynamic or pump variables to satisfy control objective(s). These objectives may include a constant differential pressure [76], a constant pump inlet pressure [151], a constant pump flow [109] and a Starling-like controller which sets target flow rate based on the left ventricular end-diastolic pressure (LVEDP) [12], [15], [16], [92], [93]. Most investigators have previously employed proportional-integral-derivative (PID) controller, with fixed gains, to implement these physiological control systems [12], [13], [15], [16].

These systems are commonly evaluated using computer simulations. However, in most of these simulations, [12], [13], [15], [16], [152], [153], only a single patient and/or condition is simulated. This is not clinically representative of the wider interpatient and intrapatient variations in cardiovascular system (CVS) dynamics. The control system, usually PID control, is tuned to provide optimal performance only for this specific patient and condition. The consequence of this is that control performance cannot be guaranteed across different patients and conditions, which may lead to more hazardous events like suction and congestion.

An adaptive control system can adjust its parameters in the face of disturbances and time-varying plants. Adaptive control can be beneficial for controlling VADs because of the time-varying nature of the CSV. In a recent study, a neural predictive controller, which is one kind of adaptive controller, was employed to control dual rotary blood VADs by using a trained Artificial Neural Network (ANN) [153], and it was shown to have improvements over non-adaptive control. However, ANN controllers need training data which is difficult and time-consuming to collect. Furthermore, ANN controllers have a heavy computational burden which is not ideal from a practical viewpoint. Other non-linear adaptive controllers, such as fuzzy logic control (FLC), require the determination of rulesets which can be time consuming to produce and result in inefficient performance due to the non-linear behavior [111], [154].

To address these issues, we propose the use of model free adaptive control (MFAC) to implement physiological control systems for rotary LVADs. MFAC

does not require the training process like an ANN controller, nor does it require knowledge about the dynamic and structural information of the controlled system. It only uses the real-time measurement data of the controlled system, resulting in a generic controller for a class of industrial practical systems and leading to more efficient control. Furthermore, unlike the FLC, MFAC also does not require any rules, which makes it much easier to implement.

This study aims to develop an adaptive physiological controller that utilizes MFAC for an implantable LVAD that provides consistent control system performance across a range of interpatient and intrapatient variations. The objective of this controller is to minimize the error between the desired and measured LVEDP, and reduce the risk of hazardous events such as ventricle suction and pulmonary congestion.

In the following sections, first the numerical model of the human CVS and heart pump adopted for the evaluation of the proposed physiological control method is introduced. Then, a novel method for detecting LVEDP robust to noise is presented. Afterwards, the MFAC is described. Then different patient conditions and scenarios used for evaluation of the MFAC are described. Subsequently, the sensitivity analysis (used to identify parameters from the CVS that most likely contribute to control performance variation) is then described. Then, the result of the simulations with interpatient and intrapatient variations is presented. Finally, a discussion according to the

simulation results, limitations of the study and future works is presented.

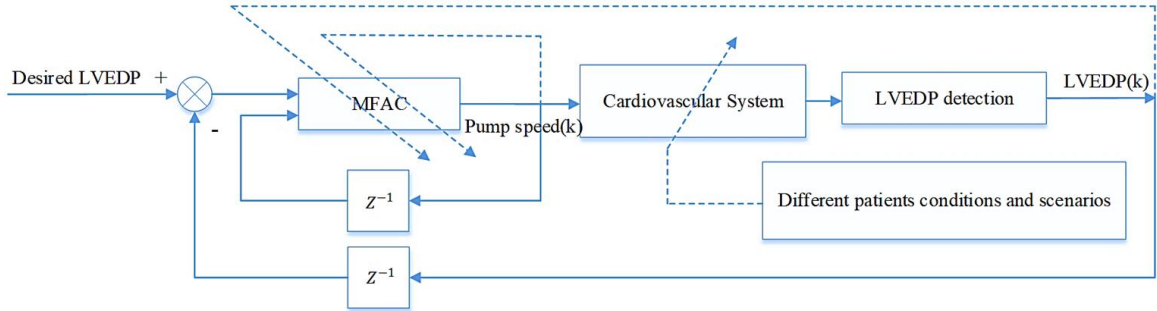


**Figure 3-1 Block diagram of developed methodology.**

### 3.3 Methodology

Figure 3-1 shows the block diagram of the control system and testing methodology used in this study. It consists of four major blocks: Numerical model of the cardiovascular system, LVEDP detection, MFAC system and evaluation using different patient conditions and scenarios. All are described in this section as follows.

#### 3.3.1 Numerical model of cardiovascular system

In this study, the simulations to investigate the implementation of the proposed LVEDP detection and MFAC, implemented in Simulink (MathWorks, Natick, MA, USA), were carried out on the numerical model of the cardiovascular system developed by Lim et al. [44] (Figure 3-2). The model was derived based on first principles and includes left and right hearts, systemic and pulmonary circulations, two heart pump models (LVAD and RVAD) and inlet and outlet cannulae. The CVS and heart pump model have been validated using *in vitro* mock-loop tests and *in vivo* animal experiments [44], [45], [155].

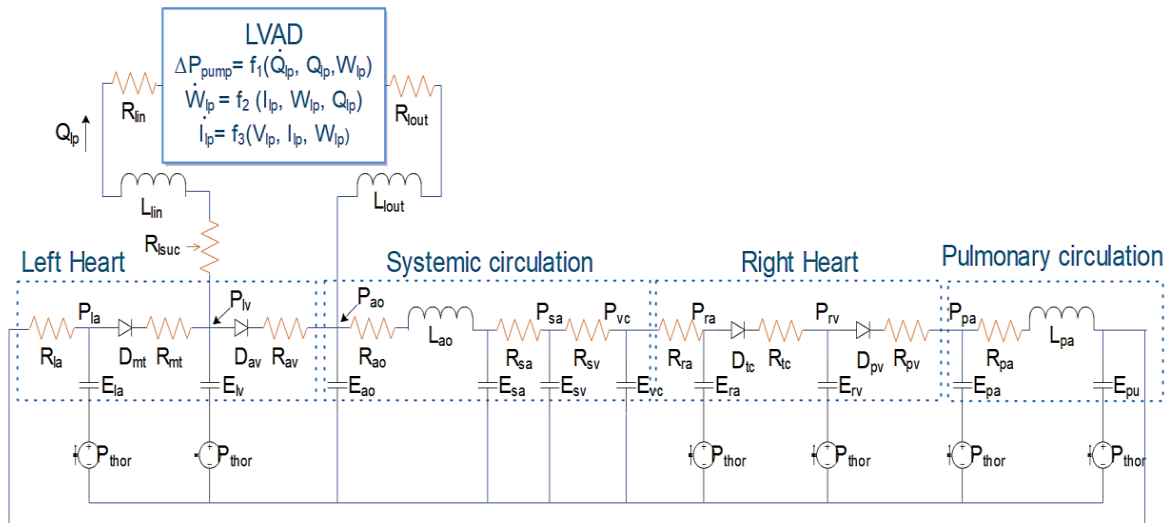


**Figure 3-2 Electrical equivalent circuit analogue of cardiovascular with heart–pump interaction model.** P, pressures; R, resistances; E, elastances ( $=1/\text{compliances}$ ); L, inertances; D, diodes. The model consists of two main components: (1) the cardiovascular model includes left heart, systemic circulation, right heart, pulmonary circulation (la, left atrium; lv, left ventricle; ao, aorta; sa, systemic peripheral vessels, including the arteries and capillaries; sv, systemic veins, including small and large veins; vc, vena cava; ra, right atrium; rv, right ventricle; pa, pulmonary peripheral vessels, including pulmonary arteries and capillaries; pu, pulmonary veins and (2) heart-pump model includes the LVAD and RVAD, ( $R_{in}$  and  $R_{out}$ , inlet and outlet cannulae resistances;  $L_{in}$  and  $L_{out}$ , inlet and outlet cannulae inertances;  $R_{lsuc}$ , left suction resistance,  $R_{rsuc}$ , right suction resistance,  $R_{band}$ , banding resistance). The intrathoracic pressure,  $P_{thor}$  was assigned  $-4 \text{ mmHg}$  during closed-chest simulated conditions [44].

The VentrAssist<sup>TM</sup> centrifugal pump was used as the LVAD in this study (Ventracor Ltd., Sydney, Australia). The VentrAssist model used was based on the model provided in [45], [155], [156]. The speed range of the pump model was constrained between 1800 and 3000 rpm, the clinical operating range of the device.

### **3.3.2 Real-time LVEDP detection**

As there is no method of LVEDP detection from LVP measurement in the literature, a real-time LVEDP detection method is described in this section. In this control system, LVEDP was used as the feedback variable because of its excellent performance in previous physiological control studies [13]. It is an important clinical variable indicative of ventricular performance and can identify clinical symptoms of heart failure in patients. It also has a much simpler feedback pathway than more complex Frank-Starling control systems. However, it is difficult to determine LVEDP accurately from pressure sensor measurement in real time due to sensor noise and a lack of ECG signal to trigger LVEDP identification. To address this, we developed a novel LVEDP detection method that has 9 steps:

1. Smoothing the left ventricle pressure using a Butterworth low-pass filter with pass frequency of 5 Hz and stop frequency of 20 Hz named as filtered LVP (FLVP).
2. Computing the slope of the FLVP (SFLVP).
3. Computing heartbeat based on the finding the time difference between two consecutive peaks from SFLVP.
4. Computing the mean of SFLVP within the last window of 10 samples (MSFLVP).
5. Finding the points which meet  $\text{FLVP} \geq \alpha \text{ MSFLVP}$

6. Computing an adaptive threshold (TH) equal to the mean of 15 highest values in the SFLVP from previous cardiac cycle to current time, multiplied by  $\beta$ .
7. Finding the first point meeting the step 5 and 6 at the same time (LVEDP detection time).
8. Finding the closest point between the local minimum of the SFLVP and the LVEDP detection time found in step 7 (LVEDP actual time).
9. Computing the LVEDP from FLVP at LVEDP actual time found in step 8.

where  $\alpha$  and  $\beta$  were scaling factors, empirically adjusted to give a latency of 30 ms and sum of the absolute error of 1.2 mmHg when a noise signal with variance of 4 mmHg was added to the left ventricular pressure.

Figure 3-3 (a) shows the LVP in transition from rest to exercise for a simulated patient with white noise variance of 2 mmHg. Figure 3-3 (b) depicts the original LVP, LVP with added noise, filtered LVP (FLVP), slope of the FLVP (SFLVP), identified LVEDP and latency between LVEDP detection time and LVEDP actual time. As it can be seen in the Figure 3-3 (b), the green point shows the exact location of LVEDP before ventricle contraction. The sampling rate of measured variables is 200 Hz.

The LVEDP detection method was evaluated in six different patient scenarios; rising and falling pulmonary vascular resistance (PVR), rising and falling systemic vascular resistance (SVR), rest to exercise and postural change with 100 different patient conditions in each. To vary the SVR and PVR in the model,

systemic arterial resistance ( $R_{sa}$ ) and pulmonary arterial resistance ( $R_{pa}$ ) were changed, as arterial resistance is the main contributor to total vascular resistance in the numerical model. In order to evaluate the impact of the pressure sensor noise on the developed LVEDP detection, a white noise signal with different levels of variance (0 to 4) was added to the left ventricular pressure. Mean of absolute error between LVEDP detection and actual time is defined by (1-3):

$$MAE = \frac{1}{n} \sum_{i=1}^n |LVEDP \text{ detection time}_i - LVEDP \text{ actual time}_i| \quad (1-3)$$

where  $MAE$  is the mean of the absolute error (millisecond),  $LVEDP \text{ detection time}_i$  and  $LVEDP \text{ actual time}_i$  are detection and real locations (time) of the LVEDP derived from the left ventricle pressure and  $n$  is the number of total samples in each simulation which equals to the number of cardiac cycles in each scenario calculated by LVEDP detection method.

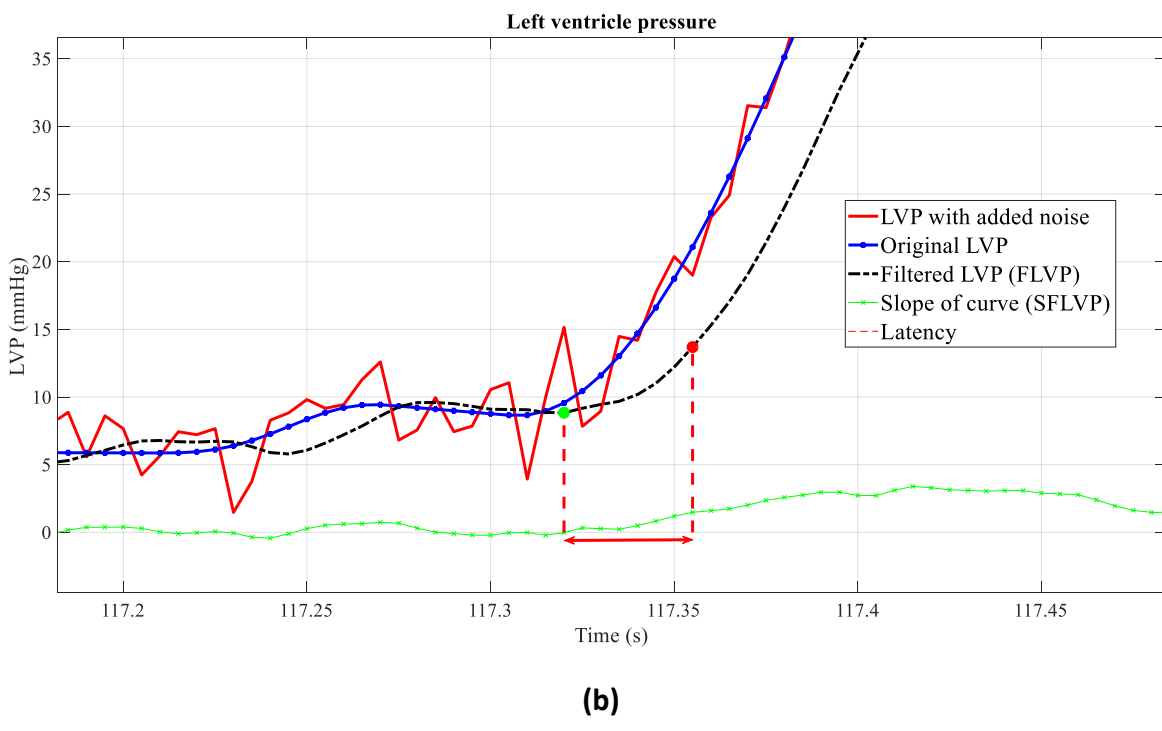
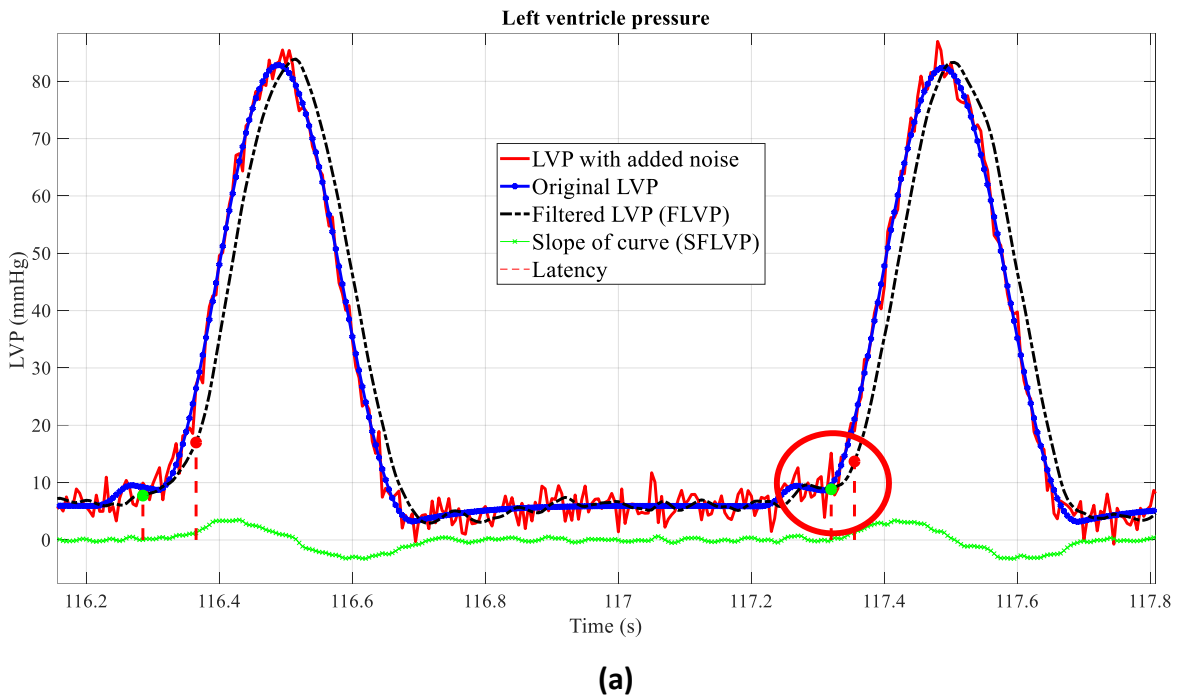


**Figure 3-3 Real-time LVEDP detection, (a) left ventricle pressure (LVP) in transition from rest to exercise for patient 1 with white noise variance of 2 mmHg, (b) zoomed LVP.**

### 3.3.3 Model free adaptive control (MFAC)

The MFAC is an adaptive control system which does not need the model of the plant to design the controller. It is designed by using the input/output measurement data of the controlled plant, without knowledge of the system structure or dynamics information of the controlled plant explicitly or implicitly. Specifically, MFAC identifies the linear or nonlinear model of the plant via a series of equivalent dynamic linearization data models within dynamic operation points of the closed-loop system by using a dynamic linearization technique (DLT) and pseudo-partial derivative (PPD) [111], [154]. A brief description of the MFAC follows.

A single input, single output (SISO) nonlinear discrete-time system can be defined as follows:

$$y(k+1) = f(y(k), \dots, y(k-n_y), u(k), \dots, u(k-n_u)) \quad (2-3)$$

where  $y(k) \in R$  and  $u(k) \in R$  are the system output and control input at time  $k$ ,  $n_y$  and  $n_u$  are unknown orders of output and input, and  $f(\dots) \in R$  is the unknown nonlinear function [154].

The compact form dynamic linearization of nonlinear system (2-3) can be defined by (3-3):

$$y(k+1) = y(k) + \varphi(k) \Delta u(k) \quad (3-3)$$

where  $\varphi(k)$  is called pseudo-partial derivative (PPD).

In order to find the control input  $u(k)$ , it is considered to minimize the following equation to have less error (difference between the desired and system output) and changes of two consecutive control inputs:

$$J(u(k)) = \|y^*(k+1) - y(k+1)\|^2 + \lambda \|u(k) - u(k-1)\|^2 \quad (4-3)$$

where  $y^*(k+1)$  and  $\lambda$  are desired output and a weighting constant respectively [154].

By substituting (3-3) into (4-3) and differentiating (4-3) with respect to  $u(k)$  equals to zero, the control input is as follows:

$$u(k) = u(k-1) + \frac{\rho \varphi(k) (y^*(k+1) - y(k))}{\lambda + \|\varphi(k)\|^2} \quad (5-3)$$

where  $\rho$  is a step constant which is added to make (5-3) more general and flexible.

As the unknown PPD parameter  $\varphi(k)$  is time-varying, the least squares algorithm cannot track it well. Therefore, a time-varying estimation algorithm is used to estimate PPD  $\varphi(k)$ . By using the modified projection algorithm, the estimated unknown PPD  $\hat{\varphi}(k)$  can be found as follows [157]:

The objective function for  $\varphi(k)$  estimation is defined as in (6-3)

$$J(\hat{\varphi}(k)) = \|\Delta y(k) - \hat{\varphi}(k) \Delta u(k-1)\|^2 + \mu \|\hat{\varphi}(k) - \hat{\varphi}(k-1)\|^2 \quad (6-3)$$

where  $\mu > 0$  is a weighing factor.

By minimizing the objective function (6-3) with respect to  $\bar{\varphi}(k)$ , estimated unknown PPD ( $\hat{\varphi}(k)$ ) is found as follows:

$$\hat{\varphi}(k) = \hat{\varphi}(k - 1) \quad (7-3)$$

$$+ \frac{\eta \Delta u(k - 1) (\Delta y(k) - \hat{\varphi}(k - 1) \Delta u(k - 1))}{\mu + \| \Delta u(k - 1) \|^2}$$

$$\begin{aligned} \hat{\varphi}(k) = \hat{\varphi}(1), & \text{ if } |\hat{\varphi}(k)| \leq \varepsilon \text{ or } \Delta u(k - 1) \leq \varepsilon \\ & \text{or } \text{sign}(\hat{\varphi}(k)) \neq \text{sign}(\hat{\varphi}(1)) \end{aligned} \quad (8-3)$$

where  $\eta \in (0,1]$  is a step constant which is added to make (7-3) more general and flexible,  $\bar{\varphi}(1)$  is the initial value of  $\bar{\varphi}(k)$  and  $\varepsilon$  is a very small positive constant. The reset algorithm (8-3) is employed to make a stronger ability in estimating the time-varying parameter by the parameter estimation algorithm [154]. MFAC is dependent on following four assumptions:

Assumption 1: The partial derivative of  $f(\dots)$  in (2-3) with respect to the  $(n_y + 2)th$  variable is continuous.

Assumption 2: (2-3) satisfies the generalized Lipschitz condition.

Assumption 3: For a given bounded desired output signal  $y^*(k + 1)$ , there exists a bounded control input  $u^*(k)$  such that the system output reaches to the  $y^*(k + 1)$ .

Assumption 4: The sign of PPD  $\bar{\varphi}(k)$  is assumed to be unchanged.

Nonlinear system (2-3) satisfying assumption 1, 2, 3 and 4 is controlled by (5-3), (7-3) and (8-3) for a regulation problem; i.e.,  $y^*(k + 1) = y^* = \text{const}$ , then there exists a constant  $\lambda_{min}$  such that [111]:

1.  $u(k)$  and  $y(k)$  are bounded and the closed loop system is bounded input, bounded output (BIBO) stable.
2. The tracking error converges monotonically; i.e.,  $\lim_{k \rightarrow \infty} |y^* - y(k + 1)| = 0$

### 3.3.4 Different patient condition and scenarios

The MFAC was subject to a range of inter- and intrapatient variations for evaluation. In order to simulate these variations, some of the cardiovascular model parameters from Table 3-1 were changed from -20% to +20% of their nominal values to create 100 different patient conditions in each of six patient scenarios. To identify which parameters to vary, sensitivity analysis was used to find which model parameters had the greatest effect on the control tracking performance, defined in (9-3), in each patient scenario. The tracking performance derived under PID control was calculated in each simulation.

$$SAE = \sum_{i=1}^n |LVEDP_d - LVEDP_m| \quad (9-3)$$

where  $LVEDP_d$  is desired output (target),  $LVEDP_m$  is model output (measured output), SAE is the sum of absolute error and  $n$  is number of samples.

Afterward, dimensionless parameter sensitivity coefficient  $S_j$  was evaluated in each of the six patient scenarios using (10-3).

$$S_j = \frac{\theta_j \Delta F}{F_0 \Delta \theta_j} \quad (10-3)$$

where  $F_0$  is the initial nominal value of the objective function in (9-3),  $\theta_j$  is the value of parameter from its baseline,  $\Delta F$  is the difference between objective function derived by perturbed parameter and  $F_0$ , and  $\Delta \theta_j$  is the difference between value perturbed parameter and  $\theta_j$ . The higher the sensitivity coefficients  $S_j$ , the greater the effect that parameter has on control tracking performance. Sensitivity analysis was performed for the six common patient scenarios used to evaluate the MFAC. These scenarios were simulated by changing vascular resistance, heart rate and reservoir volume. These scenarios were rapid  $R_{pa}$  changes (increasing and decreasing), rapid  $R_{sa}$  changes (increasing and decreasing), transition from rest to exercise and a passive postural change (similar to a head-up tilt) experiment [13]. The simulation conditions for each scenario are shown in Table 3-2. In transition from rest to exercise and passive postural change scenarios, each parameter is varied using a first order system with a time constant of 10 (s) which simulates the response of the native circulatory system. The other scenarios are simulated to change the  $R_{pa}$  and  $R_{sa}$  in rapid mode (step change). If a controller can respond properly to these extreme scenarios, it is assumed the controller can also respond to mild changes appropriately [13].

In each scenario, parameters were deemed significant if the sum of the sensitivity coefficient for both +20% and -20% parameter variations was at least 0.45.

**Table 3-1 Normal values and description of cardiovascular model parameters for interpatient and intrapatient simulations**

No	Parameter (unit)	Description	Normal Value
1	Eeslvf (mmHg.mL <sup>-1</sup> )	LV end systolic elastance	3.54
2	Eesrvf (mmHg.mL <sup>-1</sup> )	RV end systolic elastance	1.75
3	Eao (mmHg.mL <sup>-1</sup> )	Aortic elastance	1.04
4	Eesla (mmHg.mL <sup>-1</sup> )	LA end systolic elastance	0.2
5	Eesra (mmHg.mL <sup>-1</sup> )	RA end systolic elastance	0.2
6	Epa (mmHg.mL <sup>-1</sup> )	Pulmonary arterial elastance	0.15
7	Epu (mmHg.mL <sup>-1</sup> )	Pulmonary vein elastance	0.04
8	Esa (mmHg.mL <sup>-1</sup> )	Systemic arterial elastance	0.37
9	Esv (mmHg.mL <sup>-1</sup> )	Systemic vein elastance	0.013
10	Evc (mmHg.mL <sup>-1</sup> )	Vena cava elastance	0.03
11	Rao (mmHg.s.mL <sup>-1</sup> )	Aortic resistance	0.2
12	Rra (mmHg.s.mL <sup>-1</sup> )	Right atrium resistance	0.012
13	Rpv (mmHg.s.mL <sup>-1</sup> )	Pulmonary valve resistance	0.02
14	Rsv (mmHg.s.mL <sup>-1</sup> )	Systemic venous resistance	0.12
15	Tc (s)	Heart rate coefficient	1
16	Tsys0 (s)	Maximum systolic heart period	0.5
17	V0la (mL)	LA end diastolic volume at zero pressure	20
18	V0lvf (mL)	LV end diastolic volume at zero pressure	40
19	V0ra (mL)	RA end diastolic volume at zero pressure	20
20	V0rvf (mL)	RV end diastolic volume at zero pressure	50
21	Vdla (mL)	LA end systolic volume at zero pressure	10
22	Vdlvf (mL)	LV end systolic volume at zero pressure	16.77

23	Vdra (mL)	RA end systolic volume at zero pressure	10
24	Vdrvf (mL)	RV end systolic volume at zero pressure	40
25	Rmt (mmHg.s.mL <sup>-1</sup> )	Mitral valve resistance	0.01
26	Rav (mmHg.s.mL <sup>-1</sup> )	Aortic valve resistance	0.02
27	Vuao (mL)	Aortic unstressed volume	230.88
28	Vupa (mL)	Pulmonary arterial unstressed volume	91.67
29	Vupu (mL)	Pulmonary vein unstressed volume	132.39
30	Vusa (mL)	Systemic arterial unstressed volume	231.04
31	Vusv (mL)	Systemic vein unstressed volume	1976.1
32	Vvc (mL)	Vena cava unstressed volume	136.17
33	P0la (mmHg)	LA end diastolic stiffness scaling term	0.5
34	P0lvf (mmHg)	LV end diastolic stiffness scaling term	0.98
35	P0ra (mmHg)	RA end diastolic stiffness scaling term	0.5
36	P0rvf (mmHg)	RV end diastolic stiffness scaling term	0.91
37	Vtotal (mL)	Total blood volume	5200
38	$\lambda_{la}$ (mL <sup>-1</sup> )	LA end diastolic stiffness coefficient	0.025
39	$\lambda_{lvf}$ (mL <sup>-1</sup> )	LV end diastolic stiffness coefficient	0.028
40	$\lambda_{ra}$ (mL <sup>-1</sup> )	RA end diastolic stiffness coefficient	0.025
41	$\lambda_{rvf}$ (mL <sup>-1</sup> )	RV end diastolic stiffness coefficient	0.028
42	Lao (mmHg.s <sup>2</sup> .ml <sup>-2</sup> )	Aortic inertance	0.0001
43	Lpa (mmHg.s <sup>2</sup> .ml <sup>-2</sup> )	Pulmonary arterial inertance	7.70e-05

**Table 3-2 Six different patient scenarios and their simulations conditions**

Patient scenarios	Simulation conditions	Reference
Increasing $R_{pa}$ changes	100 to 500 dyne.s.cm $^{-5}$	[13]
Decreasing $R_{pa}$ changes	100 to 40 dyne.s.cm $^{-5}$	[13]
Increasing $R_{sa}$ changes	1300 to 2600 dyne.s.cm $^{-5}$	[13]
Decreasing $R_{sa}$ changes	1300 to 600 dyne.s.cm $^{-5}$	[13]
Transition from rest to exercise	1. Increasing heart rate from 60 to 80 bpm 2. Decreasing $R_{pa}$ from 100 to 40 dyne.s.cm $^{-5}$ 3. Decreasing $R_{sa}$ from 1300 to 670 dyne.s.cm $^{-5}$ 4. Adding 500 mL fluid from a reservoir into the heart via the right atrium	[13]
Passive postural change	Removing 300 mL fluid from the heart into a reservoir	[13]

### 3.3.5 MFAC evaluation

In order to evaluate the PID and MFAC responses across interpatient and intrapatient variations, a suite of simulated LVAD patients were created for each of the six scenarios (totaling 600 “patients”). To create each patient, the most significant of the 43 cardiovascular model parameters (as determined by the results of the sensitivity analysis) were randomly changed between -20% to 20% from their nominal values.

In each patient for each scenario, an MFAC system was developed to maintain LVEDP at a constant value, according to the following protocol. In the first 100 seconds, the heart pump works in a constant speed mode (2400 rpm) which allows the cardiovascular system to reach steady state. From time 100 sec, the MFAC was activated. At this point, if the measured LVEDP is between 3 mmHg to 15 mmHg, the initial set point is chosen as 0.2 mmHg greater than the current value of LVEDP. This enables a simple step response to be evaluated. 150 seconds after commencement, one of the six patient scenarios were simulated. This process was repeated for a system controlled with PID control. PID gains with an anti-windup mechanism were tuned using a quasi-Newtonian optimization algorithm to minimize (9-3) as the same approach provided in [12]. The PID parameters were  $k_p = 133.09$ ,  $k_i = 17.17$ ,  $k_d = 10.21$ . The MFAC parameters were chosen empirically as  $\mu = 0.1$ ,  $\lambda = 0.1$ ,  $\rho = 1$ ,  $\eta = 1$ ,  $\varphi(1) = 0.001$  and  $\varepsilon = 10^{-4}$ .

To assess the difference between PID and MFAC performance, the sum of absolute error between desired LVEDP and measured LVEDP defined in (9-3) was employed to compare the two controllers. Wilcoxon's test was performed to compare the SAE of PID and MFAC across the 100 simulated patients for each scenario, with a p-value less than 0.05 considered significant. Additionally, the number of scenarios in which pulmonary congestion occurred was noted. Based on the normal range of measured LVEDP (3 to 15 mmHg) [158], pulmonary congestions was defined the measured LVEDP above 15

mmHg. All values are expressed as mean  $\pm$  standard deviation unless otherwise stated.

## 3.4 Results

### 3.4.1 LVEDP detection

Table 3-3 shows the result of the developed real-time LVEDP detection in six different patient scenarios (rising and falling  $R_{pa}$ , rising and falling  $R_{sa}$ , rest to exercise and postural change) for 100 different patient conditions in each case. The results show that in all scenarios (600 simulations) with different levels of white noise, the developed LVEDP detection method has a very small latency ( $31.62 \pm 12.67$  ms) for all simulations. Accuracy of LVEDP detection method was assigned by calculating of mean and standard deviation of the absolute error between the actual and detected LVEDP with different level of noises in each scenario shown in Table 3-3. The accuracy of the developed method for all the simulations is  $0.71 \pm 0.61$  mmHg.

**Table 3-3 Evaluation of LVEDP detection (number of cardiac cycles in each simulation)**

Scenarios	Total number of simulations in each scenario	White noise variance (mean of SNR)	Accuracy of developed method (mean±std)	Latency of developed method, ms (mean±std)
Rising R <sub>pa</sub>	100 different patient conditions and 190 cardiac cycles in each simulation	0 (NaN)	0.32 ± 0.10	31.11 ± 4.98
		1 (30.11)	0.38 ± 0.34	32.65 ± 9.87
		2 (24.11)	0.64 ± 0.55	33.20 ± 14.61
		3 (20.60)	0.93 ± 0.75	32.03 ± 15.76
		4 (18.14)	1.27 ± 0.98	30.69 ± 16.45
Falling R <sub>pa</sub>	100 different patient conditions and 190 cardiac cycles in each simulation	0 (NaN)	0.36 ± 0.08	30.02 ± 0.36
		1 (31.53)	0.41 ± 0.32	32.31 ± 7.66
		2 (25.52)	0.63 ± 0.54	33.86 ± 13.19
		3 (22.01)	0.91 ± 0.73	33.65 ± 15.20
		4 (19.53)	1.22 ± 0.96	32.60 ± 16.45
Rising R <sub>sa</sub>	100 different patient conditions and 190 cardiac cycles in each simulation	0 (NaN)	0.39 ± 0.31	29.24 ± 6.78
		1 (30.31)	0.41 ± 0.44	30.99 ± 9.80
		2 (24.32)	0.62 ± 0.59	31.98 ± 14.20
		3 (20.84)	0.89 ± 0.77	31.74 ± 16.16
		4 (18.40)	1.18 ± 0.97	30.76 ± 17.00
Falling R <sub>sa</sub>	100 different patient conditions and 190 cardiac cycles in each simulation	0 (NaN)	0.39 ± 0.07	29.02 ± 2.57
		1 (30.67)	0.40 ± 0.31	30.74 ± 8.18
		2 (24.66)	0.62 ± 0.50	32.16 ± 13.11
		3 (21.16)	0.90 ± 0.72	31.66 ± 14.79
		4 (18.68)	1.23 ± 0.97	30.75 ± 15.83
Rest to Exercise	100 different patient conditions and 217 cardiac cycles in each simulation	0 (NaN)	0.41 ± 0.08	29.04 ± 2.15
		1 (31.23)	0.44 ± 0.40	31.27 ± 10.23
		2 (25.22)	0.67 ± 0.63	32.83 ± 15.06
		3 (21.71)	0.94 ± 0.81	32.56 ± 16.37
		4 (19.24)	1.26 ± 1.02	31.41 ± 16.75
Postural	100 different patient conditions and 190 cardiac cycles in each simulation	0 (NaN)	0.38 ± 0.08	30.36 ± 2.36
		1 (31.34)	0.40 ± 0.30	32.18 ± 7.66
		2 (25.33)	0.63 ± 0.54	33.43 ± 12.89
		3 (21.83)	0.90 ± 0.72	33.05 ± 14.85
		4 (19.35)	1.22 ± 0.97	32.07 ± 15.98

**Table 3-4 Sensitivity analysis of  $R_{pa}$  change based on PID controller (5 most effective parameters highlighted from dark to light green in each category)**

No	Parameters	$R_{pa}$ Increase		$R_{pa}$ decrease	
		+20% variation	-20% variation	+20% variation	-20% variation
1	Eeslvf	1.46E-01	1.41E-01	2.33E-01	6.13E-02
2	Eesrvf	6.85E-01	2.25E-01	4.36E-01	4.81E-01
3	Eao	3.57E-05	3.57E-05	7.25E-08	7.25E-08
4	Eesla	1.58E-02	1.24E-02	1.40E-02	1.86E-02
5	Eesra	2.63E-02	2.71E-01	2.31E-01	2.23E-01
6	Epa	1.23E-01	3.06E-01	8.15E-02	1.23E-01
7	Epu	2.01E-03	2.25E-01	1.67E-02	2.22E-02
8	Esa	2.62E-01	5.40E-01	8.04E-02	1.13E-01
9	Esv	1.77E+00	3.47E+00	4.46E-01	2.47E-01
10	Evc	2.56E-01	5.63E-01	6.92E-02	9.40E-02
11	Rao	5.37E-02	2.91E-01	8.29E-02	9.49E-02
12	Rra	3.57E-05	3.57E-05	7.25E-08	7.25E-08
13	Rpv	3.57E-05	3.57E-05	7.25E-08	7.25E-08
14	Rsv	1.25E+00	1.34E+00	4.69E-01	5.55E-01
15	Tc	3.57E-05	3.57E-05	7.25E-08	7.25E-08
16	Tsys0	3.57E-05	3.57E-05	7.25E-08	7.25E-08
17	V0la	1.80E-02	1.35E-02	6.12E-03	6.19E-03
18	V0lvf	3.20E-02	1.57E-01	2.65E-02	2.68E-02
19	V0ra	8.48E-03	1.43E-02	3.24E-02	3.12E-02
20	V0rvf	3.57E-05	3.57E-05	7.25E-08	7.25E-08
21	Vdla	7.18E-03	3.65E-03	4.26E-03	4.36E-03
22	Vdlvf	1.91E-01	3.16E-04	1.35E-02	1.35E-02
23	Vdra	1.86E-02	1.86E-02	1.45E-02	1.48E-02
24	Vdrvf	5.68E-02	5.35E-02	5.61E-03	5.89E-03
25	Rmt	3.42E-01	1.61E-01	8.40E-02	8.62E-02
26	Rav	2.32E-04	7.53E-05	1.47E-04	3.74E-06
27	Vuao	3.57E-05	3.57E-05	7.25E-08	7.25E-08
28	Vupa	2.97E-01	1.21E-01	1.18E-02	1.22E-02
29	Vupu	3.49E-01	1.76E-01	1.69E-02	1.81E-02

30	Vusa	4.81E-01	3.10E-01	3.02E-02	3.13E-02
31	Vusv	3.35E+00	2.47E+00	1.42E-01	8.76E-01
32	Vuvc	3.54E-01	1.81E-01	1.81E-02	1.84E-02
33	P0la	5.64E-02	7.14E-02	1.07E-02	1.38E-02
34	P0lvf	1.27E-01	1.62E-01	1.62E-02	2.05E-02
35	P0ra	2.12E-01	1.05E-02	5.54E-02	7.35E-02
36	P0rvf	1.70E-01	1.50E-01	1.82E-01	2.54E-01
37	Vtotal	6.65E+00	4.21E+00	2.10E+00	1.04E+00
38	$\lambda_{la}$	2.34E-02	2.37E-01	2.72E-02	4.53E-02
39	$\lambda_{lvf}$	2.21E-01	3.13E-01	2.47E-02	3.81E-02
40	$\lambda_{ra}$	2.00E-01	9.34E-02	1.72E-01	3.27E-01
41	$\lambda_{rvf}$	3.00E-01	2.60E-01	4.81E-01	9.78E-01
42	Lao	9.77E-05	3.44E-05	7.39E-05	2.37E-05
43	Lpa	3.20E-04	1.50E-04	2.36E-04	5.48E-04

**Table 3-5 Sensitivity analysis of  $R_{sa}$  change based on PID controller (5 most effective parameters highlighted from dark to light green in each category)**

No	Parameters	$R_{sa}$ Increase		$R_{sa}$ decrease	
		+20% variation	-20% variation	+20% variation	-20% variation
1	Eeslvf	1.22E-01	1.36E-02	7.07E-01	8.17E-01
2	Eesrvf	8.47E-02	6.87E-02	4.48E-01	5.38E-01
3	Eao	1.60E-04	1.60E-04	1.98E-04	1.98E-04
4	Eesla	1.85E-03	2.09E-03	1.14E-01	1.62E-01
5	Eesra	6.62E-02	5.48E-02	3.99E-01	4.65E-01
6	Epa	2.22E-02	3.03E-02	3.75E-02	6.74E-02
7	Epu	4.41E-03	1.28E-03	6.96E-02	9.14E-02
8	Esa	2.25E-01	3.19E-01	2.91E-01	4.51E-01
9	Esv	4.81E-03	1.63E-01	1.79E+00	1.78E+00
10	Evc	3.00E-02	4.20E-02	1.87E-01	3.01E-01
11	Rao	4.99E-02	4.97E-02	4.59E-02	6.50E-02
12	Rra	1.60E-04	1.60E-04	1.98E-04	1.98E-04
13	Rpv	1.60E-04	1.60E-04	1.98E-04	1.98E-04

<b>14</b>	Rsv	8.51E-03	1.53E-02	7.40E-01	9.16E-01
<b>15</b>	Tc	1.60E-04	1.60E-04	1.98E-04	1.98E-04
<b>16</b>	Tsys0	1.60E-04	1.60E-04	1.98E-04	1.98E-04
<b>17</b>	V0la	8.02E-05	3.21E-04	5.70E-02	5.72E-02
<b>18</b>	V0lvf	8.67E-03	8.42E-03	7.17E-01	5.68E-01
<b>19</b>	V0ra	1.80E-02	1.66E-02	6.96E-02	6.89E-02
<b>20</b>	V0rvf	1.60E-04	1.60E-04	1.98E-04	1.98E-04
<b>21</b>	Vdla	2.41E-04	7.22E-04	3.78E-02	3.80E-02
<b>22</b>	Vdlvf	4.57E-03	4.97E-03	2.53E-01	2.52E-01
<b>23</b>	Vdra	8.83E-03	9.63E-03	4.38E-02	4.39E-02
<b>24</b>	Vdrvf	2.65E-03	3.21E-03	3.81E-02	3.78E-02
<b>25</b>	Rmt	9.71E-03	9.07E-03	2.31E-01	2.48E-01
<b>26</b>	Rav	3.21E-04	2.41E-04	1.90E-02	1.80E-02
<b>27</b>	Vuao	1.60E-04	1.60E-04	2.21E-05	1.98E-04
<b>28</b>	Vupa	6.02E-03	6.26E-03	8.67E-02	8.38E-02
<b>29</b>	Vupu	8.83E-03	8.99E-03	1.27E-01	1.20E-01
<b>30</b>	Vusa	1.61E-02	1.52E-02	2.25E-01	2.04E-01
<b>31</b>	Vusv	9.12E-02	4.46E-01	2.06E+00	3.88E+00
<b>32</b>	Vuvc	9.47E-03	9.07E-03	1.30E-01	1.23E-01
<b>33</b>	P0la	5.62E-04	4.01E-04	8.86E-02	1.09E-01
<b>34</b>	P0lvf	5.54E-03	7.22E-03	3.36E-01	4.23E-01
<b>35</b>	P0ra	2.63E-02	3.71E-02	1.17E-01	1.47E-01
<b>36</b>	P0rvf	5.32E-02	8.89E-02	2.72E-01	3.62E-01
<b>37</b>	Vtotal	9.21E-01	9.32E-01	7.62E+00	6.63E-01
<b>38</b>	$\lambda$ la	1.20E-03	3.21E-04	1.90E-01	2.56E-01
<b>39</b>	$\lambda$ lvf	9.71E-03	1.36E-02	5.99E-01	1.23E+00
<b>40</b>	$\lambda$ ra	5.33E-02	1.10E-01	3.24E-01	5.19E-01
<b>41</b>	$\lambda$ r vf	9.42E-02	3.76E-01	6.66E-01	3.74E+00
<b>42</b>	Lao	2.41E-04	2.41E-04	6.60E-05	4.38E-04
<b>43</b>	Lpa	3.21E-04	3.21E-04	1.99E-04	1.84E-04

**Table 3-6 Sensitivity analysis of transition from rest to exercise and passive postural changes based on PID controller (5 most effective parameters highlighted from dark to light green in each category)**

No	Parameters	Transition from rest to exercise		Passive postural change	
		+20% variation	-20% variation	+20% variation	-20% variation
1	Eeslvf	1.30E-01	7.17E-01	1.35E+00	8.15E-02
2	Eesrvf	3.87E-01	6.30E-01	4.57E-01	3.46E-02
3	Eao	2.03E-05	2.03E-05	1.95E-04	3.91E-04
4	Eesla	2.49E-01	3.48E-01	1.80E-01	7.31E-02
5	Eesra	2.51E-01	4.29E-01	4.39E-01	5.86E-03
6	Epa	6.30E-02	1.17E-01	1.53E-01	1.50E-01
7	Epu	1.66E-01	2.24E-01	9.10E-02	5.94E-02
8	Esa	1.39E-01	2.76E-01	2.81E-01	1.14E-01
9	Esv	2.55E-01	3.70E-01	1.97E+00	3.65E-01
10	Evc	2.48E-01	4.39E-01	4.77E-01	1.97E-01
11	Rao	3.54E-03	9.21E-02	9.30E-02	5.92E-02
12	Rra	2.03E-05	2.03E-05	1.95E-04	3.91E-04
13	Rpv	2.03E-05	2.03E-05	1.95E-04	3.91E-04
14	Rsv	1.45E-02	4.88E-01	1.88E-01	1.22E+00
15	Tc	2.03E-05	2.03E-05	1.95E-04	3.91E-04
16	Tsys0	2.03E-05	2.03E-05	1.95E-04	3.91E-04
17	V0la	8.75E-02	9.63E-02	9.16E-02	6.97E-02
18	V0lvf	2.15E-01	3.96E-01	9.13E-01	7.64E-02
19	V0ra	2.58E-02	3.75E-02	4.55E-02	2.93E-02
20	V0rvf	2.03E-05	2.03E-05	1.95E-04	3.91E-04
21	Vdla	5.65E-02	4.86E-02	4.90E-02	5.76E-02
22	Vdlvf	1.48E-01	1.04E-01	6.90E-02	3.98E-01
23	Vdra	2.88E-02	1.74E-02	2.77E-02	3.40E-02
24	Vdrvf	3.00E-02	1.86E-02	4.24E-02	5.04E-02
25	Rmt	3.07E-01	2.90E-01	1.30E-01	4.75E-01
26	Rav	1.75E-02	1.32E-02	4.49E-03	6.06E-03
27	Vuao	2.03E-05	2.03E-05	1.95E-04	3.91E-04
28	Vupa	6.50E-02	4.80E-02	5.68E-02	1.15E-01

29	Vupu	9.62E-02	6.67E-02	5.25E-02	1.65E-01
30	Vusa	1.70E-01	1.09E-01	4.18E-02	2.83E-01
31	Vusv	1.00E+00	2.28E-01	4.40E-01	1.37E+00
32	Vuvc	9.68E-02	6.94E-02	5.27E-02	1.69E-01
33	P0la	1.56E-01	1.81E-01	7.60E-02	1.82E-01
34	P0lvf	1.71E-01	1.14E-01	7.17E-02	6.67E-01
35	P0ra	6.64E-02	5.77E-02	1.91E-02	1.02E-01
36	P0rvf	2.32E-01	2.13E-01	2.58E-02	2.73E-01
37	Vtotal	6.10E-02	9.25E-01	1.34E+00	5.95E+00
38	$\lambda_{la}$	3.77E-01	5.19E-01	8.58E-02	4.40E-01
39	$\lambda_{lvf}$	1.85E-01	1.15E-01	7.33E-02	1.27E+00
40	$\lambda_{ra}$	2.37E-01	2.42E-01	1.47E-02	4.21E-01
41	$\lambda_{rvf}$	7.15E-01	6.08E-01	8.18E-02	7.99E-01
42	Lao	2.76E-03	1.86E-03	1.95E-04	1.95E-04
43	Lpa	3.14E-04	2.24E-03	3.91E-04	1.95E-04

**Table 3-7 Simulation of interpatient and intrapatient variations via changing the most effective parameters in each scenario**

Patient scenarios	Most effective parameters
$R_{pa}$ increase	Eesrvf, Esa, Esv, Evc, Rsv, Rmt, Vusv, Vupu, Vusa, Vusv, Vuvc, Vtotal, $\lambda_{lvf}$ and $\lambda_{rvf}$
$R_{pa}$ decrease	Eesrvf, Eesra, Esv, Rsv, Vusv, Vtotal, $\lambda_{ra}$ and $\lambda_{rvf}$
$R_{sa}$ increase	Esa, Vusv, Vtotal and $\lambda_{rvf}$
$R_{sa}$ decrease	Eeslvf, Eesrvf, Eesra, Esa, Esv, Evc, Rsv, V0lvf, Vdlvf, Rmt, Vusv, P0lvf, P0rvf, Vtotal, $\lambda_{lvf}$ , $\lambda_{ra}$ and $\lambda_{rvf}$
Transition from rest to exercise	Eeslvf, Eesrvf, Eesla, Eesra, Esv, Evc, Rsv, V0lvf, Rmt, Vusv, Vtotal, $\lambda_{la}$ , $\lambda_{ra}$ and $\lambda_{rvf}$
Passive postural change	Eeslvf, Eesrvf, Esv, Evc, Rsv, V0lvf, Vdlvf, Rmt, Vusv, P0lvf, Vtotal, $\lambda_{la}$ , $\lambda_{lvf}$ and $\lambda_{rvf}$

### 3.4.2 Sensitivity analysis

The result of the sensitivity analysis performed by variation of each 43 parameters in six patient scenarios (Table 3-7) shows that the cardiovascular model parameters total blood volume ( $V_{\text{total}}$ ), systemic vein unstressed volume ( $V_{\text{usv}}$ ), RV end diastolic stiffness coefficient ( $\lambda_{\text{rvf}}$ ), systemic vein elastance ( $E_{\text{sv}}$ ), RV end systolic elastance ( $E_{\text{esrf}}$ ), systemic vein resistance ( $R_{\text{sv}}$ ) have the most impact on the control tracking performance in all the patient scenarios (whole results are demonstrated in Table 3-4, Table 3-5 and Table 3-6). These parameters were therefore varied to simulate the 100 patients for each scenario.

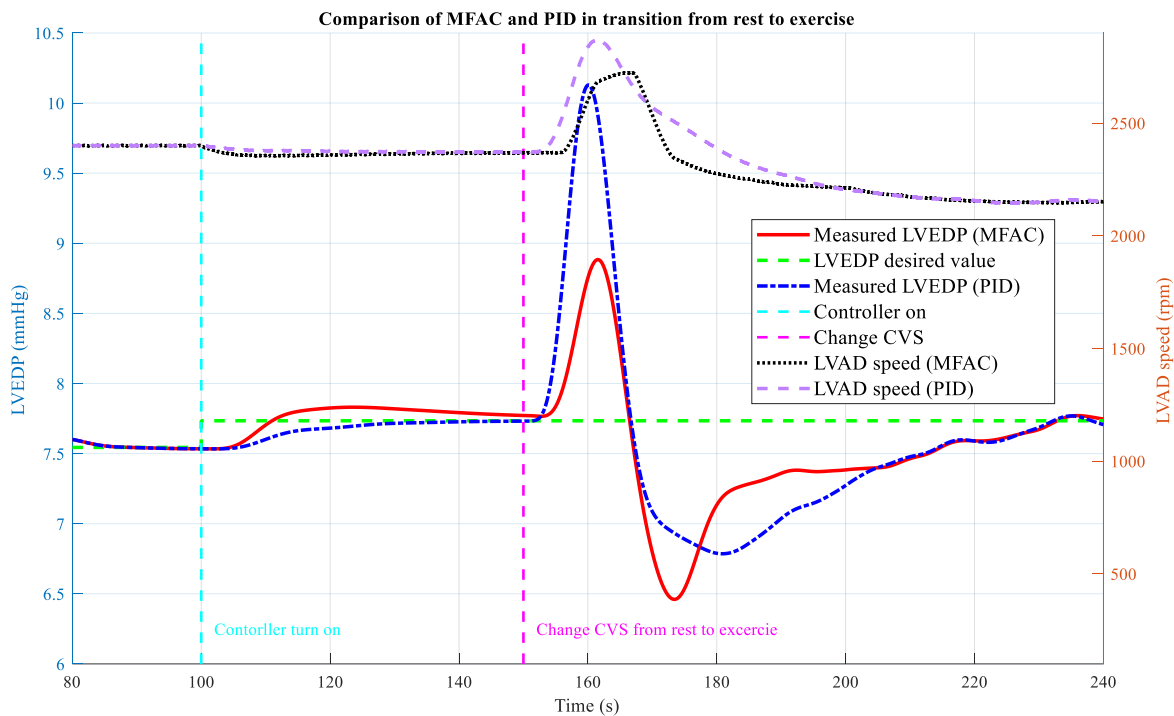


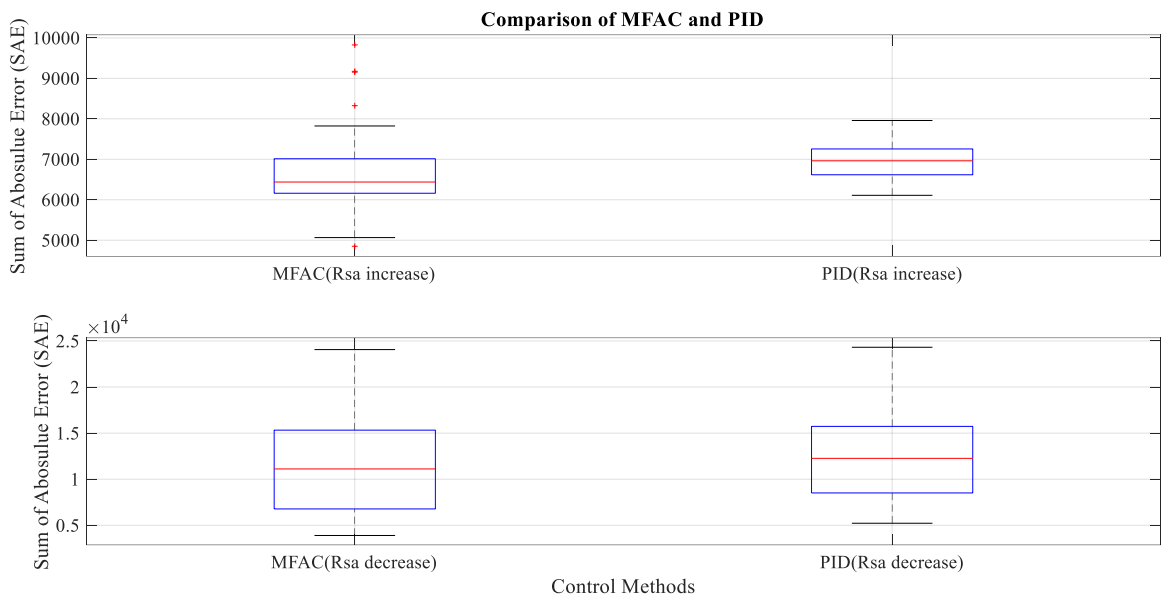
**Figure 3-4 A sample simulation for comparison of MFAC and PID in transition from rest to exercise for patient 45.**

### 3.4.3 MFAC evaluation

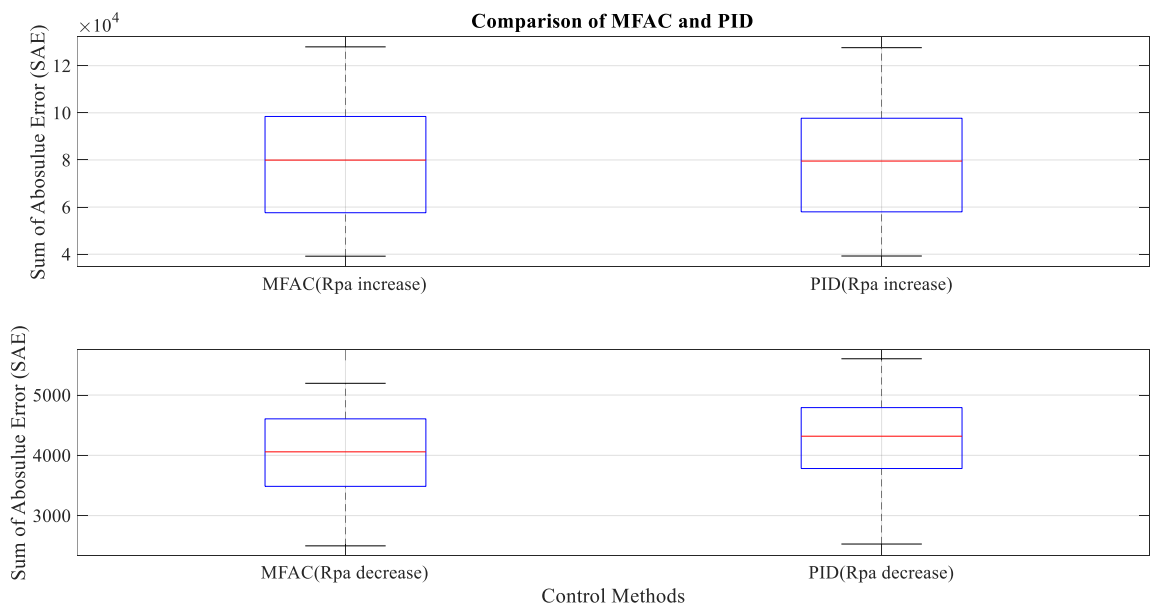
As can be seen from Figure 3-4, MFAC responds faster to patient changes, resulting in a smaller SAE than PID (solid red line compared to dash-dot blue line). Furthermore, in three simulations out of 100 simulations in transition from rest to exercise, PID controller led to transient pulmonary congestions; however, MFAC could prevent pulmonary congestion due to the lower peak on the measured LVEDP in those three simulations.

Figure 3-5 shows the comparison of SAE of MFAC and PID control for all patients in all scenarios. From the figure, in four patient scenarios (decreasing  $R_{pa}$ , increasing  $R_{sa}$ , rest to exercise and postural change), SAE (mmHg) derived from MFAC are much less than SAE from PID control ( $3989.48 \pm 700.84$  and  $5869.55 \pm 1157.66$  for  $R_{pa}$  decrease, and  $6608.90 \pm 830.94$  and  $10841.26 \pm 1745.66$  for  $R_{sa}$  increase,  $7353.51 \pm 1165.62$  and  $16948.92 \pm 4104.39$  for rest to exercise, and  $2945.74 \pm 403.39$  and  $3330.475 \pm 428.37$  for postural change corresponding to MFAC and PID controller respectively). In two other scenarios (increasing  $R_{pa}$  and decreasing  $R_{sa}$ ) SAE (mmHg) derived from MFAC is almost similar or better than the PID controller ( $80270.31 \pm 23575.38$  and  $80087.31 \pm 23356.09$  for  $R_{pa}$  increase, and  $11715.23 \pm 5161.54$  and  $31687.86 \pm 9183.17$  for decrease  $R_{sa}$  corresponding to MFAC and PID controller respectively). Mean and standard deviation of the SAE for all the 600 simulations are  $18813.86 \pm 29345.78$  and  $24794.22 \pm 28380.48$  corresponding to MFAC and PID controller, respectively.

Table 3-8 demonstrates the statistical result of the Wilcoxon's test in comparison of MFAC and PID controller for different patient conditions. In four out of six patient scenarios (decreasing  $R_{pa}$ , increasing  $R_{sa}$ , rest to exercise and postural change) the  $p$ -values are less than 0.05, indicating that MFAC has better performance than PID control.



**(a)**



**(b)**

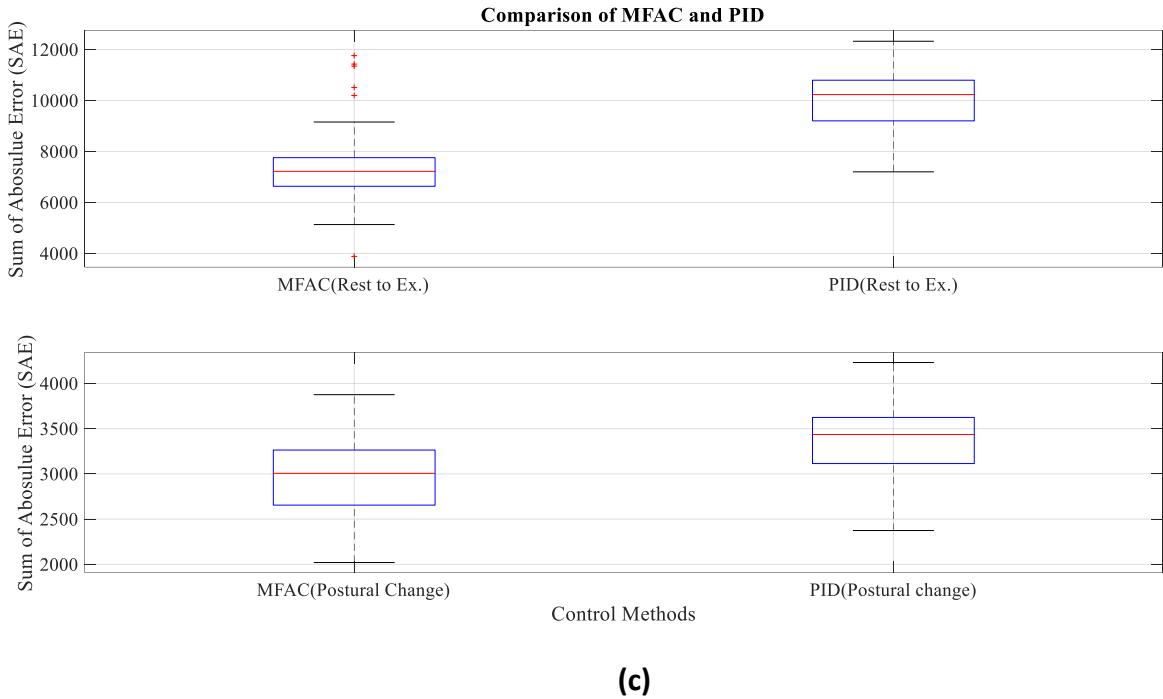


**Figure 3-5 Comparison of SAE of MFAC and PID controller in different scenarios via box plot, the central mark (red line) shows the median, and the bottom and top edges (blue lines) of each box show the 25th and 75th percentiles. The whiskers extend to the most extreme data points not considered outliers, and the outliers are plotted individually using the '+' symbol. (a) rising  $R_{sa}$  (1300 to 600 dyne.s.cm<sup>-5</sup>) and falling  $R_{sa}$  (1300 to 2600 dyne.s.cm<sup>-5</sup>) (b) rising  $R_{pa}$  (100 to 40 dyne.s.cm<sup>-5</sup>) and falling  $R_{pa}$  (100 to 500 dyne.s.cm<sup>-5</sup>) (c) transition from rest to exercise and passive postural change.**

**Table 3-8 Results of the Wilcoxon's test in comparison of MFAC and PID for different patient scenarios**

Scenarios	p-value
Increasing $R_{pa}$	0.9542
Decreasing $R_{pa}$	<b>0.0198</b>
Increasing $R_{sa}$	<b>1.7067e-06</b>
Decreasing $R_{sa}$	0.0998
Rest to exercise	<b>9.9469e-28</b>
Postural change	<b>1.5741e-10</b>

### 3.5 Discussion

One of the key issues of current physiological control systems [12], [13], [15], [16], [153] is that they have been simulated in very specific conditions for single patient scenarios. This is not realistic, as each patient's cardiovascular system dynamics vary throughout the day and are unlikely to be identical to another patient. We argue that the control systems evaluated against a single simulated patient cannot be guaranteed to be robust against a wide patient cohort. The use of single-patient evaluation may also be another reason for the popularity of simple linear PID control in LVAD control systems [12], [15], [92], [93]. It has yet to be established how simple PID control fares in the context of a wider patient suite.

In this study, we compared linear PID control and MFAC across a range 600 randomized patient scenarios. The results indicate that MFAC offers either similar or consistently better performance across all scenarios when compared to PID control. This indicates that the previous evaluation techniques were remiss in not considering the effect of plant variation on control system performance.

The results from Figure 3-5 and Table 3-8 show that MFAC can improve the tracking performance compared to PID control since MFAC adjusts its parameters adaptively only based on the input/output data of the cardiovascular system. In fact, MFAC parameters were automatically changed by interpatient and intrapatient variations and any unpredicted changes on hemodynamics can be responded by MFAC due to the adaptive structure of the controller. There is also a mathematical proof that confirms the error between desired and measured output converges to zero by using the MFAC method. The lower SAE on control tracking performance means the measured LVEDP follows the desired LVEDP in the range of 3 to 15 mmHg faster and with less amplitude oscillations leading to fewer ventricular suctions and pulmonary congestion events. From the results it is clear that in the four patient scenarios (increasing  $R_{sa}$ , rest to exercise, decreasing  $R_{pa}$  and postural change) MFAC tracking performance is much better compared to PID controller, in the other two scenarios (increasing  $R_{pa}$  and decreasing  $R_{sa}$ ) SAE derived from MFAC is not significantly different than compared to PID. Optimization of finding the MFAC parameters can lead to further improvement in control tracking performance compared to the optimized PID controller.

Another advantage of MFAC over PID is that tuning and optimization of PID controllers must be performed offline by a control engineer. If the performance is unsatisfactory, a control engineer familiar with the cardiovascular system may be required to make adjustments, as clinicians do not have the specialist engineering knowledge to make these adjustments. On the other hand, MFAC just uses the real-time measurement I/O data of the controlled system to self-adjust its parameters and so no additional input is required. Clinicians can therefore focus on treating their patient and not worry about underperforming or unstable control systems.

Although an adaptive physiological controller of rotary blood pumps using intrinsic pump parameters on two different pumps was proposed by Wu [113], it was based on a linear state-space model of cardiovascular system. This approach is difficult to use for simulation of different patient conditions, as the model linearization may not be constant across the suite of patients. This may lead to inaccuracy of simulation and therefore inconsistent control performance. Furthermore, the pump flow derived from feedback signals of intrinsic pump parameters was assumed to be the total flow to the human circulation system, which increases the estimation error of aortic pressure [113]. In addition, there was no methodology to prevent the possible suction and congestion events [113]. However, in this study, a stable model-free adaptive controller was employed to provide guaranteed controller performance across a range of 600 different patient conditions (six different scenarios), preventing suction and congestion events. In addition, the MFAC does not have the common issues of other model-free adaptive controllers like

ANN and Fuzzy controllers (i.e., difficulty to collect training data and finding the rules). Model predictive controllers and optimal controllers require a simplified and generalized state-space model that cannot be modified for different patients' conditions.

As reported in the literature [12], [15], [16], Starling-like controllers have been proposed to restore Frank-Starling response of the native heart. One of the issues with the Frank-Starling mechanism is that the desired flow for Frank-Starling curve must be set manually by clinicians for each patient. As there is no automatic procedure on finding the Frank-Starling curve without clinical check-up, employing Starling-like controller for different patient conditions is impossible. In order to minimize clinical check-up and find an automatic procedure to set desired flow or LVEDP, constant LVEDP scheme was used in this study to maintain LVEDP in the range of 3 mmHg to 15 mmHg for each patient (to prevent ventricle suction and pulmonary congestion). This can be an appropriate way to respond to the interpatient and intrapatient variations.

The evaluation of the developed LVEDP detection in Table 3-3 shows that the proposed method can identify the end-diastolic pressure across a range of different levels of noise with very low delay in a real-time mode. To the author's knowledge, there are no other LVEDP detection methods like this. Other investigators have previously addressed this by utilizing the minimum left ventricular pressure, which is not a realistic measure of preload in the ventricle [11]. The LVEDP detection method proposed in this paper will enable

robust detection of LVEDP for physiological control, improving the performance of physiological control systems.

This study has some limitations. The first limitation is that our developed methodology has not employed the Frank-Starling mechanism to balance systemic and pulmonary flow. Frank-Starling-like controllers setting flow rate as a function of preload have been developed in [45], [93] and shown to be one of the best performing physiological control systems [13]. However, finding the Frank-Starling function for each different patient with various conditions is difficult. Therefore, to simplify the controller, LVEDP was maintained as a constant value in the range between 3 mmHg to 15 mmHg.

Second, the baroreflex was not simulated in this study which may influence performance and hemodynamics [159]. However, the MFAC can compensate its impact properly since any changes due to the baroreflex can be interpreted as a nonlinearity like to a different patient condition or scenario.

Third, this study assumes the left ventricular pressure can be measured. However, currently, there are no commercial long-term implantable pressure sensors. Alternatively, the pressure sensor can be replaced by pressure estimation algorithms which have been used in several original implementations of evaluated control systems like that for constant pump flow [109]. Further investigation is required to determine if the developed physiological control system can use pressure estimation algorithms instead of sensors [18], [117], [160].

Fourthly, this study was completed *in silico*. Most LVAD physiological control systems are evaluated on the bench top using mock circulation loops, to verify numerical model findings. However, the numerical model used in this study was extensively validated using animal data. Additionally, the numerical model is easily scalable: it enabled us to easily simulate 600 patient conditions across 6 different scenarios. This is a laborious process to conduct using bench top testing. Future work will involve validating this system on the bench top and *in vivo*.

Fifthly, this study used a model of the VentrAssist LVAD. The VentrAssist is no longer used clinically, however as it is a centrifugal pump like the commonly used HeartWare HVAD (Medtronic Inc., FL, USA), it is hypothesized that there would be little difference in performance. Future work will involve repeating this experiment using models of clinically available pumps.

Finally, pathological states of the heart may drastically alter left ventricular pressure waveform shapes. Future work will include adding pathological states to the numerical heart failure model.

Controlling LVEDP at the expense of aortic pressure or inappropriate LVAD flow that could result in thrombogenesis or hemolysis also needs to be taken into consideration. Future work will involve developing an adaptive target for LVEDP that considers both arterial pressure and flow rate.

### **3.6 Conclusion**

In this study, a novel physiological control for an implantable heart pump has been developed to respond to interpatient and intrapatient variations to maintain the LVEDP in the normal range of 3 to 15 mmHg to prevent ventricle suctions and pulmonary congestions. A new algorithm was developed to detect LVEDP from pressure sensor measurement in real-time mode. Interpatient and intrapatient variations have been simulated based on sensitivity analysis, in which the most effective parameters of CVS have been determined by changing the CVS parameter between -20% to +20 of their nominal values. Tracking controller performance has been assessed via simulation of 100 different patient conditions in each of six different patient scenarios showing the preference of MFAC compared to PID control reducing the risk of suction and congestion events in patients.

### **3.7 Acknowledgment**

The authors would like to recognize the financial assistance provided by the National Health and Medical Research Council Centers for Research Excellence (APP1079421).

In the next chapter, we address the second objective of this study, which is design a sensorless physiological control system for LVADs that can accommodate interpatient and intrapatient variations.

# **Chapter 4. A Sensorless Control System for an Implantable Heart Pump using a Real-time Deep Convolutional Neural Network**

The study presented in Chapter 4 has been published in *IEEE Transactions on Biomedical Engineering*:

[161] **M. Fetanat**, M. Stevens, C. Hayward, and N. H. Lovell, “A Sensorless Control System for an Implantable Heart Pump using a Real-time Deep Convolutional Neural Network.”, *IEEE Trans. Biomed. Eng.*, vol. 68, no. 10, pp. 3029-3038, 2021.

## 4.1 Abstract

Left ventricular assist devices (LVADs) are mechanical pumps, which can be used to support heart failure (HF) patients as bridge to transplant and destination therapy. To automatically adjust the LVAD speed, a physiological control system needs to be designed to respond to variations of patient hemodynamics across a variety of clinical scenarios. These control systems require pressure feedback signals from the cardiovascular system. However, there are no suitable long-term implantable sensors available. In this study, a novel real-time deep convolutional neural network (CNN) for estimation of preload based on the LVAD flow was proposed. A new sensorless adaptive physiological control system for an LVAD pump was developed using the full dynamic form of model free adaptive control (FFDL-MFAC) and the proposed preload estimator to maintain the patient conditions in safe physiological ranges. The CNN model for preload estimation was trained and evaluated through 10-fold cross validation on 100 different patient conditions and the proposed sensorless control system was assessed on a new testing set of 30 different patient conditions across six different patient scenarios. The proposed preload estimator was extremely accurate with a correlation coefficient of 0.97, root mean squared error of 0.84 mmHg, reproducibility coefficient of 1.56 mmHg, coefficient of variation of 14.44 %, and bias of 0.29 mmHg for the testing dataset. The results also indicate that the proposed sensorless physiological controller works similarly to the preload-based physiological control system for LVAD using measured preload to prevent

ventricular suction and pulmonary congestion. This study shows that the LVADs can respond appropriately to changing patient states and physiological demands without the need for additional pressure or flow measurements.

## 4.2 Introduction

Heart failure (HF) affects more than 100,000 adults, 6.5 million and 23 million people in Australia, USA and worldwide, respectively [1], [2], [5]. HF prevalence in the USA is expected to increase by 46% from 2012 to 2030, leading to more than 8 million people diagnosed with HF [1]. Although heart transplantation is the gold standard treatment for end-stage HF patients, due to the lack of donor hearts, only 113 heart transplantation were performed in Australia in 2019 [6]. Mechanical circulatory support (MCS) is a standard clinical therapy for advanced HF patients, achieved by implantation of a mechanical pump in HF patients. Left ventricular assist devices (LVADs) are a type of MCS for a failing left ventricle by pumping blood from the left ventricle to the aorta. These devices are used during bridge to transplant, bridge to recovery and destination therapy [10].

Currently, clinicians set the LVAD speed in a constant mode, which can lead to hazardous events such as insufficient perfusion, ventricular suction (ventricular collapse caused by low pressure in the ventricle) or pulmonary congestion (excess fluid in the lungs due to high pressure in the ventricle). While ventricular suction can lead to hemolysis, myocardial damage, right ventricular dysfunction, ventricular thrombus and subsequent stroke, pulmonary congestion can result in pulmonary edema and shortness of breath.

[10], [128], [162]. A physiological control system, which automatically adjusts pump speed according to hemodynamic variations or pump variables, can mitigate these hazardous events. Physiological control systems can be designed to follow different objectives such as constant differential pressure [76], constant pump flow [109], constant pump inlet pressure [151] or a Starling-like controller which sets target flow rate based on the preload (left ventricular end-diastolic pressure) [12], [15], [16], [93], [163]. Whilst many physiological control systems have been proposed, there are several issues associated with these approaches.

First, most of these physiological control systems have only been evaluated using a single simulated patient or condition [12], [13], [15], [16], [152], [153], which does not represent the wide clinical range of interpatient and intrapatient variations in cardiovascular system (CVS) dynamics. Furthermore, in most studies of physiological control systems for LVADs [12], [13], [15], [16], a proportional-integral-derivative (PID) controller was employed, which was tuned for a specific patient and condition, and control performance cannot be guaranteed across different patients and conditions, which may lead to hazardous events [29]. In recent studies, adaptive control systems such as artificial neural network (ANN) control [153] and fuzzy logic control (FLC) [53], which can automatically adjust their parameters according to feedback from the controlled system, have been used in the control of LVADs. However, these controllers need large training data and precise determination of rules for different patient conditions, respectively. Fetanat *et al.* proposed a preload-based physiological control for an LVAD using model free adaptive control

(MFAC) to maintain the preload between 3 to 15 mmHg, which was validated on 100 different patient conditions in which control performance can be guaranteed across different patients and conditions [28], [29]. However, the compact linearization form of MFAC was employed to control the LVAD speed, which cannot identify the full dynamics of the controlled system and therefore can lead to inaccurate control. The full dynamic linearization form of model free adaptive control (FFDL-MFAC) could be used to identify the dynamic characteristics of the CVS and LVAD using the memories of the past inputs and outputs of the CVS and LVAD without knowledge of the mathematical model or dynamic information of the controlled system. FFDL-MFAC also does not require any training process or rules like ANNs and fuzzy controllers.

Additionally, while most of the current physiological control systems require direct measurement of pressure [13], [28], [29], flow [88] or ventricular volume [98] via implantation of a sensor, these sensors are faced with several challenges such as drift, additional power consumption, interference from radiation, thrombus formation and device failure [10]. These challenges have limited real-world application, leading researchers to focus on estimating these measurements. Although these measurements can be estimated using machine learning (ML) algorithms, finding appropriate features as inputs for these algorithms is a difficult task. ML methods are a part of artificial intelligence (AI), which can learn a pattern from a training dataset and then accurately predict output on a new dataset [143]. ML algorithms have been widely used in classification and regression problems for cardiovascular medicine [29]. Deep learning (DL) is a new type of ML, which is usually made

by several layers of a convolutional neural network (CNN), pooling and a multi-layer perceptron (MLP) [29]. Applying deep CNNs for estimation of preload can automatically extract suitable features from the input signals, using pump flow in real-time mode across the range of interpatient and intrapatient CVS variations.

The aim of this study is to design a sensorless adaptive physiological control system for an implantable LVAD using deep CNNs and FFDL-MFAC to provide consistent control performance across interpatient and intrapatient variations without needing any implantable flow or pressure sensors. The objective of the proposed control system is to prevent hazardous events such as ventricular suction and pulmonary congestion and maintain the patient conditions in the physiological range, without reliance on an implantable sensor. To our knowledge, this is the first study, where a CNN was employed for the purpose of estimation combined with a controller in a real-time mode.

In this paper, first the numerical model of the human CVS and LVAD for the evaluation of the proposed sensorless physiological control system is introduced. Afterward, the novel real-time method for preload estimation using deep CNNs is presented. Then, the FFDL-MFAC and different patient conditions and scenarios used for evaluation of the sensorless physiological control system are described. Subsequently, the results of the proposed preload estimation and sensorless adaptive physiological control system using deep CNN and FFDL-MFAC across interpatient and intrapatient variations is

presented. Finally, a discussion including merits and limitations of the study and future work is presented.

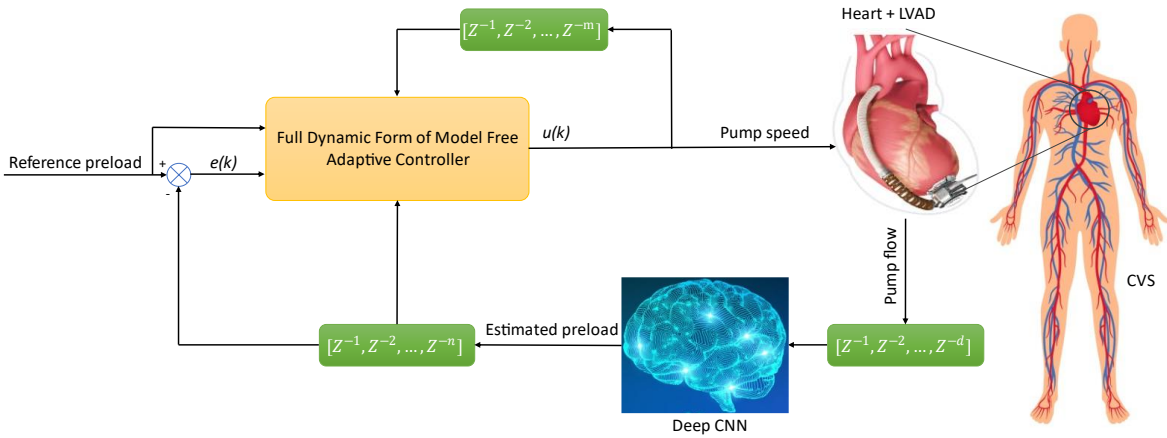


**Figure 4-1 Block diagram of the proposed sensorless physiological control system for LVAD.**  $u(k)$  is the control signal (pump speed), and  $e(k)$  is the error between reference and estimated preload.  $m$ ,  $d$  and  $n$  are the number of delays from pump speed, pump flow and estimated preload, respectively. CNN: convolutional neural network, CVS: cardiovascular system and LVAD: left ventricular assist device. Medtronic Heartware HVAD Illustration, "Reproduced with permission of Medtronic".

## 4.3 Methodology

Figure 4-1 demonstrates the block diagram of the proposed estimator and controller evaluated in this study. It includes three main blocks: the model of the CVS and LVAD, deep CNN for preload estimation and FFDL-MFAC system.

### 4.3.1 Model of Cardiovascular System and LVAD

In this work, the implementation of the model of cardiovascular system and LVAD were performed in Simulink (MathWorks, Natick, MA, USA). Figure 4-2 shows the numerical model of the cardiovascular system used in this study,

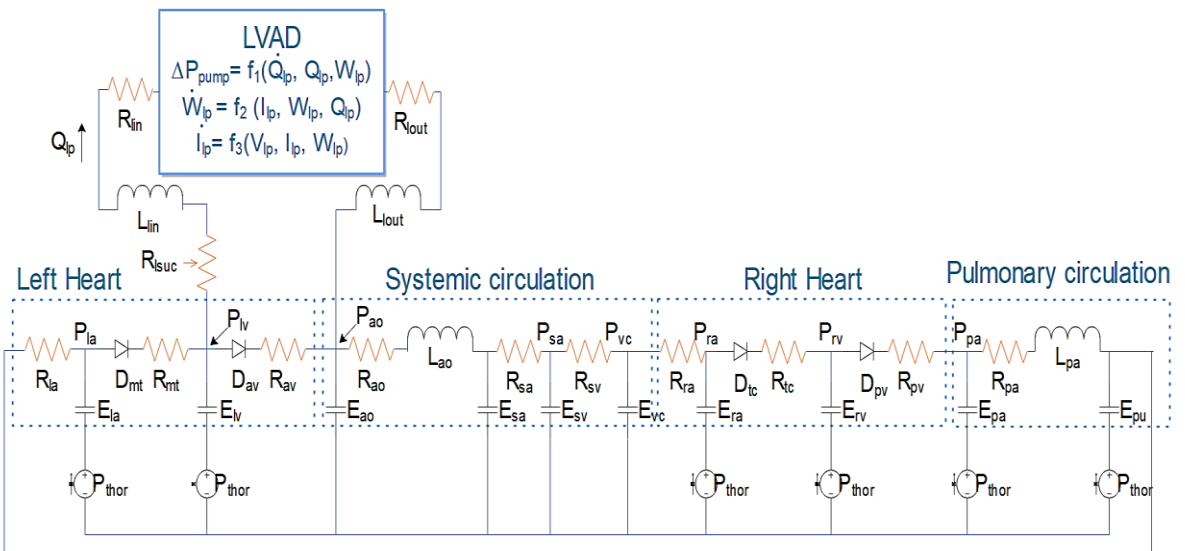


**Figure 4-2** Electrical equivalent circuit analogue of cardiovascular system with LVAD interaction model. P, pressures; R, resistances; E, elastances ( $=1/\text{compliances}$ ); L, inertances; D, diodes. The model consists of two main components: (1) the cardiovascular model includes left heart, systemic circulation, right heart, pulmonary circulation (la, left atrium; lv, left ventricle; ao, aorta; sa, systemic peripheral vessels, including the arteries and capillaries; sv, systemic veins, including small and large veins; vc, vena cava; ra, right atrium; rv, right ventricle; pa, pulmonary peripheral vessels, including pulmonary arteries and capillaries; pu, pulmonary veins and (2) LVAD model includes Rin and Rout, inlet and outlet cannulae resistances; Lin and Lout, inlet and outlet cannulae inertances; Rlsuc, left suction resistance, Rrsuc, right suction resistance, Rband, banding resistance. The intrathoracic pressure, Pthor was assigned  $-4 \text{ mmHg}$  during closed-chest simulated conditions [29].

which was proposed by Lim *et al.* in 2010 [44]. The CVS model includes systemic and pulmonary circulations, left and right hearts and LVAD inlet and outlet cannulae. It was derived using first principles and validated using in-vitro tests and in-vivo animal experiments [44], [45], [155].

The HVAD (Medtronic, Minneapolis, MN, USA) centrifugal pump was employed as the LVAD in this study. The HVAD pump model used was derived from the model proposed by Boes *et al.* [164] including the pump and peripheral models of components connected to the pump. The speed range of

the HVAD pump model was limited to 1800 and 4000 rpm, which is the clinical operating range of the device.

### **4.3.2 Deep Convolutional Neural Network for Preload Estimation**

Deep CNNs are hierarchical neural networks and one of the most popular deep learning methods. The structure of CNNs commonly include convolutional, pooling (subsampling), fully-connected and dropout layers [165], [166]. While in the convolutional layer, the features of input signal are automatically extracted using different filters, in the dropout layer, only essential features are maintained using subsampling operations [147]. A fully-connected layer basically works as a conventional MLP, which includes neurons connected to each other using weights, biases and activation functions. A dropout layer removes unnecessary neuron connections [147].

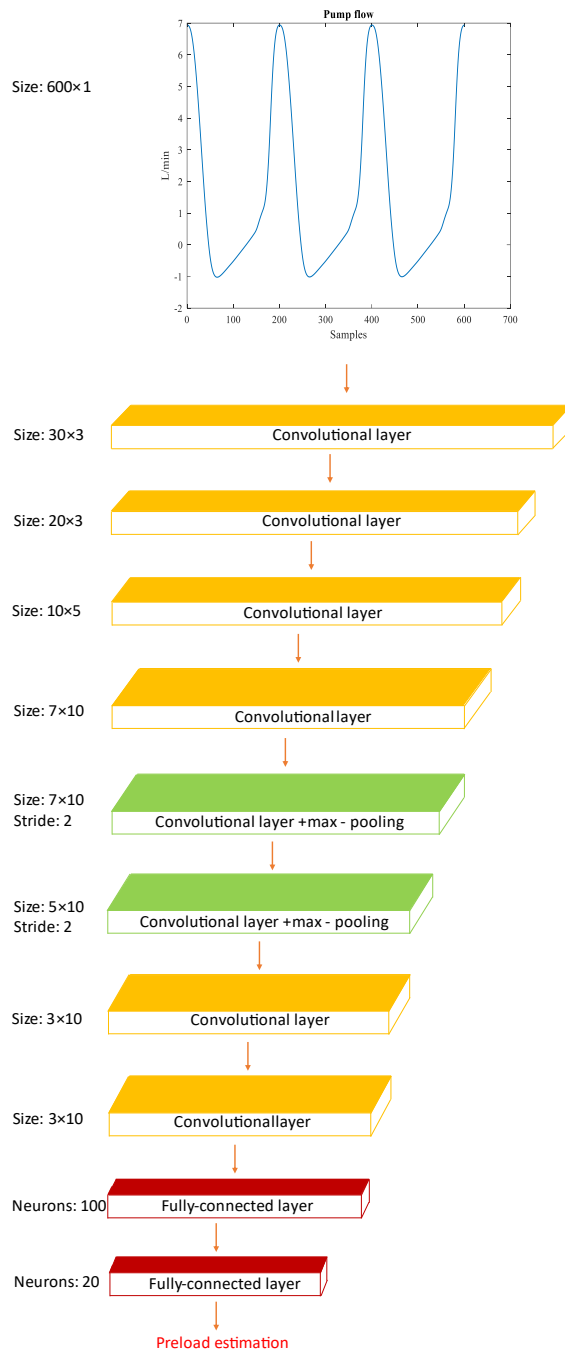


**Figure 4-3 Architecture of the proposed deep CNN model for estimation of preload.** 600 samples from the peak of the pump flow signal in each cardiac cycle are fed to the CNN as input. Afterwards, it is followed by four convolutional layers including batch normalization layers. Subsequently, two convolutional, max-pooling layers with stride 2 and batch normalization layers are placed. Then, it is followed by two convolutional layers including batch normalization layers. Finally, fully-connected layers with 100 and 20

**neurons, activation function of LeakyReLU and a dropout layer with probability of 20% are then used to estimate preload.**

Figure 4-3 depicts the architecture of the proposed deep CNN model for estimation of preload based on the 600 samples from the peak of the pump flow. The whole process can be described as follows: first, in each cardiac cycle the peak of pump flow is identified using a heuristic peak detector. Once the peak is detected 600 samples (three seconds) of the pump flow before the peak is fed to the deep CNN model. The number of samples fed to deep CNN was optimized to achieve minimum root mean square error (RMSE) between actual and estimated preload through 10-fold cross validation. It is then followed by four convolutional layers with the filter size of  $30 \times 3$ ,  $20 \times 3$ ,  $10 \times 5$  and  $7 \times 10$ . Each convolutional layer includes one batch normalization layer. Afterward, two convolutional and max-pooling layers with the filter size of  $7 \times 10$  and  $5 \times 10$  and stride length of 2 are placed. Subsequently, it is followed by two convolutional layers with the filter size of  $3 \times 10$ . Finally, fully-connected layers with 100 and 20 neurons, an activation function of LeakyReLU and a dropout layer with probability of 20% are employed to estimate preload. All these parameters were empirically adjusted to minimize RMSE between actual and estimated preload through 10-fold cross validation.

The proposed deep CNN method for preload estimation was evaluated using the same method previously used by our group [29]. Briefly, the estimation method was applied in six different patient scenarios; rising and falling pulmonary vascular resistance (PVR), rising and falling systemic vascular resistance (SVR), rest to exercise and passive postural changes. Each scenario

was simulated using 100 different patient conditions and four speeds of the HVAD pump (2000, 2600, 3000 and 3400), which generated preloads between -1 to 25 mmHg. SVR and PVR variations were performed by changes in systemic arterial resistance ( $R_{sa}$ ) and pulmonary arterial resistance ( $R_{pa}$ ) since the arterial resistances contribute a major part of total vascular resistance in the CVS model. Evaluation of the deep CNN model for estimation of preload was performed using 100 different LVAD patients for each of the six scenarios.

To compare the difference between measured and estimated preload, correlation coefficient ( $R$ ), RMSE, reproducibility coefficient (RPC), coefficient of variation (CV) and bias were used in terms of Bland-Altman analysis [167].

RMSE can be defined by (1-4):

$$RMSE = \sqrt{\frac{1}{n} \sum_{i=1}^n (actual\ preload_i - estimated\ preload_i)^2} \quad (1-4)$$

where  $actual\ preload_i$  and  $estimated\ preload_i$  are measured and estimated preload at time instant of  $i$  and  $n$  is the number of total samples in each simulation. The sampling rate of measured variables is 200 Hz.

RPC or limits of agreement and CV are defined as follows respectively:  $RPC = 1.96 * standard\ deviation$  and  $CV = standard\ deviation\ over\ mean\ values\ of\ estimated\ and\ measured\ preload$ .

Bias presents the mean of difference between estimated and actual preload. The less RMSE, RPC and bias, the more accurate preload estimation. CV can be referred as a measure of precision. Although the acceptable range of CV is different in each research field, CV of 20% or less is generally assumed as an acceptable range [168]. However, the lower value of the CV, the more precise the estimate [168].

The proposed deep CNN was trained using the Adam algorithm [169] with 1000 iterations, a batch size of 1102 and the He algorithm [170] for weights initialization.

#### **4.3.3 Full Dynamic Form of Model Free Adaptive Control (FFDL-MFAC)**

MFAC is a type of data-driven control (DDC) system in which the controller is designed by input and output data achieved from the controlled system in an online mode instead of using a mathematical model or system structure of the controlled system. Our group has previously shown that a control system using an MFAC produces more consistent control performance across a range of different patient scenarios than PID control [29]. However, one of the limitations of using MFAC is that the control input is determined only by single input and output samples. This can be overcome by a full form dynamic linearization technique (FFDL). FFDL-MFAC is a type a MFAC which employs FFDL and pseudo gradient (PG) to capture full dynamic behavior of the controlled system using the memories of the past inputs and outputs of the

controlled system [111], [171]. The fundamental operation of FFDL-MFAC is described in [111], [171], with a brief description as follows.

An unknown nonaffine single input single output (SISO) nonlinear discrete-time system can be presented as follows:

$$y(k+1) = f(y(k), y(k-1), \dots, y(k-n_y), u(k), u(k-1), \dots, u(k-n_u)) \quad (2-4)$$

where  $y(k) \in R$  and  $u(k) \in R$  are the system output and control input at time instant  $k$  respectively,  $n_y$  and  $n_u$  are unknown orders of output and input, and  $f(\cdot) : R^{n_u+n_y+2} \rightarrow R$  is an unknown nonlinear function.

The full dynamic linearization form of nonlinear system (2-4) can be defined by (3-4):

$$\begin{aligned} y(k+1) &= y(k) + \varphi_{f, L_u, L_y}^T(k) \Delta H_{L_y, L_u}(k) \\ \varphi_{f, L_u, L_y}(k) &= [\varphi_1(k), \dots, \varphi_{L_y-1}(k), \varphi_{L_y}(k), \dots, \varphi_{L_u+L_y}(k)]^T \\ H_{L_y, L_u}(k) &= [y(k), \dots, y(k-L_y+1), u(k), \dots, u(k-L_u+1)] \\ \Delta H_{L_y, L_u}(k) &= H_{L_y, L_u}(k) - H_{L_y, L_u}(k-1) \end{aligned} \quad (3-4)$$

where  $\varphi_{f, L_u, L_y}(k)$  is called PG and  $H_{L_y, L_u}(k)$  is a vector, including of all control input and system output signals within a moving time window.

For finding the control input  $u(k)$ , the following cost function is minimized to have less error (difference between the desired and system output) and changes of two consecutive control inputs:

$$J(u(k)) = \|y_d(k+1) - y(k+1)\|^2 + \lambda \|u(k) - u(k-1)\|^2$$

(4-4)

where  $y_d(k+1)$  and  $\lambda > 0$  are desired output and a weighting factor, respectively.

By substituting (3-4) into (4-4) and differentiating (4-4) with respect to control signal  $u(k)$  equals to zero, the control input is derived as follows:

$$\begin{aligned} u(k) = u(k-1) + & \frac{\varphi_{L_y+1}(k)[\rho_{L_y+1}(y_d(k+1) - y(k))]}{\lambda + \|\varphi_{L_y+1}(k)\|^2} \\ & - \frac{\sum_{i=1}^{L_y} \rho_i \varphi_i(k) \Delta y(k-i+1)}{\lambda + \|\varphi_{L_y+1}(k)\|^2} \\ & - \frac{\varphi_{L_y+1}(k) \sum_{i=L_y+2}^{L_y+L_u} \rho_i \varphi_i(k) \Delta u(k+L_y-i+1)}{\lambda + \|\varphi_{L_y+1}(k)\|^2} \end{aligned} \quad (5-4)$$

where  $\rho_i \in (0,1]$ ,  $i = 1, \dots, L_y + L_u$  are step constants which are added to make (5-4) more flexible.

A suitable parameter estimation algorithm for capturing the time-varying characteristics of PG needs to be employed. The cost function for estimation of PG is defined as follows:

$$\begin{aligned}
J\left(\varphi_{f, L_u, L_y}(k)\right) &= \left| \Delta y(k) - \varphi_{f, L_u, L_y}^T(k) \Delta H_{L_y, L_u}(k-1) \right|^2 \\
&\quad + \mu \left\| \varphi_{f, L_u, L_y}(k) - \hat{\varphi}_{f, L_u, L_y}(k) \right\|^2
\end{aligned} \tag{6-4}$$

where  $\mu > 0$  is a weighing factor and  $\hat{\varphi}_{f, L_u, L_y}(k) \in R^{L_u+L_y}$  is the estimated value of  $\varphi_{f, L_u, L_y}(k)$ .

By minimizing the objective function (6-4) with respect to  $\hat{\varphi}(k)$ , the PG estimation algorithm is found as follows

$$\begin{aligned}
\hat{\varphi}_{f, L_u, L_y}(k) &= \hat{\varphi}_{f, L_u, L_y}(k-1) \\
&\quad + \frac{\eta \Delta H_{L_y, L_u}(k-1) (y(k) - y(k-1))}{\mu + \left\| \Delta H_{L_y, L_u}(k-1) \right\|^2} \\
&\quad - \frac{\eta \Delta H_{L_y, L_u}(k-1) \hat{\varphi}_{f, L_u, L_y}^T(k-1) \Delta H_{L_y, L_u}(k-1)}{\mu + \left\| \Delta H_{L_y, L_u}(k-1) \right\|^2} \\
\hat{\varphi}_{f, L_u, L_y}(k) &= \left[ \hat{\varphi}_1(k), \dots, \hat{\varphi}_{L_y-1}(k), \hat{\varphi}_{L_y}(k), \dots, \hat{\varphi}_{L_u+L_y}(k) \right]^T
\end{aligned} \tag{7-4}$$

$$\begin{aligned}
\hat{\varphi}_{f, L_u, L_y}(k) &= \hat{\varphi}_{f, L_u, L_y}(1), \text{ if } \left\| \hat{\varphi}_{f, L_u, L_y}(k) \right\| \leq \varepsilon \\
&\quad \text{or } \left\| \Delta H_{L_y, L_u}(k-1) \right\| \leq \varepsilon \\
&\quad \text{or } \text{sign}(\hat{\varphi}_{f, L_u, L_y}(k)) \neq \text{sign}(\hat{\varphi}_{f, L_u, L_y}(1))
\end{aligned}$$

(8-4)

where  $\eta \in (0,2]$  is a step constant which is added to make (7-4) flexible,  $\hat{\phi}_{f,L_u,L_y}(1)$  is the initial estimated value of  $\hat{\phi}_{f,L_u,L_y}(k)$  and  $\varepsilon$  is a very small positive constant. The reset algorithm (8-4) is employed strengthen the ability to estimate the time-varying parameter by the parameter estimation algorithm. The FFDL-MFAC works on the following four assumptions:

Assumption 1: The partial derivative of  $f(\cdot)$  in (2-4) with respect to all the variables are continuous.

Assumption 2: (2-4) satisfies the following generalized Lipschitz condition:

$$|y(k_1 + 1) - y(k_2 + 1)| \leq b \left\| H_{L_y,L_u}(k_1) - H_{L_y,L_u}(k_2) \right\| \quad (9-4)$$

where  $H_{L_y,L_u}(k) \in R^{L_u+L_y}$ . This assumption means that the output changes are bounded by the variations of control input ( $u$ ) and system output ( $y$ ) at  $k$  and past time instances.

Assumption 3: There exists a bounded control input  $u^*(k)$  such that the system output reaches the desired output signal  $y_d(k)$ , which means the system is controllable.

Assumption 4: The sign of  $\varphi_{L_{y+1}}(k)$  is assumed to be unchanged, i.e.,  $\varphi_{L_{y+1}}(k) > \varepsilon > 0$  or  $\varphi_{L_{y+1}}(k) < -\varepsilon < 0$ , where  $\varepsilon$  is a small positive

constant. This assumption means that the system output will not decrease if the difference control input  $\Delta u$  increases or vice versa.

If the nonlinear system (2-4) satisfying assumption 1-4 is controlled by FFDL-MFAC method through (5-4), (7-4) and (8-4) with a constant desired signal;  $y_d(k + 1) = y_d = const$ , then there exists a  $\lambda_{min}$  such that  $\lambda > \lambda_{min}$  and the closed loop system guarantees:

1.  $u(k)$  and  $y(k)$  are bounded for all  $k$  and the closed loop system is bounded input, bounded output (BIBO) stable.
2. The system output tracking error asymptotically converges to zero;  
$$\lim_{k \rightarrow \infty} |y_d - y(k + 1)| = 0$$
3. The closed-loop system is internally stable.

The model of CVS used in this study stratify all the four above assumptions. In addition, our group has previously shown that the CVS model satisfies the four similar assumptions [29].

#### **4.3.4 Different Patient Conditions and Scenarios**

In order to simulate interpatient and intrapatient variations, all of the CVS model parameters from Table 4-1 were varied from -20% to +20% of their nominal values to create 100 different patient conditions for training and validation of deep CNN for preload estimation. In the same manner, 30 new patient conditions were generated for testing FFDL-MFAC on unseen simulated patients. The FFDL-MFAC combined with measured or estimated preload using the deep CNN was evaluated in each patient for six different scenarios. These six scenarios were simulated by variation of different vascular

resistances, volumes, and heart rate. These scenarios were rapid  $R_{pa}$  changes (rising and falling), rapid  $R_{sa}$  changes (rising and falling), transition from rest to exercise and passive postural change experiments [29]. Table 4-2 shows the simulation conditions for each scenario. The CVS parameters in transition from rest to exercise and passive postural change scenarios were changed using a first order system with a time constant of 10 s, which simulates the response of the native CVS. The other scenarios were simulated using a step-change in parameters [29]. These rapid time-domain responses were chosen because if the proposed methodology can respond properly to these extreme scenarios, it can also respond to slower and milder changes appropriately [13].

**Table 4-1 Normal values and description of cardiovascular model parameters for interpatient and intrapatient simulations**

No	Parameter (unit)	Description	Normal Value
1	$Eeslvf$ ( $\text{mmHg.mL}^{-1}$ )	LV end systolic elastance	3.54
2	$Eesrvf$ ( $\text{mmHg.mL}^{-1}$ )	RV end systolic elastance	1.75
3	$Eao$ ( $\text{mmHg.mL}^{-1}$ )	Aortic elastance	1.04
4	$Eesla$ ( $\text{mmHg.mL}^{-1}$ )	LA end systolic elastance	0.2
5	$Eesra$ ( $\text{mmHg.mL}^{-1}$ )	RA end systolic elastance	0.2
6	$Epa$ ( $\text{mmHg.mL}^{-1}$ )	Pulmonary arterial elastance	0.15
7	$Epu$ ( $\text{mmHg.mL}^{-1}$ )	Pulmonary vein elastance	0.04
8	$Esa$ ( $\text{mmHg.mL}^{-1}$ )	Systemic arterial elastance	0.37
9	$Esv$ ( $\text{mmHg.mL}^{-1}$ )	Systemic vein elastance	0.013
10	$Evc$ ( $\text{mmHg.mL}^{-1}$ )	Vena cava elastance	0.03
11	$Rao$ ( $\text{mmHg.s.mL}^{-1}$ )	Aortic resistance	0.2
12	$Rra$ ( $\text{mmHg.s.mL}^{-1}$ )	Right atrium resistance	0.012
13	$Rpv$ ( $\text{mmHg.s.mL}^{-1}$ )	Pulmonary valve resistance	0.02

14	$R_{sv}$ (mmHg.s.mL $^{-1}$ )	Systemic venous resistance	0.12
15	$T_c$ (s)	Heart rate coefficient	1
16	$T_{sys0}$ (s)	Maximum systolic heart period	0.5
17	$V_{0la}$ (mL)	LA end diastolic volume at zero pressure	20
18	$V_{0lvf}$ (mL)	LV end diastolic volume at zero pressure	40
19	$V_{0ra}$ (mL)	RA end diastolic volume at zero pressure	20
20	$V_{0rvf}$ (mL)	RV end diastolic volume at zero pressure	50
21	$V_{dla}$ (mL)	LA end systolic volume at zero pressure	10
22	$V_{dlvf}$ (mL)	LV end systolic volume at zero pressure	16.77
23	$V_{dra}$ (mL)	RA end systolic volume at zero pressure	10
24	$V_{drvf}$ (mL)	RV end systolic volume at zero pressure	40
25	$R_{mt}$ (mmHg.s.mL $^{-1}$ )	Mitral valve resistance	0.01
26	$R_{av}$ (mmHg.s.mL $^{-1}$ )	Aortic valve resistance	0.02
27	$V_{ua0}$ (mL)	Aortic unstressed volume	230.88
28	$V_{upa}$ (mL)	Pulmonary arterial unstressed volume	91.67
29	$V_{upu}$ (mL)	Pulmonary vein unstressed volume	132.39
30	$V_{usa}$ (mL)	Systemic arterial unstressed volume	231.04
31	$V_{usv}$ (mL)	Systemic vein unstressed volume	1976.1
32	$V_{uvc}$ (mL)	Vena cava unstressed volume	136.17
33	$P_{0la}$ (mmHg)	LA end diastolic stiffness scaling term	0.5
34	$P_{0lvf}$ (mmHg)	LV end diastolic stiffness scaling term	0.98

35	P0ra (mmHg)	RA end diastolic stiffness scaling term	0.5
36	P0rvf (mmHg)	RV end diastolic stiffness scaling term	0.91
37	Vtotal (mL)	Total blood volume	5200
38	$\lambda_{la}$ ( $\text{mL}^{-1}$ )	LA end diastolic stiffness coefficient	0.025
39	$\lambda_{lvf}$ ( $\text{mL}^{-1}$ )	LV end diastolic stiffness coefficient	0.028
40	$\lambda_{ra}$ ( $\text{mL}^{-1}$ )	RA end diastolic stiffness coefficient	0.025
41	$\lambda_{rvf}$ ( $\text{mL}^{-1}$ )	RV end diastolic stiffness coefficient	0.028
42	Lao ( $\text{mmHg.s}^2.\text{ml}^{-2}$ )	Aortic inertance	0.0001
43	Lpa ( $\text{mmHg.s}^2.\text{ml}^{-2}$ )	Pulmonary arterial inertance	7.70e-05

**Table 4-2 Six different patient scenarios and their simulations conditions**

Patient scenarios	Simulation conditions	Reference
Increasing $R_{pa}$ changes	100 to 500 dyne.s.cm <sup>-5</sup>	[29]
Decreasing $R_{pa}$ changes	100 to 40 dyne.s.cm <sup>-5</sup>	[29]
Increasing $R_{sa}$ changes	1300 to 2600 dyne.s.cm <sup>-5</sup>	[29]
Decreasing $R_{sa}$ changes	1300 to 600 dyne.s.cm <sup>-5</sup>	[29]
Transition from rest to exercise	1. Increasing heart rate from 60 to 80 bpm 2. Decreasing $R_{pa}$ from 100 to 40 dyne.s.cm <sup>-5</sup> 3. Decreasing $R_{sa}$ from 1300 to 670 dyne.s.cm <sup>-5</sup> 4. Adding 500 mL fluid from systemic vein into the right atrium	[29]
Passive postural change	Removing 300 mL fluid from the volume of systemic arteries	[29]

### 4.3.5 Evaluation of Sensorless Control

Evaluation of the FFDL-MFAC system for controlling of the HVAD pump speed was performed across interpatient and intrapatient variations using 30 different LVAD patients for each of the six scenarios. The 43 CVS model parameters were randomly varied between -20% to 20% from their nominal values at the beginning of the experiments to create each new patient.

Importantly, these were 30 “unseen” simulated patients, in which the preload estimator was not trained using any of these 30 patients.

In each simulation for each scenario and each patient, an FFDL-MFAC system was implemented to maintain preload (measured or estimated) at a target constant value based on the following protocol. In the first 25 seconds, the pump was off. In the next 25 seconds, the heart pump works in a constant speed mode, in which the speed is tuned to have cardiac output and mean aortic pressure (MAoP) in the range of 4 to 6 l/min and 70 to 90 mmHg, respectively. This process is similar to the actions that clinicians perform to adjust the pump speed for LVAD patients. The 25 second period allows the CVS system to reach a steady state. The desired (target) preload is then set as the preload during this steady state period. At time 50 s, the FFDL-MFAC was then activated. At time 70 s, one of the six patient scenarios was simulated and finally at time 120 s. the simulations ended. The FFDL-MFAC parameters were chosen empirically as  $L_u = 3, L_y = 3, \mu = 1, \lambda = 1, \eta = 0.3, \varepsilon = 10^{-4}$ ,  $\varphi(1) = [1, 1, 1, 1, 1, 1]^T$  and  $\rho = [0.05, 0.05, 0.05, 0.05, 0.05, 0.05]$ . Ventricular suction and pulmonary congestion were defined based on the preload below 0 and above 20 mmHg, respectively. The occurrence of these two important hazardous events was used to assess preload-based FFDL-MFAC for measured and estimated preload. The experiments were performed on a computer with 16 GB of RAM, CPU of Core i7-8700K 3.70 GHz, GPU of GTX 1650 SUPER Windforce 4GB and MATLAB software of 2020b.

In this study, 10-fold cross validation was used to validate the results of preload estimation using the proposed deep CNN. In 10-fold cross validation, the original data is randomly split into 10 equal sections. One out of 10 sections is used as the validation data and the remaining nine sections are used as the training data. This process is then repeated 10 times to each of 10 sections as the validation data. The advantage of 10-fold cross validation is that each section is used for validation once and all 10 sections are used for both training and validation, which leads to more robust results [172].

## 4.4 Results

### 4.4.1 Preload Estimation Using Deep Convolutional Neural Network

Table 4-3 shows the result of the proposed deep CNN model for estimation of preload through 10-fold cross validation for 100 different patient conditions and four speed (2000, 2600, 3000 and 3400 rpm) in six different patient scenarios (rising and falling  $R_{pa}$ , rising and falling  $R_{sa}$ , rest to exercise and postural change). The results show that the proposed method has a small RMSE (0.88 mmHg) for all simulations (2400 simulations). The average values of the correlation coefficient, RPC, CV and bias for all the folds are 0.99, 1.73 mmHg, 15.29 % and 0.02 mmHg, respectively.

**Table 4-3 Performance of the proposed deep CNN on the estimation preload for each validation fold through 10-fold cross-validation on 100 patients**

Fold	Correlation coefficient	RMSE (mmHg)	RPC (mmHg)	CV (%)	Bias (mmHg)
1	0.98	1.00	1.97	17.17	-0.09
2	0.98	0.83	1.64	14.37	-0.02
3	0.99	0.85	1.67	14.71	0.06
4	0.99	0.70	1.39	12.24	0.05
5	0.99	0.80	1.57	13.85	0.03
6	0.99	0.80	1.57	13.78	-0.01
7	0.99	0.88	1.73	15.29	0.07
8	0.98	1.13	2.21	19.57	0.07
9	0.98	0.95	1.87	16.44	0.02
10	0.99	0.89	1.76	15.52	0.04
<b>Average</b>	<b>0.99</b>	<b>0.88</b>	<b>1.73</b>	<b>15.29</b>	<b>0.02</b>

#### **4.4.2 Evaluation of Sensorless Control Using Deep Convolutional Neural Network and FFDL-MFAC**

Figure 4-4 demonstrates a sample simulation for the combined FFDL-MFAC and deep CNN model for estimation of preload and its comparison with the FFDL-MFAC and measured preload for adjusting the LVAD speed. The simulation was performed for falling SVR from 1300 to 600 dyne.s.cm<sup>-5</sup> in patient 23. As can be seen from the figure, there is only a small difference between the estimated and measured preload before and after the CVS change. In addition, the LVAD speed curve for both controllers are very similar. This indicates that the estimator is working accurately and that the control performance is minimally effected by the use of an estimator.

Table 4-4 shows the performance of the proposed deep CNN combined with FFDL-MFAC on the estimation of the preload for six different scenarios on new 30 patients.

In transition from rest to exercise scenario, the results show a correlation coefficient of 0.94, RMSE of 1.07 mmHg, RPC of 2.09 mmHg, CV of 18.49 % and bias of 0.13 mmHg. Rising R<sub>pa</sub> scenario has the least bias, while falling R<sub>pa</sub> has the most bias. The highest CV, RPC and RMSE were produced by the rest to exercise scenario and the postural change scenario produced the least RMSE and RPC.

Finally, the results for all scenarios show a correlation coefficient of 0.97, RMSE of 0.84 mmHg, RPC of 1.56 mmHg, CV of 14.44 % and bias of 0.29 mmHg.

Furthermore, none of 30 simulations in all six scenarios (180 simulations) led to ventricular suction or pulmonary congestion, as shown in Table 4-5.

#### Comparison of FFDL-MFAC for measured and estimated preload in falling SVR

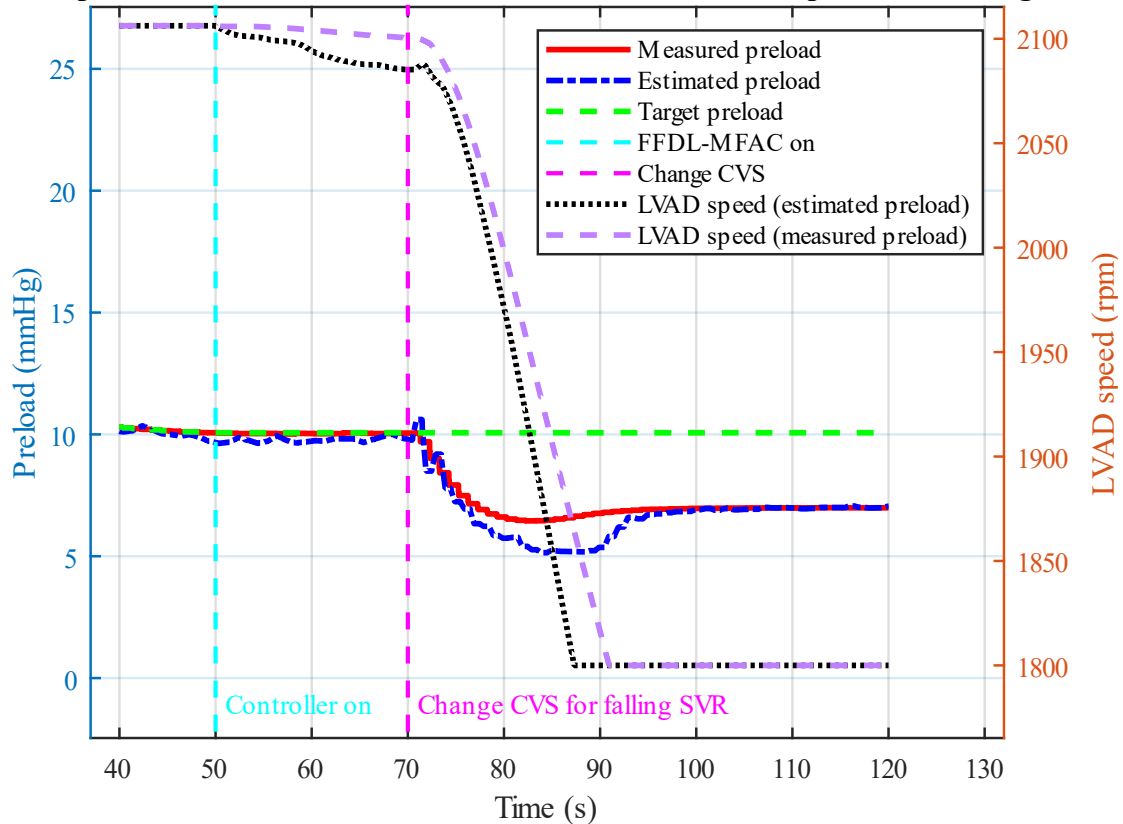


**Figure 4-4 A sample simulation for comparison of FFDL-MFAC for measured and estimated preload in falling SVR (patient 23).**

**Table 4-4 Performance of the proposed deep CNN combined with FFDL-MFAC on the estimation of preload for each scenario on new 30 patients**

Fold	Correlation coefficient	RMSE (mmHg)	RPC (mmHg)	CV (%)	Bias (mmHg)
Falling R <sub>pa</sub>	0.98	0.90	1.26	10.83	0.63
Rising R <sub>pa</sub>	0.97	0.72	1.41	16.87	0.11
Falling R <sub>sa</sub>	0.97	0.68	1.21	13.70	0.30
Rising R <sub>sa</sub>	0.97	0.94	1.78	12.75	0.27
Rest to exercise	0.94	1.07	2.09	18.49	0.13
Postural change	0.98	0.63	1.13	10.65	0.27
All scenarios	<b>0.97</b>	<b>0.84</b>	<b>1.56</b>	<b>14.44</b>	<b>0.29</b>

**Table 4-5 Comparison of the proposed physiological control system using FFDL-MFAC for measured and estimated preload on new 30 patients in six different scenarios**

Methodology	Number of suctions	Number of congestions
FFDL-MFAC using measured preload	0	0
FFDL-MFAC using estimated preload	0	0

## 4.5 Discussion

In this study, we proposed a real-time deep CNN model for estimation of preload based on the pump flow, which was trained and validated across a range of 2400 randomized patient conditions. In addition, a sensorless physiological control system using FFDL-MFAC and deep CNN for preload estimation was proposed for adjusting LVAD speed to respond to interpatient intrapatient variations. The results of the preload estimator indicate that the proposed estimator can predict preload with a low amount of error. The results for the sensorless physiological control system showed that there was not any pulmonary congestion or ventricular suction when the control system was subject to 30 unseen patient conditions across six different patient scenarios. Our proposed method can work on both adults and pediatric patients, as the mean aortic valve flow and pump flow for the 30 unseen patient datasets are in the range of [0, 4.69] and [0.83, 5.87] L/min (when the

proposed controller is on), respectively. The novelty of this work is that it is the first time (to the knowledge of the authors) a study has combined an accurate preload estimator with a robust control algorithm and tested it across a wide range of patient scenarios.

The results from Table 4-4 demonstrate that the proposed deep CNN can estimate preload accurately based on the 600 samples (from the peak) of the pump flow on unseen patient dataset over six common patient scenarios. The advantage of deep CNN over conventional machine learning algorithms like MLPs and support vector machines (SVM) is that features from the input signal are automatically extracted by applying different sizes of convolutional filters and functions. Manually finding suitable features from the input signals is a difficult and time-consuming task, as it relies on both deep understanding of the morphology of the HVAD signals and an iterative approach to identifying useful features for the estimation model.

Other researchers have presented pressure estimation methods in the literature, but none have been as accurate nor as robustly assessed as that presented in this paper. An adaptive physiological controller for rotary blood pumps using pump intrinsic variables and a linear state-space model of CVS was proposed by Wu [173]. The pump flow and aortic pressure were estimated via pump intrinsic variables. However, the pump flow derived from pump intrinsic variables was assumed to be the total flow of the CVS [173], which makes the simplified assumption that the aortic valve is always closed. Moreover, the model linearization cannot be used to simulate different

patient conditions which can result in inaccuracy of simulation and inconsistent physiological control performance. Furthermore, there was no strategy to avoid the possible suction and congestion events [173].

A sensorless control for continuous flow LVAD was proposed by Meki *et al.* to maintain physiological perfusion and avoid ventricular suction using pump speed [24]. The proposed controller was used to maintain the differential pump speed setpoint of 800 rpm. However, unlike our proposed solution, the simulations were only performed on one patient with different scenarios and therefore it is not clear how the proposed methodology can respond to different patient conditions and how the differential pump speed setpoint should be set for different patients.

The slope of the pump flow over the ventricular filling phase was used to estimate pulmonary arterial wedge pressure (PAWP) as a surrogate of preload using linear regressions [22], [23], [139]. However, in these studies, estimation of PAWP was according to distinguish PAWP to two classes of high PAWP ( $PAWP \geq 18$  or  $PAWP \geq 30$ ) and low PAWP ( $PAWP \leq 18$ ), which make them impossible to be used in real-time physiological control of LVADs. HeartPod as an implantable pressure sensor for measuring left atrial pressure resulted in an error of  $0.8 \pm 4.0$  mmHg, which can lead to 4.7 mmHg drift after three months [84]. However, in this study, preload can be accurately estimated with error of about 0.9 mmHg in the worst case. An inaccurate estimator can result in poorer control performance. Furthermore, we have shown that even with

this error, there is little difference in control performance between using our estimator and a sensor.

The use of the proposed FFDL-MFAC preload-based control system in this paper showed excellent performance across a wide range of unseen patient conditions. FFDL-MFAC can automatically adjust the pump speed in an adaptive mode using the memories of the past inputs and output from the CVS and LVAD in real-time. The adaptive structure of the FFDL-MFAC can respond to the interpatient and intrapatients variations and unpredicted changes on hemodynamics.

The mathematical proof for FFDL-MFAC shows that the closed-loop system is internally and BIBO stable and the tracking error between desired and actual output asymptotically converges to zero. Another advantage of FFDL-MFAC over the conventional PID controller used for physiological control of LVAD is that no tuning and optimization in needed for the parameters of the controller, which can facilitate working with physiological control systems for clinicians without any knowledge of control engineering.

In healthy hearts, cardiac output (CO) varies based on the preload via Frank-Starling (FS) mechanism. Therefore, preload is a vital clinical variable. Physiological control systems that work based on the measuring of prelaod can improve perfusion, HF patients' quality of lives, and their lifespans, prevent incidence of the hazardous events such suction and congestion and increase the exercise capacity by providing higher pump flow [13], [28], [29]. Therefore,

the proposed preload-based physiological controller can have the same benefits.

A physiological control for LVAD using MFAC was proposed in [28], [29] to maintain the preload in the physiological range of 3 to 15 mmHg for 100 different patient conditions. In the proposed control approach, a sensor for measuring the left ventricular pressure (LVP) was used and then the preload was extracted by a novel algorithm from the LVP in real-time mode. However, there is no commercial long-term implantable sensor for LVP measurement, making our solution that uses an accurate preload estimator more viable. In addition, the LVAD speed was controlled using the compact linearization form of MFAC, which is not able to identify all the plant dynamics. In contrast, in this study, the preload was estimated using deep CNNs based on the pump flow and FFDL-MFAC was used to identify the full dynamics of the CVS and LVAD and control the pump speed. Moreover, the use of an FFDL-MFAC in this study is advantageous because it does not have the common issues of other adaptive controllers such as ANN [153] and fuzzy controllers [53]. These controllers generate a high computational burden and rely on accurate rules for different patient conditions, respectively. Other controllers such as model predictive control (MPC) and optimal control need a simplified state-space model that cannot be generalized and modified for different patient conditions [38].

Frank Starling-like controllers have been proposed, which can restore physiological response of the native heart, can prevent suction, congestion and improve the patient's mobility [12], [13], [15], [16]. However, in these

types of controller, clinicians need to manually set a desired flow across different patient conditions such as sleeping, walking or doing exercise. Furthermore, FS curves are patient-dependent. Finding the ideal FS curve for each patient requires frequent clinical check-ups, which makes implantation of Starling-like controller for different patients impossible. In contrast, a constant preload-based control strategy is simpler: the accurate preload estimation means that the clinician could adjust target preload without performing a speed ramp under the guidance of ultrasound. This is the reason that a preload-based physiological control system for LVADs was employed in this study, which can also prevent ventricular suction, pulmonary congestion and improve cardiac perfusion.

CNN can be implanted for application of super-resolution 4K ultra high-definition videos at 60 frames per second using FPGA in real-time mode [174]. Our proposed deep CNN is much simpler compared to the one proposed by Kim *et al.* [174]. FFDL-MFAC also needs very low computational burden since it is made by some simple equations. Therefore, there is not any issue for implementation of CNN and FFDL-MFAC with current technology in real-time.

This study has some limitations. First, the baroreflex effect was not considered in this study which may influence CVS hemodynamics and therefore control performance [159]. However, the baroreflex can be simulated as variations in CVS, which we have shown that the FFDL-MFAC can compensate for any changes in CVS well due to its adaptive structure.

Second, the proposed preload estimator in this study works based on the ideal pump flow estimator. Although there are no perfect pump estimators, several studies reported an estimator for pump flow with a very low value error between 0.002 to 0.38 L/min [121], [126], [138]. Further investigation should be done to improve the accuracy of pump flow estimators based on the pump intrinsic variables.

Third, although most physiological control systems for LVADs are evaluated through in-vitro studies, this study was performed only using numerical models of the CVS and LVAD. Ideally, the estimator would be trained on human or animal data. However, it is very time-consuming and expensive to obtain enough invasive pressure and flow data to robustly train a CNN. The advantage of using the numerical model (which was validated from animal experiments) was that it enabled us to easily simulate 2400 different patient conditions for validation of preload estimator. This would be a laborious and expensive process to complete in-vivo or in humans. Similarly, the numerical model facilitated simulation of 180 different patient conditions for validation of the preload estimation and physiological controller.

Future work will include validating the proposed estimator and the physiological controller via in-vitro and in-vivo experiments. Future work will also involve long term simulation of the proposed sensorless control system on patients with LVAD over the years via analysis of rapid changes of the CVS parameters. If the proposed method can handle these rapid changes as the worst-case scenarios, then it should be able to handle the long-term changes.

## **4.6 Conclusion**

In this study, a novel real-time deep CNN model for estimation of preload based on the LVAD flow was proposed. Furthermore, this estimator was combined with a new adaptive sensorless physiological control system for adjusting HVAD pump speed. This combined system was shown to be robust to a wide variety of inter- and intrapatient variations. When tested on 30 unseen patient datasets, no ventricular suction or pulmonary congestion events occurred. This shows that the inclusion of a preload estimator instead of an implantable pressure sensor that is likely to have long-term reliability issues, has no detrimental effects on the performance of the physiological controller.

## **4.7 Acknowledgment**

The authors would like to recognize the financial assistance provided by the National Health and Medical Research Council Centers for Research Excellence (APP1079421).

In the next chapter, we address the third objectives of this study, which is design an improved non-invasive preload estimator using advanced machine and deep learning methods based on the pump variables and test on a clinical dataset.

# **Chapter 5. Fully Elman Neural Network: A Novel Deep Recurrent Neural Network Optimized by an Improved Harris Hawks Algorithm for Classification of Pulmonary Arterial Wedge Pressure**

The study presented in Chapter 5 has been accepted in the journal of *IEEE Transactions on Biomedical Engineering*:

[175] **M. Fetanat**, M. Stevens, P. Jain, C. Hayward, E. Meijering and N. H. Lovell, “Fully Elman Neural Network: A Novel Deep Recurrent Neural Network Optimized by an Improved Harris Hawks Algorithm for Classification of Pulmonary Arterial Wedge Pressure.”, accepted, *IEEE Transactions on Biomedical Engineering*, 2021.

## 5.1 Abstract

Heart failure (HF) is one of the most prevalent life-threatening cardiovascular diseases in which 6.5 million people are suffering in the USA and more than 23 million worldwide. Mechanical circulatory support of HF patients can be achieved by implanting a left ventricular assist device (LVAD) into HF patients as a bridge to transplant, recovery or destination therapy and can be controlled by measurement of normal and abnormal pulmonary arterial wedge pressure (PAWP). While there are no commercially available long-term implantable pressure sensors to measure PAWP, real-time non-invasive estimation of abnormal and normal PAWP becomes vital. In this work, first an improved Harris Hawks optimizer algorithm called HHO+ is presented and tested on 24 unimodal and multimodal benchmark functions. Second, a novel fully Elman neural network (FENN) is proposed to improve the classification performance. Finally, four novel 18-layer deep learning methods of convolutional neural networks (CNNs) with multi-layer perceptron (CNN-MLP), CNN with Elman neural networks (CNN-ENN), CNN with fully Elman neural networks (CNN-FENN), and CNN with fully Elman neural networks optimized by HHO+ algorithm (CNN-FENN-HHO+) for classification of abnormal and normal PAWP using estimated HVAD pump flow were developed and compared. The estimated pump flow was derived by a non-invasive algorithm embedded into the commercial HVAD controller. The proposed methods are evaluated on an imbalanced clinical dataset using 10-fold cross-validation. The proposed CNN-FENN-HHO+ method outperforms the proposed CNN-MLP,

CNN-ENN and CNN-FENN methods and improved the classification performance metrics across 10-fold cross-validation with an average sensitivity of 89%, accuracy of 88% and specificity of 86%. The proposed methods can reduce the likelihood of hazardous events like pulmonary congestion and ventricular suction for HF patients and notify identified abnormal cases to the hospital, clinician and cardiologist for emergency action, which can decrease the mortality rate of HF patients.

## 5.2 Introduction

Cardiovascular disease (CVD) is a highly prevalent illness affecting 26.7 million people in the United States of America [1]. 6.5 million people are suffering from heart failure (HF) in the USA and more than 23 million worldwide [5]. The prevalence of HF will increase by 46% from 2012 to 2030, leading to more than 8 million adult with HF according to the American Heart Association [1]. Although heart transplantation is the gold standard treatment for end-stage HF patients, the number of donor hearts is significantly less than the demand for heart transplantation and therefore the mortality of people on the waitlist is high. Mechanical circulatory support is one of the most suitable treatments for HF patients, and is achieved by implanting a mechanical pump, called a left ventricular assist device (LVAD), into the body of the HF patients [1], [5].

Currently LVADs are operated at constant speed which makes them insensitive to changes in demand as physiological conditions change [10]. This can lead to hazardous events like ventricular suction (ventricular collapse due to low pressure in the ventricle) or pulmonary congestion (a condition caused by

excess fluid in the lungs due to high pressure in the ventricle) [29]. Physiological control systems for LVADs can be used to automatically adjust pump speed to maintain a constant left ventricular end-diastolic pressure (LVEDP) [29]. Maintaining this important clinical variable can supplement the Frank-Starling response of the native heart and therefore can prevent these hazardous events for HF patients [12], [25], [59], [93].

This physiological control system approach requires an implantable pressure sensor to measure LVEDP in HF patients. However, there are currently no commercial long-term implantable pressure sensors available. An alternative is to use pulmonary arterial wedge pressure (PAWP) as it can be measured more easily as a surrogate index for LVEDP by catheterization [10], [23], [28], [29]. Nevertheless, measuring the PAWP by pulmonary artery catheterization can only work for a short period of time in hospital settings as most of these patients are discharged home, and this technique not being suitable of safe outside the hospital environment. Therefore, the non-invasive prediction of abnormal and normal PAWP becomes more critical. If these values can be predicted, a physiological control system can automatically adjust the pump speed to restore PAWP to a safe level.

Machine learning algorithms can be employed for identifying the abnormal and normal PAWP using a non-invasive signal from the implanted pump [23]. These algorithms mainly include feature extraction, feature selection and classification parts. However, manually extracting and selecting suitable features is time-consuming and can lead to overfitting [176]. Furthermore,

extracting features manually can reduce the generalization ability of the machine learning methods [176].

To overcome this issue, deep learning methods such as convolutional neural networks (CNNs) can be used to automatically extract and select the features from the raw input signals [176]. Previously, a variety of deep learning methods have been used for the classification of cardiovascular disease using electrocardiogram (ECG) signals [177]–[186]. Furthermore, several previous studies have employed recurrent neural networks (RNN) for classification of CVDs. The results demonstrated that RNNs outperform static conventional neural networks like a multi-layer perceptron (MLP) as RNNs have a dynamic processing ability [176], [187], [188]. However, the Elman neural network (ENN) is standing out among many classical types of RNNs and is widely applied in different research fields [188]–[191]. An ENN, which has a dynamic memory ability, can use the previous and current features of the input signals for improving the classification performance metrics and is more suited for the small imbalanced dataset used in this work. Modification of ENN can further improve the classification performance.

CNNs suffer from the need for many hyper-parameters, which should be optimized during training of the networks. However, optimizing hyper-parameters manually is very challenging [192]–[194].

Moreover, the hyper-parameters are data dependent and therefore may not be appropriate in another dataset. Obtaining the appropriate values of the hyper-parameters of CNNs is not an easy task since there is no robust

mathematical approach which can be employed. Hence, determining the values of the hyper-parameters of CNNs necessitates many iterations to achieve better performance [193]. Random and grid searches could be employed to determine the hyper-parameters automatically, however these are time consuming [193]. In addition, Bayesian optimization methods could be also used to achieve the hyper-parameters. However, it requires estimation of several statistics of the error function, which can lead to an inefficient results [195], [196]. Proposing an automatic method based on the metaheuristic algorithms for optimization of the values of these parameters can significantly result in less computational cost and higher performance [197]. These metaheuristic algorithms can also work on non-continuous, and non-differentiable problems [198].

There are many metaheuristic algorithms such as Particle Swarm Optimization (PSO) [199], Differential Evolution (DE) [200], Gravitational Search Algorithm (GSA) [201], Harris Hawks Optimization (HHO) [198], Marine Predators Algorithm (MPA) [202], Slime Mould Algorithm (SMA) [203], Equilibrium Optimizer (EO) [204], Salp Swarm Algorithm (SSA) [205] and Grey Wolf Optimizer (GWO) [206]. In metaheuristics, two major strategies of exploration and exploitation of random search are executed. While exploration refers to finding relevant areas in the solution space, exploitation concerns the extraction of useful information from these areas [207]. Based on the “no free lunch (NFL)” theorem [208], which states that there is no ideal metaheuristic to solve all types of optimization problems well [209], any given problem may benefit from an improved metaheuristic algorithm. The HHO algorithm

outperformed many other metaheuristic algorithms for finding optimal solution in different benchmark functions [198], [209], [210], and several applications such as image thresholding problems [211], estimation of photovoltaic models [212] and drug design [213]. The HHO algorithm was inspired by chasing and escaping behavior between Harris Hawks and rabbits as was recently introduced by Heidari et al. [198]. Furthermore, Heidari et al. showed that HHO can fail in providing optimal solutions in some cases [198], [209]. These findings motivated us to try to improve the well-known HHO algorithm for our application.

This study aims to develop a non-invasive method for detection of abnormal and normal PAWP for HF in patients with implanted LVADs. The classification of PAWP based on the pump flow signal from the commercial HVAD controller can be used to adjust the pump speed in real-time and therefore reduce the likelihood of hazardous events like pulmonary congestion and ventricular suction. Furthermore, the proposed method can be implemented on a mobile software platform and notify identified abnormal cases to the hospital, clinician and cardiologist for emergency action, which can decrease the mortality rate of HF patients.

The novelty of this work is multifold, first a modified HHO algorithm called HHO+ is proposed. Second, a new fully Elman neural network called FENN is proposed, which employs long-term and temporal information of the input and output variables that can improve the classification performance. Third, the hyper-parameters of FENN were optimized by the proposed HHO+

algorithm to further improve the classification performance. Finally, four non-invasive approaches for the classification of abnormal and normal PAWP via combination of CNN, ENN, FENN and HHO+ using the pump flow signal are proposed and compared. Relevant features are automatically extracted from the input pump flow signal by a CNN.

In the following sections, first the clinical dataset and preprocessing are described. Next, the HHO, CNN and ENN algorithms are introduced. Then, an improved Harris Hawks algorithm (HHO+) and novel fully Elman neural network (FENN) are presented. The proposed HHO+ is compared with recent metaheuristics such as HHO [198], MPA [202], SMA [203], EO [204], SSA [205] and GWO [206]. Subsequently, four novel methods for classification of PAWP, namely CNN-MLP, CNN-ENN, CNN-FENN and CNN-FENN-HHO+, are fully proposed. Afterwards, the performance evaluation metrics, K-fold stratified cross validation procedure and weighted cross-entropy loss function are described. Then, the proposed HHO+ is validated on 24 unimodal and multimodal benchmark functions. Subsequently, the comparative classification results of CNN-MLP, CNN-ENN, CNN-FENN and CNN-FENN-HHO+ on 10-fold cross-validation using a clinical patient dataset are presented. Finally, a discussion of the results, study limitations and future work concludes the paper.

## **5.3 Methodology**

### **5.3.1 Dataset**

The clinical data set was obtained from 25 stable and ambulatory patients with implanted HVAD pump (HeartWare, Medtronic). PAWP was measured using right heart catheterization (7.5-French double transducer Swan-Ganz CCO catheter; Edwards Lifesciences, Irvine, CA) into the pulmonary artery of the implanted patients. HVAD pump flow was estimated by a non-invasive algorithm embedded into the commercial HVAD controller. PAWP and pump flow were recorded in various exercise workloads and pump speeds and the sampling rate for the pressure and flow measurements were 50 Hz. The experimental study was approved by St Vincent's hospital research ethics committee [23]. The data were used for a 10-fold cross-validation dataset for evaluation of the proposed methods. PAWP of less than 8 or greater than 16 mmHg was taken to be abnormal, and other values as a normal condition, based on the clinicians' suggestions from St Vincent hospital in Sydney, Australia. The recorded dataset is an imbalanced dataset which has 459 abnormal PAWP and 1338 normal PAWP samples.

### **5.3.2 Data pre-processing**

A Butterworth low-pass filter with stop frequency of 15 Hz was employed to remove the higher frequency noise and smooth the PAWP and pump flow signals. The pump flow signal was then segmented with a length of 6 s (300 samples). The mean PAWP was calculated for each segment from all the

samples between two consecutive minima over 6 seconds. PAWP has a pulsatile waveform due to heart contractility, and inhalation and exhalation.

### 5.3.3 Background materials

#### 5.3.3.1 The Harris Hawks optimizer (HHO)

The HHO algorithm is a population-based and gradient-free optimization algorithm, which was inspired by exploring a prey (rabbit), surprising pounce, collaborative behavior of hawks, and different attacking strategies for catching a prey. Although the hawks first look for different potential locations to hunt, the rabbit exhibits escaping behavior to improve its survival chance.

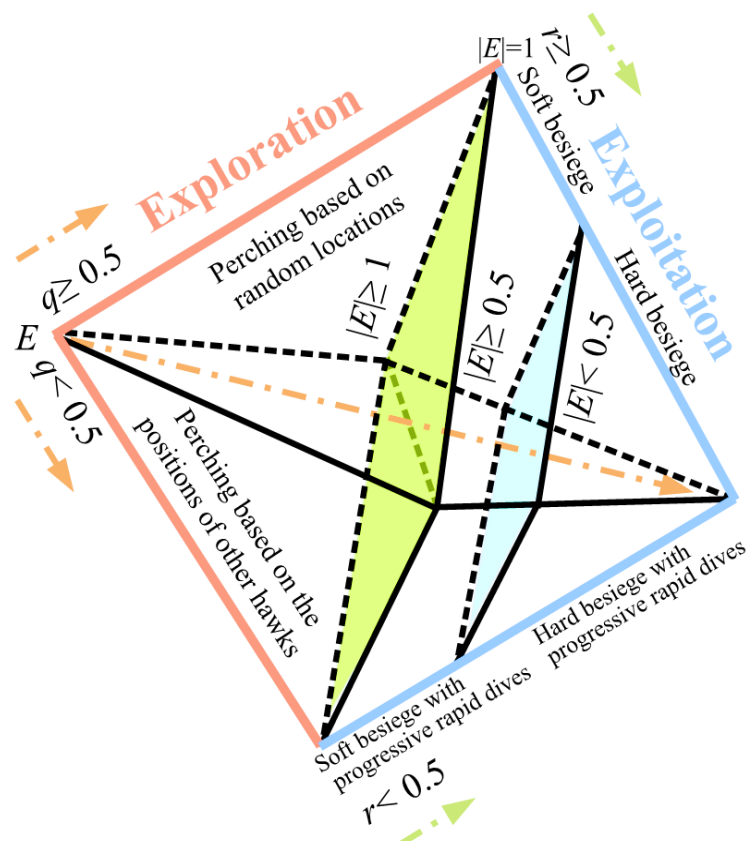


Figure 5-1 Main phases of classical HHO [198].

In this analogy, the rabbit represents the best solution, and the hawks represent candidate solutions in each iteration. The main phases of HHO are shown in Figure 5-1. While the exploration phase of HHO includes two different search methods, the exploitation phase includes four different search methods. The descriptions of these phases are presented in the next subsections [198].

### 5.3.3.2 Exploration phase

In this phase, the hawks perch at different random locations and wait to detect a prey based on the two following strategies. The mathematical model of the exploration mechanism of HHO is presented as follows [198]:

$$X_{t+1} = \begin{cases} X_{rand,t} - r_1 |X_{rand,t} - 2r_2 X_t| & q \geq 0.5 \\ (X_{rabbit,t} - X_{m,t}) - r_3 (lb + r_4(ub - lb)) & q < 0.5 \end{cases} \quad (1-5)$$

where  $X_{t+1}$  and  $X_t$  are the position vectors of hawks in iteration  $t + 1$  and  $t$ , respectively.  $X_{rabbit,t}$  denotes the position of the rabbit (best solution) in iteration  $t$ . The variables  $r_1, r_2, r_3, r_4$  and  $q$  are random numbers in the interval  $(0,1)$ , which change in each iteration.  $X_{rand,t}$  represents the position of one of the hawks, chosen randomly in the iteration  $t$ .  $X_{m,t}$  is the average position of the hawk population in the iteration  $t$ .  $lb$  and  $ub$  are the lower and upper bounds of variables to be optimized. The average position of the hawk population in the iteration  $t$  ( $X_{m,t}$ ) is calculated as follows [198]:

$$X_{m,t} = \frac{1}{N} \sum_{i=1}^N X_{i,t} \quad (2-5)$$

where  $X_{i,t}$  denotes the location of  $i^{th}$  hawk in iteration  $t$ .  $N$  is the total number of hawks.

### 5.3.3.3 Transition from exploration to exploitation

A suitable transition phase between exploration and exploitation is a key factor for any metaheuristic algorithm. The HHO algorithm can switch from exploration to exploitation behaviors based on the decreasing energy function of the rabbit, which is mathematically modeled as follows [198]:

$$E = 2 E_0 \left(1 - \frac{t}{T}\right) \quad (3-5)$$

Where  $E$  represent the escaping energy of the rabbit,  $E_0$  is the initial state of rabbit energy, which is calculated by  $E_0 = 2 * rand - 1$ .  $rand$  is a random number in the interval  $(0,1)$ .  $t$  and  $T$  are the current and maximum number of iterations, respectively. The maximum number of iterations is used as the stopping criterion for the HHO algorithm.

### 5.3.3.4 Exploitation phase

In this phase, the hawks perform the surprise pounce to attack the rabbit detected in the previous phase and the rabbit attempts to escape the danger. Four different chasing styles are performed by hawks to catch the rabbit [198].

Let  $r$  be a chance, which indicates whether the rabbit escape is successful ( $r < 0.5$ ) or not ( $r \geq 0.5$ ) before the surprise pounce. The hawks perform soft or hard besiege to catch the rabbit regardless of the rabbit's action. They encircle the rabbit from different directions softly or hardly based on the retained energy of the rabbit. Then the hawks get closer to the rabbit to improve their chances in collaboratively hunting the rabbit by performing the surprise pounce. After some time, the escaping rabbit will lose its energy and the hawks perform the besiege process to catch the exhausted prey. Soft and hard besiege happen when  $|E| \geq 0.5$  and  $|E| < 0.5$ , respectively [198]. These four possible strategies are described as follows:

### **1. Soft besiege**

When ( $r \geq 0.5$ ) and  $|E| \geq 0.5$ , the rabbit still has enough energy to escape via some random jumps. In this situation, the hawks encircle the rabbit softly to make the rabbit more exhausted. This behavior is mathematically modeled as follows [198]:

$$X_{t+1} = \Delta X_t - E |JX_{rabbit,t} - X_t| \quad (4-5)$$

$$\Delta X_t = X_{rabbit,t} - X_t \quad (5-5)$$

where  $\Delta X_t$  is the difference between the position vector of the rabbit and hawk in the iteration  $t$ .  $J = 2(1 - r_5)$  denotes the random jump the rabbit takes via the escaping procedure, which simulates the rabbit motion in a random behavior.  $r_5$  is random number in the interval (0,1).

## 2. Hard besiege

When ( $r \geq 0.5$ ) and  $|E| < 0.5$ , the rabbit is exhausted and has low escaping energy. The hawks then encircle the rabbit to perform the surprise pounce. This behavior is mathematically modeled as follows [198]:

$$X_{t+1} = X_{rabbit,t} - E|\Delta X_t| \quad (6-5)$$

## 3. Soft besiege with progressive rapid dives (PRD)

When ( $r < 0.5$ ) and  $|E| \geq 0.5$ , the rabbit has enough energy to escape successfully. A soft besiege is performed by the hawks before the surprise pounce. To mathematically model the escaping behaviors and leapfrog movements of the rabbit [214], the Levy-flight algorithm [215] is integrated into HHO to imitate the zigzag motion of rabbits during the escaping phase. The rapid and irregular dives of the hawks are also simulated by Levy-flight algorithm. The position of the hawks can be modeled using the following equations [198]:

$$Y = X_{rabbit,t} - E|JX_{rabbit,t} - X_t| \quad (7-5)$$

$$Z = Y + S \times LF(D) \quad (8-5)$$

where  $D$  is the dimension of the problem and  $S$  indicates a random vector of size  $1 \times D$ . LF represents the levy flight distributed function, which is calculated as:

$$LF(y) = \frac{u \times \sigma}{|v|^{\frac{1}{\alpha}}}, \sigma = \left( \frac{\Gamma(1 + \alpha) \times \sin\left(\frac{\pi\alpha}{2}\right)}{\Gamma\left(\frac{1 + \alpha}{2}\right) \times \alpha \times 2^{\left(\frac{\alpha-1}{2}\right)}} \right)^{\frac{1}{\alpha}} \quad (9-5)$$

where  $u$  and  $v$  are random numbers in the interval  $(0,1)$ .  $\alpha$  is a constant set to 1.5.

In this situation, the final updated position of the hawks is performed as:

$$X_{t+1} = \begin{cases} Y & \text{if } f(Y) < F(X_t) \\ Z & \text{if } f(Z) < F(X_t) \end{cases} \quad (10-5)$$

Where  $Y$  and  $Z$  are calculated using Eqs. (7-5) and (8-5) respectively.

#### 4. Hard besiege with progressive rapid dives (PRD)

When  $(r < 0.5)$  and  $|E| < 0.5$ , the rabbit does not have enough energy to escape. In this situation, the hawks build hard besiege is created before the surprise pounce to kill the rabbit. Although this situation is similar to soft besiege, the hawks attempt to decrease the distance between their average locations and the location of the escaping rabbit. A 2-D schematic of hard besiege with progressive rapid dives is depicted in Figure 5-2. The following equation can mathematically model this behavior [198]:

$$X_{t+1} = \begin{cases} Y^* & \text{if } f(Y^*) < F(X_t) \\ Z^* & \text{if } f(Z^*) < F(X_t) \end{cases} \quad (11-5)$$

where  $Y^*$  and  $Z^*$  are calculated as follows:

$$Y^* = X_{rabbit,t} - E|JX_{rabbit,t} - X_{m,t}| \quad (12-5)$$

$$Z^* = Y^* + S \times LF(D) \quad (13-5)$$

where  $X_{m,t}$  is calculated in Eq. (2-5)

The pseudocode of the HHO algorithm is indicated in Algorithm 1.

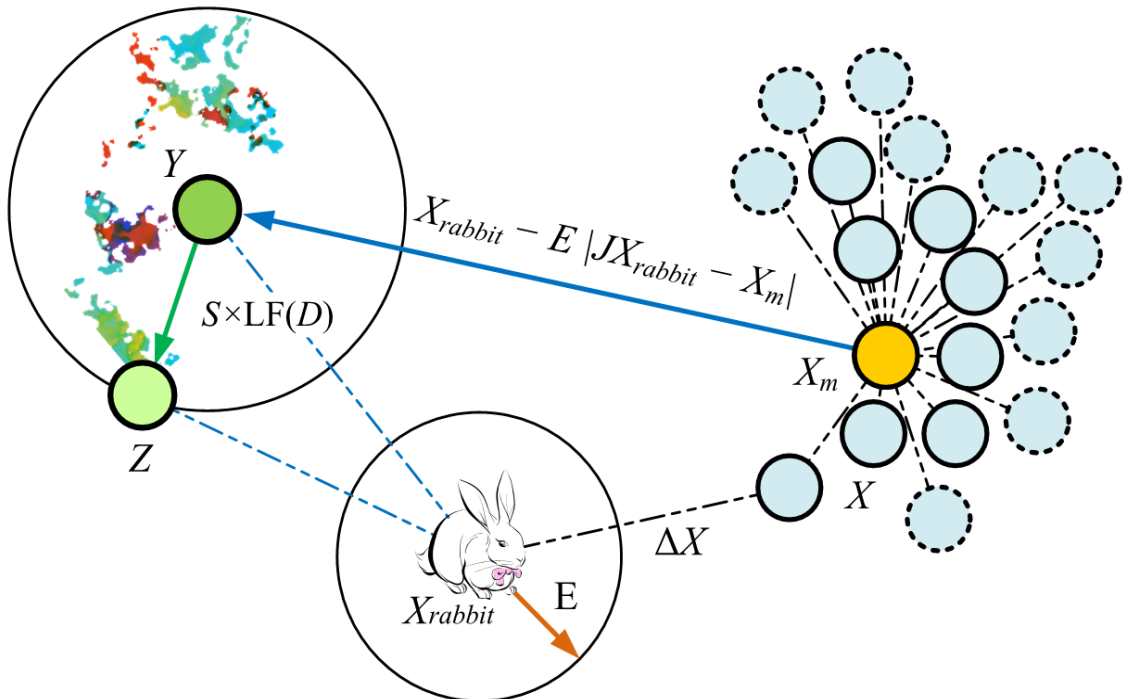


**Figure 5-2 A 2-D schematic of hard besiege with progressive rapid dives [198].**

---

**Algorithm 1** Pseudo code of classical HHO algorithm

---

**Inputs:** The population size  $N$  and maximum number of iterations  $T$   
Initialize the random hawk populations  $X_i(i = 1, 2, \dots, N)$  in the specific search space

**while** (maximum iteration is not met) **do**

- Calculate the fitness values of hawks
- Set  $X_{rabbit}$  as best solution of hawks
- for** (each hawk ( $X_i$ )) **do**

  - Update the initial energy  $E_0$  and jump strength  $J$
  - Update the  $E$  using Eq. (3-5)
  - If** ( $|E| \geq 1$ ) **then** Exploration phase
    - | Update the hawk vectors using Eq. (1-5)
  - else if** ( $|E| < 1$ ) **then** Exploitation phase
    - if** ( $r \geq 0.5$  and  $|E| \geq 0.5$ ) **then** Soft besiege
      - | Update the hawk vectors using Eq. (4-5)
    - else if** ( $r \geq 0.5$  and  $|E| < 0.5$ ) **then** Hard besiege
      - | Update the hawk vectors using Eq. (6-5)
    - else if** ( $r < 0.5$  and  $|E| \geq 0.5$ ) **then** Soft besiege with PRD
      - | Update the hawk vectors using Eq. (10-5)
    - else if** ( $r < 0.5$  and  $|E| < 0.5$ ) **then** Hard besiege with PRD
      - | Update the hawk vectors using Eq. (11-5)
  - end**

- end**

- end**

**Return** The location of rabbit ( $X_{rabbit}$ ) and its fitness value

---

### **5.3.3.5 Convolutional neural network with multi-layer perceptron (CNN-MLP)**

The CNN is one of the most popular deep learning methods and was proposed by Fukushima in 1980 and improved by Lecun in 1998 [145], [146]. CNNs can automatically extract features from the raw input signals and then map the features to the labeled classes [188]. The structure of CNN mainly includes an input layer, convolutional layer, max-pooling layer, fully-connected layer and dropout layer, which are described as follows:

**Input layer:** In this layer, the input signal is fed into the CNN and normalization is performed on the input signal.

**Convolutional layer:** This layer is the most essential layer, which automatically extracts features from the input data using kernels (filters). The kernels are convolved with the input data to produce the feature maps.

**Max-pooling layer:** In this layer, the features are sub-sampled, and only important features are kept, which helps in mitigating over-fitting problems.

**Fully-connected layer:** This layer is actually a conventional MLP which can map the final features to the labeled classes.

**Dropout layer:** This layer can help to prevent overfitting problems and provides a way for testing many different fully-connected architectures effectively by dropping out a portion of the neurons, which means removing all their incoming and outgoing connections [216].

In this study, the CNN with fully connected layers is called CNN-MLP as MLP was employed in the last two final layers. Table 5-1 shows the type of each layer, kernel sizes, activation functions and other parameters of the proposed CNN. Layers 1 to 8 were created by convolution and batch normalization layers with the leaky rectified linear unit (LeakyReLU) as activation function. Subsequently, layers 9 to 13 were constructed by convolutional layers, max-pooling layers with stride 2 and batch normalization layers with LeakyReLU activation. Then, layers 13 to 16 were made by convolution and batch normalization layers with LeakyReLU activation. Finally, a fully-connected layer with 20 neurons, LeakyReLU activation and a dropout layer with a probability of 20%, and a fully-connected layer with two neurons and softmax activation were employed in layer 17 and 18, respectively. At the end, the classification labels of the target and output of CNN are compared, and an error function called the loss function is calculated. In the training phase, the weights and biases are updated by an Adam optimization algorithm [169] to minimize the loss function presented in the later sections. The configuration and layer settings were optimized by testing different filter sizes, numbers and the types of each layer to minimize the loss function using a combined grid search, and trial and error.

**Table 5-1 Detail of CNN-MLP structure**

Layer	Type	Kernel size	Number of kernels or neurons	Other layer parameters
1	Convolution	30	3	Activation=LeakyReLU, stride=1
2	Batch Normalization	-	3	-
3	Convolution	20	3	Activation=LeakyReLU, Stride=1
4	Batch Normalization	-	3	-
5	Convolution	10	5	Activation=LeakyReLU, stride=1
6	Batch Normalization	-	5	-
7	Convolution	7	10	Activation=LeakyReLU, stride=1
8	Batch Normalization	-	10	-
9	Convolution	7	10	Activation=LeakyReLU, stride=2
10	Batch Normalization	-	10	-
11	Convolution	5	10	Activation=LeakyReLU, stride=2
12	Batch Normalization	-	10	-
13	Convolution	3	10	Activation=LeakyReLU, stride=1
14	Batch Normalization	-	10	-
15	Convolution	3	10	Activation=LeakyReLU, stride=1
16	Batch Normalization	-	10	-
17	Fully connected	-	20	Hidden layer activation=Tansig Output layer activation=Softmax
18	Fully connected	-	2	Activation=LeakyReLU, stride=1

### 5.3.3.6 Elman neural network (ENN)

ENNs are similar to feed-forward neural networks, except that the hidden layer has a recurrent connection with a certain delay to each neuron, allowing the network a dynamic response to time dependent input data, which can improve the classification performance [176]. Figure 5-3 shows the architecture of the ENN model including input layer, hidden layer, context layer and output layer. The context layer in ENNs is used to store the output values of the previous hidden layer neurons and feed back to the next moment of the neurons in the hidden layer, which leads to a dynamic ability compared to traditional static networks [176], [217]. The mathematical model of an ENN can be described as follows [176], [217]:

$$y(t) = f(w_2 \cdot x(t) + b_2) \quad (14-5)$$

$$x(t) = g(w_1 \cdot u(t-1) + b_1 + w_c \cdot c(t)) \quad (15-5)$$

$$c(t) = x(t-1) \quad (16-5)$$

where  $w_2$ ,  $w_1$  and  $w_c$  are the connection weights of hidden layer to output layer, input layer to hidden layer, and hidden layer to context layer, respectively.  $b_2$  and  $b_1$  are the bias for output layer and hidden layer.  $y(t)$ ,  $x(t)$  and  $c(t)$  represent the vector of the output layer, hidden layer, and context layer at the moment  $t$ , respectively, and  $u(t-1)$  is the vector of the input layer at the moment  $t-1$ .  $f$  and  $g$  represent the activation function of

the output layer and hidden layer, which were chosen as softmax and hyperbolic tangent sigmoid, respectively.

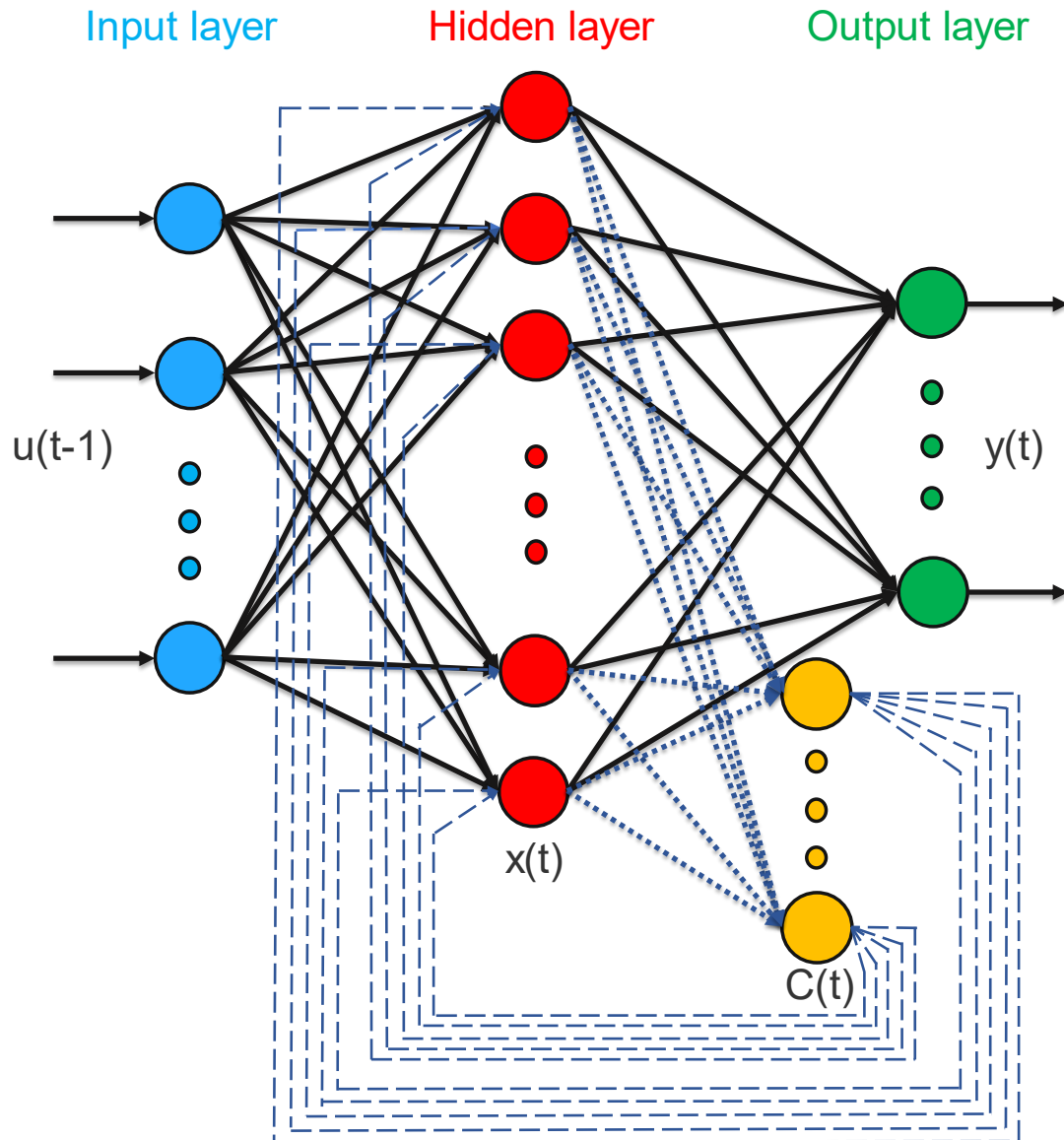


**Figure 5-3 Architecture of the ENN model.**  $u(t-1)$ , which is the vector of the input layer at the moment  $t-1$ , is fed to the input layer,  $x(t)$  and  $c(t)$  represent the vector of hidden layer and context layer at the moment  $t$ , and  $y(t)$  is the vector of output layer at the time  $t$ .

### **5.3.4 The improved Harris Hawks algorithm (HHO+)**

#### **5.3.4.1 Improving exploration and exploitation algorithm (IEEA)**

In the original HHO algorithm, the exploration and exploitation phases were only defined based on the escaping energy of the rabbit. However, this cannot give the whole required information for different attacking strategies on catching a prey as other factors such as velocity of the hawks and rabbit are also very important in each step of the HHO algorithm.

The marine predator algorithm (MPA) [202] is a new metaheuristic algorithm mimicking the whole life of a predator and prey in terms of their velocities. The results showed that MPA is extensively able to explore and exploit the solution space [202]. However, the solutions derived from MPA can be trapped in local optima. Therefore, a new algorithm to improve the global solution and avoid trapping in local optima is presented here, which was inspired from MPA. In the improved exploration and exploitation algorithm (IEEA), some phases of MPA were modified and then combined, and an adaptive decreasing threshold was added to the algorithm, in which all have been determined experimentally. This algorithm mimics the process of hawks hunting a rabbit and the rabbit escaping in terms of their velocities and rapid movements. Accordingly, employing the IEEA can prevent the solutions being trapped into local optima and improve the optimal solution.

The improved exploration and exploitation algorithm includes two sections:  
(1) when the rabbit is escaping equal to or faster than the hawks are moving

and (2) when the hawks are moving faster than the escaping rabbit. The first phase occurs in the initial iteration of optimization, where exploration is more important than exploitation. The second phase happens in the intermediate and last phases of optimization, where the exploration attempts are converted to exploitation gradually or exploitation matters more than exploration.

These two phases are mathematically described as follows

$$X_{t+1} = \begin{cases} X_t + rand \times R_G \times (X_{rabbit,t} - R_G \times X_t) & \text{if } rand < a \\ (X_{rabbit,t} + rand \times R_G \times (R_G \times X_{rabbit,t} - X_t)) & \text{otherwise} \end{cases} \quad (17-5)$$

where  $X_{t+1}$  and  $X_t$  are the position vectors of the hawks in iteration  $t + 1$  and  $t$ , respectively.  $X_{rabbit,t}$  denotes the position of the rabbit (best solution) in iteration  $t$ .  $a$  is an adaptive decreasing threshold for switching between exploration and exploitation algorithms.  $rand$  denotes a uniformly distributed random number in the interval  $(0,1)$  and  $R_G$  is a vector including random numbers based on the zero-mean and unit-variance Gaussian distribution:

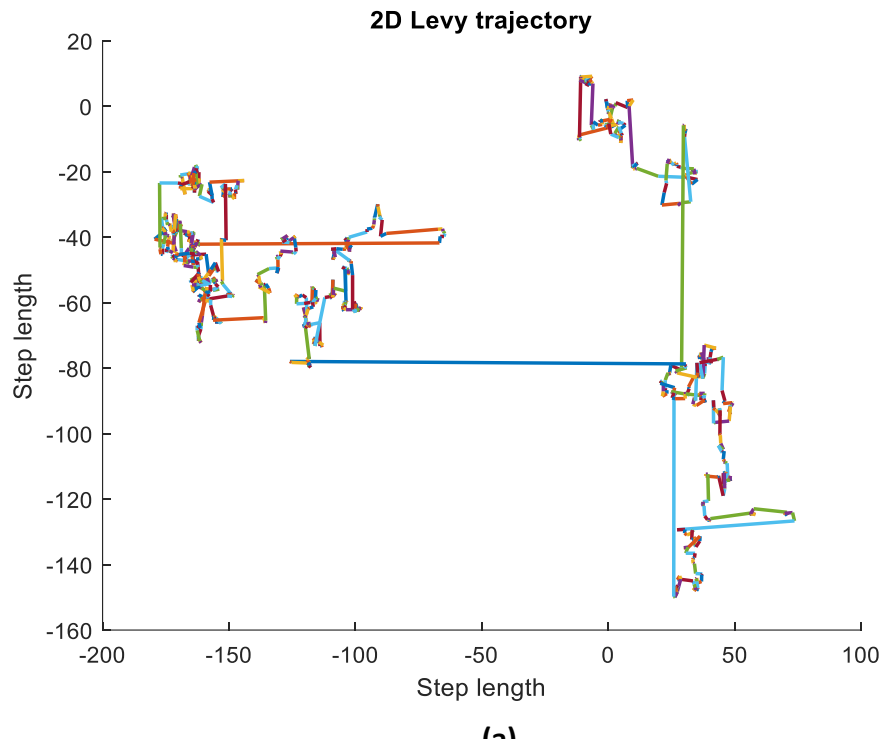
$$R_G(x) = \frac{1}{\sqrt{2\pi\sigma^2}} \exp\left(-\frac{(x-\mu)^2}{2\sigma^2}\right) = \frac{1}{\sqrt{2\pi}} \exp\left(-\frac{x^2}{2}\right) \quad (18-5)$$

$\mu$  and  $\sigma$  denote the mean and variance of the Gaussian distribution, respectively.

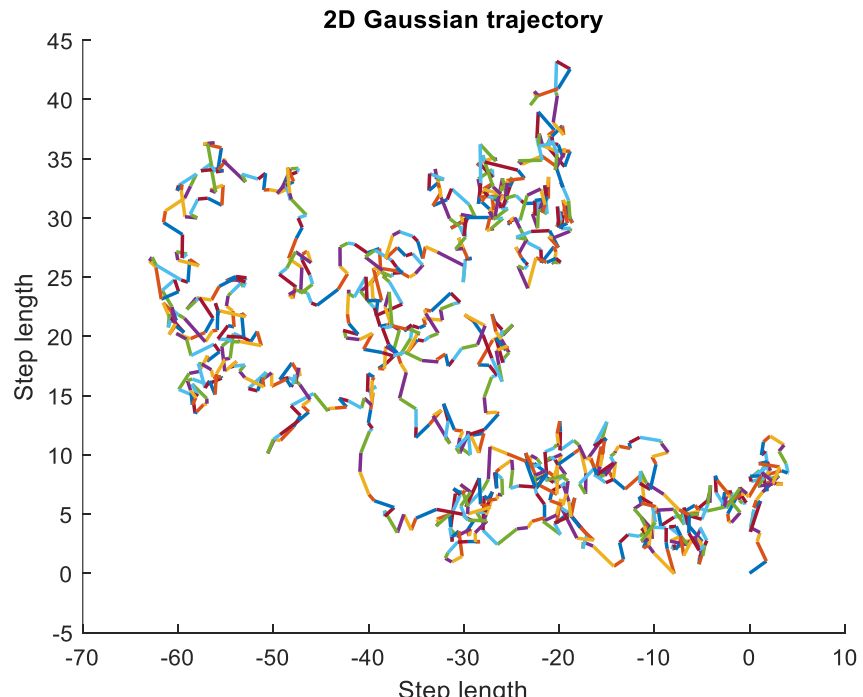
The adaptive decreasing threshold  $a$  is defined as follows:

$$a = \tanh\left(-\left(\frac{t}{T}\right) + 1\right) \quad (19-5)$$

where  $t$  and  $T$  are the current and maximum number of iterations, respectively. A maximum number of iterations is used as the stopping criterion for the HHO+ algorithm. To compare Levy-flight and Gaussian distributions, 2D trajectory of Levy-flight and Gaussian distributions are shown in Figure 5-4a and 5-4b, respectively.



(a)



(b)

**Figure 5-4** 2D trajectory of (a) Levy-flight distribution and (b) Gaussian distribution. Each color shows one step of the distribution.

### 5.3.4.2 Quasi-oppositional based learning (QOBL)

Oppositional based learning (OBL) was originally proposed by Tizhoosh [218], which put forward the concept of an opposite point. Tizhoosh showed that opposite numbers can improve searching ability, solution accuracy and convergence speed of population-based optimization algorithms compared with random numbers [218]. Rahnamayan et al. [219] proposed a new OBL method called quasi-oppositional based learning, which can further improve the solution accuracy for finding the global optimal points, as follows.

Let  $X(x_1, x_2, \dots, x_n)$  be a point,  $X^0(x_1^0, x_2^0, \dots, x_n^0)$  an opposite point, and  $X^{q0}(x_1^{q0}, x_2^{q0}, \dots, x_n^{q0})$  the quasi-opposite point, all in n-dimensional space.  $x_i^0$  and  $x_i^{q0}$  can be defined by as:

$$x_i^0 = a_i + b_i - x_i \quad (20-5)$$

where  $x_i \in R$  and  $x_i \in [a_i, b_i]$ ,  $\forall i \in 1, 2, \dots, n$ .

$$x_i^{q0} = \text{rand}\left(\frac{a_i + b_i}{2}, x_i^0\right) \quad (21-5)$$

If the current solution is far away from the optimal solution, then computing the quasi-oppositional location can result in the opposite direction, which can get closer to the optimal solution. Therefore, employing QOBL algorithm can improve the exploration ability of population-based optimization algorithms and prevent the solutions falling into local optima [220]. The pseudo code of (QOBL) is shown in Algorithm 2.

---

**Algorithm 2** Pseudo code of quasi-oppositional based learning (QOBL)

---

**Inputs:** The population size ( $N$ ), dimension ( $N$ ), lower and upper bounds of search space ( $lb, ub$ ) and current population  $X$

```
for (each population) do
    for (each dimension) do
         $X^0 = lb + up - X$ 
         $C = \frac{lb+up}{2}$ 
        if ( $X < C$ ) then
            |  $X^{q0} = C + (X - C) \times rand$ 
        else
            |  $X^{q0} = X + (C - X) \times rand$ 
        end
    end
end

Return  $X^{q0}$ 
```

---

### 5.3.4.3 The proposed HHO+

The proposed HHO+ is made by combining HHO, IEEA, and QOBL. The pseudo code of HHO+ is given in Algorithm 3. As shown in the pseudo code, first hawk populations are randomly generated. In the second step, the fitness of each hawk is calculated, and the best location of hawks is stored in  $X_{rabbit}$  same as the classical HHO. Then, the locations of hawks are updated based on the values of  $E$  and  $r$  using Eqs. (4-5), (6-5), (10-5) and (11-5). Afterward, IEEA and QOBL are executed and  $X_{rabbit}$  is updated. Finally, the algorithm returns  $X_{rabbit}$  if the current iteration reaches the maximum number of iterations, otherwise the process is repeated.

In the experiments, the proposed HHO+ is compared with some well-known and recent metaheuristic algorithms such as HHO [198], MPA [202], SMA [203], EO [204], SSA [205] and GWO [206]. The average results of the proposed HHO+ and other algorithms are ranked by the non-parametric statistical Friedman and Wilcoxon rank sum test.

**Algorithm 3** Pseudo code of the proposed HHO+ algorithm (The red italic lines show the new added parts of the HHO+ compared to the original HHO method in Algorithm 1)

**Inputs:** The population size N and maximum number of iterations T

Initialize the random hawk populations  $X_i(i = 1, 2, \dots, N)$  in the specific search space

**while** (maximum iteration is not met) **do**

- Calculate the fitness values of hawks
- Set  $X_{rabbit}$  as best solution of hawks
- for** (each hawk ( $X_i$ )) **do**

  - Update the initial energy  $E_0$  and jump strength  $J$
  - Update the  $E$  using Eq. (3-5)
  - if** ( $|E| \geq 1$ ) **then** Exploration phase

    - | Update the hawk vectors using Eq. (1-5)

  - else if** ( $|E| < 1$ ) **then** Exploitation phase

    - if** ( $r \geq 0.5$  and  $|E| \geq 0.5$ ) **then** Soft besiege

      - | Update the hawk vectors using Eq. (4-5)

    - else if** ( $r \geq 0.5$  and  $|E| < 0.5$ ) **then** Hard besiege

      - | Update the hawk vectors using Eq. (6-5)

    - else if** ( $r < 0.5$  and  $|E| \geq 0.5$ ) **then** Soft besiege with PRD

      - | Update the hawk vectors using Eq. (10-5)

    - else if** ( $r < 0.5$  and  $|E| < 0.5$ ) **then** Hard besiege with PRD

      - | Update the hawk vectors using Eq. (11-5)

  - end**

- end**

*Update  $X_{rabbit}$  by the proposed IEEA using Eqs. (17-5), (18-5) and (19-5)*

*Apply QOBL in Algorithm 2 and update  $X_{rabbit}$*

**end**

**end**

**Return** The location of rabbit ( $X_{rabbit}$ ) and its fitness value

### 5.3.5 The proposed fully Elman neural network (FENN)

In the standard ENN, there is only one feedback between the context layer and hidden layer at time  $t$ . This feedback is not able to fully use the long-term, spatial and temporal information of the input and output variables [188]. Accordingly, to improve the performance of the ENN, a fully Elman neural network structure is created in this work, which has connections between two consecutive time points for the output layer, two consecutive time points for the hidden layer, input layer to output layer, and output layer to hidden layer.

Figure 5-5 depicts the architecture of the proposed FENN model. The mathematical model of the FENN is presented as follows:

$$y(t) = f(w_2 x(t) + w_3 u(t-1) + y_{c2}(t) + b_2) \quad (22-5)$$

$$x(t) = g(x_c(t) + w_1 u(t-1) + y_{c1}(t) + b_1) \quad (23-5)$$

$$x_c(t) = w_4 x_c(t-1) + w_5 x(t-1) \quad (24-5)$$

$$y_{c1}(t) = w_6 y_{c1}(t-1) + w_7 y(t-1) \quad (25-5)$$

$$y_{c2}(t) = w_8 y_{c2}(t-1) + w_9 y(t-1) \quad (26-5)$$

where  $w_2$ ,  $w_3$  and  $w_1$  are the connection weights between hidden layer to output layer, input layer to hidden layer, and input layer to hidden layer, respectively.  $y_{c1}(t)$ ,  $y_{c2}(t)$  and  $x_c(t)$  denote the output context layer 1,

output context layer 2 and context layer for hidden layer at  $t$ , respectively.  $b_2$  and  $b_1$  are the bias for output layer and hidden layer.  $w_4, w_6$  and  $w_8$  represent the recurrent connection weights between the moment  $t$  and  $t - 1$  of  $x_c, y_{c1}$  and  $y_{c2}$ , respectively.  $w_5, w_7$  and  $w_9$  indicate the connection weights of  $x(t - 1)$  to  $x_c(t)$ ,  $y(t - 1)$  to  $y_{c1}(t)$ , and  $y(t - 1)$  to  $y_{c2}(t)$ .  $y(t)$  and  $x(t)$  represent the vector of the output layer and hidden layer at  $t$ , respectively, and  $u(t - 1)$  is the vector of the input layer at  $t - 1$ .  $f$  and  $g$  represent the activation function of the output layer and hidden layer, which were chosen as softmax and hyperbolic tangent sigmoid, respectively.

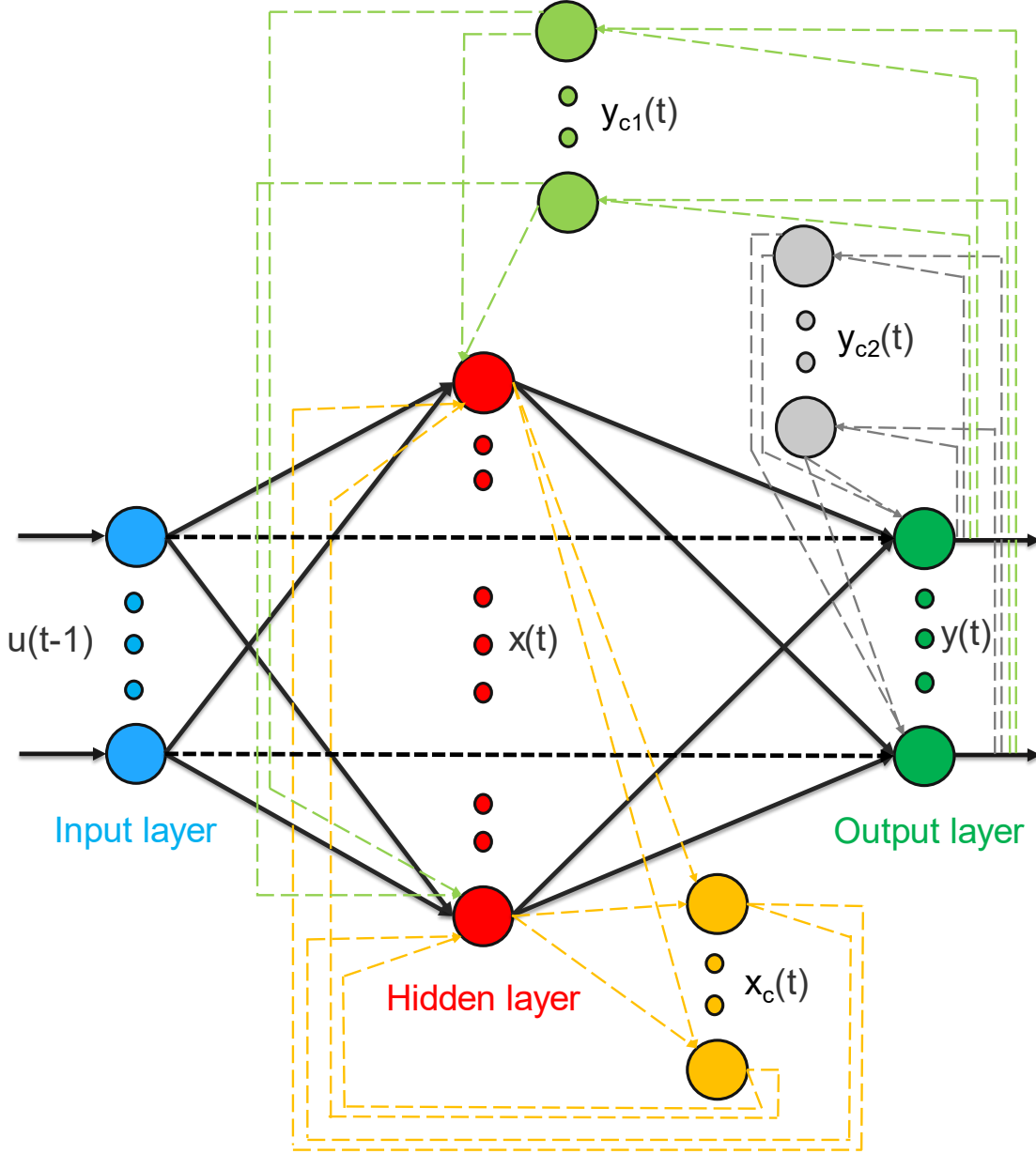


**Figure 5-5 Architecture of the proposed FENN model.**  $u(t-1)$  is the vector of the input layer at the moment  $t-1$ ,  $x(t)$  represents the vector of hidden layer, and  $x_c(t), y_{c1}(t)$  and  $y_{c2}(t)$  represent context layer for hidden layer, output context layer 1 and output context layer 2 at the moment  $t$ , and  $y(t)$  is the vector of output layer at the time  $t$ .

### **5.3.6 The proposed combined CNN with fully Elman neural network (FENN) and improved Harris Hawks optimizer algorithm (CNN-FENN and CNN-FENN-HHO+)**

In this study, a CNN with FENN (CNN-FENN) and CNN with FENN optimized by HHO+ (CNN-FENN-HHO+) are proposed and compared to CNN with MLP (CNN-MLP) for classification of abnormal and normal PAWP using the features from the pump flow signal. All three CNNs are trained and validated with the same patient dataset.

In standard CNNs, a MLP is employed in the final layers to map the features to the labeled classes. However, the combination of CNN with MLP may result in poor classification performance on time-related data [176]. Therefore, in this study, the CNN-MLP in which the last two layers (fully-connected layers) are substituted with a FENN (CNN-FENN), is trained by the Adam algorithm [169] to classify the abnormal and normal PAWP. Figure 5-6 depicts the architecture of the proposed CNN-FENN model.

To further improve the classification performance of CNN-FENN, three parameters of training CNNs, namely initial learning rate (ILR), learning rate drop factor (LRDF), and dropout probability (DP), are optimized by the proposed HHO+. Figure 5-7 shows the flowchart of the proposed CNN-FENN-HHO+ system for classification of the abnormal and normal PAWP. In this hybrid algorithm, first the hawk populations are randomly generated, as in the classical HHO algorithm. Then, the fitness function in Eq. (30-5) is calculated

by training the CNN-FENN and taking the average of the 10 results of training datasets. Afterward, the positions of hawks are updated using the proposed Algorithm 3. Once the current iteration reaches the maximum number of iterations, the found optimal values of ILR, LRDF and DP are fed to the CNN-FENN for validation on the test dataset. The final result is obtained by taking the average of the 10 results of the test dataset through 10-fold cross validation using the optimal parameters found by the proposed HHO+ algorithm.

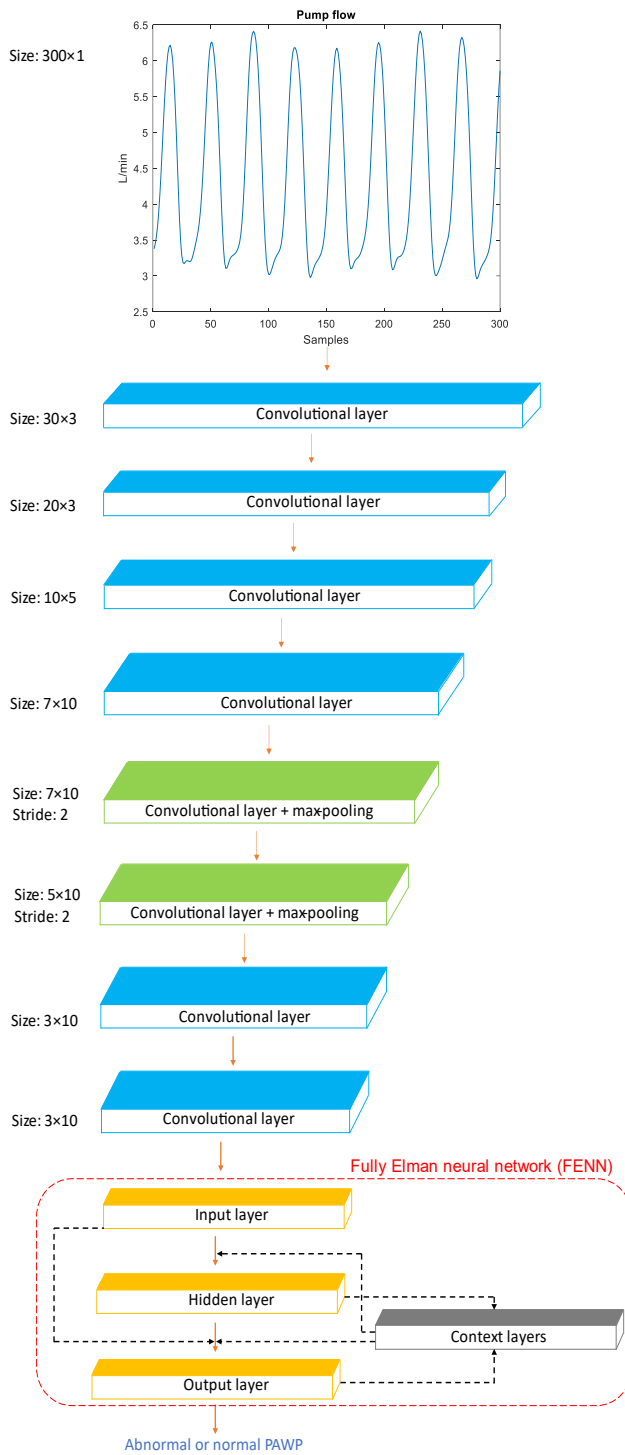


**Figure 5-6 Architecture of the proposed CNN-FENN model for classification of the abnormal and normal PAWP. 300 samples of pump flow signal are fed to the CNN-FENN as input. This is followed by three convolutional layers as well as batch normalization layers. Five convolutional, max-pooling layers with stride 2 and batch normalization layers**

are placed in the subsequent layers. The proposed FENN layer is located in the last layer of the CNN-FENN model to classify the abnormal and normal PAWP.

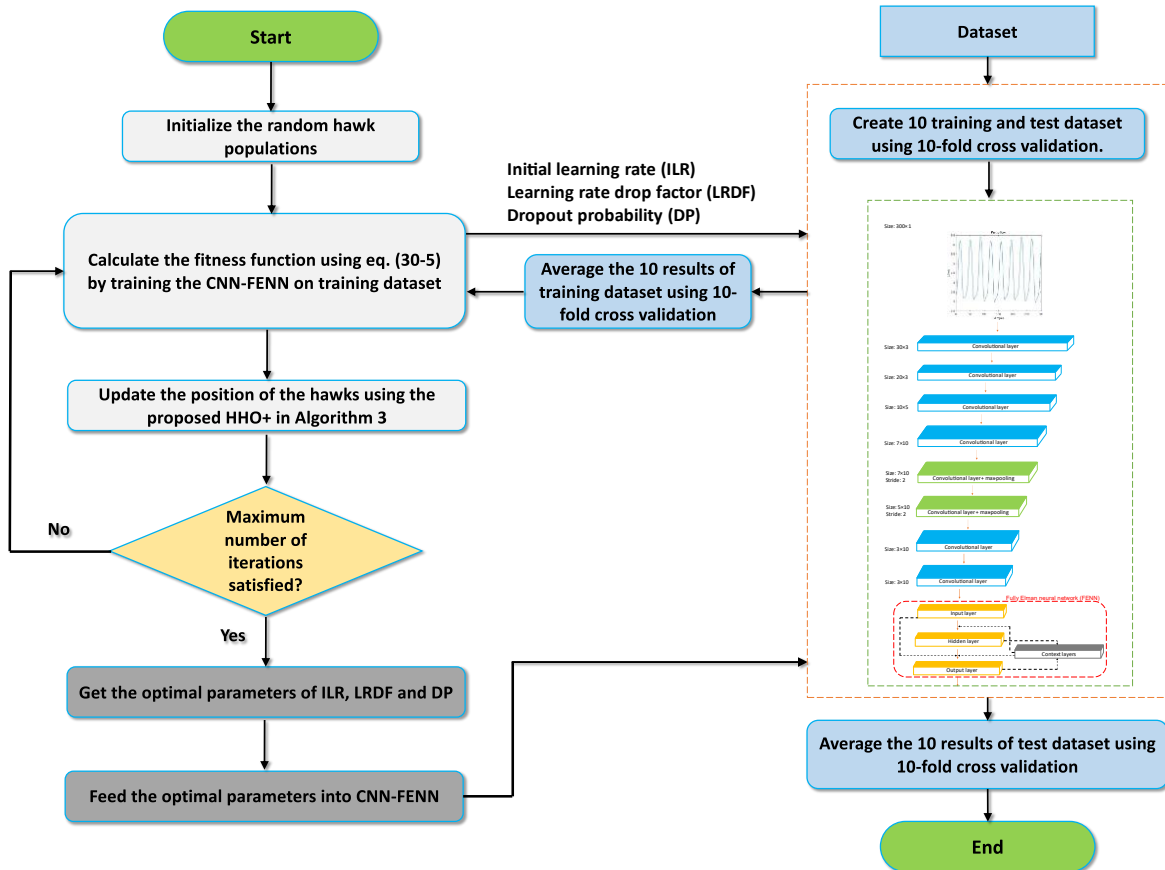


Figure 5-7 Flowchart of the proposed CNN-FENN-HHO+ system.

### 5.3.7 Experimental setup, structure and parameters of HHO+, CNN-FENN and CNN-FENN-HHO+

Table 5-2 shows the parameter settings for the optimization algorithms: HHO [198], MPA [202], SMA [203], EO [204], SSA [205] and GWO [206]. The proposed HHO+ is compared with these algorithms on 24 unimodal and multimodal benchmark optimization functions [206], [221] with the dimension

of 1000. Table 5-3 shows the mathematical equations of these benchmark functions, depicted in Figure 5-8. The population size for all the optimization algorithms and maximum iterations were set to 30 and 500, respectively [198]. All the optimization algorithms were randomly initialized. To increase the robustness of the result due to used random values in the optimization algorithms, each algorithm is initialized and run 30 times.

Table 5-4 represents the type of each layer, kernel sizes, activation functions and other parameters of the proposed CNN-FENN and CNN-FENN-HHO+, respectively. Layers 1 to 8 were created by convolution and batch normalization layers with LeakyReLU activation. Afterwards, layers 9 to 12 were constructed by convolution layers with LeakyReLU activation, max-pooling layers with stride 2 and batch normalization layers. Then, layers 13 to 16 were made by convolution and batch normalization layers with LeakyReLU activation. Finally, a ENN and FENN with 20 neurons in the hidden layer and activation function of hyperbolic tangent sigmoid (Tansig) and two neurons in the output layer with softmax activation were employed in layer 17 and 18 of CNN-FENN and CNN-FENN-HHO+, respectively.

As can be seen from Table 5-1 and Table 5-4 the same convolutional layers, batch normalization layers, size of kernels and activation functions were used for CNN-MLP, CNN-FENN and CNN-FENN-HHO+. The main difference among these methods is the last two layers which are used for classification of the features automatically extracted by the convolutional kernels.

The Adam algorithm was employed to optimize the weights and biases of the proposed CNN-MLP, CNN-FENN and CNN-FENN-HHO+ methods [169]. The algorithm by He was used to initialize the weights for CNN-MLP, CNN-FENN and CNN-FENN-HHO+ as it outperforms the well-known Xavier algorithm [170]. Furthermore, the proposed CNN-MLP, CNN-FENN and CNN-FENN-HHO+ were trained with 1000 iterations and a batch size of 179. This batch size value was set to one tenth of the total number of samples used in this study.

All methods were implemented and run in MATLAB version 2020b (MathWorks, USA) and the experiments were performed on a computer with 16 GB of RAM, Core i7-8700K CPU@3.70 GHz.

**Table 5-2 Parameter settings for the optimization algorithms. All these parameters were taken from the original papers**

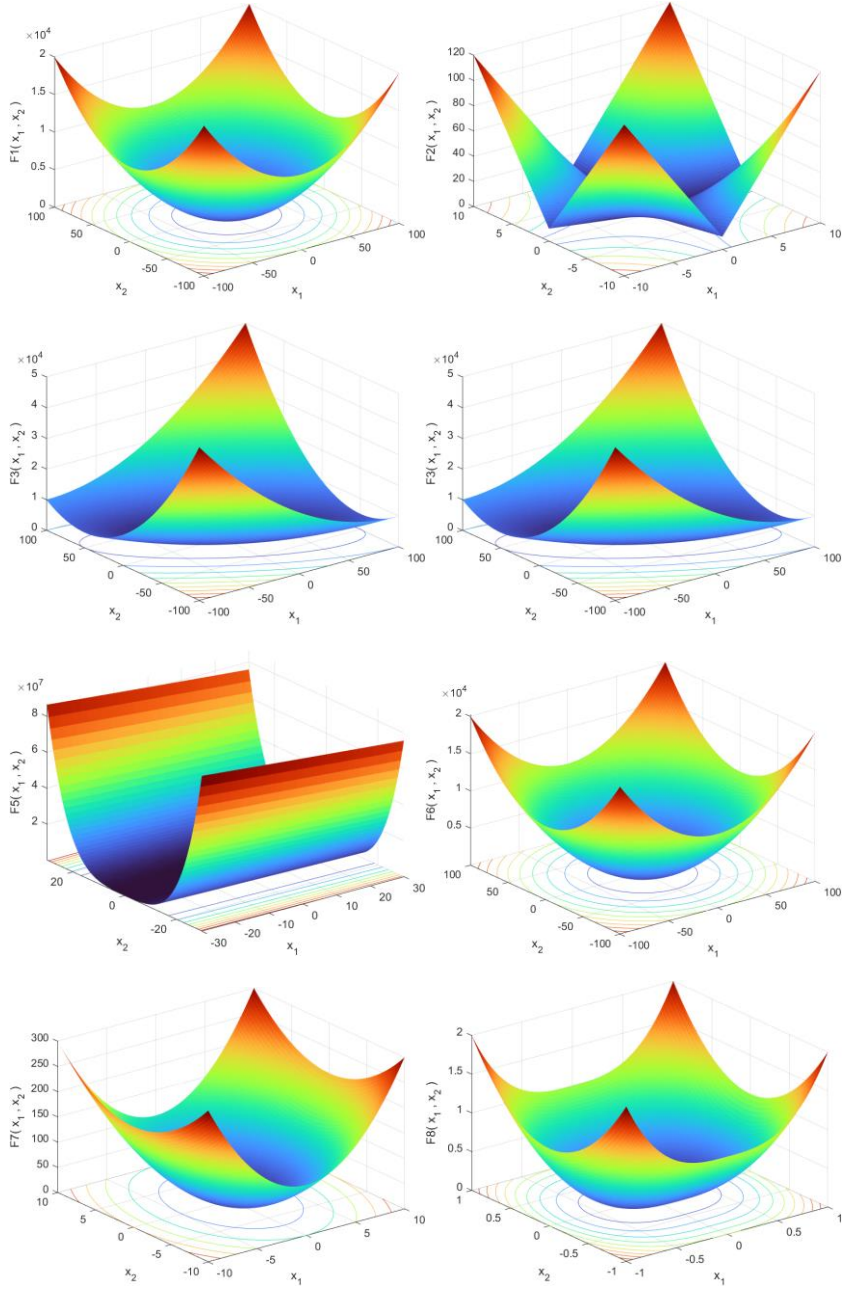
Algorithms	Parameters	Value
HHO	Initial energy of the prey (E0)	In the range of [-1 1]
MPA	Coefficient of stepsize (P)	0.5
SMA	vc	In the decreasing range of [1 0]
	z	0.03
EO	a1	2
	a2	1
GP	GP	0.5
	Leader position update probability	0.5
GWO	Convergence constant (a)	In the decreasing range of [2 0]

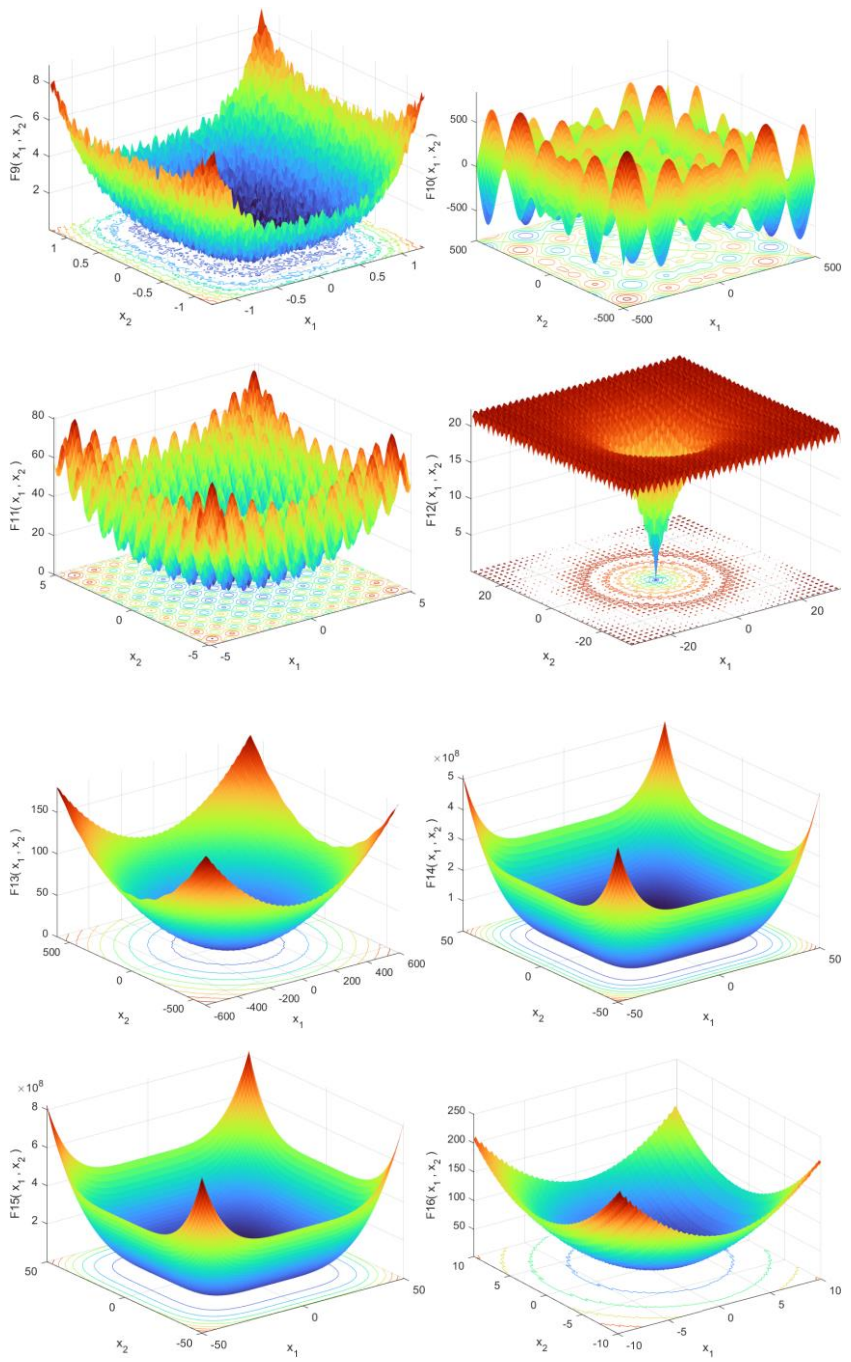
**Table 5-3 Detail of benchmark functions for dimension 1000**

No	Formula of function	Range of search space	Type	$F_{\min}$
F1	$f(x) = \sum_{i=1}^D x_i^2$	[-100,100]	Unimodal	0
F2	$f(x) = \sum_{i=1}^D  x_i  + \prod_{i=1}^D  x_i $	[-10,10]	Unimodal	0
F3	$f(x) = \sum_{i=1}^D \left( \sum_{j=1}^i x_j \right)^2$	[-100,100]	Unimodal	0
F4	$f(x) = \max \{  x_i , 1 \leq i \leq D \}$	[-100,100]	Unimodal	0
F5	$f(x) = \sum_{i=1}^{D-1} 100 (x_{i+1} - x_i^2)^2 + (x_i - 1)^2$	[-30,30]	Unimodal	0
F6	$f(x) = \sum_{i=1}^D ([x_i + 0.5])^2$	[-100,100]	Unimodal	0
F7	$f(x) = \sum_{i=1}^D i x_i^2$	[-10,10]	Unimodal	0
F8	$f(x) = \sum_{i=1}^D  x_i ^{i+1}$	[-1,1]	Unimodal	0
F9	$f(x) = \sum_{i=1}^D i x_i^4 + \text{random}[0,1]$	[-1.28,1.28]	Multimodal	0
F10	$f(x) = \sum_{i=1}^D -x_i \sin(\sqrt{ x_i })$	[-500,500]	Multimodal	.982 xD -418
F11	$f(x) = \sum_{i=1}^D [x_i^2 - 10 \cos(2\pi x_i) + 10]$	[-5.12,5.12]	Multimodal	0

F12	$f(x) = \sum_{i=1}^D -20 \exp(-0.2 \sqrt{\frac{1}{D} \sum_{i=1}^D x_i^2}) \\ - \exp\left(\frac{1}{D} \sum_{i=1}^D \cos(2\pi x_i)\right) + 20 \\ + e$	[-32,32]	Multimodal	0
F13	$f(x) = \frac{1}{4000} \sum_{i=1}^D x_i^2 - \prod_{i=1}^D \cos\left(\frac{x_i}{\sqrt{i}}\right) + 1$	[-600,600]	Multimodal	0
F14	$f(x) = \frac{\pi}{D} \left\{ 10 \sin^2(\pi y_1) \sum_{i=1}^{D-1} (y_i - 1)^2 [1 \\ + 10 \sin^2(\pi y_{i+1})] \\ + (y_D - 1)^2 \right\} \\ + \sum_{i=1}^D u(x_i, 10, 100, 4)$	[-50,50]	Multimodal	0
F15	$y_i = \frac{x_i + 5}{4}$ $u(x_i, a, k, m) = \begin{cases} k(x_i - a)^m, & x_i > a \\ 0, & -a \leq x_i \leq a \\ k(-x_i - a)^m, & x_i < -a \end{cases}$ $f(x) = 0.1 \{ \sin^2(3\pi x_1) \\ + \sum_{i=1}^D (x_i - 1)^2 [1 \\ + \sin^2(1 + 3\pi x_i)] \\ + (x_D - 1)^2 [1 + \sin^2(2\pi x_D)] \} \\ + \sum_{i=1}^D u(x_i, 5, 100, 4)$ $u(x_i, a, k, m) = \begin{cases} k(x_i - a)^m, & x_i > a \\ 0, & -a \leq x_i \leq a \\ k(-x_i - a)^m, & x_i < -a \end{cases}$	[-50,50]	Multimodal	0
F16	$f(x) = \sum_{i=1}^D (x_i - 1)^2 + [1 + \sin^2(3\pi x_i + 1)] \\ + \sin^2(3\pi x_1) +  x_n - 1 (1 + \sin^2(3\pi x_n))$	[-10,10]	Multimodal	0

F17	$f(x) = \sum_{i=1}^D  x_i \sin(x_i) + 0.1x_i $	[-10,10]	Multimodal	0
F18	$f(x) = 0.1D - 0.1 \sum_{i=1}^D \cos(5\pi x_i) - \sum_{i=1}^D x_i^2$	[-1,1]	Multimodal	- 0.8 xD
F19	$f(x) = \sum_{i=1}^D x_i^2 + \left( \sum_{i=1}^D 0.5ix_i \right)^2 \\ + \left( \sum_{i=1}^D 0.5ix_i \right)^4$	[-100,100]	Multimodal	0
F20	$f(x) = \sum_{i=2}^D 0.5 + \frac{\sin^2(\sqrt{100x_{i-1}^2 + x_i^2} - 0.5)}{1 + 0.001(x_i^2 - 2x_{i-1}x_i + x_{i-1}^2)^2}$	[-5,10]	Multimodal	0.49 9 xD
F21	$f(x) = 0.1 \sin^2(3\pi x_1) + \sum_{i=1}^{D-1} (x_i - 1)^2 + \sin^2(3\pi x_i) \\ + (x_D - 1)^2 (1 + \sin^2(3\pi x_D))$	[-5,5]	Multimodal	0
F22	$f(x) = \sum_{i=1}^D (10^6)^{\frac{i-1}{D-1}} x_i^2$	[-100,100]	Multimodal	0
F23	$f(x) = 1 - \cos \left( 2\pi \sqrt{\sum_{i=1}^D x_i^2} \right) + 0.1 \sqrt{\sum_{i=1}^D x_i^2}$	[-100,100]	Multimodal	0
F24	$f(x) = 0.5 + \frac{\sin^2(\sqrt{\sum_{i=1}^D x_i^2}) - 0.5}{(1 + 0.001(\sum_{i=1}^D x_i^2))^2}$	[-100,100]	Multimodal	0





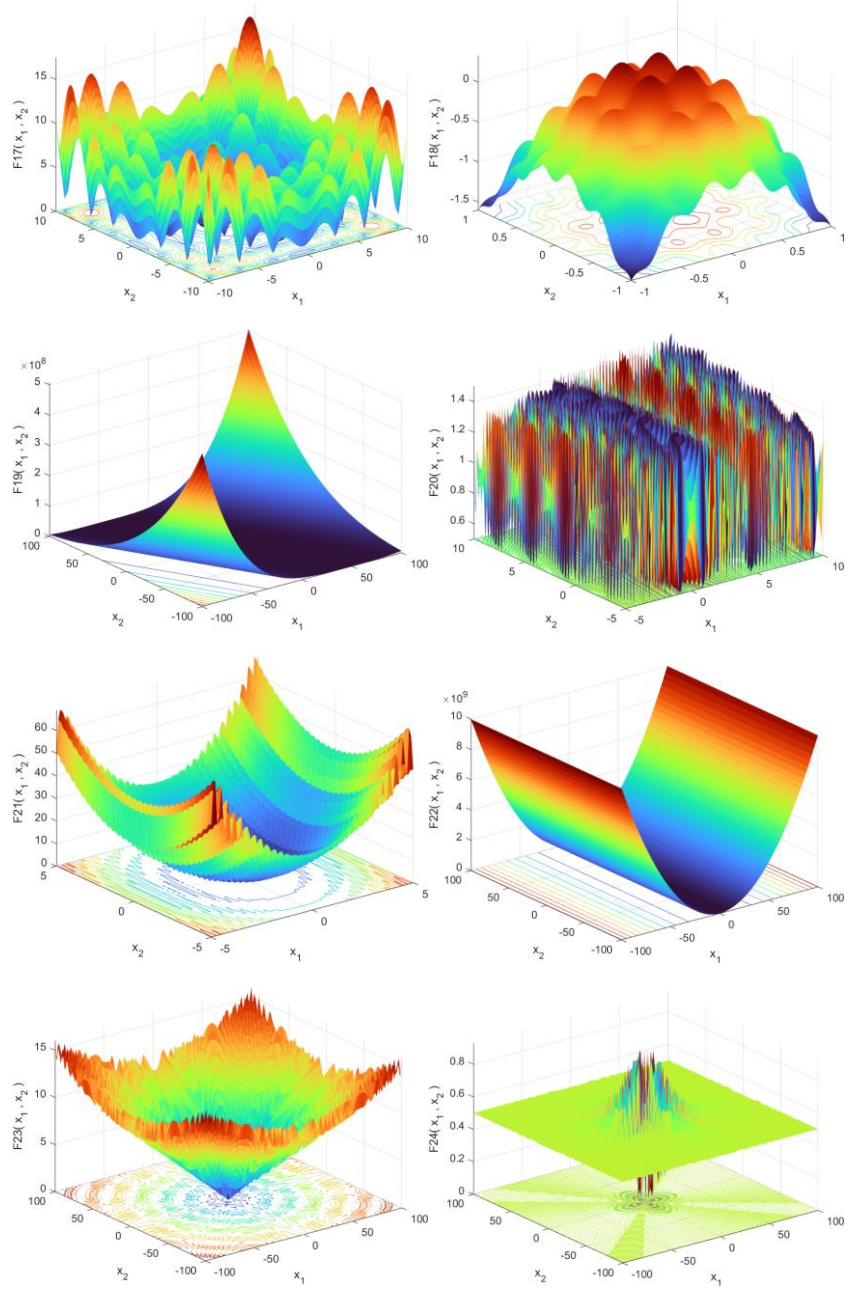


**Figure 5-8 3D demonstration of benchmark functions F1 to F24.**

**Table 5-4 Detail of CNN-ENN and CNN-FENN structures**

Layer	Type	Kernel size	Number of kernels or neurons	Other layer parameters
1	Convolution	30	3	Activation=LeakyReLU, stride=1
2	Batch Normalization	-	3	-
3	Convolution	20	3	Activation=LeakyReLU, stride=1
4	Batch Normalization	-	3	-
5	Convolution	10	5	Activation=LeakyReLU, stride=1
6	Batch Normalization	-	5	-
7	Convolution	7	10	Activation=LeakyReLU, stride=1
8	Batch Normalization	-	10	-
9	Convolution	7	10	Activation=LeakyReLU, stride=2
10	Batch Normalization	-	10	-
11	Convolution	5	10	Activation=LeakyReLU, stride=2
12	Batch Normalization	-	10	-
13	Convolution	3	10	Activation=LeakyReLU, stride=1
14	Batch Normalization	-	10	-
15	Convolution	3	10	Activation=LeakyReLU, stride=1
16	Batch Normalization	-	10	-
17 & 18	ENN or FENN	-	20, 2	Hidden layer activation=Tansig Output layer activation=Softmax

### 5.3.8 Performance evaluation metrics

Three standard performance metrics including accuracy, sensitivity and specificity were used to assess and evaluate the proposed methods:

$$Accuracy = \frac{TP + TN}{TP + FN + TN + FP} \quad (27-5)$$

$$Sensitivity = \frac{TP}{TP + FN} \quad (28-5)$$

$$Specificity = \frac{TN}{TN + FP} \quad (29-5)$$

where true positive (TP) denotes the number of abnormal PAWP classified correctly, true negative (TN) the number of the normal PAWP classified correctly, false positive (FP) indicates the number of normal PAWP classified incorrectly as abnormal PAWP, and false negative (FN) the number of the abnormal PAWP classified incorrectly as normal PAWP.

Accuracy refers to the proposed methods' ability to identify both abnormal and normal PAWP correctly, sensitivity is the proposed methods' ability to correctly detect abnormal PAWP, and specificity refers to the proposed methods' ability to identify the normal PAWP correctly.

### 5.3.9 K-fold stratified cross validation

A 10-fold stratified cross validation [183] was employed to evaluate the ability of the proposed methods to classify abnormal and normal PAWP. Stratified cross validation was chosen due to the imbalanced dataset. It selects an equal

portion of abnormal and normal PAWP for each fold of the dataset. First, the abnormal and normal PAWP samples were partitioned into ten parts, and nine parts of abnormal and normal PAWP samples were used to train the proposed methods and the rest were used for testing. Then, this process was repeated nine times to consider each of the ten folds for testing and the remaining folds for training.

### 5.3.10 Loss function

The classical cross-entropy function is not a suitable loss function due to the imbalanced clinical dataset used in this work. This function may result in high accuracy but very low sensitivity or specificity or will bias toward the majority class. Although it is important that the proposed methods correctly detect abnormal PAWP (high sensitivity), they should also be able to correctly identify normal PAWP (high specificity). The following weighted cross-entropy loss function [222] was employed to train the proposed deep neural networks for classifying abnormal and normal PAWP:

$$\text{Loss Function} = - \sum_{j=1}^K w_j \times T_j \times \log(p_j), \sum_{j=1}^K w_j = 1 \quad (30-5)$$

$$w_j = 1 - \frac{\text{number of samples in the } j^{\text{th}} \text{ class}}{\text{number of total samples}} \quad (31-5)$$

where  $w_j$  is the specific weight assigned to the class  $j$ ,  $K$  is the number of classes,  $T_j$  is the  $j^{\text{th}}$  element of the ground truth (target) vector and  $p_j$  is the  $j^{\text{th}}$  element of the estimated vector.

## 5.4 Results

### 5.4.1 Benchmark function validation

The comparative results of the proposed HHO+ on 24 unimodal and multimodal benchmark optimization functions for dimension 1000 are presented in Table 5-5.

The mean and standard deviation of 30 runs of each HHO+, HHO, MPA, SMA, EO, SSA and GWO algorithm are shown. According to this table, HHO+ achieved the best solutions on all the unimodal and multimodal benchmark optimization functions. As can be observed, the proposed HHO+ achieved an optimal fitness of 0 within 500 iterations with average and standard deviation of 0 in the benchmark functions of F1, F2, F7, F8, F11, F13, F21, F22, F23, and F24.

Table 5-6 shows the comparative statistical results of the Wilcoxon rank sum test and Friedman's test for dimension 1000. According to this table, HHO+ obtained the best average ranking followed by HHO, SMA, MPA, EO, GWO and SSA, respectively. In the table, the signs '+', '=', and '-' indicate that the proposed HHO+ is significantly better than, equal or worse than the other optimization algorithms, respectively. The best results are marked in bold in Table 5-5 and Table 5-6.

Figure 5-9 show convergence curves for F1 to F24, respectively. As can be seen from these figures, the HHO+ convergence curve is better (converges faster) than other optimization algorithms for both unimodal and multimodal

benchmark optimization functions, except F11, F12 and F13, in which the HHO+ is ranked in second place.

Figure 5-10 depicts the scalability results of the proposed HHO+ with different dimensions from 100 to 5000 in logarithm scale for the selected benchmark functions of F5, F6, F9, F15, F16 and F19 as the most challenging (not very close to the global minimum) functions shown in Table 5-5. Figure 5-11 also shows the scalability results of the proposed HHO+ with different dimensions for F16 and F19 in normal scale to show the superiority of HHO+ more clearly. It can be observed from these figures that HHO+ outperforms the other optimization algorithms in both lower and higher dimensional problems.

**Table 5-5 The fitness value of each benchmark function for dimension 1000. Bold indicates the minimum value across all methods**

Fun	Index	HHO+	HHO	MPA	SMA	EO	SSA	GWO
F1	Mean	<b>0</b>	2.34e-94	5.16e-16	2.18e-232	7.01e-21	2.37e+05	2.47e-01
	STD	<b>0</b>	1.26e-93	3.12e-16	0	8.77e-21	1.23e+04	5.63e-02
F2	Mean	<b>8.22e-231</b>	1.80e-49	1.13e+03	1.67e+00	4.79e-13	1.20e+03	6.40e-01
	STD	<b>0</b>	8.12e-49	1.11e+02	6.54e+00	3.35e-13	2.73e+01	3.48e-01
F3	Mean	<b>0</b>	1.48e-22	2.99e+04	3.91e-132	2.48e+05	5.70e+06	1.56e+06
	STD	<b>0</b>	8.13e-22	1.87e+04	2.14e-131	2.35e+05	2.19e+06	3.59e+05
F4	Mean	<b>2.53e-234</b>	1.25e-47	1.84e-04	2.02e-73	7.94e+01	4.39e+01	7.95e+01
	STD	<b>0</b>	6.79e-47	1.27e-04	1.10e-72	1.30e+01	2.79e+00	3.97e+00

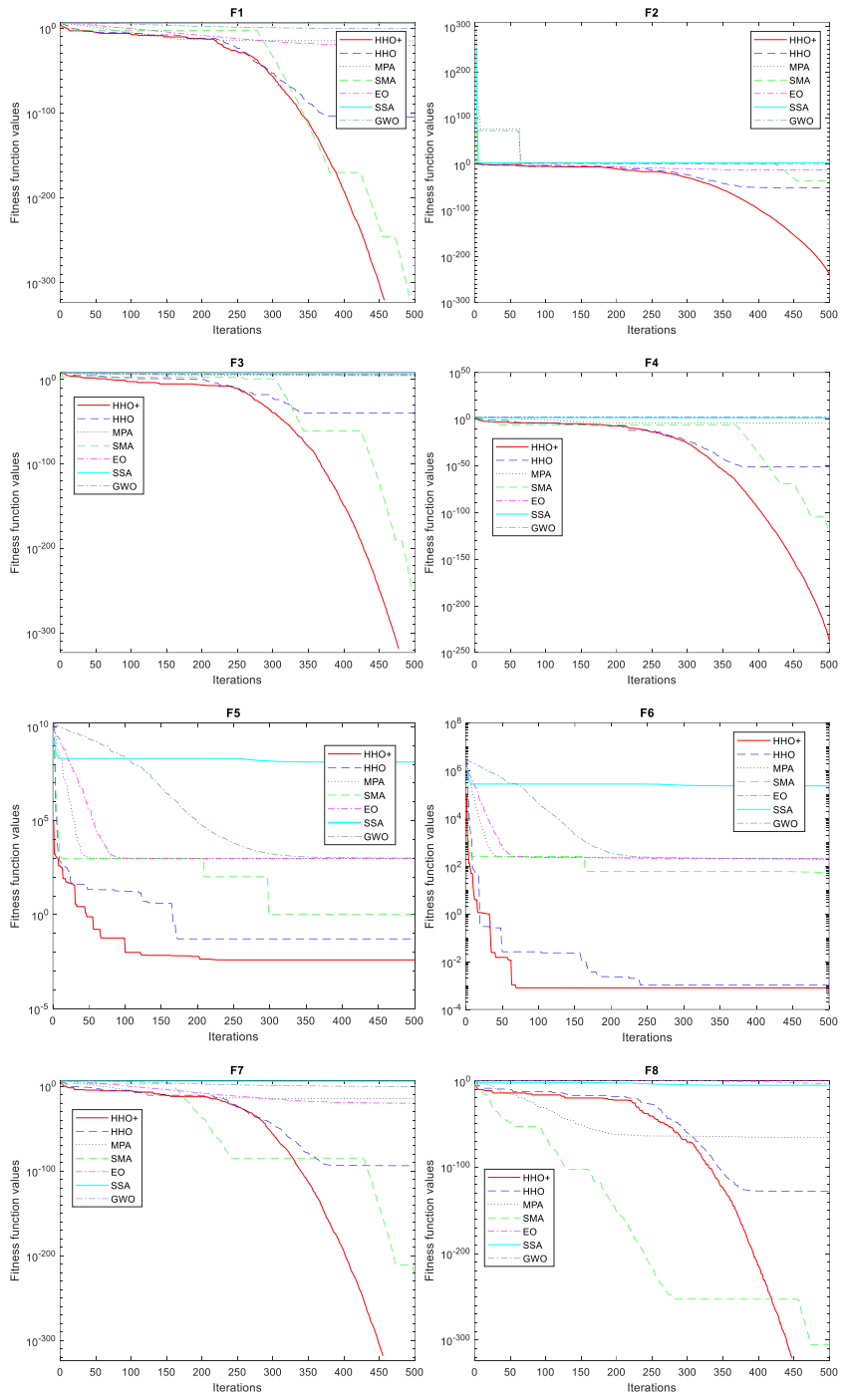
F5	Mean	<b>4.84e-01</b>	5.77e-01	9.96e+02	3.84e+02	9.97e+02	1.18e+08	1.05e+03
	STD	7.75e-01	1.18e+00	<b>1.36e-01</b>	3.99e+02	1.94e-01	1.16e+07	3.04e+01
F6	Mean	<b>4.12e-03</b>	5.00e-03	1.89e+02	5.45e+01	2.06e+02	2.33e+05	2.02e+02
	STD	<b>5.01e-03</b>	7.61e-03	3.30e+00	7.48e+01	2.15e+00	1.05e+04	3.06e+00
F7	Mean	<b>0</b>	7.99e-93	2.75e-15	<sup>9.06e-230</sup>	2.34e-20	1.08e+06	9.86e-01
	STD	<b>0</b>	4.20e-92	2.28e-15	<b>0</b>	4.67e-20	5.42e+04	2.98e-01
F8	Mean	<b>0</b>	<sup>2.28e-121</sup>	4.20e-56	<sup>2.29e-307</sup>	3.70e-01	3.88e-06	7.94e-03
	STD	<b>0</b>	<sup>8.75e-121</sup>	2.26e-55	<b>0</b>	5.88e-01	6.66e-06	2.29e-02
F9	Mean	<b>4.89e-05</b>	1.18e-04	2.36e-03	7.93e-04	5.81e-03	1.74e+03	1.48e-01
	STD	<b>5.27e-05</b>	1.02e-04	1.07e-03	5.53e-04	2.51e-03	1.53e+02	2.91e-02
F10	Mean	-	<b>4.18e+05</b>	<b>4.18e+05</b>	-	-	-	-
	STD	<b>1.22e+01</b>	2.45e+01	3.84e+03	5.56e+02	9.88e+03	7.59e+03	1.39e+04
F11	Mean	<b>0</b>	<b>0</b>	<b>0</b>	<b>0</b>	7.88e-13	7.61e+03	2.21e+02
	STD	<b>0</b>	<b>0</b>	<b>0</b>	<b>0</b>	1.48e-12	1.87e+02	4.59e+01
F12	Mean	<b>8.88e-16</b>	<b>8.88e-16</b>	8.74e-10	<b>8.88e-16</b>	2.26e-12	1.45e+01	1.80e-02
	STD	<b>0</b>	<b>0</b>	3.05e-10	<b>0</b>	1.86e-12	1.67e-01	2.40e-03
F13	Mean	<b>0</b>	<b>0</b>	4.07e-17	<b>0</b>	1.55e-16	2.14e+03	4.97e-02
	STD	<b>0</b>	<b>0</b>	5.44e-17	<b>0</b>	5.53e-17	9.36e+01	7.46e-02
F14	Mean	<b>1.77e-06</b>	2.45e-06	6.49e-01	1.20e-02	8.16e-01	1.14e+07	1.27e+00
	STD	<b>1.80e-06</b>	2.75e-06	2.01e-02	2.15e-02	1.74e-02	3.50e+06	3.38e-01
F15	Mean	<b>5.25e-04</b>	9.10e-04	9.86e+01	2.23e+00	9.93e+01	1.47e+08	1.22e+02

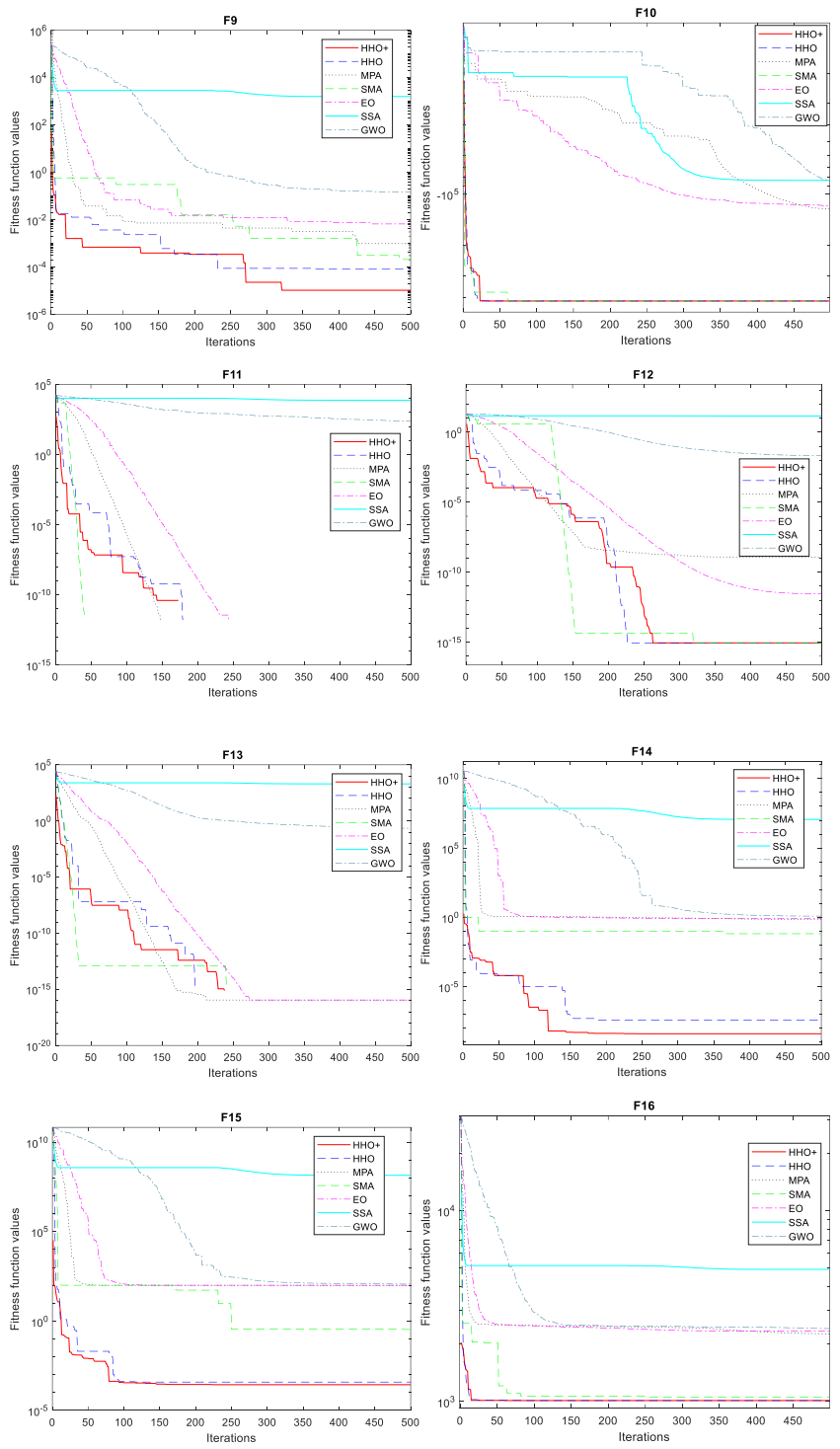
	STD	<b>7.05e-04</b>	1.42e-03	2.72e-01	3.26e+00	2.11e-01	1.88e+07	1.00e+01
F16	Mean	<b>1.01e+03</b>	1.01e+03	2.22e+03	1.05e+03	2.33e+03	4.98e+03	2.42e+03
	STD	1.13e+00	<b>4.84e-01</b>	2.03e+01	4.80e+01	1.66e+01	1.55e+02	1.16e+01
F17	Mean	<b>2.71e-233</b>	3.69e-05	1.77e-10	2.18e-70	1.14e-13	7.27e+02	8.21e-01
	STD	<b>0</b>	2.02e-04	1.38e-10	1.19e-69	7.39e-14	2.42e+01	8.11e-01
F18	Mean	-	<b>8.00e+02</b>	<b>8.00e+02</b>	<b>8.00e+02</b>	-	7.97e+02	5.46e+02
	STD	<b>0</b>	<b>0</b>	<b>0</b>	3.91e+00	1.11e+00	3.95e+00	3.28e+00
F19	Mean	<b>8.91e+04</b>	2.18e+06	9.78e+04	5.93e+06	2.47e+06	3.45e+06	2.06e+06
	STD	3.23e+05	1.41e+06	<b>1.15e+04</b>	1.95e+06	7.40e+05	1.50e+06	1.73e+05
F20	Mean	<b>4.99e+02</b>	<b>4.99e+02</b>	8.03e+02	<b>4.99e+02</b>	9.00e+02	8.30e+02	9.40e+02
	STD	1.25e-01	1.34e-02	5.99e+00	<b>2.81e-02</b>	6.84e+01	6.27e+00	3.37e+00
F21	Mean	<b>0</b>	4.44e-94	9.67e-17	<b>3.60e-226</b>	2.00e-21	1.05e+03	1.31e+01
	STD	<b>0</b>	1.75e-93	1.07e-16	<b>0</b>	6.88e-21	4.14e+01	2.15e+00
F22	Mean	<b>0</b>	4.77e-85	7.44e-12	<b>9.50e-107</b>	4.69e-17	7.00e+09	6.42e+02
	STD	<b>0</b>	2.61e-84	4.74e-12	<b>5.20e-106</b>	7.91e-17	6.56e+08	1.73e+02
F23	Mean	<b>0</b>	9.74e-45	2.03e-01	1.39e-57	2.36e-01	5.31e+01	1.96e+00
	STD	<b>0</b>	5.33e-44	1.82e-02	7.64e-57	4.90e-02	1.08e+00	1.46e-01
F24	Mean	<b>0</b>	<b>0</b>	3.72e-02	<b>0</b>	7.13e-02	4.99e-01	4.77e-01
	STD	<b>0</b>	<b>0</b>	6.33e-17	<b>0</b>	1.55e-02	8.93e-07	5.49e-03

**Table 5-6 Statistical results of Wilcoxon rank sum test and Friedman's test for dimension 1000. NaN refers to not a number showing all the elements of two compared vectors using Wilcoxon rank sum test are equal to zero.**

Fun	HHO+	HHO	MPA	SMA	EO	SSA	GWO
F1	-	1.21e-12	1.21e-12	1.27e-05	1.21e-12	1.21e-12	1.21e-12
F2	-	3.02e-11	3.02e-11	3.02e-11	3.02e-11	3.02e-11	3.02e-11
F3	-	1.21e-12	1.21e-12	6.25e-10	1.21e-12	1.21e-12	1.21e-12
F4	-	3.02e-11	3.02e-11	5.57e-10	3.02e-11	3.02e-11	3.02e-11
F5	-	7.96e-01	3.02e-11	9.92e-11	3.02e-11	3.02e-11	3.02e-11
F6	-	7.28e-01	3.02e-11	8.10e-10	3.02e-11	3.02e-11	3.02e-11
F7	-	1.21e-12	1.21e-12	2.93e-05	1.21e-12	1.21e-12	1.21e-12
F8	-	1.21e-12	1.21e-12	3.34e-01	1.21e-12	1.21e-12	1.21e-12
F9	-	9.03e-04	3.02e-11	6.70e-11	3.02e-11	3.02e-11	3.02e-11
F10	-	1.26e-01	3.02e-11	1.44e-03	3.02e-11	3.02e-11	3.02e-11
F11	-	NaN	NaN	NaN	5.51e-03	1.21e-12	1.21e-12
F12	-	NaN	1.21e-12	NaN	1.21e-12	1.21e-12	1.21e-12
F13	-	NaN	2.85e-04	NaN	4.17e-13	1.21e-12	1.21e-12
F14	-	5.20e-01	3.02e-11	3.82e-10	3.02e-11	3.02e-11	3.02e-11
F15	-	7.28e-01	3.02e-11	3.02e-11	3.02e-11	3.02e-11	3.02e-11
F16	-	1.05e-01	3.02e-11	1.86e-09	3.02e-11	3.02e-11	3.02e-11
F17	-	3.02e-11	3.02e-11	3.02e-11	3.02e-11	3.02e-11	3.02e-11

F18	-	NaN	NaN	1.21e-12	1.21e-12	1.21e-12	1.21e-12
F19	-	3.50e-09	1.86e-06	2.61e-10	4.08e-11	4.08e-11	3.02e-11
F20	-	4.04e-01	3.02e-11	5.49e-01	3.02e-11	3.02e-11	3.02e-11
F21	-	1.21e-12	1.21e-12	1.37e-03	1.21e-12	1.21e-12	1.21e-12
F22	-	1.21e-12	1.21e-12	4.57e-12	1.21e-12	1.21e-12	1.21e-12
F23	-	1.21e-12	1.06e-12	1.21e-12	9.56e-13	1.21e-12	1.21e-12
F24	-	NaN	8.93e-13	NaN	1.14e-12	1.19e-12	1.21e-12
Winner (+) / equal (=) / loser (-)	-	12/12/0	22/2/0	18/6/0	24/0/0	24/0/0	24/0/0
Friedman mean rank	<b>1.52</b>	<b>2.41</b>	<b>4.11</b>	<b>2.64</b>	<b>4.70</b>	<b>6.62</b>	<b>5.98</b>
Rank	<b>1</b>	<b>2</b>	<b>4</b>	<b>3</b>	<b>5</b>	<b>7</b>	<b>6</b>





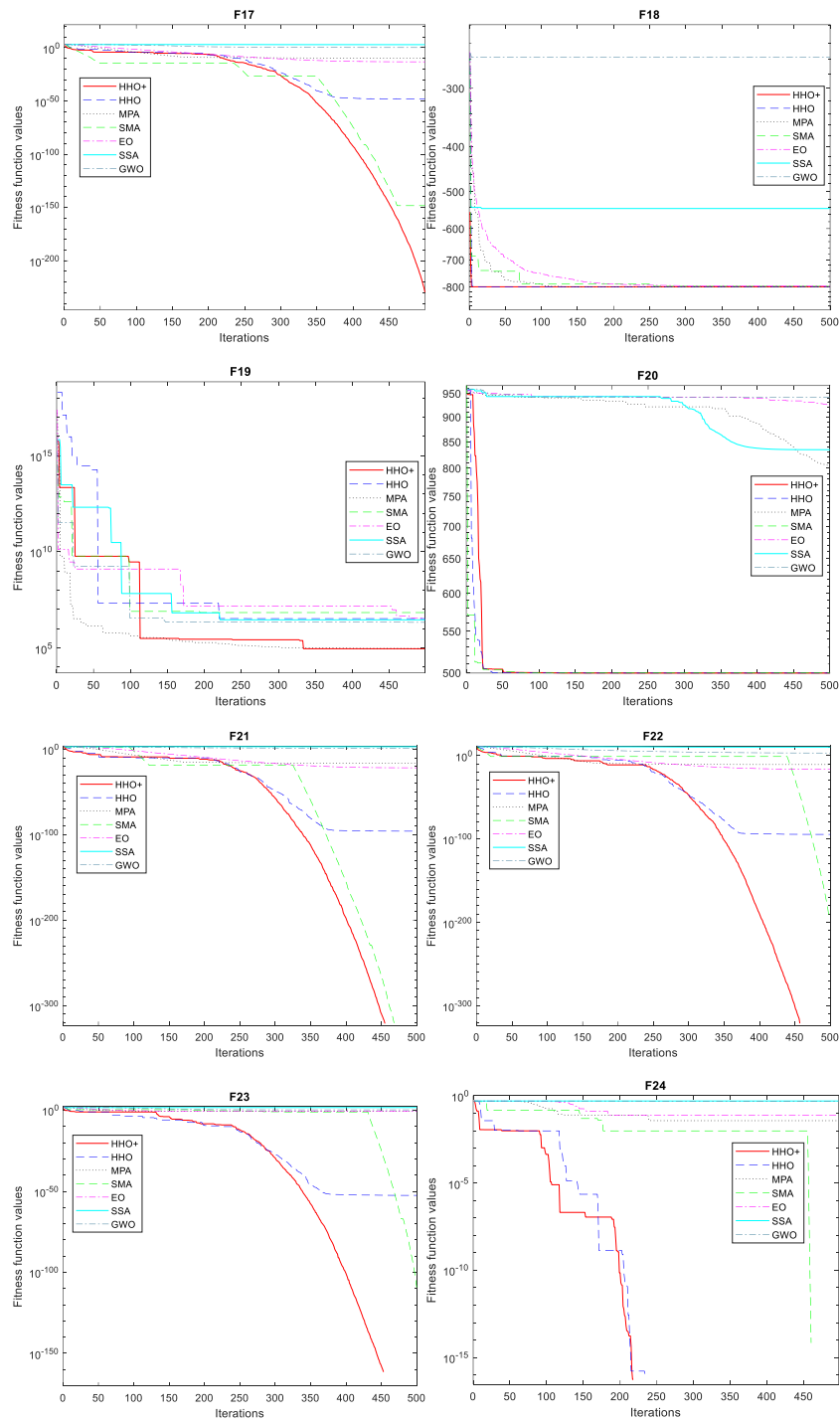


**Figure 5-9 Convergence curves for F1 to F24.**

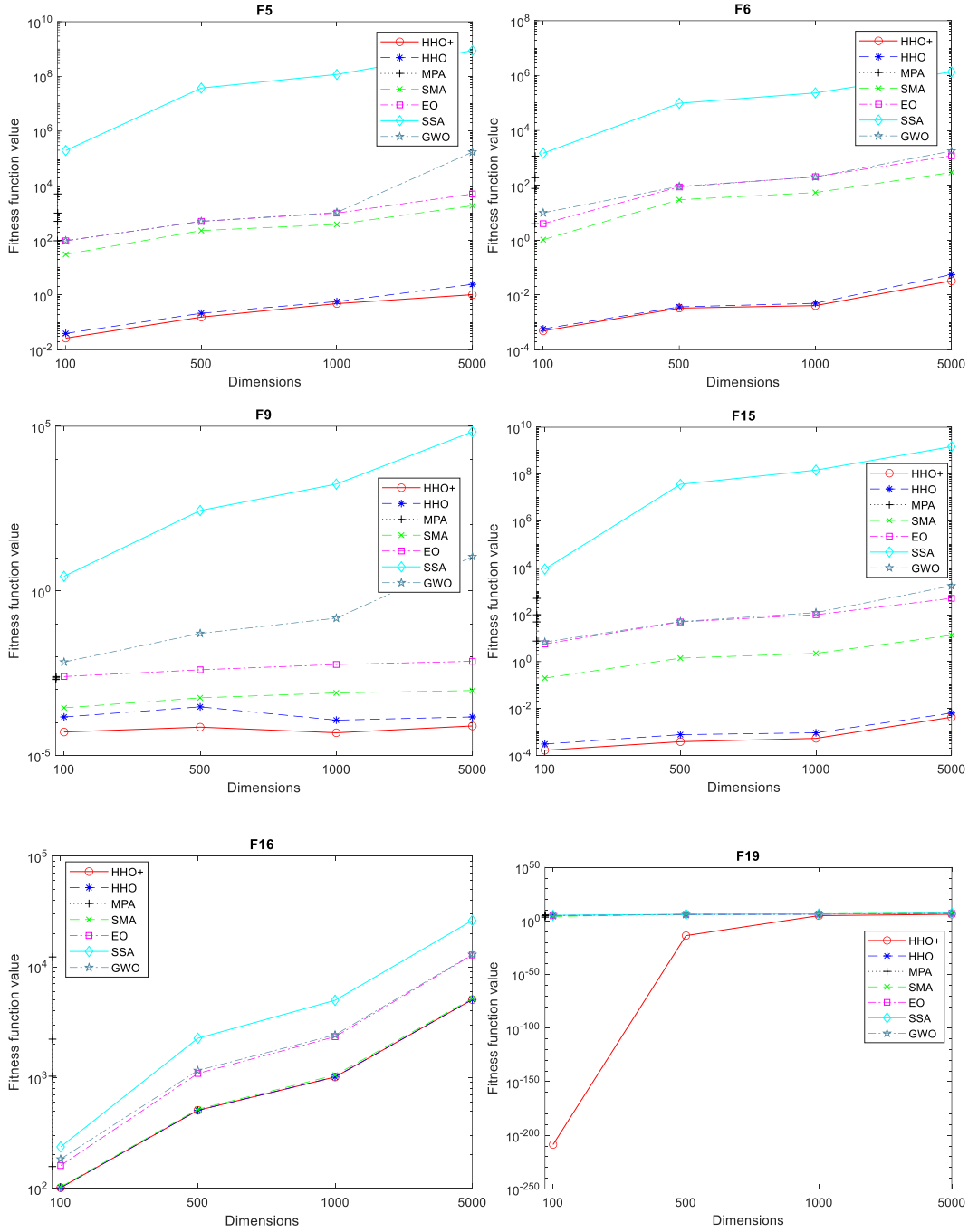


**Figure 5-10 Scalability results of the proposed HHO+ with different dimensions.**

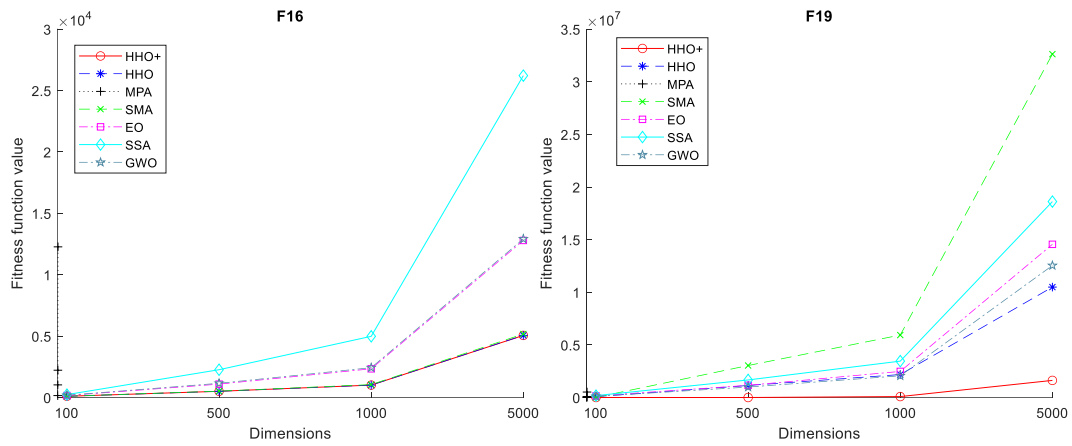


**Figure 5-11 Scalability results of the proposed HHO+ with different dimensions for F16 and F19 (normal scale).**

## **5.4.2 Application of the proposed FENN and HHO+ on the classification of pulmonary arterial wedge pressure**

The average classification results of PAWP across 10-fold cross validation are presented in Table 5-7. The results show that the proposed CNN-FENN-HHO+ outperforms CNN-MLP and CNN-FENN methods.

**Table 5-7 The comparison of performances of the proposed classification methods across 10-fold cross-validation**

<b>Methodology</b>	<b>Network structure</b>	<b>Accuracy (%)</b>	<b>Sensitivity (%)</b>	<b>Specificity (%)</b>
CNN-MLP	CNN+MLP	85.07	87.12	79.13
CNN-ENN	CNN+ENN	86.19	88.32	80.00
CNN-FENN	CNN+FENN	87.30	88.62	83.47
<b>CNN-FENN-HHO+</b>	<b>CNN+FENN</b>	<b>88.86</b>	<b>89.82</b>	<b>86.08</b>

## **5.5 Discussion**

In this work, an improved HHO (HHO+) algorithm was proposed by combination of HHO, IEEA and QOBL algorithms, being validated on 24 unimodal and multimodal benchmark functions. It can be seen from Table 5-6 that HHO+ outperformed HHO, MPA, SMA, EO, SSA, GWO in 12, 22, 18, 24, 24, 24 benchmark functions, respectively, for a p-value of less than 0.05. Although

the HHO+ achieved better results than the other optimization methods for the majority of the benchmark functions, this merit was not statistically significant for the rest of the functions. The proposed IEEA and employed QOBL concepts generate a set of solutions that can improve the convergence rate and global solution. Accordingly, stagnation in HHO can be avoided more efficiently. The average and standard deviation of 0 in the benchmark functions of F1, F3, F7, F8, F11, F13, F21, F22, F23 and F24 indicate the robustness of the proposed HHO+ on both unimodal and multimodal benchmark functions. Overall, the experimental and statistical (Friedman mean rank and Wilcoxon rank tests) analyzes from Table 5-5 and Table 5-6 showed the superiority of the proposed HHO+ over the classical HHO and other state-of-the-art algorithms to find the global optima. Figure 5-10 and Figure 5-11 demonstrate that the performance of HHO+ remains consistently superior even in high-dimensional problems, while the performance of other methods is degraded by increasing dimensions.

A novel Elman neural network called FENN was proposed to improve the classification performance for the considered problem. Moreover, the proposed HHO+ was employed to optimize the three hyper-parameters of CNN-FENN called ILR, LRDF and DP for classification of abnormal and normal PAWP. Four 18-layer deep learning methods called CNN-MLP, CNN-ENN, CNN-FENN and CNN-FENN-HHO+ for classification of abnormal and normal PAWP using pump flow were developed and compared. The results shown in Table 5-7 indicate that the proposed CNN-FENN-HHO+ method improves accuracy

and specificity, and outperforms the proposed CNN-MLP, CNN-ENN and CNN-FENN methods.

An imbalanced clinical dataset was used in this study for classification of abnormal and normal PAWP. An imbalanced training dataset can impede the convergence of the training process by biasing the training algorithm toward the majority class. Furthermore, it may affect the generalizability of the proposed methods and the performance on the test dataset. Although data augmentation strategies such as oversampling and down-sampling can balance the samples of the classes, they are prone to cause overfitting or losing useful information [223], [224]. Therefore, in this work, the weighted loss function was proposed to overcome the problem.

Lai et al. [23] employed multiple linear regression to estimate PAWP using the slope of the HVAD flow waveform at diastole for HF patients. However, the method resulted in poor  $r^2$  of 0.54. Furthermore, the ability of the slope of the HVAD flow waveform at diastole to discriminate PAWP  $\geq 20$  mmHg (high PAWP) was evaluated by sensitivity and specificity. The results showed a sensitivity of 77% and specificity of 86% for identifying high PAWP. However, in our study, both low and high PAWP were set to abnormal PAWP and the rest as normal. In addition, it is not clear how much data was used for training, validation, and testing which can change the results significantly.

Estimation of high PAWP (PAWP  $\geq 18$  mmHg) using the slope of the ventricular filling phase based on 15 HVAD patients was proposed by Grinstein [139]. Although here, too, it is not clear how much data was used for training,

validation and testing, the results derived from multivariable regression demonstrated a sensitivity of 87% and specificity of 95% for only high PAWP. However, in our work, both low and high PAWP was set to abnormal PAWP and 10-fold cross-validation on 25 HVAD patients was used to assess the results. Imamura et al. [22] employed the slope of the ventricular filling phase to estimate high PAWP ( $\text{PAWP} \geq 18 \text{ mmHg}$ ) using a linear regression. The results show a sensitivity and specificity of 91.5% and 95.2% to predict only high PAWP, respectively.

The accuracy, sensitivity and specificity of the proposed method can still be improved by using a more sophisticated neural network for mapping the final features derived by CNN filters to the labeled classes. Furthermore, the performance of deep networks may be improved by using larger training datasets. The relatively small clinical dataset used in this study may have limited the performance of the compared network. Accordingly, future work will include testing other neural networks architectures and collecting additional clinical data for training them.

## 5.6 Conclusion

A novel improved HHO (HHO+) algorithm was proposed by combination of HHO, IEEA and QOBL algorithms, which is validated for optimization of 24 unimodal and multimodal benchmark functions. Furthermore, a novel Elman neural network called FENN was proposed to improve the performance metrics of classification problems. The proposed HHO+ was employed to optimize the three hyper-parameters of CNN-FENN called ILR, LRDF and DP.

Furthermore, four 18-layer deep learning methods called CNN-MLP, CNN-ENN, CNN-FENN and CNN-FENN-HHO+ for classification of abnormal and normal PAWP using pump flow were developed and compared. The proposed methods were evaluated on an imbalanced clinical dataset using 10-fold cross-validation. Useful features were automatically extracted from the low-pass filtered pump flow signal by convolutional filters. The results demonstrated that the combination of CNN, FNN and HHO+ for classification of abnormal and normal PAWP improved the classification performance. The classification of PAWP based on the pump flow signal can be used to adjust the pump speed in real-time and therefore reduce the likelihood of hazardous events like pulmonary congestion and ventricular suction for HF patients. Furthermore, the proposed method can be implemented on a mobile software platform and report the identified abnormal cases to the hospital, which can decrease the mortality rate of HF patients.

## **5.7 Acknowledgement**

The authors would like to recognize the financial assistance provided by the National Health and Medical Research Council Centers for Research Excellence grant (APP1079421).

In the next chapter, we summarize the conclusions from all chapters, discuss the limitations of this research and recommend areas of future work.

## **Chapter 6. Conclusion, limitations and future work**

## 6.1 Conclusions

The aim of this thesis was to design, develop and evaluate novel methods for estimation of preload and sensorless physiological control systems for LVADs than can accommodate interpatient and intrapatient variations. To meet this thesis aim, three main objectives were proposed as follows:

1. Design a physiological control system for an implantable heart pump that accommodates for interpatient and intrapatient variations.
2. Design a sensorless physiological control system for LVADs across different patient conditions.
3. Design an improved non-invasive preload estimator using advanced machine and deep learning methods based on the pump variables and test on a clinical dataset.

With respect to the first objective, a physiological control system for an implantable heart pump that accommodates interpatient and intrapatient variations was designed. A novel adaptive physiological control system was developed that maintained the LVEDP in the normal range of 3 to 15 mmHg to prevent ventricular suction and pulmonary congestion, using a new algorithm to detect LVEDP from pressure sensor measurement in real-time. MFAC was employed to control the pump speed and provide consistent control performance regardless of the patient condition. This control system was evaluated via simulation of 100 different patient conditions in six different patient scenarios and compared to standard PID control. The results show that the control performance can be robust across different patients and

conditions when using MFAC over PID control. However, this control system relies on the implantation of a left ventricular pressure sensor. This limitation is overcome in the next objective by proposing new methods for estimation of preload in real-time.

With respect to the second objective, a novel real-time deep CNN for estimation of preload based on the LVAD flow was proposed. A new sensorless adaptive physiological control system for an LVAD pump was developed using the full dynamic form of model free adaptive control and the proposed preload estimator to maintain the patient conditions in safe physiological ranges. The CNN model for preload estimation was trained and evaluated through 10-fold cross validation on 100 different simulated patient conditions and the proposed sensorless control system was assessed on a new testing set of 30 different patient conditions across six different patient scenarios. The results showed that the proposed preload estimator was extremely accurate and the proposed sensorless physiological controller works similarly to the preload-based physiological control system for LVADs using measured preload to prevent ventricular suction and pulmonary congestion. Furthermore, the results showed that the proposed sensorless adaptive physiological control system can respond appropriately to changing patient states and physiological demands without the need for additional pressure or flow measurements. However, the proposed method was only tested in-silico. Therefore, this method should be validated using in-vitro, in-vivo and clinical datasets. This limitation is overcome in the next objective by proposing advanced deep learning methods for estimation of preload on a clinical dataset.

With respect to the third objective, first an improved Harris Hawks optimizer algorithm was proposed and tested on 24 unimodal and multimodal benchmark functions. Second, a novel fully Elman neural network was proposed to improve the classification performance. Finally, four novel 18-layer deep learning methods comprising of a CNN with a multi-layer perceptron (CNN-MLP), a CNN with Elman neural networks (CNN-ENN), a CNN with fully Elman neural networks (CNN-FENN), and a CNN with fully Elman neural networks optimized by HHO+ algorithm (CNN-FENN-HHO+) were developed and evaluated for classification of abnormal and normal PAWP. The proposed methods were evaluated on an imbalanced clinical dataset across 10-fold cross-validation. The proposed CNN-FENN-HHO+ method outperforms the proposed CNN-MLP, CNN-ENN and CNN-FENN methods and improved the classification performance metrics across 10-fold cross-validation. The proposed methods can reduce the likelihood of hazardous events like pulmonary congestion and ventricular suction for HF patients and notify identified abnormal cases to the hospital, clinician and cardiologist for emergency action, which can decrease the mortality rate of HF patients.

## 6.2 Thesis limitations

The limitations of this study can be summarized as follows:

1. The baroreflex effect was not considered in this study which may influence CVS hemodynamics and therefore control performance.

2. The proposed preload estimator in this study is based on an ideal pump flow estimator. However, there are no perfect pump estimators. This might have degraded the preload estimator performance.
3. Although most physiological control systems for LVADs are evaluated through in-vitro studies, this study was only performed using numerical models of the CVS and LVAD. The advantage of this approach however is that a huge number of simulations can be done for validation of the proposed methods.
4. A small clinical dataset (25 patients' data) for training and validation of preload estimator using deep learning methods was employed in this study. By increasing the number of patients to many hundred, the performance of the proposed preload estimator can be better assessed and improved.

### **6.3 Future work**

The suggested future work can be summarized as follows:

1. Validation of the proposed preload estimator and the sensorless physiological controller via in-vitro and in-vivo experiments.
2. Long-term simulation of the proposed sensorless control system on patients with an implanted LVAD over the course of years.
3. Developing an adaptive target for LVEDP that considers both arterial pressure and flow rate.
4. Adding pathological states to the numerical heart failure model.

## References

- [1] M. A. Simon, J. Watson, J. T. Baldwin, W. R. Wagner, and H. S. Borovetz, “Current and future considerations in the use of mechanical circulatory support devices,” *Annu. Rev. Biomed. Eng.*, vol. 10, no. 1, pp. 59–84, 2019, doi: 10.1146/annurev.bioeng.9.060906.151856.
- [2] W. R. Adams, “Cardiovascular disease.,” *Aust. Inst. Heal. Welfare, Canberra*, 2019.
- [3] S. S. Virani *et al.*, *Heart disease and stroke statistics—2020 update: A report from the American Heart Association*. 2020.
- [4] “Disease expenditure in Australia,” (AIHW), *Aust. Inst. Heal. Welf.*
- [5] A. W. Cai, S. Islam, S. R. Hankins, W. Fischer, and H. J. Eisen, “Mechanical circulatory support in the treatment of advanced heart failure,” *Am. J. Transplant.*, vol. 17, no. 12, pp. 3020–3032, 2017, doi: 10.1111/ajt.14403.
- [6] “Australian donation and transplantation reports,” *Aust. Gov. (Organ Tissue Authority)*, 2019.
- [7] M. C. Stevens, “Automatic control of dual LVADs as a BiVAD,” The University of Queensland, 2014.
- [8] E. A. Rose *et al.*, “Long-term use of a left ventricular assist device,” *N. Engl. J. Med.*, vol. 345, no. 20, pp. 1435–1443, 2001, doi: 10.1056/NEJMoa012175.
- [9] J. P. Pauls, “Development of a passive control system for ventricular assist devices,” Griffith University, 2017.

- [10] S. D. Gregory, M. C. Stevens, and J. F. Fraser, *Mechanical circulatory and respiratory support*. Academic Press, 2017.
- [11] A. Shiose, K. Nowak, D. J. Horvath, A. L. Massiello, L. A. R. Golding, and K. Fukamachi, “Speed modulation of the continuous-flow total artificial heart to simulate a physiologic arterial pressure waveform,” *ASAIO J.*, vol. 56, no. 5, pp. 403–409, 2010, doi: 10.1097/MAT.0b013e3181e650f8.
- [12] M. C. Stevens, S. Wilson, A. Bradley, J. Fraser, and D. Timms, “Physiological control of dual rotary pumps as a biventricular assist device using a master/slave approach,” *Artif. Organs*, vol. 38, no. 9, pp. 766–774, 2014, doi: 10.1111/aor.12303.
- [13] J. P. Pauls, M. C. Stevens, N. Bartnikowski, J. F. Fraser, S. D. Gregory, and G. Tansley, “Evaluation of physiological control systems for rotary left ventricular assist devices: An in-vitro study,” *Ann. Biomed. Eng.*, vol. 44, no. 8, pp. 2377–2387, 2016, doi: 10.1007/s10439-016-1552-3.
- [14] E. Bullister, S. Reich, and J. Sluetz, “Physiologic control algorithms for rotary blood pumps using pressure sensor input,” *Artif Organs*, vol. 26, no. 11, pp. 931–938, 2002.
- [15] N. R. Gaddum *et al.*, “Starling-like flow control of a left ventricular assist device: In vitro validation,” *Artif. Organs*, vol. 38, no. 3, 2014, doi: 10.1111/aor.12221.
- [16] M. Mansouri *et al.*, “Preload-based Starling-like control of rotary blood pumps: An in-vitro evaluation,” *PLoS One*, vol. 12, no. 2, pp. 1–15, 2017, doi: 10.1371/journal.pone.0172393.
- [17] B. C. Ng *et al.*, “Application of multiobjective neural predictive control to

- biventricular assistance using dual rotary blood pumps," *Biomed. Signal Process. Control.*, vol. 39, pp. 81–93, 2018, doi: 10.1016/j.bspc.2017.07.028.
- [18] M. Stevens, P. Jain, S. Shehab, D. Vickers, P. MacDonald, and C. Hayward, "Estimation of preload using an implantable left ventricular assist device," *Hear. Lung Circ.*, vol. 27, pp. S367–S368, 2018, doi: 10.1016/j.hlc.2018.06.728.
- [19] A.-H. H. AlOmari *et al.*, "Developments in control systems for rotary left ventricular assist devices for heart failure patients: a review.,," *Physiol. Meas.*, vol. 34, no. 1, pp. R1-27, 2013, doi: 10.1088/0967-3334/34/1/R1.
- [20] C. Reyes *et al.*, "Accuracy of the HVAD pump flow estimation algorithm," *ASAIO J.*, vol. 62, no. 1, pp. 15–19, 2015, doi: 10.1097/MAT.0000000000000295.
- [21] J. Grinstein *et al.*, "HVAD waveform analysis as a noninvasive marker of pulmonary capillary wedge pressure: a first step toward the development of a smart left ventricular sssist device pump," *ASAIO J.*, vol. 64, no. 1, pp. 10–15, 2018, doi: 10.1097/MAT.0000000000000604.
- [22] T. Imamura *et al.*, "HVAD flow waveform estimates left ventricular filling pressure," *J. Card. Fail.*, vol. 26, no. 4, pp. 342–348, 2020, doi: 10.1016/j.cardfail.2020.01.012.
- [23] J. V. Lai, K. Muthiah, P. S. Macdonald, P. Jansz, and C. S. Hayward, "Estimation of left ventricular assist device pre-load using pump flow waveform analysis," *J. Hear. Lung Transplant.*, vol. 36, no. 2, pp. 240–242, 2017, doi: 10.1016/j.healun.2016.10.015.

- [24] M. H. Meki, Y. Wang, P. Sethu, M. Ghazal, A. El-Baz, and G. A. Giridharan, “A sensorless rotational speed-based control system for continuous flow left ventricular assist devices,” *IEEE Trans. Biomed. Eng.*, vol. 64, no. 4, pp. 1050–1060, 2020, doi: 10.1109/TBME.2019.2928826.
- [25] A. C. Guyton and J. E. Hall, *Textbook of Medical Physiology*. 2006.
- [26] “Circulatory System,” <http://flipper.diff.org/app/items/info/879>.
- [27] A. Petrou, “Intelligent rotary blood pumps with physiological response,” ETH Zurich, 2018.
- [28] M. Fetanat, M. Stevens, and N. Lovell, “Physiological control system for an LVAD that can accommodate interpatient and intrapatient variation,” *Artif. Organs*, vol. 43, no. 9, p. E198, 2019, doi: 10.1111/aor.13530 A.
- [29] M. Fetanat, M. Stevens, C. Hayward, and N. H. Lovell, “A physiological control system for an implantable heart pump that accommodates for interpatient and intrapatient variations,” *IEEE Trans. Biomed. Eng.*, vol. 67, no. 4, pp. 1167–1175, 2020, doi: 10.1109/tbme.2019.2932233.
- [30] C. A. Thunberg, B. D. Gaitan, F. A. Arabia, D. J. Cole, and A. M. Grigore, “Ventricular assist devices today and tomorrow,” *J. Cardiothorac. Vasc. Anesth.*, vol. 24, no. 4, pp. 656–680, 2010, doi: 10.1053/j.jvca.2009.11.011.
- [31] R. Krishnamani, D. Denofrio, and M. A. Konstam, “Emerging ventricular assist devices for long-term cardiac support,” *Nat. Rev. Cardiol.*, vol. 7, no. 2, pp. 71–76, 2010, doi: 10.1038/nrcardio.2009.222.
- [32] V. Tchantchaleishvili, F. Sagebin, R. E. Ross, W. Hallinan, K. Q. Schwarz, and H. T. Massey, “Evaluation and treatment of pump thrombosis and

- hemolysis.," *Ann. Cardiothorac. Surg.*, vol. 3, no. 5, pp. 490–495, 2014, doi: 10.3978/j.issn.2225-319X.2014.09.01.
- [33] N. Moazami *et al.*, "Axial and centrifugal continuous-flow rotary pumps: A translation from pump mechanics to clinical practice," *J. Heart. Lung Transplant.*, vol. 32, no. 1, pp. 1–11, 2013, doi: 10.1016/j.healun.2012.10.001.
- [34] M. Ketelhut, S. Stemmler, J. Gesenhues, M. Hein, and D. Abel, "Iterative learning control of ventricular assist devices with variable cycle durations," *Control Eng. Pract.*, vol. 83, no. October 2018, pp. 33–44, 2019, doi: 10.1016/j.conengprac.2018.10.012.
- [35] R. Amacher *et al.*, "Numerical optimal control of turbo dynamic ventricular assist devices," *Bioengineering*, vol. 1, no. 1, pp. 22–46, 2014, doi: 10.3390/bioengineering1010022.
- [36] Y. Wang, S. C. Koenig, Z. Wu, M. S. Slaughter, and G. A. Giridharan, "Sensor-based physiologic control strategy for biventricular support with rotary blood pumps," *ASAIO J.*, vol. 64, no. 3, pp. 338–350, 2018, doi: 10.1097/MAT.0000000000000671.
- [37] Y. Wang, S. C. Koenig, Z. J. Wu, M. S. Slaughter, and G. A. Giridharan, "Sensorless physiologic control, suction prevention, and flow balancing algorithm for rotary biventricular assist devices," *IEEE Trans. Control Syst. Technol.*, vol. 27, no. 2, pp. 717–729, 2019, doi: 10.1109/TCST.2017.2773518.
- [38] V. C. A. Koh *et al.*, "A centralized multi-objective model predictive control for a biventricular assist device: An in silico evaluation," *Biomed. Signal*

*Process. Control*, vol. 49, pp. 137–148, 2019, doi: 10.1016/j.bspc.2018.10.021.

- [39] Y. Wang, S. C. Koenig, M. S. Slaughter, and G. A. Giridharan, “Rotary blood pump control strategy for preventing left ventricular suction,” *ASAIO J.*, vol. 61, no. 1, pp. 21–30, 2015, doi: 10.1097/MAT.0000000000000152.
- [40] Y. Wu, P. E. Allaire, and T. Gang, “Modeling, estimation, and control of human circulatory system with a left ventricular assist device,” *IEEE Trans Control Syst Technol.*, vol. 15, no. 4, pp. 754–767, 2007.
- [41] M. Ketelhut *et al.*, “Iterative learning control of a left ventricular assist device,” *IFAC-Papers OnLine*, vol. 50, no. 1, pp. 6684–6690, 2017, doi: 10.1016/j.ifacol.2017.08.1161.
- [42] M. A. Simaan, A. Ferreira, S. Chen, J. F. Antaki, and D. G. Galati, “A dynamical state space representation and performance analysis of a feedback-controlled rotary left ventricular assist device,” *IEEE Trans Control Syst Technol.*, vol. 17, no. 1, pp. 15–28, 2009, doi: 10.1109/TCST.2008.912123.
- [43] V. C. A. Koh, E. Lim, B. C. Ng, Y. K. Ho, and N. H. Lovell, “A simplified state-space model of biventricular assist device-cardiovascular system interaction,” *Proc. Annu. Int. Conf. IEEE Eng. Med. Biol. Soc. EMBS*, vol. 2016-Octob, pp. 4317–4320, 2016, doi: 10.1109/EMBC.2016.7591682.
- [44] E. Lim *et al.*, “Parameter-optimized model of cardiovascular-rotary blood pump interactions.,” *IEEE Trans. Biomed. Eng.*, vol. 57, no. 2, pp. 254–266, 2010, doi: 10.1109/TBME.2009.2031629.
- [45] E. Lim, S. Dokos, R. F. Salamonsen, F. L. Rosenfeldt, P. J. Ayre, and N. H.

- Lovell, "Numerical optimization studies of cardiovascular-rotary blood pump interaction," *Artif. Organs*, vol. 36, no. 5, pp. E110–E124, 2012, doi: 10.1111/j.1525-1594.2012.01449.x.
- [46] D. L. Timms, S. D. Gregory, N. A. Greatrex, M. J. Pearcy, J. F. Fraser, and U. Steinseifer, "A compact mock circulation loop for the in vitro testing of cardiovascular devices," *Artif. Organs*, vol. 35, no. 4, pp. 384–391, 2011, doi: 10.1111/j.1525-1594.2010.01088.x.
- [47] S. D. Gregory, M. C. Stevens, E. Wu, J. F. Fraser, and D. Timms, "In vitro evaluation of aortic insufficiency with a rotary left ventricular assist device," *Artif. Organs*, vol. 37, no. 9, pp. 802–809, 2013, doi: 10.1111/aor.12143.
- [48] A. Stephens, S. Gregory, G. Tansley, A. Busch, and R. Salamonsen, "In vitro evaluation of an adaptive Starling-like controller for dual rotary ventricular assist devices," *Artif. Organs*, no. January, pp. 1–14, 2019, doi: 10.1111/aor.13510.
- [49] V. C. A. Koh *et al.*, "A centralized multi-objective model predictive control for a biventricular assist device: An in vitro evaluation," *Biomed. Signal Process. Control*, vol. 59, 2020, doi: 10.1016/j.bspc.2020.101914.
- [50] E. Wu *et al.*, "A Starling-like total work controller for rotary blood pumps: An in vitro evaluation," *Artif. Organs*, vol. 44, no. 3, pp. E40–E53, 2020, doi: 10.1111/aor.13570.
- [51] N. R. Gaddum *et al.*, "Starling-like flow control of a left ventricular assist device: In vitro validation," *Artif. Organs*, vol. 38, no. 3, 2014, doi: 10.1111/aor.12221.

- [52] A. F. Stephens, M. C. Stevens, S. D. Gregory, M. Kleinheyer, and R. F. Salamonsen, “In vitro evaluation of an immediate response Starling-like controller for dual rotary blood pumps,” *Artif. Organs*, vol. 00, no. 00, 2017, doi: 10.1111/aor.12962.
- [53] T. Leao, B. Utiyama, J. Fonseca, E. Bock, and A. Andrade, “In vitro evaluation of multi-objective physiological control of the centrifugal blood pump,” *Artif. Organs*, no. January, pp. 1–12, 2020, doi: 10.1111/aor.13639.
- [54] J. P. Pauls *et al.*, “In vitro comparison of active and passive physiological control systems for biventricular assist devices,” *Ann. Biomed. Eng.*, vol. 44, no. 5, pp. 1370–1380, 2016, doi: 10.1007/s10439-015-1425-1.
- [55] A. Petrou, M. Monn, M. Meboldt, and M. Schmid Daners, “A novel multi-objective physiological control system for rotary left ventricular assist devices,” *Ann. Biomed. Eng.*, vol. 45, no. 12, pp. 2899–2910, 2017, doi: 10.1007/s10439-017-1919-0.
- [56] K. W. Gwak *et al.*, “In vitro evaluation of multiobjective hemodynamic control of a heart-assist pump,” *ASAIO J.*, vol. 51, no. 4, pp. 329–335, 2005, doi: 10.1097/01.mat.0000169122.64794.28.
- [57] S. D. Gregory, M. Stevens, D. Timms, and M. Pearcy, “Replication of the Frank-starling response in a mock circulation loop,” *Proc. Annu. Int. Conf. IEEE Eng. Med. Biol. Soc. EMBS*, pp. 6825–6828, 2011, doi: 10.1109/IEMBS.2011.6091683.
- [58] S. D. Gregory *et al.*, “In vivo evaluation of active and passive physiological control systems for rotary left and right ventricular assist devices,” *Artif.*

- Organs*, vol. 40, no. 9, pp. 894–903, 2016, doi: 10.1111/aor.12654.
- [59] M. C. Stevens *et al.*, “In vitro and in vivo characterization of three different modes of pump operation when using a left ventricular assist device as a right ventricular assist device,” *Artif. Organs*, vol. 38, no. 11, pp. 931–939, 2014, doi: 10.1111/aor.12289.
- [60] G. Ochsner *et al.*, “In vivo evaluation of physiologic control algorithms for left ventricular assist devices based on left ventricular volume or pressure,” *ASAIO J.*, vol. 63, no. 5, pp. 568–577, 2017, doi: 10.1097/MAT.0000000000000533.
- [61] V. Koh, “A centralized multi-objective model predictive control for a biventricular assist device,” University of Malaya, 2019.
- [62] M. Vollkron, H. Schima, L. Huber, R. Benkowski, G. Morello, and G. Wieselthaler, “Development of a reliable automatic speed control system for rotary blood pumps,” *J. Hear. Lung Transplant.*, vol. 24, no. 11, pp. 1878–1885, 2005, doi: 10.1016/j.healun.2005.02.004.
- [63] H. Schima *et al.*, “First clinical experience with an automatic control system for rotary blood pumps during ergometry and right-heart catheterization,” *J. Hear. Lung Transplant.*, vol. 25, no. 2, pp. 167–173, 2006, doi: 10.1016/j.healun.2005.09.008.
- [64] R. F. Salamonsen, D. G. Mason, and P. J. Ayre, “Response of rotary blood pumps to changes in preload and afterload at a fixed speed setting are unphysiological when compared with the natural heart,” *Artif. Organs*, vol. 35, no. 3, 2011, doi: 10.1111/j.1525-1594.2010.01168.x.
- [65] K. Fukamachi *et al.*, “Preload sensitivity in cardiac assist devices,” *Ann.*

*Thorac. Surg.*, vol. 95, no. 1, pp. 373–380, 2013, doi: 10.1016/j.thoracsur.2012.07.077.

- [66] E. Lim *et al.*, “A method for control of an implantable rotary blood pump for heart failure patients using noninvasive measurements,” *Artif. Organs*, vol. 35, no. 8, pp. E174–E180, 2011, doi: 10.1111/j.1525-1594.2011.01268.x.
- [67] K. W. Gwak, “Application of extremum seeking control to turbodynamic blood pumps,” *ASAIO J.*, vol. 53, no. 4, pp. 403–409, 2007, doi: 10.1097/MAT.0b013e31806ada0a.
- [68] S. Bozkurt, “Physiologic outcome of varying speed rotary blood pump support algorithms: a review study,” *Australasian Physical and Engineering Sciences in Medicine*, vol. 39, no. 1. Springer Netherlands, pp. 13–28, 2016, doi: 10.1007/s13246-015-0405-y.
- [69] F. Huang, Z. Gou, and Y. Fu, “Preliminary evaluation of a predictive controller for a rotary blood pump based on pulmonary oxygen gas exchange,” *Proc. Inst. Mech. Eng. Part H J. Eng. Med.*, vol. 233, no. 2, pp. 267–278, 2019, doi: 10.1177/0954411918823035.
- [70] Y. Wu and Q. Zheng, “ADRC or adaptive controller - A simulation study on artificial blood pump,” *Comput. Biol. Med.*, vol. 66, pp. 135–143, 2015, doi: 10.1016/j.combiomed.2015.09.006.
- [71] D. Rüschen, S. Opitz, P. von Platen, L. Korn, S. Leonhardt, and M. Walter, “Robust physiological control of rotary blood pumps for heart failure therapy,” *- Autom.*, vol. 66, no. 9, pp. 767–779, 2018, doi: 10.1515/aut-2018-0014.

- [72] M. Habigt *et al.*, “Comparison of novel physiological load-Adaptive control strategies for ventricular assist devices,” *Biomed. Tech.*, vol. 62, no. 2, pp. 149–160, 2017, doi: 10.1515/bmt-2016-0073.
- [73] A. Arndt, P. Nüsser, K. Graichen, J. Müller, and B. Lampe, “Physiological control of a rotary blood pump with selectable therapeutic options: Control of pulsatility gradient,” *Artif. Organs*, vol. 32, no. 10, pp. 761–771, 2008, doi: 10.1111/j.1525-1594.2008.00628.x.
- [74] J. P. Pauls, S. D. Gregory, M. Stevens, and G. Tansley, “In-vitro evaluation of physiological controller response of rotary blood pumps to changes in patient state,” *Conf. Proc. Annu. Int. Conf. IEEE Eng. Med. Biol. Soc. IEEE Eng. Med. Biol. Soc. Annu. Conf.*, vol. 2014, pp. 294–297, 2014, doi: 10.1109/EMBC.2014.6943587.
- [75] G. A. Giridharan and M. Skliar, “Nonlinear controller for ventricular assist devices,” *Artif Organs*, vol. 26, no. 11, pp. 980–984, 2002.
- [76] G. A. Giridharan and M. Skliar, “Control strategy for maintaining physiological perfusion with rotary blood pumps,” *Artif. Organs*, vol. 27, no. 7, pp. 639–648, 2003, doi: 10.1046/j.1525-1594.2003.07089.x.
- [77] T. Waters *et al.*, “Motor feedback physiological control for a continuous flow ventricular assist device,” *Artif Organs*, vol. 23, no. 6, pp. 480–486, 1999.
- [78] G. A. Giridharan and M. Skliar, “Physiological control of blood pumps using intrinsic pump parameters: A computer simulation study,” *Artif. Organs*, vol. 30, no. 4, pp. 301–307, 2006.
- [79] G. A. Giridharan, G. M. Pantalos, K. J. Gillars, S. C. Koenig, and M. Skliar,

- "Physiologic control of rotary blood pumps: An in vitro study," *ASAIO J.*, vol. 50, no. 5, pp. 403–409, 2004, doi: 10.1097/01.MAT.0000136652.78197.58.
- [80] A. Arndt, P. Nüsser, and B. Lampe, "Fully autonomous preload-sensitive control of implantable rotary blood pumps," *Artif Organs*, vol. 34, no. 9, pp. 726–735, 2010.
  - [81] Y. Wu, P. Allaire, G. Tao, H. Wood, D. Olsen, and C. Tribble, "An advanced physiological controller design for a left ventricular assist device to prevent left ventricular collapse," *Artif Organs*, vol. 27, no. 10, pp. 926–930, 2003.
  - [82] E. Bullister, S. Reich, P. D'Entremont, N. Silverman, and J. Sluetz, "A blood pressure sensor for long-term implantation," *Artif. Organs*, vol. 25, no. 5, pp. 376–379, 2001, doi: 10.1046/j.1525-1594.2001.025005376.x.
  - [83] P. B. Adamson, W. T. Abraham, R. C. Bourge, L. W. Stevenson, and J. Yadav, "CardioMEMS heart sensor allows monitoring of pressures to improve outcomes in NYHA class III heart failure patients (CHAMPION) trial: impact of hemodynamic guided care on patients with preserved ejection fraction," *J. Card. Fail.*, vol. 16, no. 11, p. 913, 2010, doi: 10.1016/j.cardfail.2010.09.012.
  - [84] R. W. Troughton *et al.*, "Direct left atrial pressure monitoring in severe heart failure: Long-term sensor performance," *J. Cardiovasc. Transl. Res.*, vol. 4, no. 1, pp. 3–13, 2011, doi: 10.1007/s12265-010-9229-z.
  - [85] W. T. Abraham *et al.*, "Safety and accuracy of a wireless pulmonary artery pressure monitoring system in patients with heart failure," *Am. Heart J.*,

- vol. 161, no. 3, pp. 558–566, 2011, doi: 10.1016/j.ahj.2010.10.041.
- [86] A. H. H. AlOmari *et al.*, “Non-invasive estimation and control of inlet pressure in an implantable rotary blood pump for heart failure patients,” *Physiol. Meas.*, vol. 32, no. 8, pp. 1035–1060, 2011, doi: 10.1088/0967-3334/32/8/004.
  - [87] A. Petrou *et al.*, “A physiological controller for turbodynamic ventricular assist devices based on left ventricular systolic pressure,” *Artif. Organs*, vol. 40, no. 9, pp. 842–855, 2016, doi: 10.1111/aor.12820.
  - [88] H. Nishida, T. Nishinaka, and M. Endo, “Clinical application of a newly developed autoflow control System for the terumo centrifugal pump: from external control to built-in direct control,” *Artif. Organs*, vol. 20, no. 6, pp. 625–631, 1996.
  - [89] F. Casas, A. Orozco, and W. A. Smith, “A fuzzy system cardio pulmonary bypass rotary blood pump controller,” *Expert Syst. Appl.*, vol. 26, no. 3, pp. 357–361, 2004.
  - [90] S. Choi, J. F. Antaki, J. Robert Boston, and D. Thomas, “A sensorless approach to control of a turbodynamic left ventricular assist system,” *IEEE Trans. Control Syst. Technol.*, vol. 9, no. 3, pp. 473–482, 2001, doi: 10.1109/87.918900.
  - [91] E. H. Maslen *et al.*, “Feedback control applications in artificial hearts,” *IEEE Control Syst. Mag.*, vol. 18, no. 6, pp. 26–34, 1998.
  - [92] R. F. Salamonsen, E. Lim, and N. Gaddum, “Theoretical foundations of a Starling-like controller for rotary blood pumps,” *Artif Organs*, vol. 36, no. 9, pp. 787–796, 2012.

- [93] M. C. Stevens *et al.*, “Frank-Starling control of a left ventricular assist device,” *2011 Annu. Int. Conf. IEEE Eng. Med. Biol. Soc.*, pp. 1335–1338, 2011, doi: 10.1109/IEMBS.2011.6090314.
- [94] M. A. Bakouri, R. F. Salamonsen, A. V. Savkin, A. H. H. Alomari, E. Lim, and N. H. Lovell, “A sliding mode-based Starling-like controller for implantable rotary blood pumps,” *Artif. Organs*, vol. 38, no. 7, pp. 587–593, 2014, doi: 10.1111/aor.12223.
- [95] M. A. Bakouri, A. V. Savkin, and A. H. Alomari, “Nonlinear modelling and control of left ventricular assist device,” *Electron. Lett.*, vol. 51, no. 8, pp. 613–615, 2015, doi: 10.1049/el.2014.4330.
- [96] M. Mansouri, R. F. Salamonsen, E. Lim, R. Akmeliaawati, and N. H. Lovell, “Preload-based starling-like control for rotary blood pumps:Numerical comparison with pulsatility control and constant speed operation,” *PLoS One*, vol. 10, no. 4, pp. 1–16, 2015, doi: 10.1371/journal.pone.0121413.
- [97] F. Moscato, M. Arabia, F. M. Colacino, P. Naiyanetr, G. A. Danieli, and H. Schima, “Left ventricle afterload impedance control by an axial flow ventricular assist device: A potential tool for ventricular recovery,” *Artif. Organs*, vol. 34, no. 9, pp. 736–744, 2010.
- [98] G. Ochsner *et al.*, “A physiological controller for turbodynamic ventricular assist devices based on a measurement of the left ventricular volume,” *Artif. Organs*, vol. 38, no. 7, pp. 527–538, 2014, doi: 10.1111/aor.12225.
- [99] J. R. Boston, J. F. Antaki, and M. A. Simaan, “Hierarchical control of heart-assist devices,” *Robot. Autom. Mag. IEEE*, vol. 10, no. 1, pp. 54–64, 2003.

- [100] K.-W. Gwak, M. Ricci, and S. Snyder, “In vitro evaluation of multiobjective hemodynamic control of a heart-assist pump,” *ASAIO J.*, vol. 51, no. 4, pp. 329–335, 2005.
- [101] K. Ogata, *Modern Control Engineering*. Prentice Hall, 2010.
- [102] E. Lim *et al.*, “Hemodynamic response to exercise and head-up tilt of patients implanted with a rotary blood pump: A computational modeling study,” *Artif. Organs*, vol. 39, no. 2, pp. E24–E35, 2015, doi: 10.1111/aor.12370.
- [103] A. Petrou, J. Lee, S. Dual, G. Ochsner, M. Meboldt, and M. Schmid Daners, “Standardized comparison of selected physiological controllers for rotary blood pumps: In vitro study,” *Artif. Organs*, vol. 42, no. 3, pp. E29–E42, 2018, doi: 10.1111/aor.12999.
- [104] A. Verbeni *et al.*, “An innovative adaptive control strategy for sensorized left ventricular assist devices,” *IEEE Trans. Biomed. Circuits Syst.*, vol. 8, no. 5, pp. 660–668, 2014, doi: 10.1109/TBCAS.2014.2346015.
- [105] M. A. Bakouri, “Sensorless Physiological Control of Implantable Rotary Blood Pumps for Heart Failure Patients Using Modern Control Techniques,” 2014, [Online]. Available: <http://arxiv.org/abs/1405.2419>.
- [106] A. H. H. Alomari *et al.*, “Non-invasive measurements based model predictive control of pulsatile flow in an implantable rotary blood pump for heart failure patients,” *2011 19th Mediterr. Conf. Control Autom. MED 2011*, pp. 491–496, 2011, doi: 10.1109/MED.2011.5982982.
- [107] M. Charest and R. Dubay, “MPC enhancement for tracking of complex profiles - The basic technique,” *Control Eng. Pract.*, vol. 33, pp. 136–147,

- 2014, doi: 10.1016/j.conengprac.2014.09.012.
- [108] N. Öztürk and E. Çelik, "Speed control of permanent magnet synchronous motors using fuzzy controller based on genetic algorithms," *Int. J. Electr. Power Energy Syst.*, vol. 43, no. 1, pp. 889–898, 2012, doi: 10.1016/j.ijepes.2012.06.013.
- [109] F. Casas, N. Ahmed, and A. Reeves, "Minimal sensor count approach to fuzzy logic rotary blood pump flow control," *ASAIO J.*, vol. 53, no. 2, pp. 140–146, Mar. 2007, doi: 10.1097/01.mat.0000250786.56697.f2.
- [110] M. Fu and L. Xu, "Computer simulation of sensorless fuzzy control of a rotary blood pump to assure normal physiology," *ASAIO J.*, vol. 46, no. 3, pp. 273–278, 2000.
- [111] Z. Hou and S. Jin, *Model free adaptive control: theory and applications*. CRC Press, 2013.
- [112] I. D. Landau, R. Lozano, M. M'Saad, and A. Karimi, *Adaptive Control, Algorithms, Analysis and Applications*. Springer, 2011.
- [113] Y. Wu, "Adaptive physiological speed/flow control of rotary blood pumps in permanent implantation using intrinsic pump parameters," *ASAIO J.*, vol. 55, no. 4, pp. 335–339, 2009, doi: 10.1097/MAT.0b013e3181aa2554.
- [114] E. Pektok *et al.*, "Remote monitoring of left ventricular assist device parameters after heartassist-5 implantation," *Artif. Organs*, vol. 37, no. 9, pp. 820–825, 2013, doi: 10.1111/aor.12144.
- [115] T. Tsukiya, T. Akamatsu, and K. Nishimura, "Flow rate measurement for the magnetically suspended centrifugal blood pump," *Japanese J. Artif. Organs*, vol. 26, no. 1, pp. 98–102, 1997, doi: 10.11392/jsao1972.26.98.

- [116] T. Kitamura *et al.*, “Physical model-based indirect measurements of blood pressure and flow using a centrifugal pump,” *Artif. Organs*, vol. 24, no. 8, pp. 589–593, 2000, doi: 10.1046/j.1525-1594.2000.06605.x.
- [117] M. Granegger, F. Moscato, F. Casas, G. Wieselthaler, and H. Schima, “Development of a pump flow estimator for rotary blood pumps to enhance monitoring of ventricular function,” *Artif. Organs*, vol. 36, no. 8, pp. 691–699, 2012, doi: 10.1111/j.1525-1594.2012.01503.x.
- [118] F. Moscato, G. A. Danieli, and H. Schima, “Dynamic modeling and identification of an axial flow ventricular assist device,” *Int. J. Artif. Organs*, vol. 32, no. 6, pp. 336–343, 2009, doi: 10.1177/039139880903200604.
- [119] A. Tanaka, M. Yoshizawa, K. I. Abe, H. Takeda, T. Yambe, and S. I. Nitta, “In vivo test of pressure head and flow rate estimation in a continuous-flow artificial heart,” *Artif. Organs*, vol. 27, no. 1, pp. 99–103, 2003, doi: 10.1046/j.1525-1594.2003.07175.x.
- [120] M. Yoshizawam *et al.*, “Sensorless estimation of pressure head and flow of a continuous flow artificial heart based on input power and rotational speed,” *ASAIO J.*, pp. 443–448, 2002.
- [121] D. M. Karantonis, S. L. Cloherty, D. G. Mason, P. J. Ayre, and N. H. Lovell, “Noninvasive pulsatile flow estimation for an implantable rotary blood pump,” in *29th Annual International Conference of the IEEE Engineering in Medicine and Biology*, 2007, pp. 1018–1021, doi: 10.1109/IEMBS.2007.4352467.
- [122] A. H. AlOmari, A. V Savkin, D. M. Karantonis, E. Lim, and N. H. Lovell,

- “Non-invasive estimation of pulsatile flow and differential pressure in an implantable rotary blood pump for heart failure patients,” *Physiol. Meas.*, vol. 30, pp. 371–386, 2009, doi: 10.1088/0967-3334/30/4/003.
- [123] N. Malagutti *et al.*, “Noninvasive average flow estimation for an implantable rotary blood pump: A new algorithm incorporating the role of blood viscosity,” *Artif. Organs*, vol. 31, no. 1, pp. 45–52, 2007, doi: 10.1111/j.1525-1594.2007.00339.x.
- [124] W. Hijikata, J. Rao, S. Abe, S. Takatani, and T. Shinshi, “Sensorless viscosity measurement in a magnetically-levitated rotary blood pump,” *Artif. Organs*, vol. 39, no. 7, pp. 559–568, 2015, doi: 10.1111/aor.12440.
- [125] M. Schmid Daners *et al.*, “Left ventricular assist devices: Challenges toward sustaining long-term patient care,” *Annals of Biomedical Engineering*, vol. 45, no. 8, pp. 1836–1851, 2017, doi: 10.1007/s10439-017-1858-9.
- [126] A. Petrou, D. Kuster, J. Lee, M. Meboldt, and M. Schmid Daners, “Comparison of flow estimators for rotary blood pumps: an in vitro and in vivo study,” *Ann. Biomed. Eng.*, vol. 46, no. 12, pp. 2123–2134, 2018, doi: 10.1007/s10439-018-2106-7.
- [127] A. Petrou, M. Kanakis, S. Boes, P. Pergantis, M. Meboldt, and M. S. Daners, “Viscosity prediction in a physiologically controlled ventricular assist device,” *IEEE Trans. Biomed. Eng.*, vol. 65, no. 10, pp. 2355–2364, 2018, doi: 10.1109/TBME.2018.2797424.
- [128] M. Vollkron, H. Schima, L. Huber, R. Benkowski, G. Morello, and G. Wieselthaler, “Development of a suction detection system for axial blood

- pumps,” in *Artificial Organs*, Aug. 2004, vol. 28, no. 8, pp. 709–716, doi: 10.1111/j.1525-1594.2004.00011.x.
- [129] M. Vollkron, H. Schima, L. Huber, R. Benkowski, G. Morello, and G. Wieselthaler, “Advanced suction detection for an axial flow pump,” *Artif. Organs*, vol. 30, no. 9, pp. 665–670, 2006, doi: 10.1111/j.1525-1594.2006.00282.x.
- [130] D. G. Mason, A. K. Hilton, and R. F. Salamonsen, “Reliable suction detection for patients with rotary blood pumps,” *ASAIO J.*, vol. 54, no. 4, pp. 359–366, 2008, doi: 10.1097/MAT.0b013e31817b5b0e.
- [131] Y. Wang and M. A. Simaan, “A suction detection system for rotary blood pumps based on the Lagrangian support vector machine algorithm,” *IEEE J. Biomed. Heal. Informatics*, vol. 17, no. 3, pp. 654–663, 2013, doi: 10.1109/TITB.2012.2228877.
- [132] O. Voigt, R. J. Benkowski, and G. F. Morello, “Suction detection for the MicroMed DeBakey left ventricular assist device,” *ASAIO J.*, vol. 51, no. 4, pp. 321–328, 2005, doi: 10.1097/01.mat.0000169118.21639.da.
- [133] M. Granegger *et al.*, “Continuous monitoring of aortic valve opening in rotary blood pump patients,” *IEEE Trans. Biomed. Eng.*, vol. 63, no. 6, pp. 1201–1207, 2016, doi: 10.1109/TBME.2015.2489188.
- [134] C. Hayward *et al.*, “Pump speed waveform analysis to detect aortic valve opening in patients on ventricular assist device support,” *Artif. Organs*, vol. 39, no. 8, pp. 704–709, 2015, doi: 10.1111/aor.12570.
- [135] M. Granegger, H. Schima, D. Zimpfer, and F. Moscato, “Assessment of aortic valve opening during rotary blood pump support using pump

- signals," *Artif. Organs*, vol. 38, no. 4, pp. 290–297, 2014, doi: 10.1111/aor.12167.
- [136] C. J. Bishop *et al.*, "A novel non-invasive method to assess aortic valve opening in HeartMate II left ventricular assist device patients using a modified Karhunen-Loève transformation," *J. Hear. Lung Transplant.*, vol. 29, no. 1, pp. 27–31, 2010, doi: 10.1016/j.healun.2009.08.027.
- [137] A. Funakubo, S. Ahmed, I. Sakuma, and Y. Fukui, "Flow rate and pressure head estimation in a centrifugal blood pump," *Artif. Organs*, vol. 26, no. 11, pp. 985–990, 2002, doi: 10.1046/j.1525-1594.2002.07134.x.
- [138] A. H. Alomari, A. V. Savkin, D. M. Karantonis, E. Lim, and N. H. Lovell, "Non-invasive estimation of pulsatile flow and differential pressure in an implantable rotary blood pump for heart failure patients," *Physiol. Meas.*, vol. 30, no. 4, pp. 371–386, 2009, doi: 10.1088/0967-3334/30/4/003.
- [139] J. Grinstein *et al.*, "HVAD waveform analysis as a noninvasive marker of pulmonary capillary wedge pressure: A first step toward the development of a smart left ventricular assist device pump," *ASAIO J.*, vol. 64, no. 1, pp. 10–15, 2018, doi: 10.1097/MAT.0000000000000604.
- [140] F. Moscato, M. Granegger, M. Edelmayer, D. Zimpfer, and H. Schima, "Continuous monitoring of cardiac rhythms in left ventricular assist device patients," *Artif. Organs*, vol. 38, no. 3, pp. 191–198, 2014, doi: 10.1111/aor.12141.
- [141] F. Moscato, M. Granegger, P. Naiyanetr, G. Wieselthaler, and H. Schima, "Evaluation of left ventricular relaxation in rotary blood pump recipients

- using the pump flow waveform: A simulation study," *Artif. Organs*, vol. 36, no. 5, pp. 470–478, 2012, doi: 10.1111/j.1525-1594.2011.01392.x.
- [142] P. Naiyanetr, F. Moscato, M. Vollkron, D. Zimpfer, G. Wieselthaler, and H. Schima, "Continuous assessment of cardiac function during rotary blood pump support: A contractility index derived from pump flow," *J. Hear. Lung Transplant.*, vol. 29, no. 1, pp. 37–44, 2010, doi: 10.1016/j.healun.2009.05.032.
- [143] S. Haykin, *Neural Networks and Learning Machines*, 3rd ed. Pearson Education India, 2010.
- [144] C. C. Aggarwal, *Neural Networks and Deep Learning*. 2018.
- [145] K. Fukushima, "Neocognitron: A self-organizing neural network model for a mechanism of pattern recognition unaffected by shift in position," *Biol. Cybern.*, vol. 36, no. 4, pp. 193–202, 1980, doi: 10.1007/BF00344251.
- [146] Y. LeCun, L. Bottou, Y. Bengio, and P. Haffner, "Gradient-based learning applied to document recognition," *Proc. IEEE*, vol. 86, no. 11, pp. 2278–2323, 1998, doi: 10.1109/5.726791.
- [147] I. Goodfellow, Y. Bengio, and A. Courville, "Deep learning," *MIT Press*, vol. 1, no. 2, 2016, doi: 10.1016/B978-0-12-391420-0.09987-X.
- [148] A. Krizhevsky, I. Sutskever, and G. E. Hinton, "ImageNet classification with deep convolutional neural networks," 2012, doi: 10.1016/B978-008046518-0.00119-7.
- [149] E. A. Rose *et al.*, "The REMATCH trial: rationale, design, and end points. randomized evaluation of mechanical assistance for the treatment of

- congestive heart failure.," *Ann. Thorac. Surg.*, vol. 67, no. 3, pp. 723–30, Mar. 1999, Accessed: Aug. 12, 2018. [Online]. Available: <http://www.ncbi.nlm.nih.gov/pubmed/10215217>.
- [150] K. Reesink *et al.*, "Suction due to left ventricular assist: Implications for device control and management," *Artif. Organs*, vol. 31, no. 7, pp. 542–549, Jul. 2007, doi: 10.1111/j.1525-1594.2007.00420.x.
- [151] E. Bullister, S. Reich, and J. Sluetz, "Physiologic control algorithms for rotary blood pumps using pressure sensor input," *Artif Organs*, vol. 26, no. 11, pp. 931–938, 2002.
- [152] N. R. Gaddum, D. L. Timms, M. Stevens, D. Mason, N. Lovell, and J. F. Fraser, "Comparison of preload-sensitive pressure and flow controller strategies for a dual device biventricular support system," *Artif. Organs*, vol. 36, no. 3, pp. 256–265, 2012, doi: 10.1111/j.1525-1594.2011.01344.x.
- [153] B. C. Ng *et al.*, "Application of multiobjective neural predictive control to biventricular assistance using dual rotary blood pumps," *Biomed. Signal Process. Control*, vol. 39, pp. 81–93, 2018, doi: 10.1016/j.bspc.2017.07.028.
- [154] Z. Hou and S. Jin, "Data-driven model-free adaptive control for a class of MIMO nonlinear discrete-time systems," *IEEE Trans. Neural Networks*, vol. 22, no. 12 PART 2, pp. 2173–2188, 2011, doi: 10.1109/TNN.2011.2176141.
- [155] E. Lim, S. Dokos, R. F. Salamonsen, F. L. Rosenfeldt, P. J. Ayre, and N. H. Lovell, "Effect of parameter variations on the hemodynamic response

- under rotary blood pump assistance,” *Artif. Organs*, vol. 36, no. 5, pp. E125–E137, 2012, doi: 10.1111/j.1525-1594.2012.01448.x.
- [156] E. Lim *et al.*, “A dynamic lumped parameter model of the left ventricular assisted,” in *Proc. 29th Annu. Int. Conf. IEEE Eng. Med. Biol. Soc., Lyon, France*, 2007, pp. 3990– 3993.
- [157] Zhongsheng Hou and Shangtai Jin, “A novel data-driven control approach for a class of discrete-time nonlinear systems,” *IEEE Trans. Control Syst. Technol.*, vol. 19, no. 6, pp. 335–338, 2011, doi: 10.1109/TCST.2010.2093136.
- [158] L. M. Mielniczuk *et al.*, “Left ventricular end-diastolic pressure and risk of subsequent heart failure in patients following an acute myocardial infarction.,” *Congest. Heart Fail.*, vol. 13, no. 4, pp. 209–214, 2007, doi: 10.1111/j.1527-5299.2007.06624.x.
- [159] D. L. Eckberg, M. Drabinsky, and E. Braunwald, “Defective cardiac parasympathetic control in patients with heart disease,” *N. Engl. J. Med.*, vol. 285, no. 16, pp. 877–883, Oct. 1971, doi: 10.1056/NEJM197110142851602.
- [160] a Al Omari *et al.*, “Non-invasive estimation and control of inlet pressure in an implantable rotary blood pump for heart failure patients.,” *Physiol. Meas.*, vol. 32, no. 8, pp. 1035–1060, 2009, doi: 10.1088/0967-3334/32/8/004.
- [161] M. Fetanat, M. Stevens, C. Hayward, and N. H. Lovell, “A Sensorless Control System for an Implantable Heart Pump using a Real-time Deep Convolutional Neural Network,” *IEEE Trans. Biomed. Eng.*, vol. 68, no. 10,

- pp. 3029–3038, 2021, doi: 10.1109/TBME.2021.3061405.
- [162] K. Reesink *et al.*, “Suction due to left ventricular assist: Implications for device control and management,” *Artif. Organs*, vol. 31, no. 7, pp. 542–549, 2007, doi: 10.1111/j.1525-1594.2007.00420.x.
- [163] R. F. Salamonsen *et al.*, “Theoretical foundations of a Starling-like controller for rotary blood pumps,” *Artif Organs*, vol. 36, no. 9, pp. 787–796, 2012, doi: 10.1111/j.1525-1594.2012.01457.x.
- [164] S. Boës, B. Thamsen, M. Haas, M. S. Daners, M. Meboldt, and M. Granegger, “Hydraulic characterization of implantable rotary blood pumps,” *IEEE Trans. Biomed. Eng.*, vol. 66, no. 6, pp. 1618–1927, 2019, doi: 10.1109/TBME.2018.2876840.
- [165] C. Krittawong *et al.*, “Deep learning for cardiovascularmedicine: A practical primer,” *Eur. Heart J.*, vol. 40, no. 25, pp. 2058–2069C, 2019, doi: 10.1093/eurheartj/ehz056.
- [166] S. Kiranyaz, T. Ince, and M. Gabbouj, “Real-time patient-specific ECG classification by 1-D convolutional neural networks,” *IEEE Trans. Biomed. Eng.*, vol. 63, no. 3, pp. 664–675, 2016, doi: 10.1109/TBME.2015.2468589.
- [167] J. M. Bland and D. G. Altman, “Statistical methods for assessing agreement between two methods of clinical measurement,” *Lancet*, vol. 8476, no. 327, pp. 307–310, 1986, doi: 10.1016/j.ajo.2008.09.032.
- [168] G. F. Reed, F. Lynn, and B. D. Meade, “Use of coefficient of variation in assessing variability of quantitative assays,” vol. 9, no. 6, pp. 1235–1239, 2002, doi: 10.1128/CDLI.9.6.1235.

- [169] D. P. Kingma and J. L. Ba, “Adam: A method for stochastic optimization,” in *3rd International Conference on Learning Representations, ICLR 2015 - Conference Track Proceedings*, 2015, pp. 1–15.
- [170] K. He, X. Zhang, S. Ren, and J. Sun, “Delving deep into rectifiers: Surpassing human-level performance on imagenet classification,” *Proc. IEEE Int. Conf. Comput. Vis.*, vol. 2015 Inter, pp. 1026–1034, 2015, doi: 10.1109/ICCV.2015.123.
- [171] Z. Hou and S. Xiong, “On model-free adaptive control and its stability analysis,” *IEEE Trans. Automat. Contr.*, vol. 64, no. 11, pp. 4555–4569, 2019.
- [172] R. Kohavi, “A study of cross-validation and bootstrap for accuracy estimation and model selection,” *Ijcai*, vol. 14, no. 2, 1995.
- [173] Y. Wu, “Adaptive physiological speed/flow control of rotary blood pumps in permanent implantation using intrinsic pump parameters,” *ASAIO J.*, vol. 55, no. 4, pp. 335–339, 2009, doi: 10.1097/MAT.0b013e3181aa2554.
- [174] Y. Kim, J. S. Choi, and M. Kim, “A real-time convolutional neural network for super-resolution on FPGA with applications to 4K UHD 60 fps Video Services,” *IEEE Trans. Circuits Syst. Video Technol.*, vol. 29, no. 8, pp. 2521–2534, 2019, doi: 10.1109/TCSVT.2018.2864321.
- [175] M. Fetanat, M. C. Stevens, P. Jain, C. S. Hayward, E. Meijering, and N. H. Lovell, “Fully Elman Neural Network: A Novel Deep Recurrent Neural Network Optimized by an Improved Harris Hawks Algorithm for Classification of Pulmonary Arterial Wedge Pressure,” *IEEE Trans. Biomed. Eng. Eng.*, 2022.

- [176] J. Wang, “A deep learning approach for atrial fibrillation signals classification based on convolutional and modified Elman neural network,” *Futur. Gener. Comput. Syst.*, vol. 102, pp. 670–679, 2020, doi: 10.1016/j.future.2019.09.012.
- [177] G. Sannino and G. De Pietro, “A deep learning approach for ECG-based heartbeat classification for arrhythmia detection,” *Futur. Gener. Comput. Syst.*, vol. 86, pp. 446–455, 2018, doi: 10.1016/j.future.2018.03.057.
- [178] U. B. Baloglu, M. Talo, O. Yildirim, R. S. Tan, and U. R. Acharya, “Classification of myocardial infarction with multi-lead ECG signals and deep CNN,” *Pattern Recognit. Lett.*, vol. 122, pp. 23–30, 2019, doi: 10.1016/j.patrec.2019.02.016.
- [179] A. Y. Hannun *et al.*, “Cardiologist-level arrhythmia detection and classification in ambulatory electrocardiograms using a deep neural network,” *Nat. Med.*, vol. 25, no. 1, pp. 65–69, 2019, doi: 10.1038/s41591-018-0268-3.
- [180] X. Xu and H. Liu, “ECG heartbeat classification using convolutional neural networks,” *IEEE Access*, vol. 8, pp. 8614–8619, 2020, doi: 10.1109/ACCESS.2020.2964749.
- [181] W. Cai *et al.*, “Accurate detection of atrial fibrillation from 12-lead ECG using deep neural network,” *Comput. Biol. Med.*, vol. 116, no. May 2019, p. 103378, 2020, doi: 10.1016/j.combiomed.2019.103378.
- [182] O. Yildirim, U. B. Baloglu, R. S. Tan, E. J. Ciaccio, and U. R. Acharya, “A new approach for arrhythmia classification using deep coded features and LSTM networks,” *Comput. Methods Programs Biomed.*, vol. 176, pp.

- 121–133, 2019, doi: 10.1016/j.cmpb.2019.05.004.
- [183] U. R. Acharya *et al.*, “Automated identification of shockable and non-shockable life-threatening ventricular arrhythmias using convolutional neural network,” *Futur. Gener. Comput. Syst.*, vol. 79, pp. 952–959, 2018, doi: 10.1016/j.future.2017.08.039.
- [184] H. M. Lynn, S. B. Pan, and P. Kim, “A deep bidirectional GRU network model for biometric electrocardiogram classification based on recurrent neural networks,” *IEEE Access*, vol. 7, pp. 145395–145405, 2019, doi: 10.1109/ACCESS.2019.2939947.
- [185] R. He *et al.*, “Automatic cardiac arrhythmia classification using combination of deep residual network and bidirectional LSTM,” *IEEE Access*, vol. 7, pp. 102119–102135, 2019, doi: 10.1109/access.2019.2931500.
- [186] M. M. Al Rahhal, Y. Bazi, H. Almubarak, N. Alajlan, and M. Al Zuair, “Dense convolutional networks with focal loss and image generation for electrocardiogram classification,” *IEEE Access*, vol. 7, pp. 182225–182237, 2019, doi: 10.1109/ACCESS.2019.2960116.
- [187] G. Wang *et al.*, “A global and updatable ECG beat classification system based on recurrent neural networks and active learning,” *Inf. Sci. (Ny)*, vol. 501, pp. 523–542, 2019, doi: 10.1016/j.ins.2018.06.062.
- [188] J. Wang, “Automated detection of atrial fibrillation and atrial flutter in ECG signals based on convolutional and improved Elman neural network,” *Knowledge-Based Syst.*, vol. 193, p. 105446, 2020, doi: 10.1016/j.knosys.2019.105446.

- [189] G. Ren, Y. Cao, S. Wen, T. Huang, and Z. Zeng, “A modified Elman neural network with a new learning rate scheme,” *Neurocomputing*, vol. 286, pp. 11–18, 2018, doi: 10.1016/j.neucom.2018.01.046.
- [190] K. H. Lu, C. M. Hong, and Q. Xu, “Recurrent wavelet-based Elman neural network with modified gravitational search algorithm control for integrated offshore wind and wave power generation systems,” *Energy*, vol. 170, pp. 40–52, 2019, doi: 10.1016/j.energy.2018.12.084.
- [191] Y. Wang, L. Wang, F. Yang, W. Di, and Q. Chang, “Advantages of direct input-to-output connections in neural networks: The Elman network for stock index forecasting,” *Inf. Sci. (Ny)*., vol. 547, pp. 1066–1079, 2021, doi: 10.1016/j.ins.2020.09.031.
- [192] Y. Xu *et al.*, “An efficient chaotic mutative moth-flame-inspired optimizer for global optimization tasks,” *Expert Syst. Appl.*, vol. 129, no. 2019, pp. 135–155, 2019, doi: 10.1016/j.eswa.2019.03.043.
- [193] A. Darwish, D. Ezzat, and A. E. Hassanien, “An optimized model based on convolutional neural networks and orthogonal learning particle swarm optimization algorithm for plant diseases diagnosis,” *Swarm Evol. Comput.*, vol. 52, no. July 2019, p. 100616, 2020, doi: 10.1016/j.swevo.2019.100616.
- [194] R. ZahediNasab and H. Mohseni, “Neuroevolutionary based convolutional neural network with adaptive activation functions,” *Neurocomputing*, vol. 381, pp. 306–313, 2020, doi: 10.1016/j.neucom.2019.11.090.
- [195] I. Ilievski, T. Akhtar, J. Feng, and C. A. Shoemaker, “Efficient

- hyperparameter optimization of deep learning algorithms using deterministic RBF surrogates," *31st AAAI Conf. Artif. Intell. AAAI 2017*, pp. 822–829, 2017.
- [196] S. Nazir, S. Patel, and D. Patel, "Assessing hyper parameter optimization and speedup for convolutional neural networks," *Int. J. Artif. Intell. Mach. Learn.*, vol. 10, no. 2, pp. 1–17, 2020, doi: 10.4018/ijaiml.2020070101.
- [197] E. Bochinski, T. Senst, and T. Sikora, "Hyper-parameters optimization for convolutional neural network committees based on the evolutionary algorothms," *2017 IEEE Int. Conf. Image Process.*, pp. 3–7, 2017.
- [198] A. A. Heidari, S. Mirjalili, H. Faris, I. Aljarah, M. Mafarja, and H. Chen, "Harris hawks optimization: Algorithm and applications," *Futur. Gener. Comput. Syst.*, vol. 97, pp. 849–872, 2019, doi: 10.1016/j.future.2019.02.028.
- [199] R. Eberhart and James Kennedy, "A new optimizer using particle swarm theory," *Int. Symp. Micro Mach. Hum. Sci.*, pp. 39–43, 1999, [Online]. Available:  
[https://bytebucket.org/12er/pso/raw/b448ff0db375c1ac0c55855e9f19aced08b44ca6/doc/literature/Variants/topology/A new Optimizer using Particle Swarm Theory.pdf](https://bytebucket.org/12er/pso/raw/b448ff0db375c1ac0c55855e9f19aced08b44ca6/doc/literature/Variants/topology/A%20new%20Optimizer%20using%20Particle%20Swarm%20Theory.pdf).
- [200] R. Storn and K. Price, "Differential evolution – A simple and efficient heuristic for global optimization over continuous spaces," *J. of Global Optim.*, vol. 11, pp. 341–359, 1997, doi: 10.1071/AP09004.
- [201] E. Rashedi, H. Nezamabadi-pour, and S. Saryazdi, "GSA: A gravitational

- search algorithm," *Inf. Sci. (Ny)*., vol. 179, no. 13, pp. 2232–2248, 2009, doi: 10.1016/j.ins.2009.03.004.
- [202] A. Faramarzi, M. Heidarinejad, S. Mirjalili, and A. H. Gandomi, "Marine predators algorithm: A nature-inspired metaheuristic," *Expert Syst. Appl.*, vol. 152, p. 113377, 2020, doi: 10.1016/j.eswa.2020.113377.
- [203] S. Li, H. Chen, M. Wang, A. A. Heidari, and S. Mirjalili, "Slime mould algorithm: A new method for stochastic optimization," *Futur. Gener. Comput. Syst.*, vol. 111, pp. 300–323, 2020, doi: 10.1016/j.future.2020.03.055.
- [204] A. Faramarzi, M. Heidarinejad, B. Stephens, and S. Mirjalili, "Equilibrium optimizer: A novel optimization algorithm," *Knowledge-Based Syst.*, vol. 191, p. 105190, 2020, doi: 10.1016/j.knosys.2019.105190.
- [205] S. Mirjalili, A. H. Gandomi, S. Z. Mirjalili, S. Saremi, H. Faris, and S. M. Mirjalili, "Salp swarm algorithm: A bio-inspired optimizer for engineering design problems," *Adv. Eng. Softw.*, vol. 114, pp. 163–191, 2017, doi: 10.1016/j.advengsoft.2017.07.002.
- [206] S. Mirjalili, S. M. Mirjalili, and A. Lewis, "Grey wolf optimizer," *Adv. Eng. Softw.*, vol. 69, pp. 46–61, 2014, doi: 10.1016/j.advengsoft.2013.12.007.
- [207] S. Gupta, K. Deep, and S. Mirjalili, "An efficient equilibrium optimizer with mutation strategy for numerical optimization," *Appl. Soft Comput. J.*, vol. 96, p. 106542, 2020, doi: 10.1016/j.asoc.2020.106542.
- [208] D. H. Wolpert and W. G. Macready, "No free lunch theorems for optimization," *IEEE Trans. Evol. Comput.*, vol. 1, no. 1, pp. 67–82, 1997, doi: 10.1109/4235.585893.

- [209] S. Gupta, K. Deep, A. A. Heidari, H. Moayedi, and M. Wang, "Opposition-based learning Harris hawks optimization with advanced transition rules: principles and analysis," *Expert Syst. Appl.*, vol. 158, p. 113510, 2020, doi: 10.1016/j.eswa.2020.113510.
- [210] H. Chen, A. A. Heidari, H. Chen, M. Wang, Z. Pan, and A. H. Gandomi, "Multi-population differential evolution-assisted Harris hawks optimization: Framework and case studies," *Futur. Gener. Comput. Syst.*, vol. 111, pp. 175–198, 2020, doi: 10.1016/j.future.2020.04.008.
- [211] M. A. Elaziz, A. A. Heidari, H. Fujita, and H. Moayedi, "A competitive chain-based Harris hawks optimizer for global optimization and multi-level image thresholding problems," *Appl. Soft Comput. J.*, vol. 95, p. 106347, 2020, doi: 10.1016/j.asoc.2020.106347.
- [212] S. Jiao *et al.*, "Orthogonally adapted Harris hawks optimization for parameter estimation of photovoltaic models," *Energy*, vol. 203, p. 117804, 2020, doi: 10.1016/j.energy.2020.117804.
- [213] E. H. Houssein, M. E. Hosney, D. Oliva, W. M. Mohamed, and M. Hassaballah, "A novel hybrid Harris hawks optimization and support vector machines for drug design and discovery," *Comput. Chem. Eng.*, vol. 133, p. 106656, 2020, doi: 10.1016/j.compchemeng.2019.106656.
- [214] J. C. Bednarz, "Cooperative hunting in harris' hawks (*parabuteo unicinctus*)," *Science (80-.)*, vol. 239, no. 4847, pp. 1525–1527, 1988.
- [215] X.-S. Yang, *Firefly algorithm, levy flights and global optimization. In Research and development in intelligent systems*. Springer, 2010.
- [216] N. Srivastava, G. Hinton, A. Krizhevsky, I. Sutskever, and R. Salakhutdinov,

- “Dropout: A Simple Way to Prevent Neural Networks from Overfitting,” *J. Mach. Learn. Res.*, vol. 15, pp. 1924–1958, 2014, doi: 10.1109/ICAEES.2016.7888100.
- [217] Z. C. Lipton, J. Berkowitz, and C. Elkan, “A critical review of recurrent neural networks for sequence learning,” pp. 1–38, 2015, [Online]. Available: <http://arxiv.org/abs/1506.00019>.
- [218] H. R. Tizhoosh, “Opposition-based learning: A new scheme for machine intelligence,” *Proc. - Int. Conf. Comput. Intell. Model. Control Autom. CIMCA 2005 Int. Conf. Intell. Agents, Web Technol. Internet*, vol. 1, pp. 695–701, 2005, doi: 10.1109/cimca.2005.1631345.
- [219] S. Rahnamayan, H. R. Tizhoosh, and M. M. A. Salama, “Quasi-oppositional differential evolution,” in *IEEE Congress on Evolutionary Computation*, 2007, pp. 2229–2236.
- [220] H. Chen, W. Li, and X. Yang, “A whale optimization algorithm with chaos mechanism based on quasi-opposition for global optimization problems,” *Expert Syst. Appl.*, vol. 158, p. 113612, 2020, doi: 10.1016/j.eswa.2020.113612.
- [221] M. A. Elaziz and S. Mirjalili, “A hyper-heuristic for improving the initial population of whale optimization algorithm,” *Knowledge-Based Syst.*, vol. 172, pp. 42–63, 2019, doi: 10.1016/j.knosys.2019.02.010.
- [222] M. Ben naceur, M. Akil, R. Saouli, and R. Kachouri, “Fully automatic brain tumor segmentation with deep learning-based selective attention using overlapping patches and multi-class weighted cross-entropy,” *Med. Image Anal.*, vol. 63, 2020, doi: 10.1016/j.media.2020.101692.

- [223] P. Cao *et al.*, “A novel data augmentation method to enhance deep neural networks for detection of atrial fibrillation,” *Biomed. Signal Process. Control*, vol. 56, p. 101675, 2020, doi: 10.1016/j.bspc.2019.101675.
- [224] J. Jiang, H. Zhang, D. Pi, and C. Dai, “A novel multi-module neural network system for imbalanced heartbeats classification,” *Expert Syst. Appl.*, vol. 1, p. 100003, 2019, doi: 10.1016/j.eswa.2019.100003.

ProQuest Number: 31863351

INFORMATION TO ALL USERS

The quality and completeness of this reproduction is dependent on the quality  
and completeness of the copy made available to ProQuest.



Distributed by

ProQuest LLC a part of Clarivate ( 2025).

Copyright of the Dissertation is held by the Author unless otherwise noted.

This work is protected against unauthorized copying under Title 17,  
United States Code and other applicable copyright laws.

This work may be used in accordance with the terms of the Creative Commons license  
or other rights statement, as indicated in the copyright statement or in the metadata  
associated with this work. Unless otherwise specified in the copyright statement  
or the metadata, all rights are reserved by the copyright holder.

ProQuest LLC  
789 East Eisenhower Parkway  
Ann Arbor, MI 48108 USA